

# Optical Shaping of Structural Self-Organization and Topology in Soft Matter

By: Angel Martinez

B.S., California State Polytechnic University, Pomona, 2009

A thesis submitted to the  
Faculty of the Graduate School of the  
University of Colorado in partial fulfillment  
of the requirement for the degree of  
Doctor of Philosophy  
Department of Physics

2014

This thesis entitled:  
Optical Shaping of Structural Self-Organization and Topology in Soft Matter  
written by Angel Martinez  
has been approved for the Department of Physics

---

Ivan Smalyukh, Ph.D.

---

Noel Clark, Ph.D.

Date\_\_\_\_\_

The final copy of this thesis has been examined by the signatories, and we find that both the content and the form meet acceptable presentation standards of scholarly work in the above mentioned discipline.

## Abstract

Martinez, Angel (Ph.D., Physics)

Optical Shaping of Topology in Soft Matter

Thesis directed by Professor Ivan. I. Smalyukh

The study of liquid crystals has brought about many advances and innovations, not only in technology, but also in our basic understanding of the world around us. For example, recent explorations of photo-induced defects and colloidal clusters in chiral nematics reveal topologically nontrivial forms in liquid crystal director fields, such as localized field structures resembling the Hopf and Seifert fibrations. In this work, we use light to control the alignment of liquid crystal director field at surfaces, to define topologically nontrivial geometric shapes of colloidal particles, and to probe the interplay between the topology of defects, director fields and surfaces. We first explore photo-responsive, azobenzene-based surface monolayers as means to optically and dynamically control boundary conditions at liquid crystal interfaces. This enables us to induce localized regions of twisted nematic field and disclination loops, which interact elastically with particle inclusions, providing a new kind of long-range, low-power colloidal manipulation as well as a means for controlling large-scale dynamics of topological defects and colloids. Using this same surface control technique, we pattern topological defects into thin films of polymerized liquid crystals, also functionalized with azobenzene. Irradiation of these films causes internal mechanical stresses that induce changes in the films' topography, depending on the patterned topology of the internal field structure within the photoresponsive liquid crystal polymer. We then employ a two-photon photo-polymerization technique to fabricate chiral, knotted and linked polymer microstructures, which we introduce into nematic liquid crystals. Based on three-photon excitation fluorescence polarizing microscopy studies, we

reconstruct the surrounding 3D director field structure, revealing induced chiral, knotted and linked defect lines and fields. Using videomicroscopy, we characterize the inter-particle elastic forces that govern long range interactions and stabilize self-assembled colloidal configurations. Since there are few examples of practical realization of topological field configurations, these knotted and inter-linked colloids and fields provide a way to gain insights into behavior of other experimentally less accessible physical systems with similar symmetry and topology. Throughout the thesis, my research demonstrated that the topology of soft condensed matter can be shaped by light, laying a groundwork for experimental exploration of low-dimensional topology of fields and surfaces as well as for practical applications of topological relations in designing new forms of self-assembly.

## Contents

### Chapter 1

<b>Introduction</b> .....	<b>1</b>
1.1 Liquid crystals .....	1
1.2 Defects in liquid crystals .....	4
1.3 Nematic colloids.....	5
1.4 Thesis Overview.....	7
1.5 References .....	11

### Chapter 2

<b>Large-area optoelastic manipulation of colloidal particles in liquid crystals using photoresponsive molecular surface monolayers</b> .....	<b>13</b>
2.1 Introduction .....	14
2.2 Results and Discussion.....	16
2.3 Materials and Methods .....	28
2.3.1 Sample Preparation .....	28
2.3.2 Image Projection .....	29
2.4 Conclusion.....	30
2.5 References .....	31

### Chapter 3

<b>Topography from Topology: Photoinduced Surface Features Generated in Liquid Crystal Polymer Networks</b> .....	<b>34</b>
3.1 Introduction .....	34
3.2 Results and discussion.....	35
3.3 Experimental Section .....	46
3.4 Conclusion.....	48
3.5 References .....	50

### Chapter 4

<b>Three-dimensional complex-shaped photopolymerized microparticles at liquid crystal interfaces</b> .....	<b>53</b>
Chapter Overview .....	53
4.1 Introduction .....	54

4.2 Materials and Methods .....	56
4.2.1 Cell Preparation and Particle Fabrication .....	57
4.2.2 3D Imaging of Structures.....	59
4.3 Results and Discussion.....	60
4.4 Conclusion.....	67
4.5 References .....	68
<b>Chapter 5</b>	
<b>Mutually tangled colloidal knots and induced defect loops in nematic fields .....</b>	<b>70</b>
5.1 Introduction .....	71
5.2 Results and Discussion.....	72
5.3 Methods.....	83
5.3.1 Sample preparation .....	83
5.3.2 Numerical and topological modelling.....	84
5.4 Conclusion.....	85
5.5 References .....	87
<b>Chapter 6</b>	
<b>Linked topological colloids in a nematic host.....</b>	<b>89</b>
6.1 Introduction .....	90
6.2 Results and Discussion.....	91
6.3 Materials and Methods .....	105
6.3.1 Sample preparation .....	105
6.3.2 Photopolymerization of colloidal particles and their dispersion in LCs .....	106
6.4 Theoretical Modeling .....	107
6.5 Conclusion.....	108
6.6 References .....	110
<b>Chapter 7</b>	
<b>Three-dimensional patterning of solid reduced graphene oxide microstructures through precise laser reduction of aqueous liquid crystalline dispersions of graphene oxide flakes .....</b>	<b>112</b>
7.1 Introduction .....	113
7.2 Results and discussion.....	114
7.3 Materials and Methods.....	123

7.3.1 Sample preparation .....	123
7.3.2 Laser-induced reduction, photoluminescence microscopy and optical characterization .....	124
7.4 Conclusion.....	125
7.5 References .....	127
<b>Chapter 8</b>	
<b>Light-driven dynamic Archimedes spirals and periodic oscillatory patterns of topological defects in anisotropic soft matter.....</b>	<b>129</b>
8.1 Introduction .....	130
8.2 Experimental system, methods, and materials .....	131
8.3 Results .....	134
8.3.1 Experimental characterization of dynamic patterns.....	134
8.3.2 Modeling of feedback mechanisms.....	137
8.3.3 Wall structure in the pattern.....	141
8.4 Discussion .....	143
8.5 Conclusion.....	145
8.6 References .....	146
<b>Chapter 9</b>	
<b>Conclusion .....</b>	<b>148</b>
<b>Bibliography .....</b>	<b>150</b>
<b>Appendix A</b>	
<b>Details of system and characterization of optoelastic manipulation .....</b>	<b>162</b>
A.1 Details of sample preparation.....	162
A.1.1 Preparation of dMR monolayers on glass substrates. ....	162
A.1.2 Colloidal particles. ....	163
A.2 Laser scanning system integrated with holographic optical tweezers.....	163
A.3 Free energy of director structures in cells with light-controlled boundary conditions ....	164
A.4 Effects of gravity .....	165
A.5 Force characterization .....	167
A.6 References .....	177
<b>Appendix B</b>	
<b>Materials, deformations and effects of boundary conditions on photoinduced topographies .....</b>	<b>178</b>

B.1 Materials .....	178
B.2 Specific Description of Film Deformation .....	179
B.3 Boundary Conditions:.....	179
B.4 Interferometry .....	182
<b>Appendix C</b>	
<b>Materials, methods, design and modeling of knotted colloids .....</b>	<b>184</b>
C.1 Fabrication of Knotted Colloids with Different Surface Boundary Conditions.....	184
C.2 Integrated Optical Manipulation and Imaging Setup .....	187
C.3 Sample Preparation.....	188
C.4 Numerical Modeling of Nematic Colloidal Knots .....	189
C.5 Computer Simulations of 3PEF-PM Textures.....	191
C.6 References .....	207
<b>Appendix D</b>	
<b>Description of shape and modeling for linked colloids.....</b>	<b>208</b>
D.1 Geometric shapes of linked colloidal building blocs .....	208
D.2 Details of the numerical approach and specification of the model parameters.....	209
D.3 References .....	221



## List of Tables

<b>Table 6.1 Topological skeletons and graph representations of inter-linked Hopf-link colloids and accompanying closed defect loops.</b> The mutually linked, physical-particle unknots are shown as blue and yellow rings and filled circles, and the defect line loops are shown as red loops and filled circles, respectively. The individual links are indicated by black edges connecting the corresponding red-blue-yellow filled circles that represent colloidal or defect rings; the overall number of links is indicated in-between the topological skeleton and graph representations of the structures reconstructed from theoretical and experimental data (Figs. 6.2-6.8 and Appendix Figs. D.1-D.10).....	103
---	-----

# List of figures

**Fig. 1.1** Nematic liquid crystal. (a) A fluid of rod-like molecules in the nematic phase that are free to translate relative to one another, but align, on average, along the director,  $n$ . (b) The chemical structure of a common thermotropic liquid crystal, 5CB, used in this work.....2

**Fig. 1.2** Line disclinations of half-integer strength. (a) A thin film of a thermotropic nematic LC viewed between crossed polarizers. Red arrows identify two defects. The upper one has a charge of magnitude  $\frac{1}{2}$  and the lower one a magnitude of 1. Here the disclinations propagate normal to the page. (b-f) All possible line disclinations (shown as red lines) with charges ranging from -1 to +1 propagating out of the page. The director structure, represented by black dotted lines, surrounding the defect is shown in a single cross-sectional plane, normal to the defect line. The blue closed loop in (b) shows a possible choice of path for circumnavigation when determining charge strength. Note that there are two possible  $m = +1$  configurations.....3

**Fig. 1.3** Point disclinations of integer strength. (a) A nematic droplet with a radial director structure ( $s = +1$ ) and point defect at its center is suspended in an isotropic fluid and viewed between crossed polarizers. (b, c) Two integer point defects of strengths (b) +1, where the field points radially from the center defect, and (c) -1, where a single plane (not seen) contains radial structure and the remaining two contain hyperbolic. The black dotted lines represent the molecular orientations. Although the sign of the charge is arbitrary, the hyperbolic structures are typically assigned a minus sign.....4

**Fig. 1.4** Dipolar and quadrupolar field symmetries induced by spherical particles. (a) Spherical colloid (red) with a tangential surface boundary condition and surrounding quadrupolar field represented by blue lines. (b, c) Spherical colloids with homeotropic boundary conditions inducing fields with (b) dipolar and (c) quadrupolar symmetries. In all three cases, the colloid itself holds a charge of +1, while the sum of charges associated with all accompanying defects, represented by a black points or loop, adds up to -1. In panel (b), the vector  $\mathbf{p}$  shows the elastic dipole moment. ....6

**Fig. 2.1** Light-controlled patterned alignment of liquid crystals via dMR surface monolayers. (A) A schematic showing the projection of a computer-controlled light pattern onto the dMR monolayer by use of a microdisplay and an objective lens. dMR molecules of the monolayer are bound to the surface by the functional group denoted by R (Fig. A1) and align with their trans-azobenzene groups perpendicular to the linear polarization of the incident light (*Inset*), setting boundary conditions for  $\mathbf{N}$ . (B) Polarizing microscopy image of coexisting LC domains with twist configurations shown in the insets by use of cylinders depicting the structure across the cell;  $\mathbf{N}(\mathbf{r})$  between the dMR alignment directions at the bottom (red) and top (green) surfaces

is twisted clockwise by  $135^\circ$  and counterclockwise by  $45^\circ$  in the left and right square-shaped domains, respectively; the bright areas between the squares have  $\pm 90^\circ$ -twist. (C) Independent control of boundary conditions at the top and bottom surfaces generates a star-shaped twist domain within a larger, differently twisted domain while maintaining a uniform  $\mathbf{N}$  in the bottom left and top right corners of the image. Image (B) is taken between crossed polarizer  $\mathbf{P}$  and analyzer  $\mathbf{A}$  parallel to its edges and image (C) for orientations marked by white arrows. ....17

**Fig. 2.2** Optoelastic manipulation of colloidal rods and chains of spheres. (A–E) A self-assembled chain of dipolar  $2\ \mu\text{m}$  silica spheres dynamically controlled through the continuous rotation of the trans-state dMR molecules defining  $\mathbf{N}$  at the surfaces. (F–G)  $\mathbf{N}(\mathbf{r})$  around (F) a single dipolar sphere and (G) a chain of self-assembled spheres. (H) A schematic depicting the chain in the midplane of a cell with  $90^\circ$ -twisted  $\mathbf{N}(\mathbf{r})$  across the cell as it rotates by half of the twist angle; chains, such as the one in (E), often rotate to an angle slightly smaller than a half of the  $\mathbf{N}(\mathbf{r})$ -twist angle due to a combination of a small gravity-induced shift of the chain from the cell midplane downward and the proximity of the boundary between the twisted and untwisted domains. (I–Q) Rotational manipulation applied to (I–L), a glass rod of  $3\ \mu\text{m}$  in diameter and (M–Q), a silver rod of  $100\ \text{nm}$  in diameter. The insets in (M–Q), show fragments of the same images but with an enhanced contrast. ....19

**Fig. 2.3** Light-directed self-assembly and control of colloidal architectures. (A–C) Self-assembled chain-like and diamond-shaped colloidal architectures of  $3\ \mu\text{m}$  melamine resin spheres rotating with  $\mathbf{N}$  in the cell midplane (marked by a white arrow). (D–F) Schematics of  $\mathbf{N}(\mathbf{r})$  surrounding (D) a single spherical particle with tangential surface anchoring, (E) a chain of such particles aligned at about  $30^\circ$  to the far-field director  $\mathbf{N}_0$  and (F) their diamond-shaped self-assembled structure with the long axis along  $\mathbf{N}$ . We note that twisting of  $\mathbf{N}(\mathbf{r})$  breaks the quadrupolar symmetry of director distortions around the particles with tangential surface anchoring. Each particle within the colloidal self-assembled structures has two boojums (black dots), although only some of them are shown in (E, F). ....20

**Fig. 2.4** Large-scale optoelastic rotation and translation of colloids and their chains. (A) Large-scale projection of a pattern shown in the inset for massively parallel manipulation through the control of a dMR monolayer;  $\mathbf{N}$  within the illuminated regions is twisted by  $45^\circ$  throughout the LC cell thickness. (B, C) Dipolar chains in a cell with (B) uniform and (C) twisted director structures before and after illumination, respectively. (D–G) Manipulation of a self-assembled dipolar colloidal chain via a continuous lateral translation of an illuminated region along the green arrows; the inset in (D) shows an enlarged view of the chain. (H) A twisted domain in the form of a labyrinth surrounded by a uniform  $\mathbf{N}$  and used for the large-scale manipulation. (I–K) enlarged images of the labyrinth showing a particle trapped at the interface between the twisted and uniform domains [shown clearly in the inset of (K)] and translated for about  $1\ \text{mm}$  along one of the labyrinth pathways. (L, M) Individual colloids and their chains of different lengths trapped in the complex-shaped optoelastic traps formed between sample regions with different amounts of director twist controlled through polarized sample illumination; the particle trapping potential landscape can be dynamically reconfigured by varying light illumination patterns and can be also kept long-term constant without sample illumination. The dynamically controlled uniform and

twisted  $\mathbf{N}(\mathbf{r})$ -structures across the cell in marked regions are shown in the insets of (A, B, C, I, J). The far-field uniform director  $\mathbf{N}_0$  is marked by white double arrows. ....21

**Fig. 2.5** Optoelastic trapping force exerted on a colloidal particle by light-controlled twist distortions. (A) A series of video frames showing attraction of a dipolar colloid to a twist-domain optoelastic trap formed within a sample with uniform  $\mathbf{N}_0$ ; the elapsed time is marked on the frames. (B) Computer-simulated  $\mathbf{N}(\mathbf{r})$  in the midplane of a cell with a dipolar particle and an elastic distortion induced by rotating  $\mathbf{N}$  at one of the confining surfaces by  $\pi/2$  (with respect to  $\mathbf{N}_0$ ) within the illuminated region (blue); the elastic dipole moment  $\mathbf{p}$  and velocity  $\mathbf{v}$  are marked by the blue and red arrows, respectively. (C) Optoelastic trapping force and (D) interaction energy vs. trap-particle distance for the various twist angles; the inset in (C) shows the experimentally measured trap-particle distance vs. time for different angles of director twist across the cell within the optoelastic trap. (E) Optoelastic escape force (green curve) and trap stiffness (red curve) vs. twist of  $\mathbf{N}$  across the cell in the trap. ....24

**Fig. 3.1** (a) A schematic of the optical setup employed to prepare patterned liquid crystal alignment cells. A cylindrical lens focuses the light into a line that the sample was rotated with respect to. By employing a computer-controlled, actuated rotation stage, both the linear polarization and sample were rotated at a determined angular velocity. The defect strength was controlled by the ratio of polarization to sample rotation rates. (b) Illustration of the process to prepare, harvest, and characterize defect-patterned azobenzene-functionalized liquid crystal polymer network (azo-LCN) films. ....39

**Fig. 3.2** Summary of the director field, polarized optical microscopy image (1 cm diameter), photomechanical response of film (1.2 cm diameter), and illustration of photomechanical response for azo-LCN films subsumed with topological defects ranging from  $-5/2$  to  $+5/2$  when subjected to unpolarized 445 nm light. The defect strength ( $m$ ) and ratio of polarization rotation to sample rotation ( $R_1/R_2$ ) are labeled for each row. ....41

**Fig. 3.3** The photomechanical response of azo-LCN films subsumed with high order defects. The director field orientation (a, e), polarized optical microscopy image (1 cm diameter) (b, f), image of the film after photomechanical deflection (1.2 cm diameter) (c, g), and illustration of the photomechanical deflection (d, h) for a  $+10$  defect and a  $-10$  defect, respectively. ....43

**Fig. 3.4** Hexagonal arrays of  $+2$  (left) and  $+4$  (right) topological defects. The top row presents cross-polarized transmission images of defect arrays. The radius of the non-overlapping defects seen at the edge of the array is 1.55 mm. Photographs of the photoinduced deformations of the films are presented in the second row. The samples have a width of 1.6 cm and length of 2 cm. The last row presents schematic representations of the deformation of the arrays. ....45

**Fig. 4.1** Photopolymerization and nonlinear optical imaging by means of multi-photon excitation processes. (a) A schematic diagram of the multi-photon absorption photopolymerization and multi-photon excitation fluorescence microscopy setup. DM: dichroic mirror, GLP: Glan laser

polarizer, HWP: half-wave plate, OL: objective lens, PMT: photo-multiplier tube, RP: rotating polarizer, and SF: selection filters. (b) A computer-generated model of the used low-symmetry microparticle. (c) A brightfield optical image of a microparticle obtained from the model shown in (b) by means of two-photon absorption photopolymerization. (d) A brightfield image of an array of four surface-bound photopolymerized microparticles having shape corresponding to the computer-generated model shown in (b). .....56

**Fig. 4.2** Polarizing optical microscopy images of director structures around complex-shaped microparticles in uniform and twisted nematic LC cells. (a and b) POM images of a four-particle array in LC within a uniform far-field director  $\mathbf{n}_0$  (a) between crossed polarizers and (b) with an additional phase retardation plate having the slow axis at 45 degrees with respect to the crossed polarizers, marked by the green double arrow. (c and d) POM images of the same array after the far-field director was twisted by (c) 90 degrees and (d) 45 degrees across the sample thickness *via* reorientation of dMR molecules in the monolayer as the sample cell was rotated by 90 degrees and 45 degrees, respectively. The NLC far-field molecular alignment across the sample thickness is shown in the insets of (a), (c) and (d). .....61

**Fig. 4.3** 3D director field around photopolymerized surface-bound low-symmetry microparticles. (a–c) Cross-sectional 3PEF-PM images of  $\mathbf{n}(\mathbf{r})$  in the LC around the surface-attached microparticle obtained (a) in the plane parallel to confining substrates, (b and c) in the vertical cross-sections along two thin orthogonal lines shown in (a). (d) Color-coded fluorescence intensity scale used in (a–c). (e) 3D perspective of the reconstructed director field around the complex-shaped surface-bound colloidal microparticle; the green lines represent the surface boundary conditions for  $\mathbf{n}(\mathbf{r})$  at the confining cell substrates and the black lines show  $\mathbf{n}(\mathbf{r})$  in the plane coinciding with the top surface of the photopolymerized microparticle. The three columns of cylinders in (e) show that  $\mathbf{n}(\mathbf{r})$  is twisted across the cell above the particle but is uniform far from it.....63

**Fig. 4.4** Elasticity-mediated interaction between a surface-bound low-symmetry microparticle and a free-floating colloidal sphere with dipolar elastic distortions. (a) A brightfield microscopy frame from a movie showing a spherical particle at its initial position with an overlaid color-coded particle motion trajectory; the color-coded time scale is shown at the bottom of the image. (b) Elastic force exerted on the colloidal particle plotted as a function of the separation distance. The inset shows a log–log plot of this dependence over an intermediate range of distances; the red straight line shows a slope of  $-3$ . (c) The elastic interaction energy *vs.* separation distance. (d) Dipolar distortions of the director field around a spherical colloid embedded into the NLC with a uniform far-field director  $\mathbf{n}_0$ . The inset in (d) shows a POM image obtained between crossed polarizers parallel to the orthogonal image edges. The dipole moment of the elastic dipole shown in (d) is labeled by a blue arrow and “ $\mathbf{p}$ ”. .....64

**Fig. 5.1** Photopolymerized knotted particles and their arrays. (a), Optical micrographs showing photopolymerized left-handed (panels 1 and 2) and right-handed (panels 3 and 4) trefoil colloidal torus knots  $T(3,2)$  with  $c=3$  and of different sizes, with the corresponding 3D models shown in

green. The top-left inset in panel 3 shows a 3PEF-PM image of a colloidal particle of the same chirality and comparable size as that shown on the same panel. Micrographs show particles being slightly larger than their actual size because of the limited optical resolution. (b), Scanning electron micrograph of a  $4 \times 4$  array of torus knots  $T(5,3)$  with  $c=10$  on a glass substrate. (c–e), Zoomed-in scanning electron micrographs of single  $T(3,2)$  (c,d) and  $T(5,3)$  (e) knots shown from different perspectives, along with the corresponding 3D models (depicted in green), as viewed along the torus axis (c) and in an oblique direction (d,e). .....74

**Fig. 5.2** A trefoil knot particle with tangential boundary conditions in an aligned liquid crystal. (a–c), Bright-field and polarizing optical micrographs taken without polarizers (a), between crossed polarizers whose directions are shown by white double arrows (b,c), and with an additional 530 nm retardation plate having its slow axis aligned as shown by the blue double arrow (c). Locations of boojums are marked by red arrows in (a,b). (d,e), 3PEF-PM slices obtained experimentally (d) and by numerical modelling (e). Each color within these superimposed images (green and red) represents the fluorescence signal from a single 3PEF-PM scan with imaging beam polarizations aligned along the color-coded directions shown by double arrows. (f), Computer-simulated  $\mathbf{n}(\mathbf{r})$  within the top-right part of the cross-section shown in (d,e). (g), 3D fluorescence pattern of the knotted particle and surrounding director distortions reconstructed from 3PEF-PM scans. The blue plane indicates the location of the single-slice images shown in (d,e). (h), 3D representation of  $\mathbf{n}(\mathbf{r})$  deviating away from  $\mathbf{n}_0$  due to the incorporated trefoil knot particle. Colors depict the azimuthal orientation of  $\mathbf{n}(\mathbf{r})$  when projected onto a plane orthogonal to  $\mathbf{n}_0$  and according to the scheme shown in the inset. The structure is visualized on a tube following the knotted particle’s surface. Points where different colors meet are boojums. (i), 3D representation of computer-simulated  $\mathbf{n}(\mathbf{r})$  at the particle/liquid-crystal interface (black rods) and in the bulk (blue rods) induced by a trefoil knot particle. Green and magenta areas show regions of a reduced scalar order parameter of 0.42, corresponding to  $s=-1$  and  $s=1$  2D defects at the liquid-crystal/particle interface, respectively. The knots in (g–i) are shown from different perspectives in order to depict different features of the ordering. ....75

**Fig. 5.3** A colloidal trefoil knot with perpendicular surface boundary conditions. (a,b), Bright-field micrographs of a particle in an aligned nematic taken between crossed polarizers whose directions are indicated by the white arrows (a,b) and with a full-wave 530 nm retardation plate inserted with its slow axis at  $45^\circ$  (blue double arrow; b). (c), Computer-simulated  $\mathbf{n}(\mathbf{r})$  within a cross-section perpendicular to the knotted tube marked in (f). (d,e), 3PEF-PM images of  $\mathbf{n}(\mathbf{r})$  around the knotted particle shown in (a,b) and for excitation-light polarizations (green double arrows) at different orientations with respect to  $\mathbf{n}_0$ . Red arrows mark the defect lines. (f), Computer-simulated  $\mathbf{n}(\mathbf{r})$  around a trefoil knot with perpendicular boundary conditions and the torus plane orthogonal to  $\mathbf{n}_0$ . Green and magenta lines show regions with reduced scalar order parameter corresponding to the cores of the two knotted defect lines seen in the cross-sections (d,e). The inset shows a topological schematic of the mutual linking between the particle knot (blue) and defect knots (green and magenta). (g–j), Bright-field micrographs of colloidal

knots aligned with the torus plane parallel to  $\mathbf{n}_0$ , and taken without polarizers (g,i) and between crossed polarizers with an inserted full-wave retardation plate (h,j). Green arrows in (i) indicate the locations of the rewirings of defect lines, similar to the ones visible in the model shown in Appendix Fig. C.5u,v.....78

**Fig. 5.4** A colloidal knot  $T(5,3)$  with tangential boundary conditions. (a), 3D reconstruction of 3PEF-PM intensity for the  $T(5,3)$  particle with director distortions around it. (b), 3D representation of  $\mathbf{n}(\mathbf{r})$  deviation from  $\mathbf{n}_0$  around the particle. Colors depict the azimuthal orientation of  $\mathbf{n}(\mathbf{r})$  projected onto a plane orthogonal to  $\mathbf{n}_0$  according to the scheme shown in the inset of Fig. 5.2h. The structure is visualized on a tube following the surface of the colloidal knot. The points where different colors meet are boojums. (c), A 3D perspective view of the  $T(5,3)$  particle shown in (a), with the four corresponding cross-sectional planes depicted in (d). (d), 3PEF-PM scans with superimposed green and red color-coded fluorescence images obtained for linear polarizations of excitation light along the double arrows of the same color marked in panel 4.....81

**Fig. 5.5** Torus knot  $T(5,2)$  particles with tangential boundary conditions. (a–c), Optical micrographs of the  $T(5,2)$  knotted particle obtained without polarizers (a), with crossed polarizers aligned as indicated by the white double arrows (b), and with crossed polarizers and an additional phase retardation plate (blue double arrow) aligned with its slow axis at  $45^\circ$  to crossed polarizers and  $\mathbf{n}_0$  (c). Locations of boojums visible within the optical micrographs are marked by red arrows in (b). (d,e), Two different perspective views of the reconstructed 3PEF-PM intensity pattern due to the  $T(5,2)$  colloidal knot particle and director distortions induced by the particle as viewed along the torus axis (d) and perpendicular to it (e). (f,g), Numerical model showing surface defects induced by a  $T(5,2)$  particle as viewed along the torus axis (f) and in a direction perpendicular to it (g). Green and magenta areas show regions of a reduced scalar order parameter of 0.42, corresponding to  $s=-1$  and  $s=1$  defects in the 2D director field at the liquid-crystal/particle interface, respectively. ....82

**Fig. 6.1** Structure of photopolymerized colloidal links. (A) An optical brightfield micrograph of an as-fabricated Hopf-link particle attached to a glass substrate and (*inset*) the corresponding 3D model. (B) A 3D perspective view of the Hopf-link particle (corresponding to the model shown in the inset) obtained using 3PEF-PM imaging. (C) An optical brightfield micrograph of an as-fabricated Solomon-link particle attached to a glass substrate and (*inset*) the corresponding 3D model. (D) A 3D perspective view of the Solomon-link particle (corresponding to the model shown in the inset) obtained using 3PEF-PM imaging. The size of particles shown in (B,D) is the same as that of particles depicted in (A,C), respectively.....92

**Fig. 6.2** A Hopf-link colloidal particle with tangential anchoring in an aligned nematic LC. (A, B) Polarizing optical micrographs of a colloidal Hopf link in a nematic cell with the far-field director  $\mathbf{n}_0$  marked on the image as viewed between (A) crossed polarizers (white double arrows) and (B) between crossed polarizers and an additional 530nm full-wave plate (yellow double arrow) with a slow axis at  $45^\circ$  to them. (C) An in-plane cross-sectional composite 3PEF-PM image of a Hopf link and  $\mathbf{n}(\mathbf{r})$  around it obtained by superimposing two 3PEF-PM scans acquired using orthogonal, linear polarizations of excitation light along directions depicted by green and red double arrows; the fluorescence signals of the composite image corresponding to the two polarizations of excitation light are shown in green and red colors, respectively. (D) The corresponding theoretical 3PEF-PM cross-section based on the numerically calculated  $\mathbf{n}(\mathbf{r})$  shown in the panels (F-H); the green and red colors in the composite texture correspond to 3PEF-PM signals at polarizations of excitation light along the green and red double arrows marked on the image. (E) Elastic interaction energy versus deviation from the equilibrium center-to-center separation  $r-r_{\text{avg}}$  (black symbols and scale) and deviation from the equilibrium orientation  $\alpha-\alpha_{\text{avg}}$  (green symbols and scale). The inset defines the center-to-center distance and orientation, which were studied using optical videomicroscopy. (F-H) Three perspective views from mutually orthogonal directions of a numerically calculated  $\mathbf{n}(\mathbf{r})$  depicted using colors on the particle's surfaces and using rods in the LC bulk nearby. The colors on the particle surfaces show azimuthal orientations of  $\mathbf{n}(\mathbf{r})$  with respect to  $\mathbf{n}_0$  according to the color scheme shown in the bottom-left inset of F. The bottom-right inset shows details of the core structure of a boojum splitting into a semi-loop of a half-integer defect line with the handle-shaped region of reduced order parameter shown in red. ....93

**Fig. 6.3** Metastable configurations of colloidal Hopf links with tangential surface anchoring in an aligned LC. (A,B,D,E) Polarizing optical micrographs of Hopf link particles in a homeotropic nematic cell viewed between (A,D) crossed polarizers marked by white double arrows and (B,E) between crossed polarizers and an additional inserted 530 nm full-wave plate with a slow axis at  $45^\circ$  to them (yellow double arrow). (C,F) The corresponding numerically calculated  $\mathbf{n}(\mathbf{r})$  depicted using colors on the particles surfaces' and using rods in the LC bulk nearby. The colors on the particles surfaces show azimuthal orientations of  $\mathbf{n}(\mathbf{r})$  with respect to  $\mathbf{n}_0$  according to the color scheme shown in the inset. The theoretical configurations shown in (C,F) are similar to those depicted in panels (A,B) and (D, E), respectively; note that one of the rings in (F) contains no boojums.....95

**Fig. 6.4** A colloidal Hopf link with perpendicular surface boundary conditions in an aligned nematic LC. (A, B) Optical micrographs of a Hopf-link particle in a nematic LC with the far-field director  $\mathbf{n}_0$  marked on the image viewed between (A) crossed polarizers (white double arrows), (B) between crossed polarizers and an additional inserted 530nm full-wave plate with a slow axis at  $45^\circ$  to them (yellow double arrow), and (C) without polarizers or wave plate. (D) A theoretical model of the studied colloidal Hopf link configuration revealing  $\mathbf{n}(\mathbf{r})$  (shown by rods)



and defect lines (red closed loops). The inset shows a topological skeleton of linked colloidal and defect loops. (E) A zoom-in view of panel (C) focusing on the “jumping” disclination seen in both experiments and theoretical modeling, which we mark by red arrows in (D,E). .....97

**Fig. 6.5** A metastable configuration of a colloidal Hopf link with perpendicular boundary conditions in a nematic cell. (A, B) Optical micrographs of a Hopf-link particle in a nematic LC with the far-field director  $\mathbf{n}_0$  marked on the image viewed between (A) crossed polarizers (white double arrows) and (B) between crossed polarizers and an additional inserted 530nm full-wave plate with a slow axis at  $45^\circ$  to them (yellow double arrow). (C) An in-plane cross-sectional composite 3PEF-PM image of a Hopf link and  $\mathbf{n}(\mathbf{r})$  around it obtained by superimposing two 3PEF-PM scans acquired using orthogonal, linear polarizations of excitation light along directions depicted by green and red double arrows; the fluorescence signals of the composite image corresponding to the two polarizations of excitation light are shown in green and red colors, respectively. (D) A 3D theoretical model of the colloidal Hopf link configuration revealing  $\mathbf{n}(\mathbf{r})$  (shown by rods) and defect lines (red closed loops). Characteristic locations of defect lines are marked by red arrows in (B-D). The inset shows a topological skeleton of linked colloidal and defect loops. (E) Elastic interaction energy versus deviation from the equilibrium center-to-center separation  $r-r_{\text{avg}}$  (black symbols and scale) and deviation from the equilibrium orientation  $\alpha-\alpha_{\text{avg}}$  (green symbols and scale). The inset defines the center-to-center distance and orientation, which were studied using optical videomicroscopy. ....98

**Fig. 6.6** A compact metastable configuration of a colloidal Hopf link in a nematic LC. (A, B) Optical micrographs of a metastable-state Hopf-link particle in a nematic LC with the far-field director  $\mathbf{n}_0$  marked on the image as viewed between (A) crossed polarizers (white double arrows) and (B) between crossed polarizers and an additional inserted 530nm full-wave plate with a slow axis at  $45^\circ$  to them (yellow double arrow). (C) A 3D theoretical model of the studied colloidal Hopf link configuration revealing  $\mathbf{n}(\mathbf{r})$  (shown by rods) and defect lines (red closed loops). ....99

**Fig. 6.7** Colloidal Solomon links with tangential surface boundary conditions in a nematic LC. (A, B) A Solomon link in a homeotropically aligned nematic cell as viewed between (A) crossed polarizers aligned along the white-arrows and (B) between crossed polarizers and an additional 530 nm full-wave plate with slow axis at  $45^\circ$  to them (yellow double arrow). (C) A numerically calculated model of  $\mathbf{n}(\mathbf{r})$  depicted using colors on the particle surfaces and using rods in the LC bulk nearby corresponding to the experimental images shown in (A, B). The colors on the particle surfaces show azimuthal orientations of  $\mathbf{n}(\mathbf{r})$  with respect to  $\mathbf{n}_0$  (normal to the page) according to the color scheme shown in the inset. (D, E) Another configuration for a tangentially anchored Solomon link in a homeotropic nematic cell viewed between (D) crossed polarizers without and (E) with an inserted additional full-wave plate. (F) A numerically calculated  $\mathbf{n}(\mathbf{r})$

depicted using colors on the particle surfaces and using rods in the LC bulk nearby corresponding to the experimental images shown in (D, E). .....100

**Fig. 6.8** A Solomon-link particle with homeotropic surface boundary conditions in a nematic LC. (A, B) Optical micrographs of a Solomon-link particle in a nematic LC with the far-field director  $\mathbf{n}_0$  marked on the image as viewed between (A) crossed polarizers (white double arrows) and (B) between crossed polarizers and an additional inserted 530nm full-wave plate with a slow axis at  $45^\circ$  to them (yellow double arrow). (C) An in-plane cross-sectional composite 3PEF-PM image of a Solomon link and  $\mathbf{n}(\mathbf{r})$  around it obtained by superimposing two 3PEF-PM scans acquired using orthogonal, linear polarizations of excitation light along directions depicted by green and red double arrows; the fluorescence signals of the composite image corresponding to the two polarizations of excitation light are shown in green and red colors, respectively. (D, E) Two perspective views of a 3D theoretical model of the studied colloidal Solomon link configuration revealing  $\mathbf{n}(\mathbf{r})$  (shown by rods) and defect lines (red closed loops). In the insets of (D), the mutually linked, physical-particle unknots are shown as blue and yellow rings and filled circles, and the defect line loops are shown as red loops and filled circles, respectively; the double links are indicated by double black edges connecting the corresponding red-blue-yellow filled circles that represent colloidal or defect rings. ....101

**Fig. 7.1** Laser-induced reduction of GO flakes in aqueous dispersion. (a) Schematic diagram of the experiment. (b) Transmission-mode optical micrograph of an rGO plane (darker square) in the aqueous dispersion of GO flakes obtained using 850 nm laser light; the inset shows the same sample area obtained using visible white light. (c) Photoluminescence texture of rGO plane (bright square) in the aqueous dispersion of GO flakes at excitation by 850 nm laser beam. d,e, Transmission (d) and photoluminescence (e) along the yellow line respectively in (b) and (c). e,f, In-plane  $x$ - $y$  (f) and cross-section  $z$ - $y$  (g) photoluminescent textures of three rGO planes produced in a thick ( $d \approx 33 \mu\text{m}$ ) sample of an aqueous dispersion of GO flakes. The scale bars are  $10 \mu\text{m}$ . .....116

**Fig. 7.2** Reducing GO flakes in aqueous dispersion and their characterization. (a,b) Simplified structure of pristine (a) and reduced (b) GO flakes. Dark grey, red and white spheres depict carbon, oxygen and hydrogen atoms, respectively. (c,d) Schematic diagram of hydrophilic GO (c) and hydrophobic rGO (d) flakes (thick grey lines) in a water solution. (e) Raman spectra of GO and rGO flakes in a water solution taken using laser light at 514 nm. (f) Raman spectra of pristine and laser beam irradiated GO flakes near D and G peaks; laser fluence in (e, f) was  $E \approx 69 \text{ mJ cm}^{-2}$ . (g) Spectral dependence of photoluminescence intensity  $I_{\text{PL}}$  on dwell time at  $E \approx 61 \text{ mJ cm}^{-2}$ . .....118

**Fig. 7.3** Optical properties of rGO in aqueous dispersion. (a) Intensity of laser light at 850 nm transmitted through a thick ( $d \approx 27 \mu\text{m}$ ) sample versus dwell time. (b) Optical microscopy

textures of sample areas irradiated for different times. Number of texture corresponds to a point in (b). (c) Photoluminescence intensity of rGO depending on dwell time with a laser beam of 850 nm. (d) Nonlinear microscopy in-plane textures of sample areas irradiated for different times. Number of texture corresponds to a point in (c). Laser fluence was  $E \approx 61 \text{ mJ cm}^{-2}$ . Scale bars are  $10 \mu\text{m}$ .....120

**Fig. 7.4** Micropatterning of rGO structures in a bulk of a GO flakes aqueous dispersion. (a,b) Optical transmission (a) and nonlinear (b) microscopy in-plane textures of curved steps structure. (c) Nonlinear (b) microscopy cross-sectional texture of stairs-like structure acquired along a dashed yellow line in (a). Red arrows in (b,c) point to the same plane. (d-g) Optical transmission (d,f) and photoluminescence (e,g) micrographs of different parts of the text patterned at different depth.(h-j) Optical transmission (h) and photoluminescence (i,j) textures of a micropatterned resistor. (k-n) Photoluminescence (k-m) and optical transmission (n) micrographs of a micropattern mimicking a thin film capacitor or a field transistor. The same rGO buses in (k-n) are noted by numbers. (o) Three-dimensional perspective view of a structure in (k-n) reconstructed from photoluminescence data using Fluoview. Scale bars are  $10 \mu\text{m}$ . .....121

**Fig. 7.5** Topologically nontrivial rGO structures in a bulk of an aqueous GO flakes dispersion. (a-c) Optical bright field microscopy textures of an rGO trefoil knot focused on the bottom (a), middle (b) and top (c) of the knot. (d) Optical bright field microscopy texture of an array of rGO trefoil knots. (e-g) Nonlinear microscopy textures of an rGO trefoil knot scanned in the bottom (a), middle (b) and top (c) planes of the knot. (h) Three-dimensional perspective view of an rGO knot reconstructed from photoluminescence data using Fluoview. Reduction of the knot structure was done at  $E \approx 30 \text{ mJ cm}^{-2}$  and a laser beam scanning speed of  $37 \mu\text{m s}^{-1}$ . Scale bar is  $20 \mu\text{m}$  in (d) and  $5 \mu\text{m}$  in other images. ....122

**Fig. 8.1.** Pattern-forming photo-responsive LC cell construction. (a-d) Two LC cells constructed with (a, c) one substrate coated with a film of rubbed polyimide and another coated with a monolayer of the photo-responsive dMR or with (b, d) both substrates coated with dMR. The two cells are also shown in two states: (a,b) at the first moment of illumination with linearly polarized blue light and (c,d) in an evolved dynamic state sometime later when the second substrate is adaptively reorienting due to the photo-induced torque caused by polarized-light illumination. The polarization of the output light is, in general, elliptical and oriented with its long axis at some angle with respect to the director at the output plane,  $\mathbf{n}_d$ . In the “dynamic equilibrium”, the boundary condition  $\mathbf{n}_d$  for the director at the exit substrate is constantly adjusted to be orthogonal to the long axis of the polarization ellipse orientation of which is dependent on the twist of director throughout the cell while this, in turn, adjusts the amount of director twist and, subsequently, further alters the polarization state, thus providing the feedback mechanism needed for the pattern formation..... 133

**Fig. 8.2.** Dynamic spirals. (a, b) A series of videoframes, with elapsed time marked on them, for two spiral patterns shown between crossed polarizers and with (b) an additional half-wave plate inserted between the polarizers and having the slow axis oriented along the blue double arrow. The spiral arms in series (a) undergo  $2\pi$  rotation over about 2 seconds while the spiral arms in series (b) undergo  $\pi$  rotation over about 1.2 seconds. .... 135

**Fig. 8.3.** Analysis of dynamic Archimedean spirals in optically driven nematic cells. (a) A polar plot of the spiraling domain coordinates in the  $r$ - $\theta$  cylindrical coordinate system, as measured experimentally for two spiral arms (red and blue filled circles). (b) Linear plots of  $r$  versus  $\theta$  for each arm fit to an Archimedean spiral geometric configuration defined as  $r = r_0 + \lambda\theta/2\pi$ . The distance between consecutive solitons (wavelength) for a given spiral arm is defined as  $\lambda$ , and is defined in the inset of (b). The two spiraling arms have wavelengths  $\lambda_1 = 19.03 \mu\text{m}$  and  $\lambda_2 = 18.5 \mu\text{m}$ . (c)  $x$ - $y$  coordinates of the center of mass tracked over time (color-coded) to illustrate that the center exhibits meandering behavior similar to that of Archimedes spirals in chemical reaction diffusion systems. .... 135

**Fig. 8.4.** Color dependence of pattern dynamics. (a-c) Three frames of a single time series showing the dependence of defect dynamics on the color of illumination light. In panel (a), the pattern is driven by white light at a rate of  $\sim 37$  Hz. dMR being highly sensitive to blue light, the pattern is also effectively driven by blue light, as is seen in panel (b), although at a slightly lower rate ( $\sim 3$  Hz) due to decreased overall intensity. The optical micrograph in (c) shows that the interaction of the nematic cells with red light is negligible, so the pattern “freezes” under red illumination. .... 136

**Fig. 8.5.** Summary of dynamic and static patterns in addition to the propagating Archimedean spiral waves. (a-h) Eight examples of unique species of observed dynamic patterns, all driven with polarized white light. .... 138

**Fig. 8.6.** Director structure of inter-domain regions. (a,b) Numerical modeling of field configurations and free energy density corresponding to the inter-domain regions with different direction of  $\pm 80^\circ$  twist, with (b) showing details of the structure within the region marked by a dashed rectangle in (a). (c,d) Numerical modeling of field configurations and free energy density corresponding to the inter-domain regions with different amount and direction of  $+270^\circ$  and  $-90^\circ$  twist, with (d) showing details of the structure within the region marked by a dashed rectangle in (a). .... 143

**Fig. A.1** Chemical structures of used molecules and schematics of optical control of the dMR surface monolayers. (A) Molecular structure of the dMR. (B) Azobenzene moiety of the dMR in the trans and cis states. (C) Molecular structure of pentylcyanobiphenyl (5CB). (D) A

schematic depicting the photo-alignment of dMR molecules within a surface monolayer using polarized incident light. ....169

**Fig. A.2** Schematic of the integrated laser-scanning illumination and holographic optical trapping system. Integrated setup of the conventional optical trapping and the laser-scanning illumination system is built around an inverted Olympus IX81 microscope. The laser trapping system utilizes a 1064 nm laser and a spatial light modulator (SLM). The laser scanning system is a part of the FV-300 Olympus Fluoview confocal scanning unit and controls the lateral patterns of scanned focused 488 nm Ar ion laser beam used for patterned structuring of  $\mathbf{N}(\mathbf{r})$  through the control of dMR monolayers.....170

**Fig. A.3** Relaxation of elastic distortions in strongly twisted nematic domains. (A-G) A square region within a uniformly twisted sample is illuminated with blue light having linear polarization direction indicated by the green double arrows. Continuous rotation of the light polarization as marked on the images changes the amount of twist inside the illuminated square. As the bulk elastic energy increases with increasing the amount of twist, (G) a line defect within the LC domains propagates to minimize energy via transformation of the structure into the one with a less twisted state. (H,I) director structures (depicted by use of cylinders) and elastic energy densities (shown using the color scales) for (H) a domain with the light-induced  $3\pi/2$ -twist distortion and (I) a relaxed state with the  $\pi/2$ -twist obtained after propagation of the defect line that relieves some of the distortions by transforming it to the less twisted state. The polarizing microscopy images (A-G) have been obtained between uncrossed polarizers and using red probing light. The vertical cross-sections of the sample shown in (H,I) are obtained by numerical minimization of elastic free energy and correspond to the experimental image shown in (G) for cases before and after the defect line propagation. ....171

**Fig. A.4** Optoelastic control of colloidal self-assemblies. (A) A dipolar chain in a uniform sample oriented along  $\mathbf{N}_0$  (white double arrow). The red arrow represents the orientation of the trans-state azobenzene of dMR molecules and director at the bottom substrate within the square domain, while the green arrow represents their orientations at the top substrate. The director orientation in the central plane is shown by the white dotted line. (B-F) As the polarization of the projected illumination is rotated clockwise, the trans-state dMR molecules and  $\mathbf{N}$  at the top substrate follow but remain unchanged at the bottom surface. The orientation of  $\mathbf{N}$  and that of a colloidal chain in the middle plane is halfway between the bottom and top surfaces. Note that rotation of the chain in (B-F) is taking place simultaneously with its attraction to the boundary between twisted and untwisted domains, similar to that shown in Fig. 2.5A for an individual particle. (G,H) Images showing attraction of a long colloidal chain to the boundary between  $\pi$ -twisted and untwisted LC domains. ....172

**Fig. A.5** Optoelastic rotation of rods of various material compositions. (A-D) Gallium nitride nanowire rotating with the local  $\mathbf{N}$  as polarization of the illumination light and azobenzene molecules within the surface monolayer are rotated. (E-G) Simultaneous rotation of glass rods using the laser scanning system. The used illumination source is an Ar ion laser (488 nm) from the laser scanning system shown in Fig. A.2. ....173

**Fig. A.6** Translation of various colloids by use of optically controlled twisted and untwisted domains. (A) Melamine resin spheres (3  $\mu\text{m}$  in diameter) dispersed within the LC with a uniform alignment along  $\mathbf{N}_0$ . (B-D) Translation of the spheres by use of a semi-circle pattern focused onto a dMR-decorated cell substrate. The polarization of the projected light is rotated to create a  $90^\circ$  twisted director structure within the semi-circle domain as depicted by the red and green arrows showing  $\mathbf{N}$  at the bottom and top substrates, respectively. The semi-circle-shaped trap effectively collects and moves the particles as the projected pattern is translated laterally. (E) A dispersion of 3  $\mu\text{m}$  diameter glass rods in a cell with a  $90^\circ$ -twisted director. (F-H) Translation of an untwisted rectangular LC domain (obtained by adjusting the polarization of the corresponding projected illumination pattern) allows for an effective translation of the rods trapped at the domain interface. ....174

**Fig. A.7** Calibrated trap escape force vs. laser power of a circularly-polarized 1064 nm laser beam used to probe optoelastic forces. The dependence is obtained for melamine resin spheres (3  $\mu\text{m}$  in diameter) dragged through the 5CB at increasingly higher velocities: as the particle barely escapes from the trap, the optical trap escape force is equal to the calculated Stokes drag force. ....175

**Fig. A.8** Displacement of nanoparticles from the LC cell midplane due to gravity. (A) Relative displacement vs. mismatch of density of a colloidal particle and the LC host for different cell thicknesses  $h$ ; the vertical green lines mark the values of density mismatch  $\Delta\rho$  between density of different particle materials and that of 5CB. In the images in Fig. S8 “MR” stands for melamine resin and “GaN” stands for Gallium Nitride. (B) Relative displacement as a function of particle radius  $R$  for different  $h$  for the case of silica spheres in 5CB. ....176

**Fig. B.1** Chemical structures of diacrylate monomers RM257 and A6ZA6. ....178

**Fig. B.2** An example of a +2 defect with fractal-like topography with two generations of 2-fold dimples. Exposed with two sided illumination. ....180

**Fig. B.3** Films exposed on the surface of water (left is a +2 defect and right is a -9 defect). ....181

**Fig. B.4** The deformation of -1 defect flattened and pulled taut. ....182

**Fig. B.5** White light interferometry of defect deformations. The deformations resulted from: a) +1 defect, b) +1/2 defect and c) +10 defect. ....183

**Fig. C.1** Two-Photon Photopolymerization Setup. (a) A simplified schematic depicting key components of the two-photon photopolymerization system. A computer controls timing between the fast shutter and a nano-positioning stage in order to “draw” desired structures of polymerized solid particles. (b) A schematic view of the photopolymerization cell with monomer and photoinitiator in the form of a droplet sandwiched between a glass slide and a microscope coverslip of 170  $\mu\text{m}$  in thickness. ....193

**Fig. C.2** A schematic of the integrated 3D HOT manipulation and imaging setup. HWP: half-wave retardation plate. GLP: Glan laser polarizer. DM: dichroic mirror. BPF: bandpass filter. OL: objective lens. SLM: spatial light modulator. L1-L4: plano-convex lenses. f1-f4: focal length of the lenses. PMT: photomultiplier tube. BS: beam splitter. ....194

**Fig. C.3** Chemical structures of used materials. (a) Liquid Crystal molecule of 5CB. (b) Styrylethyl-Trimethoxysilane used to surface-functionalize the knotted particles with DMOAP. (c) Chemical structure of the DMOAP molecule. (d) BTBP dye used for two-photon excitation fluorescence imaging of structures around colloids when dispersed in the ZLI-2806 nematic mixture. ....195

**Fig. C.4** Director distortions in the vicinity of the knotted particle with tangential surface anchoring conditions for the LC director. (a) A view along the axis of the torus knot parallel to the far-field director. (b, c) Zoomed-in perspective views of different regions around the boojum defects. The green patches depict regions of reduced scalar order parameter. Note that this figure shows a left-handed knot while Fig. 2 in the main text shows a right-handed one; the knotted tubes and the induced director fields corresponding to the knots of opposite chirality are mirror (non-superimposable) images of each other. ....196

**Fig. C.5** Metastable states of knotted particles aligned at different orientations with respect to the far-field director. The images were obtained in (a-o) planar LC cells and (q-s) in a homeotropic LC cell. (a, e, i, m, q) brightfield transmission-mode images; (b, f, j, n, r) polarizing optical micrographs obtained between crossed polarizers marked on the images; (c, g, k, o, s) polarizing optical micrographs obtained between crossed polarizers and with an additional 530 nm phase retardation plates inserted with the slow axis as shown on the images by blue double arrows. The

orientations of studied particles with respect to the far-field director are depicted using models of knots in (d, h, l, p, t). (u, v) Two different perspective views of one of the metastable numerically simulated director structures and defects induced by the colloidal particles shown as an example. The green and magenta lines in (u, v) show regions with reduced scalar order parameter corresponding to the cores of two half-integer disclinations that are tracing the knotted particle tube. The location of rewirings in (f,g) is marked by red arrows. ....197

**Fig. C.6** Director structure induced by a T(3,2) trefoil knot with perpendicular anchoring in a stable orientational state. (a) Visualization of regions with the strongest elastic distortions induced by a trefoil knot colloidal particle depicted in orange color. The particle itself is shown in blue color and the disclination cores with reduced scalar order parameter are depicted using magenta and green colors. (b) Director distortions in the vicinity of a knotted particle with perpendicular surface anchoring conditions for the LC director; the disclination cores are shown as green lines of the reduced scalar order parameter. (c) 2PEF-PM image of a trefoil knot in a nematic LC oriented with the torus plane roughly perpendicular to  $\mathbf{n}_0$ . ....198

**Fig. C.7** Nematic colloidal (a) T(5,2) and (b) T(7,2) torus knots and the induced knotted pairs of  $s=-1/2$  defect lines in the otherwise smoothly varying director field. The disclination cores are shown via plotting the tube-like regions of reduced scalar order parameter (shown in magenta color). The torus planes of the colloidal knots are perpendicular to the far-field director. ....198

**Fig. C.8** Flattened T(3,2) knotted particles with perpendicular surface boundary conditions and different diameters of the knotted tube as viewed (a-c) along the axis of the torus knot and (d-f) in a direction perpendicular to it. The torus planes of the colloidal knots are perpendicular to the far-field director. The type and location of defects cores are depicted via showing regions with a reduced scalar order parameter (magenta color). The reduced-order regions of disclinations in otherwise continuously varying director field were obtained by minimizing the total free energy of the LC containing particles with knotted tubes of different diameter and imposing strong perpendicular surface anchoring boundary conditions. ....199

**Fig. C.9** Probing the director structure around a T(5,3) colloidal knot via 3PEF-PM slicing (a-c and e-i) of an aligned nematic LC sample with the particle. The locations of two-dimensional cross-sections of the particle and the induced director distortions are marked in the perspective view in (d) that was reconstructed from such optical slices. The knotted particle is aligned with its torus plane perpendicular to the far-field director. ....200

**Fig. C.10** Numerical study of boojum defects induced by a trefoil knot particles of different tube diameter. The torus planes of the colloidal knots are perpendicular to the far-field director. The results are presented by showing the regions with reduced scalar order parameter (depicted using magenta color) for trefoil knots of varying tube diameter. The reduced-order regions and the



corresponding director field distortions were obtained by minimizing the total free energy of the LC with incorporated knotted particles in the form of solid tubes having tangential boundary conditions and different diameter. ....201

**Fig. C.11** Numerical study of boojum defects induced by a T(5,3) particle knot. The defects are visualized via showing regions with reduced scalar order parameter (depicted using magenta color) for a T(5,3) colloidal knots of varying tube diameter. The reduced-order regions shown in (a-f) were obtained by minimizing the total free energy of the LC with knotted particles of different tube diameters. The torus planes of these colloidal knots are perpendicular to the far-field director.....202

**Fig. C.12** Numerical study of boojums induced by a torus knot T(7,2) particle with tangential boundary conditions. (a, b) Perspective views of a numerical model showing boojums (seen as magenta regions of reduced scalar order parameter) induced by a T(7,2) particle, as viewed (a) along the torus axis and (b) perpendicular to it.....203

**Fig. C.13** Trefoil-knot T(3,2) colloidal particles at different angles between the torus axis and the far-field director. (a-c, e-g, and i-k) Optical micrographs of metastable orientational states of trefoil knots with tangential surface boundary conditions in a 5CB nematic LC with the used polarizers and retardation plate labeled on the corresponding figure panels. These images were taken (a, e, i) without polarizers, (b, f, j) between crossed polarizers and (c, g, k) between crossed polarizers with a full-wave retardation plate inserted with slow axis at 45° to crossed polarizers (shown by blue double arrows). (d, h, l) The computer-generated 3D schematics depict metastable orientations of the studied topological colloids with respect to the far-field director. ....204

**Fig. C.14** T(5,3)-knot colloidal particles at different angles between the torus axis and the far-field director. (a-c, e-g, and i-k) Optical micrographs of metastable orientational states of T(5,3) knots with tangential surface anchoring in a nematic LC; the polarizers (white double arrows) and retardation plates (blue double arrows) used for imaging are labeled on the corresponding figure panels. These images were taken (a, e, i) without polarizers, (b, f, j) between crossed polarizers and (c, g, k) between crossed polarizers with a full-wave plate inserted with slow axis at 45° with respect to the crossed polarizers. (d, h, l) The computer-generated 3D schematics depict the metastable orientations of the studied colloids with respect to the far-field director. 205

**Fig. C.15** Knot-particle allocation by scanning a sphere of fixed radius along the knotted line. The snapshot shows allocation after 90 scanning steps (typically we use a total of 10000 for the knotted particle allocation). ....206

**Fig. D.1** Simulations of planar Hopf Links. (A,B) Two more perspective views of the Hopf link simulation corresponding to the configuration observed in Fig. 6.3A,B. (C,D) Two more perspective views of the Hopf link simulation corresponding to the configuration observed in Fig. 6.3D,E. (E) A simulation with parameters slightly deviated from the simulation shown in Fig. 6.3F. The vertically (parallel to the far-field) oriented ring was slightly rotated away from vertical, resulting in a configuration lacking boojums on the surface of the horizontally (perpendicular to the far-field) oriented ring, which is observed in the case shown in Fig. 6.3D,E. (F) Legend mapping molecular orientation at the surfaces of the link to color. ....210

**Fig. D.2** Metastable states of compact homeotropic Hopf Links. (A-I) Hopf links with homeotropic boundary conditions in a vertically aligned nematic field. Panels A,D and G show three unpolarized brightfield images of links with similar configurations to that in Fig. 6.6. The same links are shown imaged between crossed polarizers in panels B,E, and H and between crossed polarizers with an inserted full waveplate (slow axis along the yellow double arrow) in panels C,F, and I. The red arrows point out interesting defect lines induced by the colloidal link. ....211

**Fig. D.3** Another metastable state of a planar Solomon Link. (A) Solomon link with planar boundary conditions in a homeotropically aligned nematic field. Panel A shows an unpolarized brightfield image of a link with a similar configuration to that in Fig. 6.7A,B. The same link is shown imaged between crossed polarizers in panel B and between crossed polarizers with an inserted full waveplate (slow axis along the yellow double arrow) in panel C. ....212

**Fig. D.4** Metastable states of homeotropic Solomon Links. (A-L) Solomon links with homeotropic boundary conditions in a vertically aligned nematic field. Panels A,D,G and J show four unpolarized brightfield images of links with similar configurations to that in Fig. 6.6. The same links are shown imaged between crossed polarizers in panels B,E,H and K and between crossed polarizers with an inserted full waveplate (slow axis along the yellow double arrow) in panels C,F,I and L. Panels (A-C) and (G-I) show the same links in panels (D-F) and (J-L), respectively, but focused at two different depths. The red arrows point out interesting defect lines induced by the colloidal link. ....213

**Fig. D.5** Simplified topologies of various simulated configurations of homeotropic Hopf links. (A, C, E) 3D models of three distinct simulated Hopf links with homeotropic boundary conditions. The cyan and yellow rings represent physical colloidal particles dispersed in a nematic LC, the red lines show defect loops following the colloid-LC interface and black lines in a cross-sectional plane depict a slice of the surrounding molecular field orientations. (B, D, F)

The same simulations shown in (A, C, E) with the cyan and yellow tubes reduced in thickness. (G) Simplified diagram revealing the common linked topology of all three configurations.....214

**Fig. D.6** Simplified topologies of various simulated configurations of homeotropic Hopf links. (A, C, E) 3D models of three distinct simulated Hopf links with homeotropic boundary conditions. The cyan and yellow rings represent physical colloidal particles dispersed in a nematic LC, the red lines show defect loops following the colloid-LC interface and black lines in a cross-sectional plane depict a slice of the surrounding molecular field orientations. (B, D, F) The same simulations shown in (A, C, E) with the cyan and yellow tubes reduced in thickness. (G) Simplified diagram revealing the common linked topology of all three configurations.....215

**Fig. D.7** Simplified topologies of a simulated configuration of a homeotropic Hopf link. (A) A 3D model of a simulated Hopf link with homeotropic boundary conditions. The cyan and yellow rings represent physical colloidal particles dispersed in a nematic LC, the red lines show defect loops following the colloid-LC interface and black lines in a cross-sectional plane depict a slice of the surrounding molecular field orientations. (B) The same simulations shown in (A) with the cyan and yellow tubes reduced in thickness. (C) Simplified diagram revealing the linked topology of this configuration.....216

**Fig. D.8** Simplified topologies of two simulated configurations of homeotropic Hopf links. (A, C) 3D models of two distinct simulated Hopf links with homeotropic boundary conditions. The cyan and yellow rings represent physical colloidal particles dispersed in a nematic LC, the red lines show defect loops following the colloid-LC interface and black lines in a cross-sectional plane depict a slice of the surrounding molecular field orientations. (B, D) The same simulations shown in (A, C) with the cyan and yellow tubes reduced in thickness. (E) Simplified diagram revealing the common linked topology of both configurations.....217

**Fig. D.9** Simplified topologies of a simulated configuration of a homeotropic Hopf link. (A) A 3D model of a simulated Hopf link with homeotropic boundary conditions. The cyan and yellow rings represent physical colloidal particles dispersed in a nematic LC, the red lines show defect loops following the colloid-LC interface and black lines in a cross-sectional plane depict a slice of the surrounding molecular field orientations. (B) The same simulations shown in (A) with the cyan and yellow tubes reduced in thickness. (C) Simplified diagram revealing the linked topology of this configuration.....218

**Fig. D.10** Simplified topologies of a simulated configuration of a homeotropic Hopf link. (A) A 3D model of a simulated Hopf link with homeotropic boundary conditions. The cyan and yellow rings represent physical colloidal particles dispersed in a nematic LC, the red lines show defect loops following the colloid-LC interface and black lines in a cross-sectional plane depict a slice of the surrounding molecular field orientations. (B) The same simulations shown in (A) with the cyan and yellow tubes reduced in thickness. (C) Simplified diagram revealing the linked topology of this configuration.....219

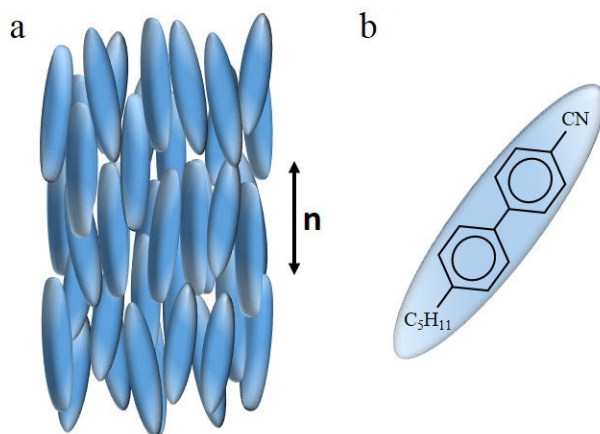
**Fig. D.11** Schematic diagram showing the two-photon photo-polymerization system used for fabrication of complex-shaped microstructures with an added spatial filter for improved beam quality. A monomer-containing cell is mounted on a computer-controlled nano-positioning stage over the microscope objective (100x). A tunable pulsed laser beam passes through a half-wave plate (HWP), glan laser polarizer (GLP), and a spatial filter before being switched by a computer controlled shutter. A dichroic mirror (DM) reflects the beam into the back aperture of the objective. A charge-coupled device (CCD) camera captures light transmitted by the dichroic mirror and allows for real-time observation of the polymerization process.....220

# Chapter 1

## Introduction

### 1.1 Liquid crystals

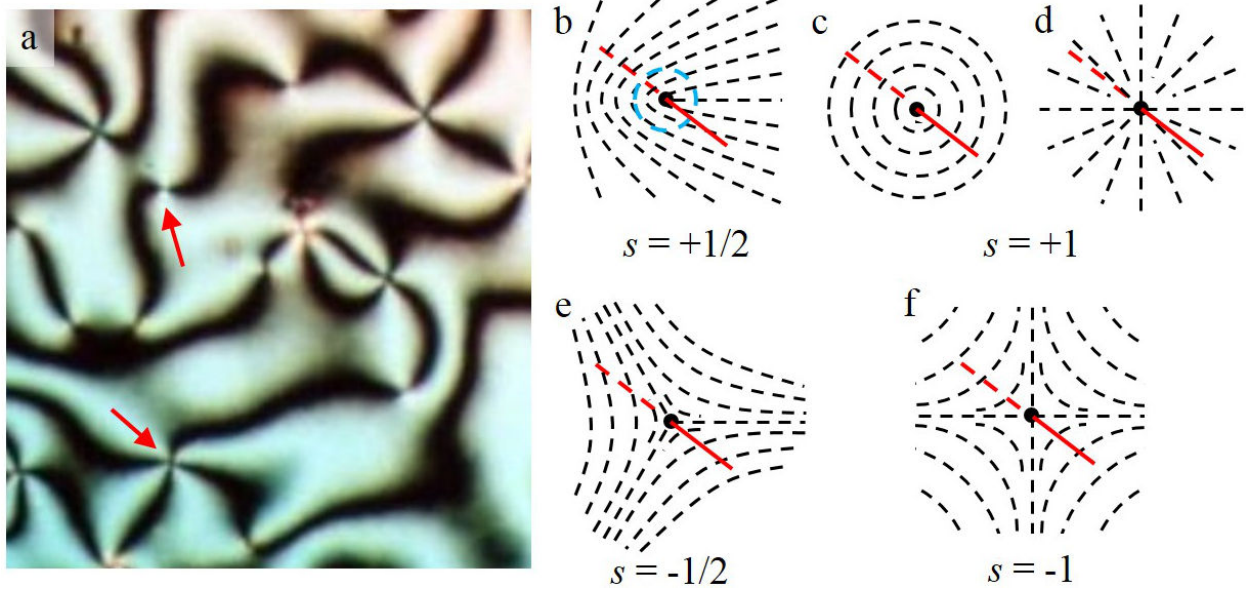
Liquid crystals (LCs) are materials that exhibit phases in between isotropic liquid and crystalline solid—they flow like liquids when poured, but can have varying degrees of molecular order, a property of crystals. There are two main classes of liquid crystals called lyotropic and thermotropic. Lyotropics are chemical mixtures that exhibit long range ordering that depends on concentration of the constituents in a solvent. Many examples of lyotropic LCs exist throughout biology, including DNA, viruses, and cell membranes. Thermotropics can be single-component fluids and they exhibit long range order that depends on temperature. Some examples of commonly observed phases include smectics, cholesterics, and nematics. In this work, we focus on nematics, which is the simplest liquid crystal phase, made up of rod- or disk-like molecules that energetically prefer to align along a common direction called the “director”,  $\mathbf{n}$ . It is also important to note that the nematic phase is nonpolar,  $\mathbf{n} \equiv -\mathbf{n}$ , which essentially determines the possible set of stable defect structures [1], discussed further in Section 2. Fig. 1.1 shows an example of a thermotropic nematic phase of rod-like molecules. In naturally occurring nematics, the director field is generally non-uniform on the macroscopic scale.



**Fig. 1.1** Nematic liquid crystal. (a) A fluid of rod-like molecules in the nematic phase that are free to translate relative to one another, but align, on average, along the director,  $n$ . (b) The chemical structure of a common thermotropic liquid crystal, 5CB, used in this work.

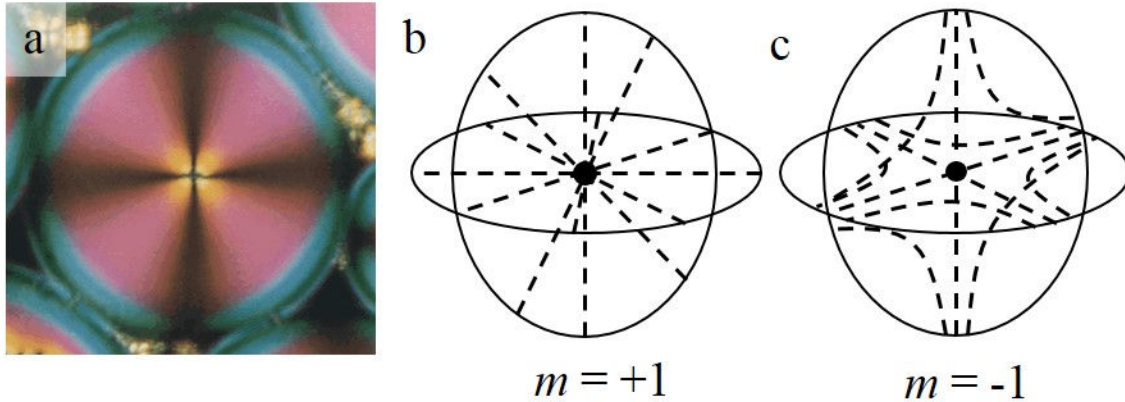
The orientational order of thermotropic nematic liquid crystals can be defined at interfaces where the liquid crystal meets solid substrates. The substrates can be chemically or mechanically treated to define a preferred direction, along which the liquid crystal molecules would align. Using uniaxially rubbed thin polymer films on glass substrates, for example, one can induce a uniform director alignment tangential to the surface on macroscopic scales. Perpendicular, or homeotropic, alignment at a substrate can also be achieved by using surface coupling agents, which consist of a bonding group that chemically bonds with the substrate and an orienting group that interacts with the LC molecules. In addition, external electric or magnetic fields can be applied to align the entire bulk of liquid crystal fluids, which is why they have become popular materials for use in displays, spatial light modulators and other technologies.

The ordered nature of liquid crystals gives rise to their birefringence, which allows us to study their field structures optically. Viewed between crossed polarizers, liquid crystals appear as textures of varying intensity and color. In Fig. 1.2a, we see a thin film of nematic LC under a



**Fig. 1.2** Line disclinations of half-integer multiple strength. (a) A thin film of a thermotropic nematic LC viewed between crossed polarizers. Red arrows identify two defects. The upper one has a charge of magnitude  $\frac{1}{2}$  and the lower one a magnitude of 1. Here the disclinations extend normal to the page. (b-f) All possible line disclinations (shown as red lines) with charges ranging from -1 to +1 extending out of the page. The director structure, represented by black dotted lines, surrounding the defect is shown in a single cross-sectional plane, normal to the defect line. The blue closed loop in (b) shows a possible choice of path for circumnavigation when determining charge strength. Note that there are two possible  $s = +1$  configurations.

microscope, with various defects dispersed throughout. In Fig. 1.3a, a micrometer-sized nematic droplet is shown suspended in an isotropic fluid. The dark areas in the textures are regions where the director field is parallel or perpendicular to the crossed polarizers, everywhere along the propagation axis (normal to the page), so that the polarization state of the light remains unaltered by the liquid crystal and is blocked by the second polarizer. In the bright regions, the polarization state is altered and some light transmits through the second polarizer. Since different optical wavelengths would experience different optical retardations by any given LC material, the transmitted colors would depend on variations of the sample thickness and the degree of optical anisotropy.



**Fig. 1.3** Point disclinations of integer strength. (a) A nematic droplet with a radial director structure ( $m = +1$ ) and point defect at its center is suspended in an isotropic fluid and viewed between crossed polarizers.[10] (b, c) Two integer point defects of strengths (b)  $+1$ , where the field points radially from the center defect, and (c)  $-1$ , where a single plane (not seen) contains radial structure and the remaining two contain hyperbolic. The black dotted lines represent the molecular orientations. Although the sign of the charge is arbitrary, the hyperbolic structures are typically assigned a minus sign.

## 1.2 Defects in liquid crystals

Liquid crystals can host a wide variety of topological defects, at which the director field orientation is undefined, that can occur as a result of symmetry-breaking phase transitions or be induced with external fields.[2] Due to its nonpolar nature, the nematic phase allows only for point and line defects (disclinations) of half-integer multiple strength to occur (see Figs. 1.2 and 1.3).[1, 3] The distortions around such defects emanate throughout the entire field. For line disclinations, the strength of the defect is determined by a simple geometrical analysis in a plane perpendicular to the line. Imagine, that while moving along a closed loop (embedded in the normal plane, blue dotted loop in Fig. 1.2b) that encircles the defect line (shown in red in Fig. 1.2b-f), you keep track of the director field orientation. The number of times the director rotates by  $2\pi$  after one full circumnavigation is called the strength or topological charge,  $s$ . If, while circumnavigating in one sense, the director orientation rotates oppositely, then the charge is

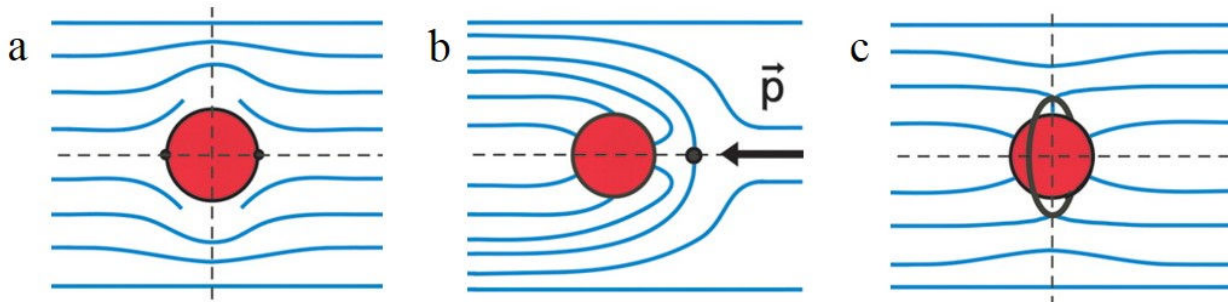


typically defined as negative. Fig. 1.2b-f shows cross-sections of the field structure surrounding line defects of charge  $s = \pm 1/2, \pm 1$ . In determining the strength,  $m$ , of a point defect you must generalize to integrating over a sphere (encompassing the point defect) instead of a closed loop. Fig. 1.3b, c shows the field structure surrounding point defects of integer strength.

The structure and dynamics of topological defects in liquid crystals bear striking similarity to defects in other physical systems. For example, cosmic strings in the early universe, which are responsible for the modern large-scale structure of the cosmos, are believed to have formed and evolved very much like the way defects in liquid crystals do, as described by the Kibble-Zurek mechanism.[4, 5, 6] Other examples include, vortices in superfluids and magnetic flux tubes in superconductors. The study of defects in liquid crystals is, therefore, a valuable testing ground for similar structures in other experimentally less-accessible physical systems.

### **1.3 Nematic colloids**

Colloidal particles dispersed in isotropic fluids have been studied for many decades. Interactions in these systems are limited to short range, however, even in the case of charged colloids due to screening effects.[7] When introduced into nematic fluids, colloidal inclusions disturb the liquid crystal director field at their surfaces and induce distortions that extend throughout the bulk. Particles can then interact elastically, over long range, via forces mediated by the nematic field. Colloids made of polymers, tend to define molecular orientations to be tangential, or planar, at their surfaces. Ones made of silica can be treated with surface coupling agents to define homeotropic orientations. Spherical colloids with tangential boundary conditions, induce a field



**Fig. 1.4** Dipolar and quadrupolar field symmetries induced by spherical particles. (a) Spherical colloid (red) with a tangential surface boundary condition and surrounding quadrupolar field represented by blue lines. (b, c) Spherical colloids with homeotropic boundary conditions inducing fields with (b) dipolar and (c) quadrupolar symmetries. In all three cases, the colloid itself holds a charge of +1, while the sum of charges associated with all accompanying defects, represented by a black points or loop, adds up to -1. In panel (b), the vector  $\mathbf{p}$  shows the elastic dipole moment. The black dotted lines represent cross-sections of planes of symmetry. In all cases, the plane of the page is a common plane of symmetry.[11]

structure with quadrupolar symmetry (Fig. 1.4a) accompanied by two surface point defects at the poles of the sphere, called “boojums”, when embedded in a uniformly aligned nematic. For spherical colloids with homeotropic boundary conditions, two basic defect configurations, either dipolar or quadrupolar (Fig. 1.4b, c), can exist when embedded in a uniform nematic field. The dipolar configuration induces a -1 point defect stabilized in the vicinity of the particle and along the dipole axis, while the quadrupolar configuration stabilizes a closed disclination loop of  $s = -1/2$  (equivalent to the 3D strength  $m = -1$ ) around the particle (commonly referred to as a “saturn ring” defect).

The appearance of bulk defects as a result of colloidal inclusions is a requirement of elastic charge conservation—the particles themselves carry topological charge and since a uniformly aligned nematic field is associated with zero charge, the only way to embed a nonzero charge is to pair it with its opposite. In all configurations of tangential and homeotropic colloidal spheres,

the particle itself can be considered to hold a charge of  $m = +1$ , while the sum of charges of all accompanying defects hold a total charge of  $m = -1$ .

The dynamics of colloidal interactions in nematics closely parallels the dynamics of electric interactions between electric charges. In particular, it has been experimentally confirmed, both in the elastic and electric cases, that forces between dipoles scale like  $d^4$  and between quadrupoles like  $d^6$ , at large separation distances,  $d$ . [7] Furthermore, multiple dipoles or quadrupoles in the vicinity of each other elastically self-assemble into chains and clusters (Figs. 2.2a-e, g and 2.3a-c, e, f), which align themselves at specific angles with respect to the uniform far-field director. Due to this self-assembling nature, micro- and nano-sized nematic colloids find a variety of existing and potential technological applications including, fabrication of photonic materials and metamaterials. [8, 9]

## **1.4 Thesis Overview**

Despite the great progress in control and understanding of colloids, defects, and director field configurations in LCs, only relatively simple topologies of colloidal surfaces (spheres or the ones homeomorphic to spheres) and defects have been realized so far (before this work). The optical control of these defects and colloids, on the other hand, was limited mainly to optical trapping and translational manipulation of defects and particles within LCs. At the same time, the potential basic scientific uses of LCs in topological explorations and modeling require more exquisite control of the topological nature and geometric shape of solid colloidal inclusions and defect loops. Furthermore, control of topological characteristics and spatial locations of defects

may even form a basis for practical applications such as topological LC origami based on polymer glasses and elastomers responsive to external stimuli such as light and temperature [12-16]. These grand challenges in the soft condensed matter physics field largely set the goals of my doctoral work presented in this thesis.

In this work, we use various optical techniques to define the alignment of liquid crystal molecular orientations at surfaces, to fabricate colloids of low-symmetry and nontrivial topology, and to study the interplay between the topology of defects, director fields and surfaces. Following this introduction, Chapter 2 begins with a demonstration of a new method of non-contact manipulation of nematic colloids. This approach relies on the use of azobenzene-based, photo-sensitive molecular monolayers at liquid crystal interfaces which enable us to directly control the molecular orientations at the boundaries surrounding the bulk material via controlled light illumination. In this way, we stabilize localized regions of twisted field and induced disclination loops, which elastically interact with colloidal inclusions. Using optical powers orders of magnitude lower than required for other conventional techniques, such as laser tweezers, we translate colloidal inclusions over large distances and rotate anisotropic particles with great precision. Through an analysis of trajectory and motion, we characterize and quantify these optically-guided elastic forces.

In chapter 3, we apply the photo-responsive monolayers to optical patterning of photo-deformable polymerized liquid crystal films. Here we show how patterned topological defects within the azobenzene-functionalized polymer network can mean interesting topographical

changes, or wrinkling, of the film, which reflects the connection between the film's internal order and its ensuing topography. Furthermore, we demonstrate a special optical system for patterning defects of arbitrary topological strength and then show examples of interesting patterns and their photo-mechanical results.

Chapter 4 introduces a non-linear optical technique used in this work for fabrication of geometrically and topologically interesting micron-sized particles. With tightly focused laser beams, we induce a two-photon photo-polymerization process within a monomer fluid, converting it into a solid polymer and by carefully guiding the beam focus, we fabricate arbitrarily shaped colloids. Employing this technique, we produced chiral, or asymmetric, particles and then studied their induced chiral field structure. Using videomicroscopy, we also characterize here the elastic interactions between surface-bound chiral structures and bulk-dispersed elastic dipoles. We find that the forces are stronger than bulk dipole-dipole interactions.

In chapters 5, and 6, we explore, for the first time, topologically knotted and linked particles suspended in a uniaxially aligned nematic field. We, again, take advantage of the two-photon photo-polymerization method to fabricate these topologically nontrivial structures on the micron scale and find that the structure of induced defects within the surrounding field itself then take on knotted and linked characteristics through a variety of configurations, all of which are subject to topological constraints. Chapter 7 extends these techniques to lyotropic nematics based on dispersions of graphene oxide flakes.

Chapter 8 introduces optically driven dynamic and static defect patterns in nematic liquid crystals. The patterns here resemble those that have been observed in other chemical and physical systems in recent past, except that ours develop as a result of a feedback mechanism involving the interactions between light polarization, photo-sensitive alignment layers and the optical anisotropy of the nematic material. We characterize the structure of a notable dynamic pattern, which resembles the famous Archimedean spiral.

The key findings of the doctoral work are summarized in the Chapter 9. The results were also presented in a series of published and under-review articles [17-22].

## 1.5 References

1. W. F. Brinkman, P. E. Cladis, *Physics Today*. 1982, **35**, 48.
2. M. Kleman, O. D. Lavrentovich, *Philosophical Magazine*. 2006, **86**, 4117.
3. G. S. Ranganath, *Current Science*. 1990, **59**, 1106.
4. T. W. Kibble, *J. Phys. A: Math. Gen.* 1976, **9**, 1387.
5. T. W. Kibble, *Phys. Rep.* 1980, **67**, 183.
6. W. H. Zurek, *Phys. Rep.* 1996, **276**, 177.
7. V. M. Pergamenschik, V. A. Uzunova, *Condensed Matter Physics*. 2010, **13**, 33602-1.
8. I. Mušević, *Liquid Crystals*. 2014, **3**, 418.
9. Q. Liu, Y. Cui, D. Gardner, X. Li, S. He, I. I. Smalyukh, *Nano Letters*. 2010, **10**, 1347.
10. J. F. Joanny, *Science*. 1997, **275**, 1751.
11. C. P. Lapointe, et. al., *Science*. 2009, **326**, 1083.
12. C. D. Modes, M. Warner, *Phys. Rev. E*. 2011, **84**, 021711/1.
13. C. D. Modes, K. Bhattacharya, M. Warner, *Phys. Rev. E*. 2010, **81**, 060701.
14. C. D. Modes, M. Warner, C. Sanchez-Somolinos, L. T. de Haan, D. Broer, *Phys. Rev. E*. 2013, **86**, 060701/1.
15. C. D. Modes, M. Warner, *Europhys. Lett.* 2012, **97**, 36007/P1.
16. C. D. Modes, M. Warner, *Proc. SPIE*. 2012, **8279**, 82790Q/1.
17. A. Martinez, H. C. Mireles, I. I. Smalyukh, *Proc. Natl. Acad. Sci.* 2011, **108**, 20891.
18. M. E. McConney, A. Martinez, V. P. Tondiglia, K. M. Lee, D. Langley, I. I. Smalyukh, T. J. White, *Adv. Mater.* 2013, **25**, 5880.
19. A. Martinez, T. Lee, T. Asavei, H. Rubinsztein-Dunlop, I. I. Smalyukh, *Soft Matter* 2012, **8**, 2432.

20. A. Martinez, M. Ravnik, B. Lucero, R. Visvanathan, S. Žumer, I. I. Smalyukh, *Nat. Mater.* 2014, **13**, 258.
21. A. Martinez, L. Hermosillo, M. Tasinkevych, I. I. Smalyukh, (2014). *Linked topological colloids in a nematic host*. Manuscript submitted for publication.
22. B. Senyuk, N. Behabtu, A. Martinez, T. Lee, D. E. Tsentalovich, G. Ceriotti, J. M. Tour, M. Pasquali, I. I. Smalyukh, (2014). *Three-dimensional patterning of solid reduced graphene oxide microstructures through precise laser reduction of aqueous liquid crystalline dispersions of graphene oxide flakes*. Manuscript submitted for publication.



## Chapter 2

# Large-area optoelastic manipulation of colloidal particles in liquid crystals using photoresponsive molecular surface monolayers

Adapted from: *Proc. Natl. Acad. Sci.* 2011, **108**, 20891.

### Chapter Overview

Noncontact optical trapping and manipulation of micrometer- and nanometer-sized particles are typically achieved by use of forces and torques exerted by tightly focused high-intensity laser beams. Although they were instrumental for many scientific breakthroughs, these approaches find few technological applications mainly because of the small-area manipulation capabilities, the need for using high laser powers, limited application to anisotropic fluids and low-refractive-index particles, as well as complexity of implementation. To overcome these limitations, recent research efforts have been directed toward extending the scope of noncontact optical control through the use of optically-guided electrokinetic forces, vortex laser beams, plasmonics, and optofluidics. Here we demonstrate manipulation of colloidal particles and self-assembled structures in nematic liquid crystals by means of single-molecule-thick, light-controlled surface

monolayers. Using polarized light of intensity from 1,000 to 100,000 times smaller than that in conventional optical tweezers, we rotate, translate, localize, and assemble spherical and complex-shaped particles of various sizes and compositions. By controlling boundary conditions through the monolayer, we manipulate the liquid crystal director field and the landscape of ensuing elastic forces exerted on colloids by the host medium. This permits the centimeter-scale, massively parallel manipulation of particles and complex colloidal structures that can be dynamically controlled by changing illumination or assembled into stationary stable configurations dictated by the “memorized” optoelastic potential landscape due to the last illumination pattern. We characterize the strength of optically guided elastic forces and discuss the potential uses of this noncontact manipulation in fabrication of novel optically- and electrically-tunable composites from liquid crystals and colloids.

## **2.1 Introduction**

Reconfigurable self-assembly of micrometer- and nanometer-sized particles of various shapes and chemical compositions is of great interest from the standpoints of both fundamental science and practical applications.[1-14] The use of anisotropic liquid crystal (LC) fluids as host media for such colloidal self-assembly is currently perhaps one of the most promising approaches.[2-14] It not only allows one to engender anisotropic long-range interaction forces and achieve oriented self-assembly guided by the long-range orientational order of the LC host [2], but also enables control of the medium-mediated interparticle forces by means of varying temperature, applying external fields, and utilizing the response of LC alignment to the presence of various chemical substances.[3-14] Properties of such tunable self-assembled LC-based composite micro- and nanostructured materials can be further engineered by controlling positions and

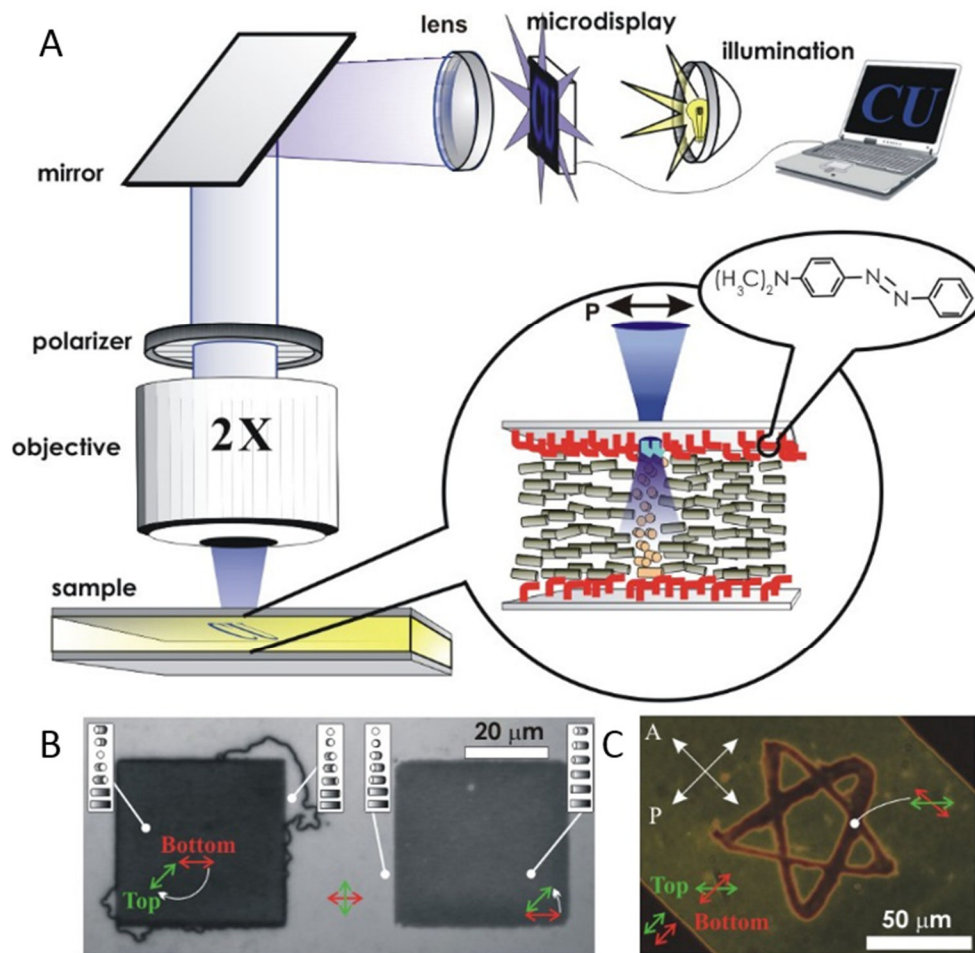
orientations of constituent particles of desired material compositions, shapes, and sizes [6], which is important for LC usage beyond the conventional display applications. For example, optical metamaterials are a new class of typically nanofabricated composites that can be engineered to have unprecedented optical properties, such as negative refraction of light.[15-20] They consist of ordered arrays of predesigned structural units that play the role of “building blocks,” similar to that of molecules and atoms in conventional condensed matter systems.[15-17] Optical control of such building blocks may potentially provide the means for large-scale fabrication and all-optical device applications of metamaterials.[20] However, conventional optical manipulation does not simultaneously achieve the required high resolution and the large-area control, owing to the need for tight focusing of high-power beams.[21-23] Although high-throughput, large-area optical manipulation has been achieved by use of optically-directed electrophoretic, dielectrophoretic, and other forces [23-30], these approaches are often restricted to specific types of particles, require application of fields in addition to the use of light, and cannot be applied to large-area manipulation in anisotropic LC fluids.[30]

In this chapter, we decorate confining plates of LC cells with photoresponsive surface monolayers of azobenzene-containing dMR (derivative of Methyl Red) and demonstrate high-throughput large-area manipulation of fluid-borne particles. Light of intensity from 1,000 to 100,000 times smaller than that in laser tweezers allows us to perform rotational and translational noncontact manipulation of particles and colloidal superstructures with varying sizes, shapes, and compositions. This is achieved by controlling surface boundary conditions for the LC alignment through the illumination of photoresponsive azobenzene-based surface monolayers [31-36]. The optical control of the landscape of ensuing elastic forces and noncontact

manipulation can be achieved on centimeter scales and are of interest for fabrication of novel optically and electrically-tunable LC-based composites.

## 2.2 Results and Discussion

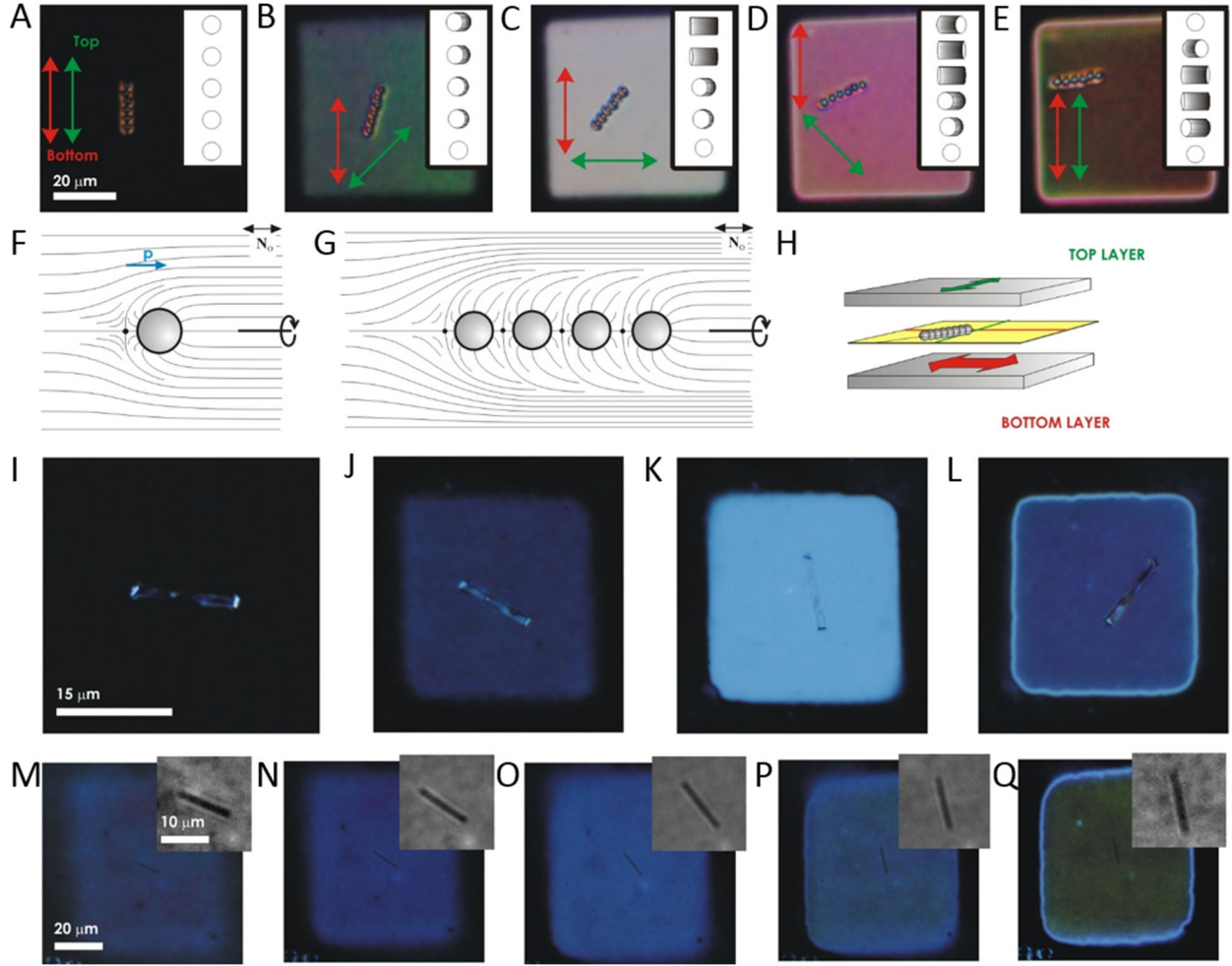
Liquid crystals are complex fluids with orientational ordering of anisotropic nanometer-sized molecules described by the director  $\mathbf{N}$  with nonpolar symmetry ( $\mathbf{N} \equiv -\mathbf{N}$ ).<sup>[1, 37]</sup> From the standpoint of optical properties, they are uniaxial crystals with an optical axis along  $\mathbf{N}$ .<sup>[37]</sup> External fields and surface boundary conditions can cause spatial patterns of molecular alignment described by the coordinate-dependent director field  $\mathbf{N}(\mathbf{r})$ . Display and electrooptic applications of LCs typically involve rubbing of polyimide-coated confining substrates to set boundary conditions for the large-scale uniform alignment described by the far-field director  $\mathbf{N}_0$ ,<sup>[2-14, 37]</sup> although optical alignment is also broadly used.<sup>[31-36]</sup> When the LC is confined between glass plates with molecular monolayers, boundary conditions for  $\mathbf{N}(\mathbf{r})$  can be set by controlling the orientation of the surface-bound dMR molecules in the so-called “trans” conformation state (Appendix Fig. A.1). Linearly polarized light in the violet-blue part of the optical spectrum promotes the alignment of trans-state dMR and  $\mathbf{N}(\mathbf{r})$  at the LC-dMR interface orthogonal to the polarization direction (Fig. 2.1A).<sup>[31-36]</sup> The desired  $\mathbf{N}(\mathbf{r})$  structures (Fig. 2.1 B and C) can be obtained either by projecting light patterns by using a microdisplay (Fig. 2.1A) or by computer-programmed scanning of a 488 nm Ar laser beam using a setup shown in Appendix Fig. A.2. By adjusting the focus to coincide with one of the two LC-dMR interfaces, one can independently define boundary conditions for  $\mathbf{N}(\mathbf{r})$  at both surfaces (Fig. 1C).  $\mathbf{N}(\mathbf{r})$  in the sample bulk adopts to satisfy these light-controlled surface boundary conditions, as seen from



**Fig. 2.1** Light-controlled patterned alignment of liquid crystals via dMR surface monolayers. (A) A schematic showing the projection of a computer-controlled light pattern onto the dMR monolayer by use of a microdisplay and an objective lens. dMR molecules of the monolayer are bound to the surface by the functional group denoted by R (Appendix Fig. A.1) and align with their trans-state azobenzene groups perpendicular to the linear polarization of the incident light (*Inset*), setting boundary conditions for  $\mathbf{N}$ . (B) Polarizing microscopy image of coexisting LC domains with twist configurations shown in the insets by use of cylinders depicting the structure across the cell;  $\mathbf{N}(\mathbf{r})$  between the dMR alignment directions at the bottom (red) and top (green) surfaces is twisted clockwise by  $135^\circ$  and counterclockwise by  $45^\circ$  in the left and right square-shaped domains, respectively; the bright areas between the squares have  $\pm 90^\circ$ -twist. (C) Independent control of boundary conditions at the top and bottom surfaces generates a star-shaped twist domain within a larger, differently twisted domain while maintaining a uniform  $\mathbf{N}$  in the bottom left and top right corners of the image. Image (B) is taken between crossed polarizer  $\mathbf{P}$  and analyzer  $\mathbf{A}$  parallel to its edges and image (C) for orientations marked by white arrows.

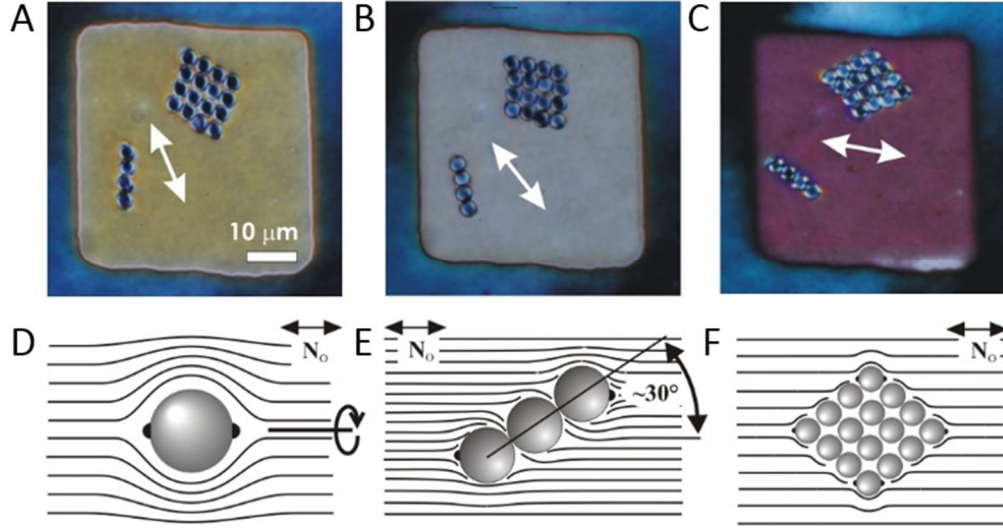
polarizing optical microscopy images (Fig. 2.1 *B* and *C*). One can induce different amounts of director twist across the cell, typically up to the maximum twist angle of about  $3\pi/2$ , at which propagation of line defects relieves the strong twist distortions by transforming it into a less twisted state to minimize the elastic energy (Appendix Fig. A.3). Lateral dimensions of the light-controlled  $\mathbf{N}(\mathbf{r})$ -structures can be varied from about a micrometer to millimeters and larger, depending on pattern projection and objective lenses (if any). This dynamic optical control of  $\mathbf{N}(\mathbf{r})$  permits manipulation of positions, orientations, and assembly of micro- and nano-sized particles (Figs. 2.2–2.4).

Colloidal inclusions set vertical boundary conditions for  $\mathbf{N}(\mathbf{r})$  at the surfactant-treated surfaces (Fig. 2.2*F*) and tangential conditions at the surfaces of bare colloids used in our studies (Fig. 2.3*D*). Director distortions and topological defects, such as the hyperbolic bulk point defect (Fig. 2.2*F*) or surface point defects called boojums (Fig. 2.3*D*), match these boundary conditions with the far-field director  $\mathbf{N}_0$ . The ensuing  $\mathbf{N}(\mathbf{r})$ -structures have either dipolar or quadrupolar symmetry (Figs. 2.2*F* and 2.3*D*, respectively). Elastic interactions between colloids with dipolar  $\mathbf{N}(\mathbf{r})$  lead to the formation of chains of particles interspaced by point defects and directed along  $\mathbf{N}_0$  (Fig. 2.2 *A* and *G*), resembling interactions between electrostatic dipoles that form chains along electric field lines.[2] Colloidal quadrupoles form chains at an angle of about  $30^\circ$  with respect to  $\mathbf{N}_0$  or diamond-shaped crystallites with one diagonal along  $\mathbf{N}_0$  (Fig. 2.3).[3, 4] All studied particles and structures elastically repel from both confining plates and localize in the cell midplane or close to it.[13] Gradual rotation of the linear polarization direction of illumination light focused onto one of the dMR monolayers induces a twist of  $\mathbf{N}$  across the sample thickness (Fig. 2.2 *A–E*). As light traverses through the cell with twisted  $\mathbf{N}$ , its linear polarization follows the director twist (due to the so-called “Mauguin regime” of light



**Fig. 2.2** Optoelastic manipulation of colloidal rods and chains of spheres. (A–E) A self-assembled chain of dipolar 2  $\mu\text{m}$  silica spheres dynamically controlled through the continuous rotation of the trans-state dMR molecules defining  $\mathbf{N}$  at the surfaces. (F–G)  $\mathbf{N}(\mathbf{r})$  around (F) a single dipolar sphere and (G) a chain of self-assembled spheres. (H) A schematic depicting the chain in the midplane of a cell with  $90^\circ$ -twisted  $\mathbf{N}(\mathbf{r})$  across the cell as it rotates by half of the twist angle; chains, such as the one in (E), often rotate to an angle slightly smaller than a half of the  $\mathbf{N}(\mathbf{r})$ -twist angle due to a combination of a small gravity-induced shift of the chain from the cell midplane downward and the proximity of the boundary between the twisted and untwisted domains. (I–Q) Rotational manipulation applied to (I–L), a glass rod of 3  $\mu\text{m}$  in diameter and (M–Q), a silver rod of 100 nm in diameter. The insets in (M–Q), show fragments of the same images but with an enhanced contrast.

propagation) [37], so that transmission of polarizing microscopy light between crossed polarizers reaches a maximum when  $\mathbf{N}$  is twisted by  $\pi/2$  (Fig. 2.2C) and a new local minimum

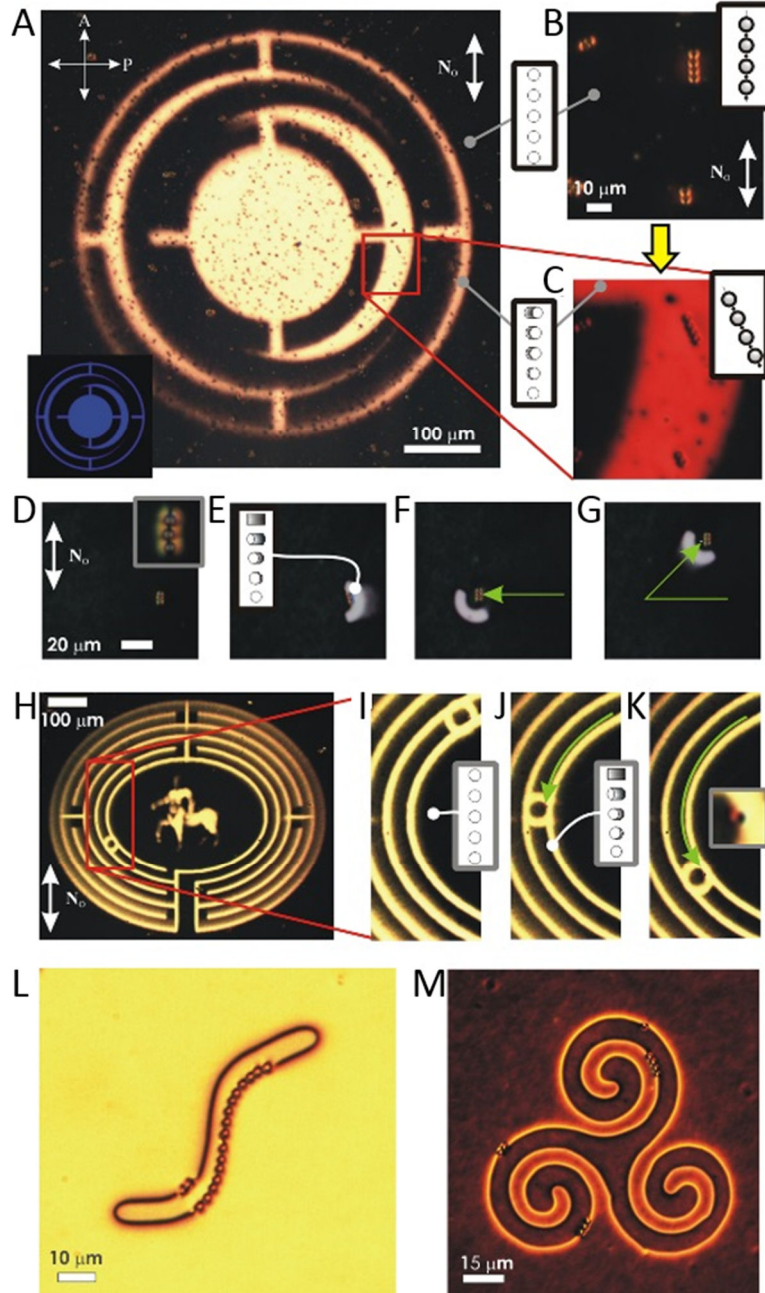


**Fig. 2.3** Light-directed self-assembly and control of colloidal architectures. (A–C) Self-assembled chain-like and diamond-shaped colloidal architectures of 3  $\mu\text{m}$  melamine resin spheres rotating with  $\mathbf{N}$  in the cell midplane (marked by a white arrow). (D–F) Schematics of  $\mathbf{N}(\mathbf{r})$  surrounding (D) a single spherical particle with tangential surface anchoring, (E) a chain of such particles aligned at about  $30^\circ$  to the far-field director  $\mathbf{N}_0$  and (F) their diamond-shaped self-assembled structure with the long axis along  $\mathbf{N}$ . We note that twisting of  $\mathbf{N}(\mathbf{r})$  breaks the quadrupolar symmetry of director distortions around the particles with tangential surface anchoring. Each particle within the colloidal self-assembled structures has two boojums (black dots), although only some of them are shown in (E, F).

when  $\mathbf{N}$  twists by  $\pi$  (Fig. 2.2E). Particles and their structures, such as the dipolar colloidal chains (Fig. 2.2 A–E and Appendix Fig. A.4), follow the rotation of  $\mathbf{N}$  due to its twist while staying in the cell midplane (Fig. 2.2H). Similar rotation is achieved for glass microrods (Fig. 2.2 I–L), silver (Fig. 2.2 M–Q) and other nanorods (Appendix Fig. A.5), as well as self-assembled chains and crystallites of particles with tangential boundary conditions (Fig. 2.3).

Optoelastic control of particles and their self-assembled architectures can be extended to large sample areas and to thousands of colloids without compromising resolution or robustness (Fig. 2.4). For example, we rotate preselected particles and their chains within illuminated regions of the projected pattern (Fig. 2.4A, *Inset*) by rotating the linear polarization of the





**Fig. 2.4** Large-scale optoelastic rotation and translation of colloids and their chains. (A) Large-scale projection of a pattern shown in the inset for massively parallel manipulation through the control of a dMR monolayer;  $\mathbf{N}$  within the illuminated regions is twisted by  $45^\circ$  throughout the LC cell thickness. (B, C) Dipolar chains in a cell with (B) uniform and (C) twisted director structures before and after illumination, respectively. (D–G) Manipulation of a self-assembled dipolar colloidal chain via a continuous lateral translation of an illuminated region along the green arrows; the inset in (D) shows an enlarged view of the chain. (H) A twisted domain in the form of a labyrinth surrounded by a uniform  $\mathbf{N}$  and used for the large-scale manipulation. (I–K) enlarged images of the labyrinth showing a particle trapped at the interface between the twisted and uniform domains [shown clearly in the inset of (K)] and translated for about 1 mm along one

of the labyrinth pathways. (*L, M*) Individual colloids and their chains of different lengths trapped in the complex-shaped optoelastic traps formed between sample regions with different amounts of director twist controlled through polarized sample illumination; the particle trapping potential landscape can be dynamically reconfigured by varying light illumination patterns and can be also kept long-term constant without sample illumination. The dynamically controlled uniform and twisted  $\mathbf{N}(\mathbf{r})$ -structures across the cell in marked regions are shown in the insets of (*A, B, C, I, J*). The far-field uniform director  $\mathbf{N}_0$  is marked by white double arrows.

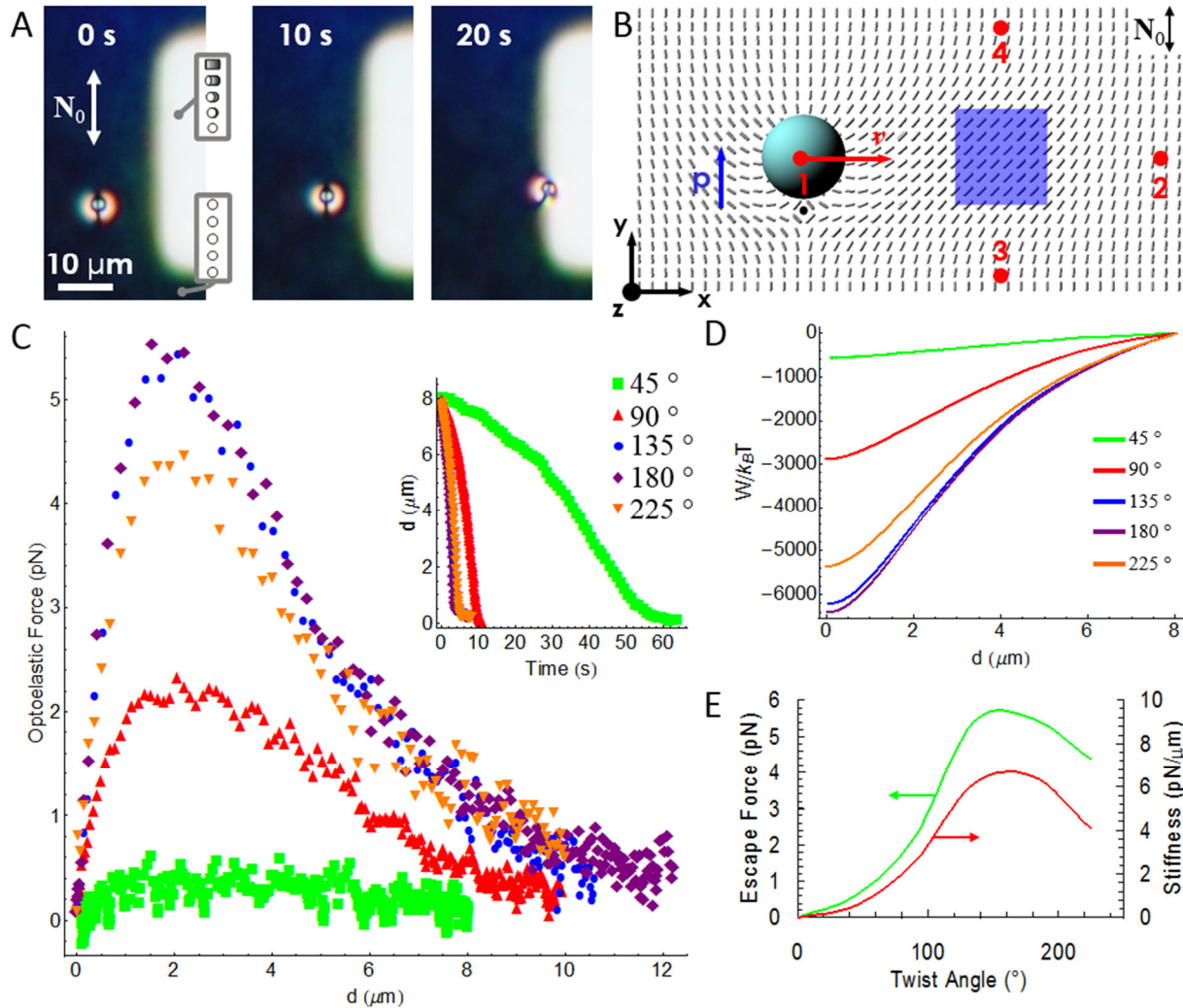
illumination light to an angle two times the desired chain alignment angle (Fig. 2.4 *A–C*). By optically inducing elastic distortions next to colloidal particles or their assemblies, we localize them in a trap region with the strongest gradient of  $\mathbf{N}(\mathbf{r})$  and then translate by continuously advancing the boundary conditions and, thus, the ensuing  $\mathbf{N}(\mathbf{r})$ -pattern (Fig. 2.4 *D–G*). Optoelastic manipulation on large lateral lengthscales (not accessible to conventional laser tweezers) is demonstrated by translating an individual particle along an optically generated labyrinth-like structure of  $\mathbf{N}(\mathbf{r})$  distortions (Fig. 2.4 *H–K*). This optoelastic control is applied to particles of various compositions and with shapes ranging from spheres to nanowires having faceted sidewalls that are simultaneously rotated and translated independently from each other (Fig. 4 and Appendix Figs. A.4–A.6).

What are the underpinning physical mechanisms that allow for the large-area low-intensity noncontact optical manipulation? Colloidal particles can either induce distortions of  $\mathbf{N}(\mathbf{r})$  or barely perturb it, depending on their size and LC molecular interactions at their surfaces. In the latter case, characteristic for particles with small submicrometer size or with weak surface boundary conditions, placing a colloidal sphere of radius  $R$  in a region of the LC with preexisting twist elastic distortions across the sample thickness  $h$  reduces the elastic energy by  $\Delta U = 2\pi K_{22} \Delta\varphi^2 R^3 / (3h^2)$ , where  $\Delta\varphi$  is the twist angle of  $\mathbf{N}$  and  $K_{22}$  is the twist Frank elastic constant.[1, 37] This effect resembles both dielectrophoretic and conventional optical trapping:

particles localize in optically manipulated regions with the strongest gradient of  $\mathbf{N}(\mathbf{r})$  to reduce the elastic energy, just like high-dielectric-constant particles localize in the regions with the strongest gradients of electric field in dielectrophoretic and optical traps. The dynamically controlled region with large  $\Delta\varphi$  is an optoelastic trap that manipulates particles when the illuminated pattern is translated laterally. For particles with  $R \geq 50$  nm and typical  $K_{22} = 5$  pN,  $\Delta U$  is much larger than  $k_B T$ , thus permitting the robust translational optoelastic manipulation (Fig. 2.5A and Appendix Figs. A.4 and A.6), in addition to rotational manipulation (Figs. 2.2–2.4 and Appendix Fig. A.5). The condition  $U \sim (5–10)k_B T$  for reliable trapping [21] yields the minimum  $R \sim 10$  nm for trapping in cells with  $h \sim (3–5)R$ . Even smaller colloids can be trapped in point or line singularities with isotropic defect cores; however, this type of manipulation is outside of the scope of this work.

Colloids with strong boundary conditions induce dipolar or quadrupolar director distortions (Figs. 2.2F and 2.3D) that mediate their anisotropic interactions with each other and with the light-controlled  $\mathbf{N}(\mathbf{r})$ -structures to minimize the elastic energy. Particle-trap interactions can be tuned from attractive to repulsive by controlling the symmetry of light-induced  $\mathbf{N}(\mathbf{r})$ -distortions using dMR monolayers. For example, a particle with a dipolar  $\mathbf{N}(\mathbf{r})$ -structure interacts attractively with the twisted domain shown in Fig. 2.5A, in order to eliminate the region of strong elastic distortions between the particle and the trap (Fig. 2.5B). A particle with the same orientation of the elastic dipole moment  $\mathbf{p}$  in the position #2 experiences repulsion, because elastic distortions of the particle and the trap do not match and elastic energy decreases with increasing separation. Reversing the twist handedness in the domain or flipping  $\mathbf{p}$  to point along the negative  $y$ -direction causes repulsion of a particle from the initial position #1 but attraction from the

position #2, consistent with the corresponding elastic distortions. Particles always weakly attract to the optoelastic trap from the initial positions #3 and #4, regardless of twist handedness and



**Fig. 2.5** Optoelastic trapping force exerted on a colloidal particle by light-controlled twist distortions. (A) A series of video frames showing attraction of a dipolar colloid to a twist-domain optoelastic trap formed within a sample with uniform  $\mathbf{N}_0$ ; the elapsed time is marked on the frames. (B) Computer-simulated  $\mathbf{N}(\mathbf{r})$  in the midplane of a cell with a dipolar particle and an elastic distortion induced by rotating  $\mathbf{N}$  at one of the confining surfaces by  $\pi/2$  (with respect to  $\mathbf{N}_0$ ) within the illuminated region (blue); the elastic dipole moment  $\mathbf{p}$  and velocity  $\mathbf{v}$  are marked by the blue and red arrows, respectively. (C) Optoelastic trapping force and (D) interaction energy vs. trap-particle distance for the various twist angles; the inset in (C) shows the experimentally measured trap-particle distance vs. time for different angles of director twist across the cell within the optoelastic trap. (E) Optoelastic escape force (green curve) and trap stiffness (red curve) vs. twist of  $\mathbf{N}$  across the cell in the trap.

orientation of  $\mathbf{p}$  parallel or antiparallel with respect to  $\mathbf{N}_0$ ; they tend to localize at the corners of the optoelastic trap, again, consistent with the symmetry of corresponding elastic distortions. Similar to the case of conventional optical trapping in LCs [30], the equilibrium spatial localization of particles within the optoelastic trap depends on the overall  $\mathbf{N}(\mathbf{r})$ . The trapped particles with dipolar elastic distortions typically localize at the interface of twisted and untwisted LC domains (Fig. 2.5A and Appendix Fig. A.4), where the  $\mathbf{N}(\mathbf{r})$ -structure around the particle matches that of the domain boundary. Particles with higher symmetry, quadrupolar  $\mathbf{N}(\mathbf{r})$  tend to localize in the central part of the twisted domains, where they displace the elastic-energy-costly LC region (Appendix Fig. A.3 H and I).

Optoelastic trap-particle interactions are rather long-range, unlike those due to optical gradient forces in conventional laser trapping. This is due to the long-range nature of  $\mathbf{N}(\mathbf{r})$ -distortions induced by the traps and particles with strong boundary conditions. Depending on the symmetry of  $\mathbf{N}(\mathbf{r})$  in the optoelastic trap, these interactions—at large distances—qualitatively resemble dipole-dipole or dipole-quadrupole interactions in electrostatics. At short distances, the optoelastic force increases linearly with the particle’s displacement  $\Delta r$  from the equilibrium trapping position, exhibiting Hookean behavior  $F_{\text{oel}} = -k_{\text{oel}}\Delta r$ , where  $k_{\text{oel}}$  is the stiffness of the optoelastic trap (Fig. 2.5C). The peak value of attractive force occurs when  $\Delta r$  is comparable to the particle size and, in analogy with the conventional optical manipulation, it can be called the “escape force,” since it determines the external force needed to remove a particle from this optoelastic trap (Fig. 2.5 C and E). Although exerted forces depend on particle size and shape, cell thickness, and the involved  $\mathbf{N}(\mathbf{r})$ -distortions, typical binding energies are within 100–

$10,000 k_B T$ , escape force within 0.1–10 pN, and  $k_{\text{oeI}}$  within 0.1–10 pN/ $\mu\text{m}$  (Fig. 2.5 C–E). Maximum achievable optoelastic forces are about an order of magnitude lower than maximum optical gradient forces in conventional tweezers. Although the strength of optoelastic forces can be controlled at constant intensity by varying the light polarization alone, this control is more difficult than in conventional tweezers having trapping force proportional to the laser power that can be easily tuned. Because of this, the optoelastic method can have only limited uses in quantitative studies of interparticle colloidal forces, especially in the case of weak forces below 0.1 pN.

Optoelastic manipulation can be used for noncontact control of inclusions of different material compositions, regardless of their refractive index or other properties. This manipulation is not restricted to the use of high numerical aperture objectives, or any objectives for that matter. Since trapping of particles and exerted forces are determined by light-controlled elastic distortions within the nematic fluid, optoelastic control is independent of the exact mechanisms of projecting the dMR-guiding light patterns, as long as the resolution of images is larger than—or comparable to—the minimum size of distorted regions in a uniformly aligned LC. This minimum size depends on the competition of bulk elastic and surface anchoring energies described by the so-called anchoring extrapolation length  $l_e = K/W = (0.1\text{--}2) \mu\text{m}$ , where  $K$  is an average Frank elastic constant and  $W$  is the surface anchoring coefficient.

Similar to the case of conventional optical trapping, it is of interest to consider if gravity can set limitations on the size and type of particles manipulated by use of optoelastic forces. The gravitational force  $F_g = (4/3)\pi R^3(\rho_p - \rho_{\text{LC}})g$ , can be significant, especially for inorganic particles

with density  $\rho_p$  much larger than the density of the LC,  $\rho_{LC}$ , where  $g$  is the acceleration gravity. However, the gravitational force is balanced by elastic forces that repel colloids from bounding plates with strong planar boundary conditions.[13, 38, 39] The elastic repulsive force between a dipolar colloid (Fig. 2.2*F*) and a substrate decays with distance  $d$  as  $F_{er} \propto K(R/d)^4$ . Such elastic interaction with the confining surfaces tends to localize the particle in the cell midplane while gravity tends to displace the particle away from it (Appendix A). Using the balance of elastic and gravitational forces, we have estimated the displacement of colloids from the cell midplane vs. particle size and particle-LC density mismatch (Appendix Fig. A.8). Surprisingly, gravity sets no limits on the size of particles that can be manipulated using this approach. This is due to the fact that elastic forces increase with the particle size as  $\propto R^4$  and easily overcome the gravitational force, which scales as  $\propto R^3$ , for large particles. The upper limit on the size of manipulated inclusions is set by the cell gap and the distance up to which the LC alignment can be reliably controlled (hundreds of microns).

Another important advantage of our approach is that—once elastic distortions are optically generated—the particles can be kept entrapped without the use of optical illumination or other external influence, which is impossible in the case of conventional optical trapping and other techniques. The LC cells preserve optically induced alignment and can maintain the landscape of optical trapping potential for long periods of time (months), as demonstrated for individual particles and colloidal chains of different length in Fig. 2.4 *L* and *M*. One can therefore form complex structures of patterned LC alignment and particles that can be dynamically changed by projecting time-varying illumination patterns or can be made stable over long time by use of the property of the LC/dMR system to “memorize” the last projected light pattern and the trapping

potential landscape. On the other hand, because of the exquisite sensitivity of our manipulation technique, even ambient light can alter the “memorized” optoelastic trapping patterns in the cell; precautions are needed to avoid unwanted exposure to light to which dMR is sensitive.

## **2.3 Materials and Methods**

### **2.3.1 Sample Preparation**

The nematic LC material pentylcyanobiphenyl (5CB) was obtained from Frinton Labs. The melamine resin and silica spheres (3 and 2  $\mu\text{m}$  in diameter, respectively), silver nanorods (100 nm in diameter), and glass microrods (3  $\mu\text{m}$  in diameter) were redispersed from aqueous dispersions to methanol and then to the LC by solvent exchange (Appendix A). To obtain vertical boundary conditions for the LC molecular alignment on the surface of particles, we have treated the silica spheres with the surfactant [3-(trimethoxysilyl)propyl]octadecyldimethylammonium chloride (DMOAP). For this, we dispersed silica spheres in a 5 wt.% aqueous solution of DMOAP and sonicated it for 30 min. The particles were extracted via centrifugation at 3,000 rotations per minute and replacement of the solvent with deionized water. This process was repeated 5 times and the remaining water was then evaporated on a hot stage at about 120  $^{\circ}\text{C}$  for 10 h. The particles were added to the LCs and the obtained dispersion was again sonicated for 3 h to break colloidal aggregates.

To fabricate cells, glass plates of 1 mm or 0.15 mm in thickness were thoroughly cleaned by using detergents, deionized water, several organic solvents and plasma. To obtain the photosensitive surface monolayer on the glass plates, we submerged them into approximately 1 wt.% solution of 2-(4-dimethylamino-phenylazo)-N-(3-triethoxysilane-propyl)-benzamide



(dMR) [43] in toluene at elevated temperature of 45 °C for 90 min to facilitate surface bonding of the dMR molecules. This was followed by a toluene rinse to wash away the excess dMR, blowing with dry nitrogen, and curing at 115 °C for 2 h. The glass cells were formed using plates bound by epoxy mixed with monodisperse spherical spacers of 4–20 μm in diameter to set the gap thickness. The cells were filled with the LC colloidal dispersions by capillary action and sealed with epoxy.

### **2.3.2 Image Projection**

We use an illumination system (Fig. 2.1A) consisting of a microdisplay with  $1,024 \times 768$  pixels (EMP-730, Epson) that controls transmitted light intensity on a pixel-by-pixel basis, an objective lens, and a lamp light source with a blue filter (since the dMR is the most sensitive to violet and blue light, we use blue light for the patterned illumination). For imaging purposes, this system is integrated with an Olympus BX51 upright polarizing optical microscope. The desired dynamic illumination patterns are typically generated using animations in Microsoft PowerPoint, similar to the case of common overhead projection of presentations, except that the projection is done to much smaller areas using different optics and typically coupling to an optical microscope (Fig. 2.1). For some illumination experiments, we use scanning mirrors and a 488 nm Ar laser of a confocal imaging system FV-300 built around Olympus IX81 inverted microscope (Appendix Fig. A.2). In both approaches, we project linearly polarized light of power within 1–100 μW onto the sample. This light is used to manipulate individual or multiple particles (tens of thousands) and their self-assembled structures at the same time and on the lateral scales ranging from microns to millimeters (Figs. 2.2–2.5). In both systems, we used objective lenses of numerical aperture within  $NA = 0.1–1.4$  and with magnifications ranging from  $2\times$  to  $100\times$ . To avoid

modification of the controlled  $N(\mathbf{r})$  patterns while imaging by means of transmission-mode polarizing microscopy, we minimized exposure of samples to white light by reducing exposure time and intensity while using maximum sensitivity of the Spot 14.2 Color Mosaic Camera (from Diagnostic Instruments, Inc.); alternatively, we used an optical filter that blocks visible light in the blue and violet ranges of the optical spectrum, to which the dMR is most sensitive (Appendix Fig. A.1).

## 2.4 Conclusion

To conclude, we have demonstrated a unique approach for large-scale optical manipulation of nano- and micro-sized objects that utilizes azobenzene-containing surface monolayers. This noncontact control of mesoscopic inclusions in LCs is of interest from the standpoint of light-guided self-assembly of tunable optical metamaterials and other reconfigurable nano- and micro-structured composites. Optoelastic manipulation will expand the available means of direct fundamental study of liquid crystalline colloidal dispersions [2–14, 30, 40], control of localized particle-like excitations in LCs [41], and generation of novel beams with phase singularities by use of light-directed liquid crystals [42]. Although the optoelastic method cannot be used in biological manipulation and in quantitative force measurements, it provides a powerful experimental platform needed for the development of optically addressed information displays, composite materials, and all-optical devices.

## 2.5 References

1. P. M. Chaikin, T. C. Lubensky, *Principles of Condensed Matter Physics*, Cambridge University Press, Cambridge, UK, 1995.
2. P. Poulin, S. Holger, T. C. Lubensky, D. A. Weitz, *Science* 1997, **275**, 1770.
3. I. Muševič, M. Skarabot, U. Tkalec, M. Ravnik, S. Žumer, *Science* 2006 **313**, 954.
4. I. I. Smalyukh, A. V. Kachynski, A. N. Kuzmin, P. N. Prasad, *Proc Natl Acad Sci USA* 2006, **103**, 18048.
5. T. C. Lubensky, D. Pettey, N. Currier, H. Stark, *Phys Rev E* 1998, **57**, 610.
6. C. P. Lapointe, T. G. Mason, I. I. Smalyukh, *Science* 2009, **326**, 1083.
7. Q. Liu, et al., *Nano Lett* 2010, **10**, 1347.
8. L. Ramos, M. Zapotocky, T. C. Lubensky, D. A. Weitz, *Phys Rev E* 2002, **66**, 031711.
9. M. Ravnik, G. P. Alexander, J. M. Yeomans, S. Žumer, *Faraday Discuss* 2010, **144**, 159.
10. T. Yamamoto, H. Yokoyama, Y. Tabe, *Mol Cryst Liq Cryst* 2007, **478**, 967.
11. J. C. Loudet, P. Barois, P. Poulin, *Nature* 2000, **407**, 611.
12. M. Zapotocky, L. Ramos, P. Poulin, T. C. Lubensky, D. A. Weitz, *Science* 1999, **283**, 209.
13. O. P. Pishnyak, S. Tang, J. R. Kelly, S. V. Shiyonovskii, O. D. Lavrentovich, *Phys Rev Lett* 2007, **99**, 127802.
14. G. M. Koenig, I. H. Lin, N. L. Abbott, *Proc Natl Acad Sci USA* 2010, **107**, 3998.
15. V. M. Shalaev, *Nat Photonics* 2007, **1**, 41.
16. V. G. Veselago, *Sov Phys Uspekhi* 1968, **10**, 509.
17. J. B. Pendry, *Phys Rev Lett* 2000, **85**, 3966.
18. C. M. Soukoulis, S. Linden, M. Wegener, *Science* 2007, **315**, 47.
19. J. Valentine, et al., *Nature* 2008, **455**, 376.

20. D. F. Gardner, J. S. Evans, I. I. Smalyukh, *Mol Cryst Liq Cryst* 2011, **545**, 1227.
21. A. Ashkin, J. M. Dziedzic, J. M. Bjorkholm, S. Chu, *Opt Lett* 1983, **11**, 288.
22. D. G. Grier, *Nature* 2003, **424**, 21.
23. P. Y. Chiou, A. T. Ohta, M. C. Wu, *Nature* 2005, **436**, 370.
24. R. Eelkema, et al., *Nature* 2006, **440**, 163.
25. A. Jamshidi, et al., *Nat Photonics* 2008, **2**, 85.
26. R. C. Hayward, D. A. Saville, I. A. Aksay, *Nature* 2000, **404**, 56.
27. Y. Iwashita, H. Tanaka, *Phys Rev Lett* 2003, **90**, 045501.
28. V. G. Shvedov, et al., *Phys Rev Lett* 2010, **105**, 118103.
29. A. N. Grigorenko, N. W. Roberts, M. R. Dickinson, Y. Zhang, *Nat Photonics* 2008, **2**, 365.
30. R. P. Trivedi, D. Engström, I. I. Smalyukh, *J Opt* 2011, **13**, 044001.
31. M. Schadt, H. Seiberle, A. Schuster, *Nature* 1996, **381**, 212.
32. S. J. Woltman, D. G. Jay, G. P. Crawford, *Nat Mater* 2007, **6**, 929.
33. C. L. van Oosten, C. W. M. Baastiansen, D. J. Broer, *Nat Mater* 2009, **8**, 677.
34. K. Ichimura, *Chem Rev* 2000, **100**, 1847.
35. W. M. Gibbons, P. J. Shannon, S-T. Sun, B. J. Swetlin, *Nature* 1991, **351**, 49.
36. J. Niitsuma, M. Yoneya, H. Yokoyama, *Liq Cryst* 2010, **37**, 31.
37. P. G. de Gennes, J. Prost, *The Physics of Liquid Crystals*, Clarendon Press, 1995.
38. V. M. V. Pergamenshchik, V. A. Uzunova, *Phys Rev E* 2009, **79**, 021704.
39. C. Lapointe, et al., *Science* 2004, **303**, 652.
40. V. J. Anderson, H. N. Lekkerkerker, *Nature* 2002, **416**, 811.
41. I. I. Smalyukh, Y. Lansac, N. Clark, R. Trivedi, *Nat Mater* 2010, **9**, 139.
42. J. Leach, M. R. Dennis, J. Courtial, M. J. Padgett, *Nature* 2004, **432**, 165.

43. Y. Yi, M. J. Farrow, E. Korblova, D. M. Walba, T. E. Furtak, *Langmuir* 2009, **25**, 997.

## Chapter 3

# Topography from Topology: Photoinduced Surface Features Generated in Liquid Crystal Polymer Networks

Adapted from: *Adv. Mater.* 2013, **25**, 5880.

### Chapter Overview

Films subsumed with topological defects are transformed into complex, topographical surface features with light irradiation of azobenzene-functionalized liquid crystal polymer networks (azo-LCNs). Using a specially designed optical setup and photoalignment materials, azo-LCN films containing either singular or multiple defects with strengths ranging from  $|\frac{1}{2}|$  to as much as  $|10|$  are examined. The local order of an azo-LCN material for a given defect strength dictates a complex, mechanical response observed as topographical surface features.

### 3.1 Introduction

The ability of biological systems to self-assemble materials into pre-programmed shapes in response to external stimuli is inspirational. Emulating the capability of self-assembling, stimuli-responsive materials with tailored functionality (actuation, shape change, surface manipulation, or other property changes) is of paramount interest to fields ranging from biomedical engineering

[1] to robotics.[2] Liquid crystalline phases and defects play a major role in the self-assembly of biological materials, including the plasma membrane, wood, silk, and the insect cuticle.[3] Here, we examine the response of complexly patterned photoresponsive liquid crystal polymer networks (LCN). The rich and diverse topographical features reported here are reminiscent to shape adaptations and topographical surface manipulation observable in nature and could be useful in a range of applications including haptic displays, optics/photonics, flow control, or even catalysis.

Liquid crystalline materials have repeatedly been demonstrated to exhibit a diverse range of stimuli-responsive behavior, such as negative thermal expansion and multi-stage phase transitions.[7, 8] The responsive nature of liquid crystal polymers are enabled and controlled by the anisotropic orientation of the mesogenic moieties. Azobenzene-functionalized LCN (azo-LCN) materials have been the subject of considerable recent examinations as adaptive materials [9] and shape memory polymers.[19] Importantly for the work presented here, the directionality of the strain generated with a stimulus in aligned LCN materials (monodomain, twisted nematic, splay) is dictated by the director orientation of the material. For example, strain generated in a monodomain (nematic) LCN is primarily observed parallel to the alignment of the mesogens.[16, 22] Offsetting the orientation of the director profile to the sample geometry (film or cantilever) results in out-of-plane deformation observable as twisting.[10, 18, 20, 23]

### **3.2 Results and discussion**

The work presented here was motivated by a series of recent papers [24] in which Modes and Warner predict that defect-containing LCNs should exhibit mechanically adaptive responses highly distinguishable to any reports to date.[24] The authors clearly show that sheets composed

of glassy LCNs subsumed with a central topological defect and resulting director profile spanning the entirety of the film will result in a complex distribution of strain that concentrates at the defect. The clearest depiction of this is the predictions that subjecting glassy LCN materials patterned with a single +1 topological defect to an appropriate stimulus will cause the sheet to spontaneously morph into a cone with the center of the defect as the apex.[25] The subsequent papers extended upon these results by introducing the design framework (so-called “grammar and vocabulary”[28]) surrounding the piece-wise use of topological defects (strengths  $|m| \leq 1$ ) as localized Gaussian curvature building blocks that could be assembled to create pre-programmed, shape-reconfigurable, non-developable surfaces from flat sheets.

One of the salient features of liquid crystalline materials is the ability to readily organize the director profile into complex patterns. Most commonly, director patterning is facilitated by the use of photoalignment surfaces based on azobenzene materials. Domain profile patterning with photoalignment has been recently reported, such as in the fabrication of arrays of axial waveplates.[36] Recently, Broer and coworkers employed photoalignment to pattern defects into glassy, LCN materials containing a heat transfer dye and demonstrated photothermal formation of cone and anti-cone surface topographies as predicted by Modes and Warner.[37] Here, we present the systematic examination of topographical transformation resulting from photomechanical response of azo-LCN films with defects ranging from  $-5/2$  to  $+5/2$ , the response of high-strength defects ( $|m| = 10$ ), as well as explore the coordinated response of periodic arrays of topological defects.

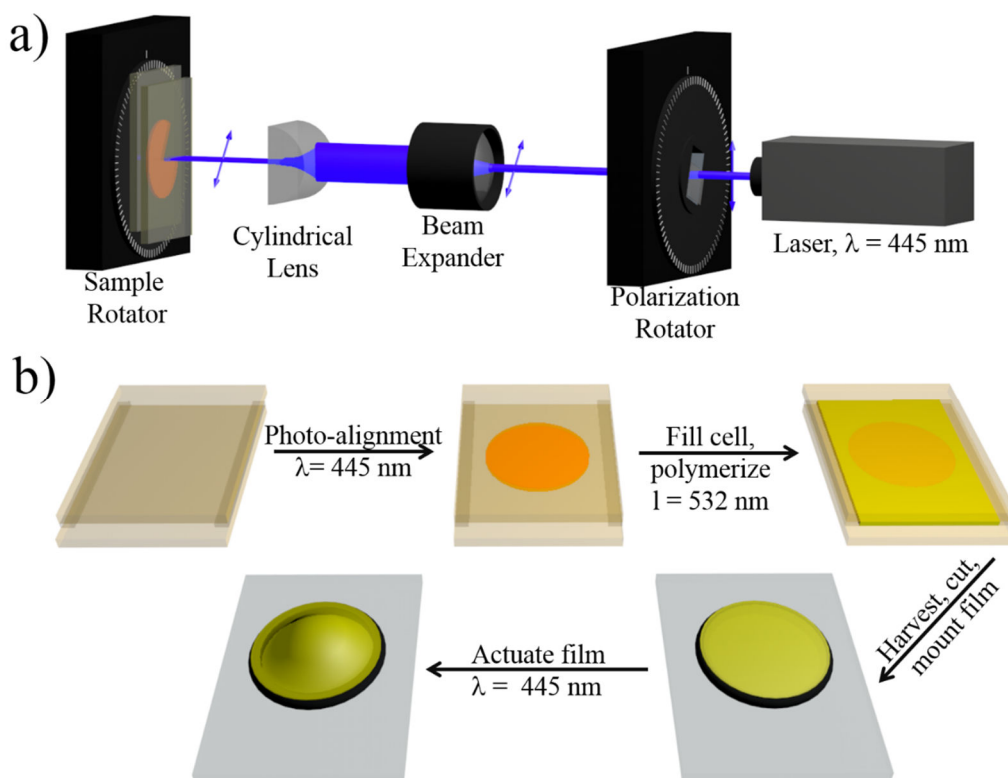


Topological defects are of fundamental interest to a variety of areas including mathematics, physics, and materials science (liquid crystals, ferromagnetic, ferroelectrics).[29, 30] In thin, planarly aligned nematic liquid crystals prepared without a preferred orientation (continuously degenerate) they commonly occur in the form of disclinations through which molecular orientation changes discontinuously and span the film thickness running in the direction perpendicular to the film. These defects are ascribed and referred to by defect strength,  $m$ , which is defined as the number of rotations of the nematic director orientation,  $n$ , around the disclination as one circumnavigates the defect core once.[31, 32] The sign of the defect strength is ascribed based on the direction of director rotation with respect to the direction of circumnavigation about the defect. A positive sign is assigned to director rotations that follow the circumnavigation direction of the point at the center of the defect, whereas a negative sign is assigned for rotations in the opposite direction. The continuous nature of the director rotation about the center of defect and the non-polar symmetry ( $\mathbf{n} = -\mathbf{n}$ ) limits allow defects strengths of integer and half integer values. Defects in liquid crystalline materials can be readily observed under crossed linear polarizers as points at the center of radiating dark brushes in the so-called “Schlieren textures”.[33] The brushes occur in regions where  $n$  is parallel or perpendicular to polarization of the incoming light, where the liquid crystal does not alter the polarization of the incoming light. Therefore the absolute value of the defect strength ( $|m|$ ) can be determined by counting the number of brushes observed under crossed polarizers,  $N$ , through the following relation,[34]

$$|m| = \frac{N}{4} \quad (3.1)$$

Allowable, naturally occurring defects in liquid crystalline materials have strengths of  $-1/2$ ,  $+1/2$ ,  $-1$ , and  $+1$ . Defects with strength  $|m| > 1$  are unstable due to the high elastic energy,  $F$ , which scales with defect strength as  $F \sim m^2$ . [34, 35] Due to the fact that we are dealing with lateral dimensions of thin films many orders of magnitude larger than the core size and film thickness, we will neglect discussion of defects that “escape in the third dimension” to form nonsingular configurations with complex structure and assume that the director field is two-dimensional,  $n(x, y)$ .

Our approach to dictating the topological defects examined here utilize photoalignment materials to generate the desired surface alignment patterns, similar to techniques employed to create axial waveplates [36, 38] and polarization independent LC lenses. [39] The optical patterning setup passes a blue laser (445 nm) through a half-wave ( $\lambda/2$ ) plate and a cylindrical lens projected onto the LC cell prepared from substrates coated with photoalignment surface material (PAAD-22, purchased from BEAM Engineering for Advanced Measurements). As illustrated in Fig. 3.1, both the  $\lambda/2$  plate and the sample cell were mounted on computer-controlled, actuated rotation stages. The  $\lambda/2$  plate allows the orientation of the linear polarization of the light to the sample to be rotated. Importantly, a cylindrical lens was used to focus the expanded laser beam into a sharp line ( $<50 \mu\text{m}$  width, 1.6 cm length). By rotating the sample with respect to this line, a circular area of the cell was exposed to 445 nm light. Both the orientation of the polarization and the sample were rotated during irradiation. The resulting defect strength was regulated by varying the ratio of polarization rotation rate,  $R_1$ , to sample rotation rate,  $R_2$ , via the following equation,  $m = 1 - R_1/R_2$ , which is valid for allowable defect strengths (i.e. strength must be an integer or half-integer value). For example, a  $+1$  strength topological defect is produced by



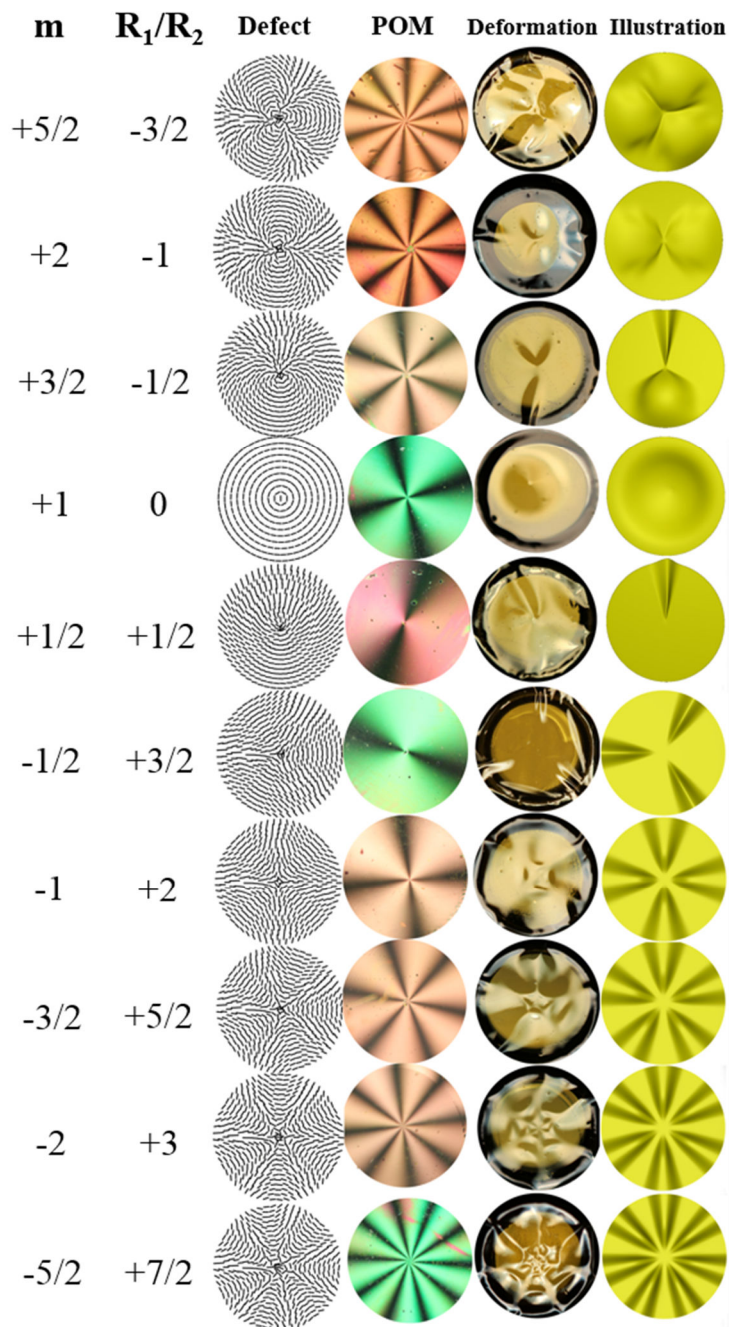
**Fig. 3.1** (a) A schematic of the optical setup employed to prepare patterned liquid crystal alignment cells. A cylindrical lens focuses the light into a line that the sample was rotated with respect to. By employing a computer-controlled, actuated rotation stage, both the linear polarization and sample were rotated at a determined angular velocity. The defect strength was controlled by the ratio of polarization to sample rotation rates. (b) Illustration of the process to prepare, harvest, and characterize defect-patterned azobenzene-functionalized liquid crystal polymer network (azo-LCN) films.

simply rotating the sample at any angular velocity without rotating the polarization ( $R_1 = 0$ ). A +2 strength defect is produced by rotating the polarization and the sample at the same rate but opposite directions ( $R_1/R_2 = -1$ ). A schematic representation of the sample preparation and harvesting procedure is presented in Fig. 3.1. After patterning the orientation of the surface alignment layer the cells were subsequently filled with the mixture of liquid crystalline monomers and photopolymerized with green light ( $\lambda = 532$  nm,  $35$  mW/cm<sup>2</sup> intensity for 30 min) at  $75$  °C (nematic phase). Green light was used to avoid disruption of the photoalignment patterns. After polymerization, the cells were split open and the film was harvested. Polarized

optical microscopy (POM) was used to confirm that the polymerized films arrest the defect written into the alignment cell.

Building upon the work of Modes et al., [24] we report on the photochemically initiated mechanical responses of azo-LCN films subsumed with the director field of a large range of topological defects. Notably, we also extend upon the theoretical predictions as well as the recent experimental examination [37] by preparing higher order defect strengths not previously considered ( $m > |1|$ , up to  $|10|$ ). Fig. 3.2 is composed of an illustration of the director field, confirmation of the defect in the circular azo-LCN film by POM (1 cm diameter), a photograph of the observed photomechanical response, as well as an illustration of the observed photomechanical response. Each column is labeled with the defect strength and ratio of rotation rates employed. As is apparent from the polarized optical microscopy images, the generated defects have  $N = |m| * 4$  brushes. Notably, although each director profile is distinctive—there are observable similarities, for example in the three-fold symmetry of the director orientation of the  $+5/2$  defect and the  $-1/2$  defect. The origin of the symmetry is more apparent when noting that the  $R_1/R_2$  ratio is equal and opposite between the  $n$ -fold pairs.

By exposing the photoresponsive, defect-patterned azo-LCN films to unpolarized blue light the materials adopt a complex topography specific to the defect. The underlying photochemical mechanism of transduction of light into mechanical response has been detailed in a number of recent reports [40] and attributable to local strain generation in the glassy polymer caused by the reorientation and isomerization of the azobenzene chromophores. Due to the complex alignment of the azobenzene mesogenic units in the azo-LCN, we employed unpolarized light as an

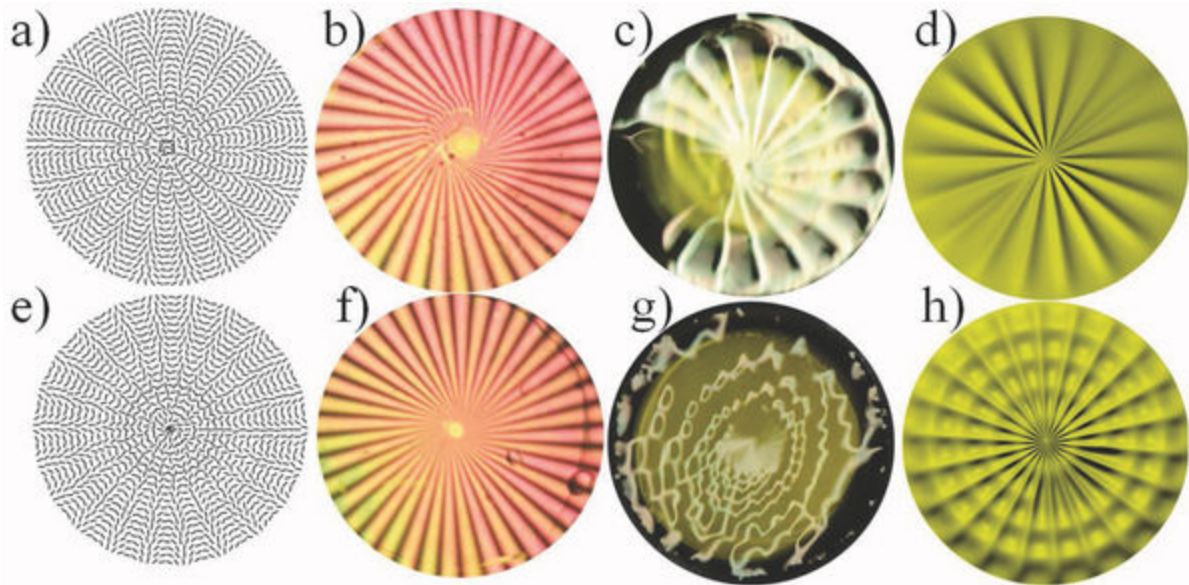


**Fig. 3.2** Summary of the director field, polarized optical microscopy image (1 cm diameter), photomechanical response of film (1.2 cm diameter), and illustration of photomechanical response for azo-LCN films subsumed with topological defects ranging from -5/2 to +5/2 when subjected to unpolarized 445 nm light. The defect strength ( $m$ ) and ratio of polarization rotation to sample rotation ( $R_1/R_2$ ) are labeled for each row.

isotropic stimulus. The photomechanical response of these films is also illustrated in Fig. 3.2. A description of the photomechanical response of each of these films is included in the Appendix

B. From the images presented in Fig. 3.2 the topographical features formed upon irradiation with 445 nm light are rich and diversified. Close examination of Fig. 3.2 reveals two general trends. First, the deformations of the negatively charged defects follow a clear pattern where the number of equally spaced valleys,  $V$ , radiating from the center of the defect is correlated to double the absolute strength of the defect plus two ( $V = 2*|m| + 2$  if  $m < 0$ ). Several times the director orientation was tracked throughout the fabrication and deformation process (illustrated in Fig. 3.1). The general trend is the radiating valleys were found to be localized to regions where the director orientation points towards the center of the defect. Second, the deformation of the positively signed defects of strength  $m > 2$  where the number of tear shaped dimples,  $T$  is related to the defect strength through  $T = 2*|m| - 2$  (if  $m > 2$ ). These relationships emphasize that the response of the films is strongly underpinned by the local anisotropy of the director profiles radiating from the topological defect.

Motivated by the complex patterns apparent in the higher-order defects examined in Fig. 3.2, we applied the defect patterning method to form azo-LCN films that retain high-strength defects of  $m = \pm 10$ . The polarized optical microscopy images presented in Fig. 3.3 confirm that indeed,  $\pm 10$  strength defects were retained in the films. As previously mentioned, the elastic energy scales with defect strength as  $F \sim m^2$ . Therefore, the nematic Frank elastic energy for the  $m = +10$  and  $m = -10$  defects is roughly two orders of magnitude larger than the other defects examined here. Because of this high energetic cost, these high-strength defects would be unstable in conventional nematic liquid crystal fluids with tangentially degenerate boundary conditions (e.g., in the case of the so-called “Schlieren texture”), however, they are stabilized by the deliberate spatial patterning of the easy axis orientation in the photopatterned alignment cells. Evident in



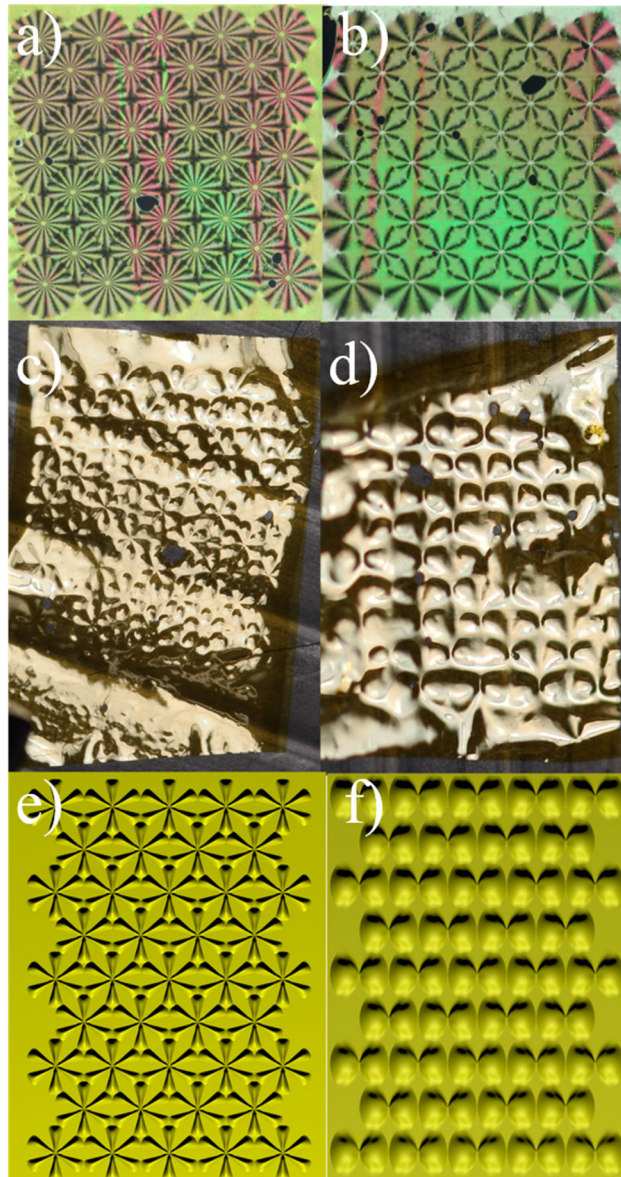
**Fig. 3.3** The photomechanical response of azo-LCN films subsumed with high order defects. The director field orientation (a, e), polarized optical microscopy image (1 cm diameter) (b, f), image of the film after photomechanical deflection (1.2 cm diameter) (c, g), and illustration of the photomechanical deflection (d, h) for a +10 defect and a -10 defect, respectively.

Fig. 3.3, the  $m = +10$  defects has eighteen tear shaped nodes, confirming that the above relationship for T holds true despite the considerable increase in elastic energy. The tear shaped nodes are very elongated due to the fact that the director makes a full rotation as one navigates the core every  $36^\circ$ . The -10 strength defect has 22 valleys as shown in Fig. 3.3, also confirming the above relationship for V holds true despite the considerable increase in elastic energy. Notably, the response of the azo-LCN film with a -10 defect has numerous rows of “struts” connecting the expected valleys that radiate from the center of the topological defect. The circumference of the struts spans the entire film and increase in diameter as the distance increases from the center of the defect. Close examination of lower strength defects in the images presented in Fig. 3.2 confirms these struts are also apparent in the -1, -3/2, -2 and -5/2 defects (see Appendix B for further discussion of these features). The scale invariance and self-similar pattern formation apparent in Figs. 3.2 and 3.3 are also common features of biological systems,

especially in response to external stimulus. An active area of biological research is the role that external mechanical stress plays in mediating scale.

We extend this examination to characterize the response of arrays of “printed” defects. Defect printing was enabled by projecting the 445 nm irradiation through either a +2 or +4 axial waveplate [36] during photoalignment. The adjacent defects spacing was 3 mm and the diagonal defect spacing was 2.1 mm. The printed defect patterns had a diameter of  $\sim 3.1$  mm such that the far field of the director profiles overlapped one another. The sample was placed on a motorized stage that allowed for x-y control of the repeated transcribing of the defect pattern onto the photoalignment material. The arrays were printed in a hexagonal pattern and the defects were oriented in the same direction with respect to each other. The resulting complex director field can be interpreted from the photograph imaged of the sample between crossed polarizers presented in Fig. 3.4. Upon exposure to unpolarized blue light both the samples demonstrated the expected N-fold topography, with the +2 defects having 2-fold topography and the +4 defect having 6-fold topography. Notably, the hexagonal array of +2 defects results in a square array of 2-fold dimpled geometry. Each defect results in a pair of dimples, thereby effectively cutting the periodic length scale in half along one axis and thus resulting in a square pattern instead of a hexagonal pattern. On the other hand, the hexagonal array of +4 defects, with 6-fold resulting topography, cut the periodic length scale in half along the 3 periodic length scales and thus resulted in a hexagonal pattern. In addition to the patterned positively charged defects, a series of defects having equal net negative charge appear in order to satisfy topological charge/strength conservation, further enriching the photoresponsive topography of these films. The contrast





**Fig. 3.4** Hexagonal arrays of +2 (left) and +4 (right) topological defects. The top row presents cross-polarized transmission images of defect arrays. The radius of the non-overlapping defects seen at the edge of the array is 1.55 mm. Photographs of the photoinduced deformations of the films are presented in the second row. The samples have a width of 1.6 cm and length of 2 cm. The last row presents schematic representations of the deformation of the arrays.

between the resulting topography of these samples serves as an illustrative example of the complexity and richness in transforming the topological patterns in to topographical features.

### 3.3 Experimental Section

Optically patternable alignment cells were fabricated by spin coating freshly cleaned pieces of glass with PAAD-22 (purchased from BEAM Co.) at 3000 rpm for 60 seconds. The coated glass substrates were subsequently baked on a hot plate at 100 °C for 10 minutes to evaporate any excess solvent. The two pieces of glass were spaced and glued together by mixing 12  $\mu\text{m}$  cylindrical spacers into an adhesive. Due to slight differences in flatness of the glass and other factors the final cell thickness varied by approximately 1  $\mu\text{m}$ . This small variation in cell thickness was the source of color changes in the cross-polarized images in Fig. 3.4, for example.

Optical patterning of the director orientation of the alignment cells was accomplished in a setup employing a blue DPSS laser (445 nm) that was first passed through a  $\lambda/2$  plate mounted on an actuated, rotation stage to allow for computer-control of the orientation of the linear polarization of the 445 nm laser to the alignment cell. Subsequent to passing through the  $\lambda/2$  plate, the beam was expanded, collimated and focused into a line with a cylindrical lens. The alignment cell was also mounted on an actuated, rotation stage which was rotated at 2°/sec for 180 seconds in all cases. The angular velocity of the rotation of the  $\lambda/2$  plate was adjusted to achieve the desired defect strength (governed by  $m = 1 - R_1/R_2$ ). Before the cylindrical lens, the light intensity was 6.5 mW/cm<sup>2</sup> (beam diameter of 1.6 cm). After passing through the cylindrical lens, the focused line had dimensions of approximately 50  $\mu\text{m}$  by 1.6 cm. Because of the Gaussian profile of the laser beam, the intensity near the end points of the line was smaller than in the center of the line. Furthermore, in this rotation method the exposure time decreases with increasing distance from the center of the topological defect. Fortunately, the photoalignment material employed here has a large range of exposure conditions in which excellent planar alignment can be achieved. Before

and after photoalignment the cell was kept in the dark (hours to days) to avoid room lighting erasing the photoalignment pattern before the cell was filled and polymerized.

The monomer mixture was prepared by mixing 20% A6ZA6 diacrylate azobenzene monomer (BEAM Co.), 78.2% RM 257 diacrylate monomer (Merck), and 1.8 wt% of the visible light photoinitiator Irgacure 784 (Ciba). The mixture of these materials was solid at room temperature. Special care was taken to mix thoroughly. This mixture was heated into the isotropic phase. The isotropic liquid was placed on the lip of the alignment cell. The monomer mixture filled the photoaligned cells by capillary action in dark room conditions on a hotplate heated to 85 °C. After filling the cell the alignment was checked under cross-polarizers with red lighting. If the alignment of the cell was deemed imperfect the cell was heated to isotropic with a heat gun on the hot plate and allowed to slowly cool to 85 °C. After proper alignment the cell was transferred to a separate hotplate set to 75 °C, allowing the material to cool to the nematic phase. The sample was left for at least 3 minutes to reach this lower temperature. The cell was subsequently exposed to green light ( $\lambda = 532 \text{ nm}$ ,  $35 \text{ mW/cm}^2$ ) for 30 minutes to initiate photopolymerization. Green light was used so as to not impact the photoalignment of the cell.

After photopolymerization, the cells were opened with a razor blade to harvest the films. The films were cut into a circle with the topological defect centered within the circle. To assure that the defect was centered, the film was mounted (still on a piece of glass) at the center of a manual rotation stage. A stationary exacto knife was brought into contact with the film and subsequently the sample was rotated to complete the cut. The samples were cut into circles with a 14 mm diameter. Sample substrates were made by gluing rubber o-rings (inner diameter of 11 mm, outer

diameter of 12.5 mm) onto a piece of glass. After the gluing, distilled water was deposited around the outside diameter of the o-ring and then the sample was gently placed onto the o-ring. Care was taken to ensure that the interface between the o-ring and the film was wet. The boundary conditions afforded by this procedure allowed for consistent and repeated demonstrations of the topographical transformations, due to the reduction of friction and allowing the film to be subjected a uniform and small tensile force. This wet o-ring sample substrate allowed for even capillary forces on the outside of the film and the wet interface allowed for some movement to accommodate photoinduced deflection. The mounted film was exposed to 55 mW/cm<sup>2</sup> of blue ( $\lambda = 445\text{nm}$ ) unpolarized light from an LED for at least 30 minutes. The newly deformed shape was photographed and analyzed after irradiation. Over several days the amplitude of the deformation nearly disappears, but without cooling the film never fully returns to the flat state. Photogenerated mechanical effects in these materials have been reported to exhibit shape memory behavior.[19]

### **3.4 Conclusion**

In conclusion, we show that light can induce rich and diverse topographical transformations of initially flat films composed of photoresponsive, azobenzene-functionalized liquid crystalline polymer networks (azo-LCN). The topographical response of the defect-containing azo-LCN films was further confirmed experimentally and expanded to examine the response of higher order topological defects that have yet to be considered theoretically or experimentally. Ultimately, the N-fold symmetry of the topography of the photoinduced response of the defect-containing azo-LCN films was inherently coupled to the strength of the defect confirming that the director profile emanating from the topological defect is governing the behavior. The topographical transformation of flat films composed of hexagonal arrays of +2 and +4

topological defects were also presented. This work stands as an experimental demonstration of a ubiquitous approach to forming stimuli-responsive surface topographies and may provide insight into self-assembly processes in nature.

### 3.5 References

1. S. J. Woltman, G. D. Jay, G. P. Crawford, *Nat. Mater.* 2007, **6**, 929.
2. S. Murata, H. Kurokawa, *IEEE Robot. Autom. Mag.* 2007, **14**, 71.
3. A. D. Rey, *Soft Matter* 2010, **6**, 3402.
4. Y. Bouligand, *C.R. Chim.* 2008, **11**, 281.
5. S. C. Cowin, *J. Non-Newton. Fluid* 2004, **119**, 155.
6. D. P. Knight, F. Vollrath, *Philos. T. R. Soc. B* 2002, **357**, 155.
7. M. E. McConney, T. J. White, V. P. apg, L. V. Natarajan, D.-k. Yang, T. J. Bunning, *Soft Matter* 2012, **8**, 318.
8. K. Urayama, Y. Okuno, T. Kawamura, S. Kohjiya, *Macromolecules* 2002, **35**, 4567.
9. K. D. Harris, R. Cuypers, P. Scheibe, C. L. van Oosten, C. W. M. Bastiaansen, J. Lub, D. J. Broer, *J. Mater. Chem.* 2005, **15**, 5043.
10. C. L. van Oosten, K. D. Harris, C. W. M. Bastiaansen, D. J. Broer, *Eur. Phys. J. E* 2007, **23**, 329.
11. C. L. van Oosten, C. W. M. Bastiaansen, D. J. Broer, *Nat. Mater.* 2009, **8**, 677.
12. Y. Yu, M. Nakano, T. Ikeda, *Nature* 2003, **425**, 145.
13. M. Yamada, M. Kondo, J.-i. Mamiya, Y. Yu, M. Kinoshita, C. J. Barrett, T. Ikeda, *Angew. Chem. Int. Edit.* 2008, **47**, 4986.
14. M. Yamada, M. Kondo, R. Miyasato, Y. Naka, J.-i. Mamiya, M. Kinoshita, A. Shishido, Y. Yu, C. J. Barrett, T. Ikeda, *J. Mater. Chem.* 2009, **19**, 60.
15. T. J. White, N. Tabiryan, V. P. Tondiglia, S. Serak, U. Hrozhyk, R. A. Vaia, T. J. Bunning, *Soft Matter* 2008, **4**, 1796.

16. T. J. White, S. V. Serak, N. V. Tabiryan, R. A. Vaia, T. J. Bunning, *J. Mater. Chem.* 2009, **19**, 1080.
17. S. Serak, N. Tabiryan, T. J. White, R. A. Vaia, T. J. Bunning, *Soft Matter* 2010, **6**, 779.
18. K. M. Lee, M. L. Smith, H. Koerner, N. Tabiryan, R. A. Vaia, T. J. Bunning, T. J. White, *Adv. Funct. Mater.* 2011, **15**, 2913.
19. K. M. Lee, H. Koerner, R. A. Vaia, T. J. Bunning, T. J. White, *Soft Matter* 2011, **7**, 4318.
20. K. M. Lee, T. J. Bunning, T. J. White, *Adv. Mater.* 2012, **24**, 2839.
21. T. J. White, *J. Polym. Sci. Poly. Phys.* 2012, **50**, 877.
22. K. M. Lee, H. Koerner, D. H. Wang, L.-S. Tan, T. J. White, R. A. Vaia, *Macromolecules* 2012, **45**, 7527.
23. Y. Sawa, F. Ye, K. Urayama, T. Takigawa, V. Gimenez-Pinto, R. L. B. Selinger, J. V. Selinger, *P. Natl. Acad. Sci. USA* 2011, **108**, 6364.
24. C. D. Modes, M. Warner, *Phys. Rev. E* 2011, **84**, 021711/1.
25. C. D. Modes, K. Bhattacharya, M. Warner, *Phys. Rev. E* 2010, **81**, 060701.
26. C. D. Modes, M. Warner, C. Sanchez-Somolinos, L. T. de Haan, D. Broer, *Phys. Rev. E.* 2013, **86**, 060701/1.
27. C. D. Modes, M. Warner, *Europhys. Lett.* 2012, **97**, 36007/P1.
28. C. D. Modes, M. Warner, *Proc. SPIE* 2012, **8279**, 82790Q/1.
29. M. Kléman, *Rep. Prog. Phys.* 1989, **52**, 555.
30. N. D. Mermin, *Rev. Mod. Phys.* 1979, **51**, 591.
31. G. Toulouse, M. Kléman, *J. Phys. Lett.-Paris* 1976, **37**, 149.
32. M. Kléman, L. Michel, G. Toulouse, *J. Phys. Lett.-Paris* 1977, **38**, 195.
33. P. G. de Gennes, J. Prost, *The Physics of Liquid Crystals*, Clarendon Press, 1995.

34. O. D. Lavrentovich, V. M. Pergamenshchik, *Int. J. Mod. Phys. B* 1995, **09**, 2389.
35. F. C. Frank, *Discuss. Faraday Soc.* 1958, **25**, 19.
36. S. Nersisyan, N. Tabiryan, D. M. Steeves, B. R. Kimball, *Opt. Express* 2009, **17**, 11926.
37. L. T. de Haan, C. Sánchez-Somolinos, C. M. W. Bastiaansen, A. P. H. J. Schenning, D. J. Broer, *Angew. Chem., Int. Edit.* 2012, **51**, 12469.
38. S. Nersisyan, N. Tabiryan, D. M. Steeves, B. R. Kimball, *J. Appl. Phys.* 2010, **108**, 033101.
39. A. Y. G. Fuh, S.-W. Ko, S.-H. Huang, Y.-Y. Chen, T.-H. Lin, *Opt. Express* 2011, **19**, 2294.
40. K. M. Lee, N. V. Tabiryan, T. J. Bunning, T. J. White, *J. Mater. Chem.* 2012, **22**, 691.



## Chapter 4

# Three-dimensional complex-shaped photopolymerized microparticles at liquid crystal interfaces

Adapted from: *Soft Matter*, 2012, **8**, 2432.

### Chapter Overview

Microparticles of arbitrary shapes immersed in the bulk of nematic fluids are known to produce dipolar or quadrupolar elastic distortions that can mediate long-range colloidal interactions. We use two-photon photopolymerization to obtain complex-shaped surface-bound microparticles that are then embedded into a nematic liquid crystal host with a uniform far-field director. By means of three-dimensional imaging with multi-photon excitation fluorescence polarizing microscopy, we demonstrate low-symmetry, long-range elastic distortions induced by the particles in the liquid crystal director field. These director distortions may provide a means for controlling elastic interactions in liquid crystals between custom-designed photopolymerized microparticles attached to confining solid substrates and nematic fluid-borne colloids, thus enabling elasticity-mediated templated self-assembly.

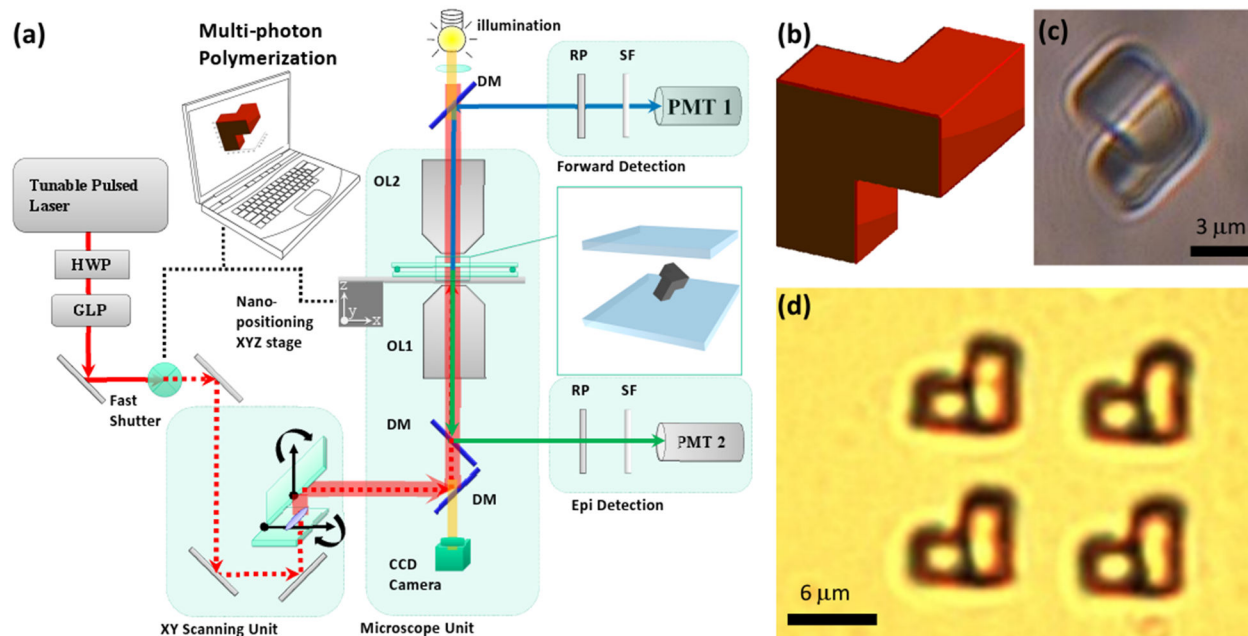
## 4.1 Introduction

A beautiful analogy between the distortion of a nematic liquid crystal (NLC) around colloidal inclusions and the electric field created by point charges, dipoles, and quadrupoles allows for understanding many interesting experimental observations in the rapidly growing research field of NLC colloids.[1-20] NLCs are anisotropic fluids with the unique properties of long-range orientational ordering and elasticity that are typically associated with crystalline solids.[16, 21, 22] They comprise anisotropic building blocks, such as rod- or disk-shaped molecules, particles, or micelles, which tend to spontaneously orient themselves along a common direction  $\mathbf{n}$ , called “director.” Unlike conventional fluids, nematics can transmit torques and induce elasticity-mediated forces that often cause relatively long-range interactions between particles, defects, and confining surfaces.[1,16] A number of factors, such as the molecular interactions at confining surfaces, presence of colloidal inclusions in the bulk or at surfaces of NLCs, chirality imposed by various chiral dopants (*i.e.*, dopants made of molecules that lack mirror symmetry), and application of external fields, can create continuous spatial variations of the molecular alignment and elastic distortions described by the spatially varying director field,  $\mathbf{n}(\mathbf{r})$ . [16] When introduced into a nematic fluid with a uniform far-field director  $\mathbf{n}_0$ , distortions of lower symmetry are expected to propagate to a longer distance.[16-20] This prediction was experimentally tested for both spherical and non-spherical colloidal particles in NLCs: the director distortions and ensuing elasticity-mediated interactions between dipolar colloids are longer ranged as compared to the case of quadrupolar colloids.[1-15]

In one of the readers' exercises of his book on *Physics of Liquid Crystals* (1<sup>st</sup> edition), [16] de Gennes considered a floating particle of an arbitrary shape in the NLC and argued that the

particle will align in such a way that the elastic torque acting on it will vanish and that the monopole-like low-symmetry distortions (decreasing with distance  $d$  as  $1/d$ ) can exist only when an external torque is acting on the particle. Although application of external forces and torques on particles can induce “elastic monopoles,”[16-20] they are unstable without external influence as the elastic torque exerted by the NLC medium causes anisotropic particles to equilibrate at an orientation with the lowest symmetry of distortions being dipolar with one or more dipole moments.[8] However, it is not clear whether interactions between surface-bound and NLC-borne particles follow a similar behavior. Furthermore, experimental demonstration of twisted director configurations induced by nanofabricated chiral structures in confined NLCs (see, for example, ref. 23) indicates the need for exploring how long-range elastic distortions can possibly be exerted by surface-bound low-symmetry micrometre- and nanometre-sized particles.

In this work, we have designed three-dimensional (3D) low-symmetry, surface-bound, photopolymerized particles to demonstrate that they can cause low-symmetry, long-range elastic distortions in  $\mathbf{n}(\mathbf{r})$ , which we probe by means of three-photon excitation fluorescence polarizing microscopy (3PEF-PM).[24,25] We demonstrate that these particles induce director twist and impose elastic torque on the NLC director field  $\mathbf{n}(\mathbf{r})$  which is transmitted to an opposite confining surface of the liquid crystal cell. Our findings may enable novel means of patterning bulk alignment of NLCs and the design of novel long-range interactions between the NLC fluid-borne and surface-attached particles for their structured elasticity-mediated self-assembly.



**Fig. 4.1** Photopolymerization and nonlinear optical imaging by means of multi-photon excitation processes. (a) A schematic diagram of the multi-photon absorption photopolymerization and multi-photon excitation fluorescence microscopy setup. DM: dichroic mirror, GLP: Glan laser polarizer, HWP: half-wave plate, OL: objective lens, PMT: photo-multiplier tube, RP: rotating polarizer, and SF: selection filters. (b) A computer-generated model of the used low-symmetry microparticle. (c) A brightfield optical image of a microparticle obtained from the model shown in (b) by means of two-photon absorption photopolymerization. (d) A brightfield image of an array of four surface-bound photopolymerized microparticles having shape corresponding to the computer-generated model shown in (b).

## 4.2 Materials and Methods

A schematic diagram of a two-photon photopolymerization and 3PEF-PM setup is shown in Fig. 4.1a. A tunable (680–1080 nm) femtosecond Ti:sapphire laser (140 fs, 80 MHz, Chameleon Ultra-II, Coherent) is used as an excitation light source for both photopolymerization and 3PEF-PM (which is an imaging modality of nonlinear optical polarizing microscopy described in detail in references 24 and 25). For the two-photon photopolymerization, a femtosecond laser beam tuned to a wavelength of 780 nm is introduced into an inverted microscope (IX-81, Olympus) and tightly focused into a sample by an oil-immersion objective (100 $\times$ , NA = 1.4). The exposure of the sample is controlled by a fast shutter (LS3Z2 obtained from Uniblitz, up to 200 Hz)

introduced into the optical train of the photopolymerization setup immediately before the microscope (Fig. 4.1a). A computer-controlled XYZ nano-positioning stage (Nanocube P-611.3SF obtained from Physik Instrumente) changes the relative 3D position of the sample with respect to the focal point of the focused femtosecond laser beam with the precision of 0.2 nm. Laser beam intensity and its polarization direction at the sample plane are controlled by a half-wave plate and a Glan laser polarizer. To impose a computer-generated 3D-shape into the photocurable resin, we continuously translate the XYZ stage and time the shutter so that the focus of the femtosecond laser beam can visit and sequentially polymerize all points of the desired volume of the complex-shaped microparticle.

#### **4.2.1 Cell Preparation and Particle Fabrication**

The cells used during the photopolymerization part of the sample preparation process consist of two coverslips, one of which is coated with a thin film of unidirectionally rubbed polyvinyl alcohol (PVA, obtained from Aldrich). The glass plates are spaced with two thin strips of parafilm. A small drop of UV-curable optical adhesive (NOA-61, obtained from Norland) is sandwiched between two coverslips held together by two pieces of Scotch tape. We then place the cell on a mounting clip attached to the Nanocube XYZ stage so that it can be scanned over the objective during the photopolymerization of 3D microparticles within the drop (Fig. 4.1c and d). In this process, the polymerization starts at the PVA–NOA interface and then advances away from the substrate as we shift the sample along the microscope's optical axis to “draw” the consecutive layers of the particle (Fig. 4.1b). After the photopolymerization of the desired surface-attached particles is completed, the cell is disassembled and the coverslip carrying the attached particles is lightly rinsed with acetone to wash away the excess, unpolymerized resin.

Obtained particles can be kept surface-bound or released from the substrate by carefully poking with a needle (Fig. 4.1c and d).

The studied LC cells were constructed using one PVA-coated substrate having the polymerized particles bound to its surface and one substrate treated with polyimide (PI-2555, obtained from HD Microsystems) or derivative of methyl red (dMR). PVA and polyimide thin coatings were rubbed using velvet cloth to provide unidirectional planar surface anchoring. Prior to coating these substrates with dMR, PVA and PI-2555 alignment layers, we first cleaned the glass substrates using organic solvents and then additionally plasma-cleaned them for about 20 minutes. To obtain dMR coated substrates, we finally submerged the clean glass into the dilute dMR solution (<1 wt%) for 90 minutes, allowing the dMR molecules to chemically bond onto the glass surfaces. We then rinsed the substrates thoroughly with toluene to wash away any excess and unbound dMR, leaving only a molecular monolayer behind. The cell substrates were spaced with 15  $\mu\text{m}$  spherical glass spacers mixed into epoxy glue. After the epoxy-spacer mix is cured, binding the glass plates together, we filled the cell with a room-temperature NLC, pentylcyanobiphenyl (5CB, obtained from Frinton Labs), and then sealed the edges with epoxy.

To study elastic interactions between colloids and the surface-bound photopolymerized particles, we have prepared an NLC colloidal dispersion of 2  $\mu\text{m}$  spheres with vertical surface boundary conditions for  $n(r)$ . We obtained these boundary conditions at the surface of particles by first dispersing the silica spheres in 5 wt% aqueous solution of the surfactant [3-(trimethoxysilyl)propyl]octadecyl-dimethylammonium chloride (DMOAP, purchased from Aldrich) and then sonicating for 30 minutes. The particles were then rinsed *via*

sequential centrifugation at 3000 rotations per minute, replacement of the solvent with deionized water, and sonication for about 30 seconds. The rinsing process was repeated five times and the remaining water was then evaporated on a hot stage at about 120 °C for 10 hours. Once the particles were added to the NLC, the obtained dispersion was again sonicated for three hours to break colloidal aggregates and then used to fill in the cells immediately after the sonication.

#### 4.2.2 3D Imaging of Structures

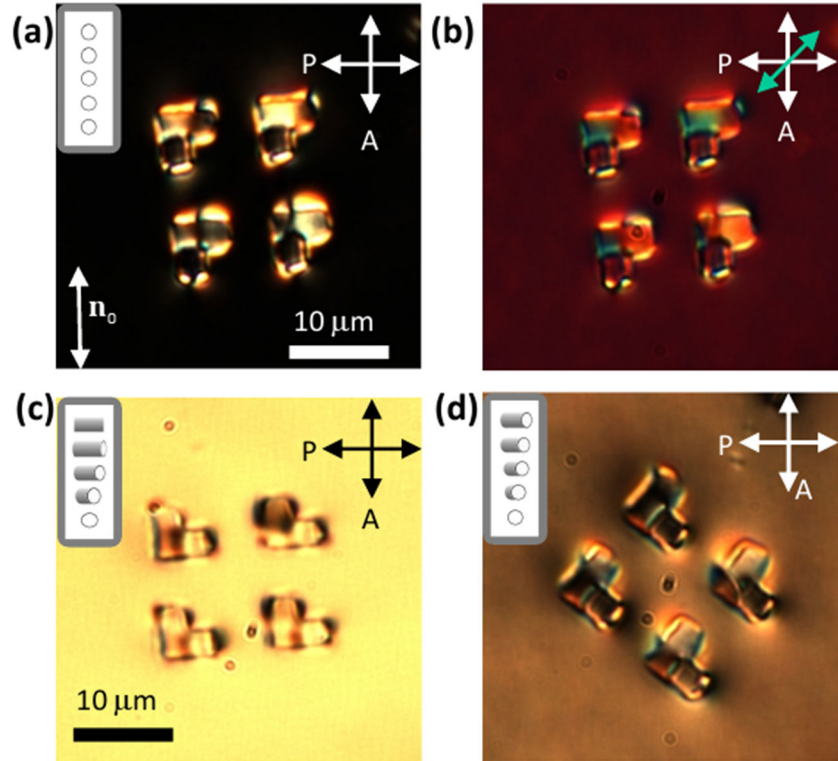
3D imaging of the NLC was performed using 3PEF-PM. A femtosecond laser beam at the wavelength of 870 nm is introduced into the laser-scanning unit (FV-300, Olympus) and is focused into a sample using an oil-immersion objective (100×, NA = 1.4) of the inverted IX-81 microscope (Fig. 4.1a). A galvano-mirror pair in the scanning unit steers the position of a focused laser beam laterally within the focal plane of the objective while the motion of the objective along the microscope's optical axis is implemented by the use of a stepper motor. The 3PEF-PM signals are collected either by the same objective and detected in epi-detection mode with a photomultiplier tube (PMT2) or by another oil-immersion objective (60×, NA = 1.42) in a forward-detection mode with PMT1 (both tubes were obtained from Hamamatsu, model H5784-20). To control the linear polarization state of excitation light, we use a Glan laser polarizer. The laser beam at 870 nm wavelength excites the NLC molecules directly *via* the three-photon absorption process and the fluorescence light is then detected using a bandpass filter centered at 417 nm (bandwidth 60 nm). Since the excitation intensities required to induce significant three-photon absorption only exist in a small volume around the focus of the objective, this imaging approach yields an intrinsic 3D resolution. The fluorescence intensity in

the 3PEF-PM with unpolarized fluorescence detection scales as  $\sim \cos^6\theta$ , where  $\theta$  is the local angle between  $\mathbf{n}(\mathbf{r})$  and the polarization of the excitation beam.[24,25] The polarized fluorescence textures allow us to reconstruct the 3D  $\mathbf{n}(\mathbf{r})$ . In addition to the 3PEF-PM imaging and photopolymerization, our setup (Fig. 4.1a) also allows for imaging using the conventional polarizing optical microscopy (POM) with and without inserted phase retardation plates.

### 4.3 Results and Discussion

NLC cells with one of the substrates coated with the photoresponsive dMR molecular monolayers allow for realization of both uniform and twisted configurations of  $\mathbf{n}(\mathbf{r})$ . Polarized illumination from a lamp source aligns the aromatic parts of dMR molecules perpendicular to the polarization direction. This allows one to set the boundary conditions for  $\mathbf{n}(\mathbf{r})$  on this surface by continuously varying the easy axis orientation between parallel and perpendicular to the rubbing direction at the opposite PVA-coated substrates, *i.e.*, achieving either uniform (Fig. 4.2a and b) or twisted director structures (Fig. 4.2c and d). POM images with and without a phase retardation plate (Fig. 4.2a and b) suggest a complex low-symmetry configuration of  $\mathbf{n}(\mathbf{r})$  around the surface-bound particle. The area near the particle is bright under crossed polarizers (Fig. 4.2a) and the structure of distortions and surrounding defects changes as one induces twist across the cell (Fig. 4.2c and d). Since the particle-induced structures are 3D in their nature and the spatial variation of the director field across the cell thickness is complex, reconstruction of the  $\mathbf{n}(\mathbf{r})$  based on the POM images alone is difficult, although these images do indicate the presence of twist across the sample thickness in the regions of particles.

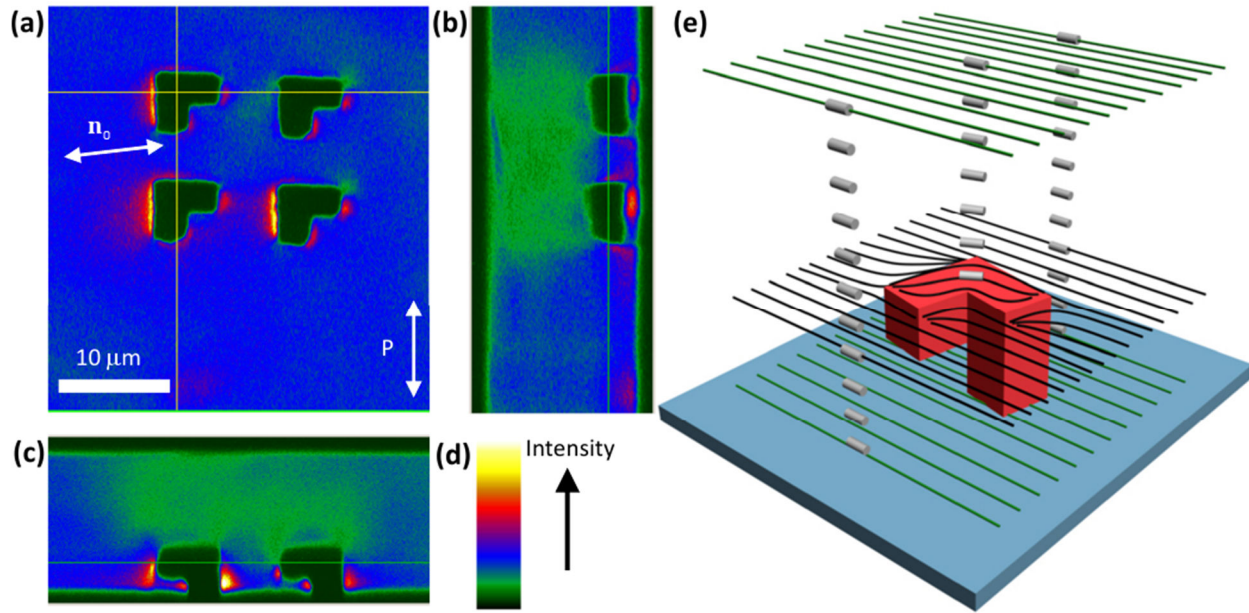




**Fig. 4.2** Polarizing optical microscopy images of director structures around complex-shaped microparticles in uniform and twisted nematic LC cells. (a and b) POM images of a four-particle array in LC within a uniform far-field director  $n_0$  (a) between crossed polarizers and (b) with an additional phase retardation plate having the slow axis at 45 degrees with respect to the crossed polarizers, marked by the green double arrow. (c and d) POM images of the same array after the far-field director was twisted by (c) 90 degrees and (d) 45 degrees across the sample thickness *via* reorientation of dMR molecules in the monolayer as the sample cell was rotated by 90 degrees and 45 degrees, respectively. The NLC far-field molecular alignment across the sample thickness is shown in the insets of (a), (c) and (d).

To get an insight into the 3D structure of  $n(\mathbf{r})$  induced by the photopolymerized particles, we perform the 3PEF-PM imaging. Using the near-infrared light excitation in 3PEF-PM allows us to mitigate the possible effects of imaging light on the dMR surface monolayer, which is sensitive to shorter-wavelength visible light. We also use excitation light of relatively low intensity to minimize its possible effects on dMR through the multiphoton absorption processes. The in-plane and vertical cross-section images obtained by 3PEF-PM are shown in Fig. 4.3a–c. Using these and other 3PEF-PM cross-sections, we construct the 3D model of  $n(\mathbf{r})$  around the particle

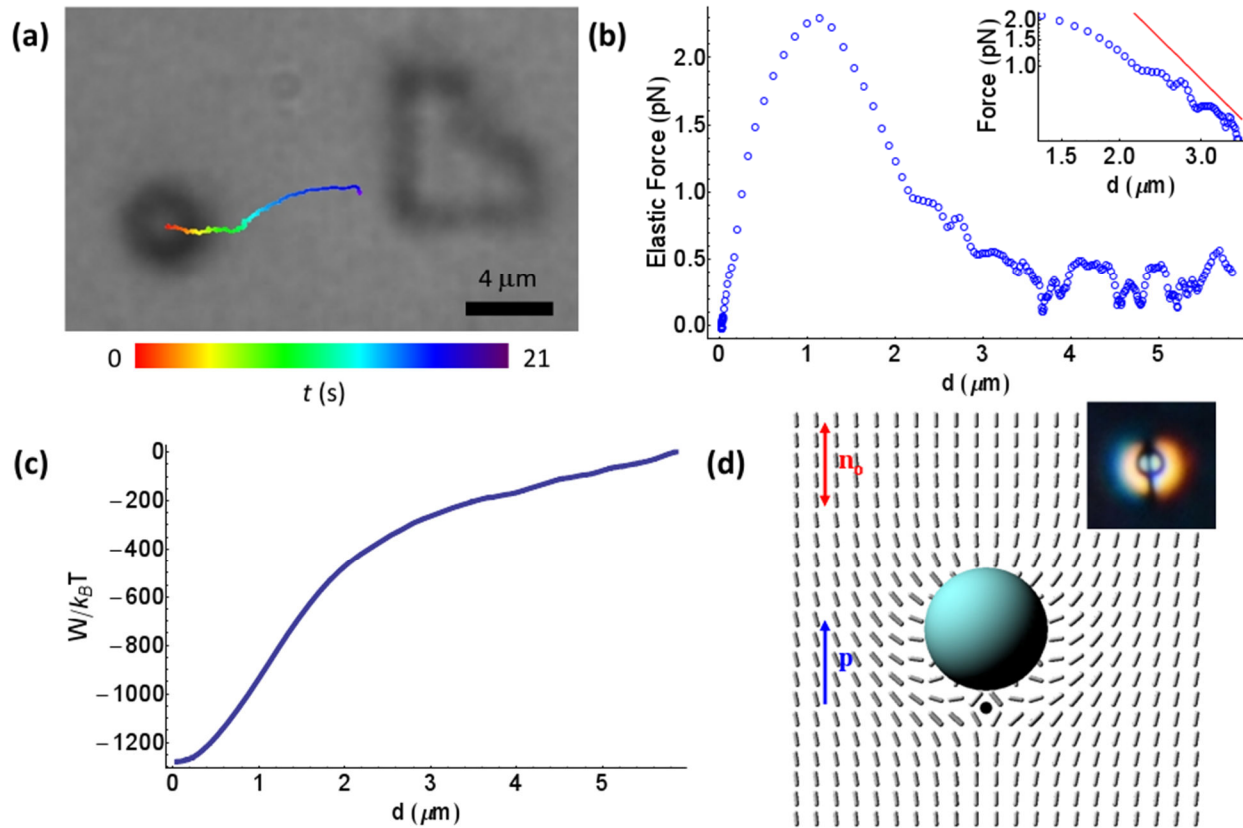
schematically shown in Fig. 4.3e. The photopolymerized particle imposes tangential degenerate boundary conditions for the director at the NLC–particle interface. Within the sample with a uniform, in-plane, far-field director  $\mathbf{n}_0$ , the substrate-bound particle is orientated so that all of its side faces are misaligned and at different angles with respect to  $\mathbf{n}_0$ . This, along with the shape of the top part of the particle, imposes strong elastic distortions of  $\mathbf{n}(\mathbf{r})$  around the particle. We observe a twisted director structure propagating from the top surface of the particle toward the opposite dMR-coated glass substrate. Although the surface boundary conditions for  $\mathbf{n}(\mathbf{r})$  at the NLC–particle interface are tangentially degenerate, the shape of the particle and the side faces lift this degeneracy so that  $\mathbf{n}(\mathbf{r})$  in the central part of the top particle–NLC interface aligns roughly along a diagonal of the L-shaped top interface, as schematically shown in Fig. 4.3e. The twist distortion of  $\mathbf{n}(\mathbf{r})$  then matches this average alignment of the director at the particle–NLC interface to the boundary conditions at the top substrate set by the optically controlled dMR monolayer (Fig. 4.3). Consistent with the results of 3PEF-PM imaging, the region above the particle appears bright in POM under crossed polarizers (Fig. 4.2a). Individual particles and their arrays (such as the  $2 \times 2$  array shown in Fig. 4.2a) exhibit a similar behavior and all induce twist of the same handedness, which is pre-determined by the symmetry and orientation of the used complex-shaped surface-bound particles (Fig. 4.2 and 4.3). Since the ensuing 3D structures of  $\mathbf{n}(\mathbf{r})$  have all mirror symmetry planes broken and induce net twist with the helical axis along the normal to the substrates of the cell, this implies that the surface-bound photopolymerized particles in this geometry exert a torque on the NLC director. Experimental images indicate that  $\mathbf{n}(\mathbf{r})$  at the NLC interface with the top dMR-coated substrate above the photopolymerized particle might slightly deviate (not shown in the schematic in Fig. 4.3e) from the easy axis set by polarized illumination, due to the fact that the surface anchoring at the dMR–NLC interface is



**Fig. 4.3** 3D director field around photopolymerized surface-bound low-symmetry microparticles. (a–c) Cross-sectional 3PEF-PM images of  $\mathbf{n}(\mathbf{r})$  in the LC around the surface-attached microparticle obtained (a) in the plane parallel to confining substrates, (b and c) in the vertical cross-sections along two thin orthogonal lines shown in (a). (d) Color-coded fluorescence intensity scale used in (a–c). (e) 3D perspective of the reconstructed director field around the complex-shaped surface-bound colloidal microparticle; the green lines represent the surface boundary conditions for  $\mathbf{n}(\mathbf{r})$  at the confining cell substrates and the black lines show  $\mathbf{n}(\mathbf{r})$  in the plane coinciding with the top surface of the photopolymerized microparticle. The three columns of cylinders in (e) show that  $\mathbf{n}(\mathbf{r})$  is twisted across the cell above the particle but is uniform far from it.

finite (soft boundary conditions) and this deviation partially relieves the twist distortion in the NLC bulk above the particle (Fig. 4.3).

We have explored interactions of NLC-borne colloidal inclusions with the complex-shaped photopolymerized particles attached to the substrates. Despite the screening caused by the confinement, these elasticity-mediated interactions are long-range and strongly anisotropic. Fig. 4.4a shows an example of a trajectory of particle motion due to the elastic interaction between the floating colloid and a surface-bound particle. Both particles generate elastic distortions of  $\mathbf{n}(\mathbf{r})$  in the NLC. The floating silica microsphere induces a hyperbolic point defect of



**Fig. 4.4** Elasticity-mediated interaction between a surface-bound low-symmetry microparticle and a free-floating colloidal sphere with dipolar elastic distortions. (a) A brightfield microscopy frame from a movie showing a spherical particle at its initial position with an overlaid color-coded particle motion trajectory; the color-coded time scale is shown at the bottom of the image. (b) Elastic force exerted on the colloidal particle plotted as a function of the separation distance. The inset shows a log–log plot of this dependence over an intermediate range of distances; the red straight line shows a slope of  $-3$ . (c) The elastic interaction energy vs. separation distance. (d) Dipolar distortions of the director field around a spherical colloid embedded into the NLC with a uniform far-field director  $\mathbf{n}_0$ . The inset in (d) shows a POM image obtained between crossed polarizers parallel to the orthogonal image edges. The dipole moment of the elastic dipole shown in (d) is labeled by a blue arrow and “ $\mathbf{p}$ ”.

charge  $N = -1$ , which compensates for the vertical boundary conditions, and the ensuing radial director structure around the particle surface (the radial director field is equivalent to a point defect of charge  $N = 1$ ), as shown in Fig. 4.4d. These elastic distortions around the microsphere have a dipolar symmetry of  $\mathbf{n}(\mathbf{r})$  while the distortions around the photopolymerized particle are monopole-like (since this surface-bound particle was intentionally fabricated to be oriented

differently from what would be its equilibrium orientation in the NLC bulk). When the mobile particle is attracted toward the stationary one, the two particles share some of the induced elastic distortions and thus minimize the elastic energy cost due to the overall  $\mathbf{n}(\mathbf{r})$  distortions in the cell. Although the elastic interactions are strongly screened by the proximity of confining substrates (especially the one to which the photopolymerized particle is bound) from which the floating dipolar colloidal particle repels,[26] the elastic binding energy of the mobile colloid to the stationary particle exceeds  $1000 k_B T$  (Fig. 4.4c) and is comparable to the elastic binding energies between floating microparticles in the NLC bulk.[9] Furthermore, despite having physical underpinnings of elastic interactions similar to those studied for colloids in the NLC bulk, they may enable a qualitatively different type of medium-mediated templated self-assembly of particles using specially designed structured surfaces.

Elastic inter-particle interaction forces are characterized by the use of their balance with viscous forces, which are measured by video-tracking particle motion. We track the particle positions *vs.* time (Fig. 4.4a) and determine their velocity  $v$ . All forces acting on the colloid sum up to the inertial force,  $ma$ . [29, 30] We neglect the inertia effects ( $ma=0$ ) (since particle motion is overdamped and the Reynolds number is small) and determine the elastic force from its balance with the viscous drag force given by the Stokes' formula for a microsphere,  $F_e = 6\pi\eta_{\text{eff}}Rv$  (Fig. 4.4b), where  $\eta_{\text{eff}}$  is the effective viscous drag coefficient for the particle with the surrounding “corona” of  $\mathbf{n}(\mathbf{r})$  distortions.  $\eta_{\text{eff}}$  depends on the motion direction of the particle with respect to  $\mathbf{n}_0$  and also on the  $\mathbf{n}(\mathbf{r})$  structure around the colloid. We use  $\eta_{\text{eff}} = 86.4$  cP, as previously determined for a particle with dipolar  $\mathbf{n}(\mathbf{r})$  in 5CB for a similar geometry.[27] We find that the maximum attractive elastic force is about 2.3 pN (Fig. 4.4b). This

is an external force needed to separate the mobile colloid from the elastic trap produced by the surface-attached particle and, in analogy to the case of optical trapping, can be called “elastic trap escape force.” Since the elastic force increases linearly (for small distances) as a function of the separation distance between the particle and its equilibrium location in the elastic trap, one can also determine the stiffness of this elastic trap, which is  $\sim 4.6 \text{ pN } \mu\text{m}^{-1}$ . The elastic force decays rather weakly with distance to the final equilibrium location of the mobile dipolar colloid at the edge of the photopolymerized surface-bound particle (Fig. 4.4b). This might be due to the fact that the low-symmetry  $n(\mathbf{r})$  around the photopolymerized particle is monopole-like. In a bulk of an NLC, the interaction force between an elastic monopole (obtained, for example, by means of exerting an external torque on a non-spherical colloid) and an elastic dipole is expected to scale with center-to-center separation  $r_{cc}$  as  $\propto r_{cc}^{-3}$ . Indeed, the log–log plot in the inset of Fig. 4.4b shows that the elastic force between the NLC-borne and surface bound particles decays with distance weaker than what is expected for bulk dipole–dipole interactions ( $\propto r_{cc}^{-4}$ ), although the slope changes from about  $-2$  to about  $-3$ , depending on the range of distances. This is likely due to the fact that the observed elastic interactions are strongly screened by the effects of confinement, which weaken these interactions, especially at larger inter-particle distances (Fig. 4.4b).[28] Furthermore, at short distances, the dipole–monopole interaction is further modified by the trap-like behavior with the NLC-borne mobile colloid coming to rest in the elastic trap generated by the surface-bound particle. New theories are needed for quantitative modelling of our experimental findings, since they cannot be fully explained within the frameworks of available theories for the elasticity-mediated interactions in the NLC bulk.

## 4.4 Conclusion

To conclude, we have demonstrated the feasibility of inducing monopole-like elastic distortions in NLCs by means of complex-shaped low-symmetry particles attached to the confining solid substrates of a liquid crystal cell and oriented differently from what would be their equilibrium orientation in the NLC bulk. This approach can be extended to particles with other surface boundary conditions, symmetry of distortions, chemical composition, *etc.* Furthermore, our findings may provide a means for the control of elastic interactions in NLCs between custom-designed particles attached to solid confining substrates and nematic fluid-borne colloids, thus enabling novel methods for templated self-assembly of colloidal superstructures.

## 4.5 References

1. P. Poulin, H. Stark, T. C. Lubensky and D. A. Weitz, *Science*, 1997, **275**, 1170.
2. U. Tkalec, M. Škarabot and I. Muševič, *Soft Matter*, 2008, **4**, 2402.
3. F. Brochard and P. G. de Gennes, *J. Phys. (Paris)*, 1970, **31**, 691.
4. T. C. Lubensky, D. Pettey, N. Currier and H. Stark, *Phys. Rev. E: Stat. Phys., Plasmas, Fluids, Relat. Interdiscip. Top.*, 1998, **57**, 610.
5. B. I. Lev, S. B. Chernyshuk, P. M. Tomchuk and H. Yokoyama, *Phys. Rev. E: Stat., Nonlinear, Soft Matter Phys.*, 2002, **65**, 021709.
6. I. Dierking, G. Biddulph and K. Matthews, *Phys. Rev. E: Stat., Nonlinear, Soft Matter Phys.*, 2006, **73**, 011702.
7. V. M. Pergamenshchik and V. A. Uzunova, *Condens. Matter Phys.*, 2010, **13**, 33602.
8. V. M. Pergamenshchik and V. A. Uzunova, *Phys. Rev. E: Stat., Nonlinear, Soft Matter Phys.*, 2011, **83**, 021701.
9. C. P. Lapointe, T. G. Mason and I. I. Smalyukh, *Science*, 2009, **326**, 1083–1086.
10. M. Škarabot and I. Muševič, *Soft Matter*, 2010, **6**, 5476.
11. D. Engström, R. P. Trivedi, M. Persson, K. A. Bertness, M. Goksör and I. I. Smalyukh, *Soft Matter*, 2011, **7**, 6304.
12. J. S. Evans, C. Beier and I. I. Smalyukh, *J. Appl. Phys.*, 2011, **110**, 033535.
13. Q. Liu, Y. Cui, D. Gardner, X. Li, S. He and I. I. Smalyukh, *Nano Lett.*, 2010, **10**, 1347.
14. I. I. Smalyukh, J. Butler, J. D. Shrout, M. R. Parsek and G. C. L. Wong, *Phys. Rev. E: Stat., Nonlinear, Soft Matter Phys.*, 2008, **78**, 030701(R).
15. G. M. Koenig, I.-H. Lin and N. L. Abbott, *Proc. Natl. Acad. Sci. U. S. A.*, 2010, **107**, 3998.
16. P. G. de Gennes, *Physics of Liquid Crystals*, Oxford University Press, London, 1st edn, 1974.



17. V. M. Pergamenschchik and V. A. Uzunova, *Phys. Rev. E: Stat., Nonlinear, Soft Matter Phys.*, 2007, **76**, 011707.
18. B. I. Lev and P. M. Tomchuk, *Phys. Rev. E: Stat. Phys., Plasmas, Fluids, Relat. Interdiscip. Top.*, 1999, **59**, 591.
19. J.-I. Fukuda, B. I. Lev and H. Yokoyama, *J. Phys.: Condens. Matter*, 2003, **15**, 3841.
20. J. B. Fournier, *Eur. J. Phys.*, 1993, **14**, 184.
21. S. J. Woltman, D. G. Jay and G. P. Crawford, *Nat. Mater.*, 2007, **6**, 929.
22. P. M. Chaikin and T. C. Lubensky, *Principles of Condensed Matter Physics*, Cambridge Univ. Press, Cambridge, 2000.
23. K. Robbie, D. J. Broer and M. J. Brett, *Nature*, 1999, **399**, 764.
24. T. Lee, R. P. Trivedi and I. I. Smalyukh, *Opt. Lett.*, 2010, **35**, 3447.
25. R. P. Trivedi, T. Lee, K. A. Bertness and I. I. Smalyukh, *Opt. Express*, 2010, **18**, 27658.
26. A. Martinez, H. Mireles and I. I. Smalyukh, *Proc. Natl. Acad. Sci. U. S. A.*, 2011, **108**, 20891.
27. H. Stark and D. Ventzki, *Phys. Rev. E: Stat., Nonlinear, Soft Matter Phys.*, 2001, **64**, 031711.
28. V. M. Pergamenschchik and V. A. Uzunova, *Phys. Rev. E: Stat., Nonlinear, Soft Matter Phys.*, 2009, **79**, 021704.
29. I. Newton, *Philosophiæ Naturalis Principia Mathematica*, 1687.
30. J. Hermann, *Phoronomia, sive De viribus et motibus corpum solidorum et fluidorum libri duo*, 1716.

## Chapter 5

# Mutually tangled colloidal knots and induced defect loops in nematic fields

Adapted from: *Nat. Mater.* 2014, **13**, 258.

### Chapter Overview

Colloidal dispersions in liquid crystals can serve as a soft-matter toolkit for the self-assembly of composite materials with pre-engineered properties and structures that are highly dependent on particle-induced topological defects.[1, 2, 3] Here, we demonstrate that bulk and surface defects in nematic fluids can be patterned by tuning the topology of colloidal particles dispersed in them. In particular, by taking advantage of two-photon photopolymerization techniques to make knot-shaped microparticles, we show that the interplay of the topologies of the knotted particles, the nematic field and the induced defects leads to knotted, linked and other topologically non-trivial field configurations.[4-12] These structures match theoretical predictions made on the basis of the minimization of the elastic free energy and satisfy topological constraints.[4, 5] Our approach may find uses in self-assembled topological superstructures of knotted particles linked by nematic fields, in topological scaffolds supporting the decoration of defect networks with

nanoparticles [1], and in modelling other physical systems exhibiting topologically analogous phenomena.[12-16]

## **5.1 Introduction**

One of the grand challenges of modern material science is to design and assemble three-dimensional (3D) structures of low-symmetry colloidal particles that can reproduce complex behavior of atomic systems with different types of bonding and a large number of chemical elements.[15-24] Interestingly, long before the nature of atoms could be understood, early mathematical developments of knot theory, one of the key branches of topology, were prompted by Lord Kelvin's conjecture from 1867 that atoms of all elements were different knotted defect lines known as 'vortices'. [4, 5, 12] Although our modern understanding of atoms is very different and naturally occurring materials are not just tangled knots of defects, applications of the mathematical knot theory are nowadays found in many branches of science, including material systems such as liquid crystals, cosmology, quantum chromodynamics, and both classical and quantum field theories.[3-11] However, there are few theoretical predictions involving knotted fields and vortices that can be tested by experiments [9], which is due to the lack of systems and techniques that allow for controlling types and spatial arrangements of defects in three dimensions. On the other hand, mastering control of topological defects in liquid crystals is also important from a practical standpoint because they are key for mediating nanoscale confinement and mesoscale self-assembly of nanoparticles.[1, 17-23]

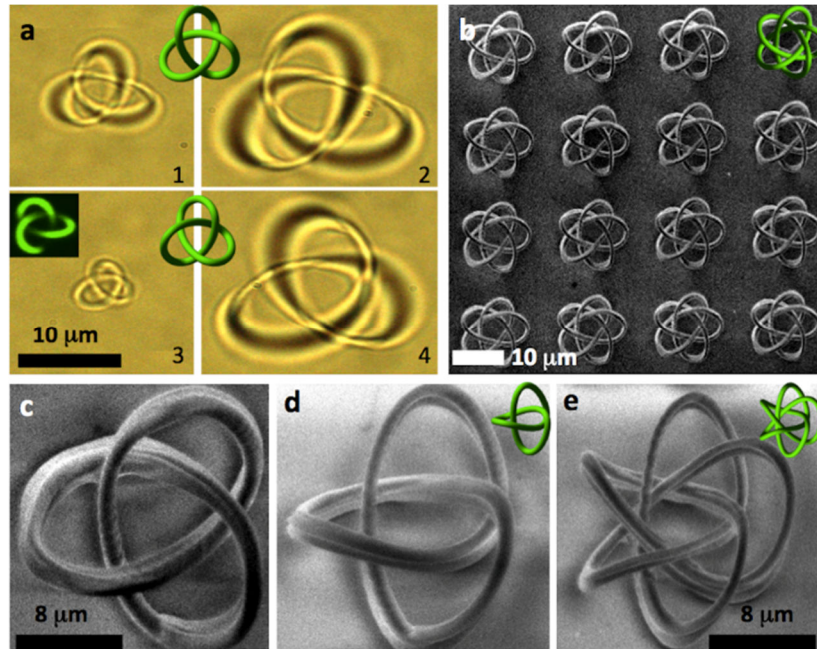
In this work, we develop knotted nematic colloids that enable the generation and control of 3D patterns of point defects and configurations of looped line defects, such as tangled knots, thus allowing for experimental insights into predictions from knot theory and into the interplay of topologies of knotted surfaces, fields and defects.[4, 5] On the one hand, this may be used for understanding other experimentally less accessible physical systems with similar topology, ranging from particle physics to cosmology.[13-16] On the other hand, our knotted colloids can be used as building blocks of topological matter, this arising from the mesoscale self-organization of knotted colloidal ‘atoms’ driven by the minimization of elastic free energy and from the mutual entanglement of induced defects. Particle-controlled configurations of defects may also serve as topologically non-trivial scaffolds for the 3D patterning of semiconductor and metal nanoparticles [1], as needed for the scalable fabrication of composite materials with pre-designed properties. Our findings show that the behavior of knotted colloidal ‘atoms’ obeys topological constraints, and, therefore, that topological theorems and mathematical knot theory can be used to guide the design of self-assembled knotted matter as envisaged by Kelvin.[12]

## **5.2 Results and Discussion**

Colloids are stable dispersions of microscopic particles in host media [16], which in the case of nematic colloids consist of particles dispersed in a host fluid of anisotropic liquid-crystal molecules that spontaneously align along the director  $\mathbf{n}$  (refs 17-23). Colloidal particles can also be anisotropic, typically in terms of the shape and chemical functionalization of their surfaces. Anisotropic particles were central to recent efforts of reproducing the complexity of atomic bonding in self-assembled colloidal structures [24] and of generating biomimetic self-propulsion capabilities.[25] However, all anisotropic colloids made so far exhibit relatively high symmetry,

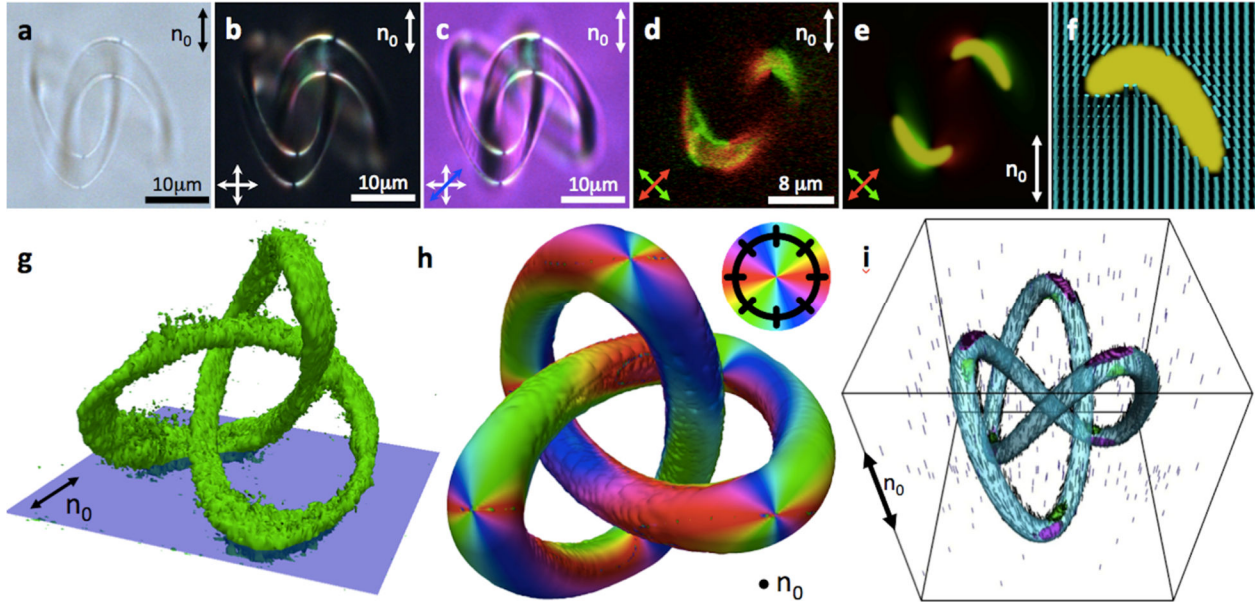
and colloidal synthesis typically offers limited control of surface topology.[23] Here, we use two-photon photopolymerization with spatially patterned pulsed femtosecond laser light (see Methods and Appendix Fig. C.1) [26] to obtain rigid particles with the surface topology of torus knots  $T(p,q)$ . The particles are formed by knotted polymeric tubes that, before having their ends joined, are looped  $p$  times through the hole of an imaginary torus, with  $q$  revolutions about the torus rotational symmetry axis [4, 5] (Fig. 5.1). The minimum number of crossings of the polymeric tube in these particles is given by the so-called crossing number  $c = \min\{p(q-1), q(p-1)\}$ . When dispersed in liquid crystals, these knotted colloids with controlled surface boundary conditions distort the director field  $\mathbf{n}(\mathbf{r})$ , which approaches the uniform far-field director  $\mathbf{n}_0$  at large distances. 3D visualization of  $\mathbf{n}(\mathbf{r})$  by means of nonlinear optical polarizing microscopy (Appendix Figs C.2 and C.3), assisted by holographic optical tweezers [27, 28], reveals a topological interplay among surfaces of knotted particles, nematic fields and defects.

Nematic dispersions of trefoil particle knots—known more formally as  $T(3,2)$  torus knots and also as  $3_1$  knots in the Alexander–Briggs notation [4]—are first explored in the regime where the nematic molecular orientation field at the particle surfaces is set to be tangential. In a stable configuration, which corresponds to the minimum of free energy, the trefoil colloids align with their torus plane perpendicular to the undistorted far-field nematic director  $\mathbf{n}_0$ . As their complex shape is incompatible with the inherently homogeneous field of the aligned nematic liquid crystal, point defects called ‘boojums’ emerge at the surfaces of the particles, and are visible in bright-field micrographs as dark points due to scattering (Fig. 5.2a). Polarizing microscopy textures show smooth variations of the molecular orientation field everywhere in the sample,



**Fig. 5.1** Photopolymerized knotted particles and their arrays. (a), Optical micrographs showing photopolymerized left-handed (panels 1 and 2) and right-handed (panels 3 and 4) trefoil colloidal torus knots  $T(3,2)$  with  $c=3$  and of different sizes, with the corresponding 3D models shown in green. The top-left inset in panel 3 shows a 3PEF-PM image of a colloidal particle of the same chirality and comparable size as that shown on the same panel. Micrographs show particles being slightly larger than their actual size because of the limited optical resolution. (b), Scanning electron micrograph of a  $4 \times 4$  array of torus knots  $T(5,3)$  with  $c=10$  on a glass substrate. (c–e), Zoomed-in scanning electron micrographs of single  $T(3,2)$  (c,d) and  $T(5,3)$  (e) knots shown from different perspectives, along with the corresponding 3D models (depicted in green), as viewed along the torus axis (c) and in an oblique direction (d,e).

except at the boojums (Fig. 5.2b,c). Using the three-photon excitation fluorescence polarizing microscopy (3PEF-PM) technique with polarized laser excitation [27, 28], we explore the full 3D molecular orientation field (Fig. 5.2d,g) by probing high-intensity fluorescence patterns (originating from both the polymer in the particle and the surrounding liquid crystal with director distortions) shaped as trefoil knots with elliptical cross-sections, which reveal the strongest director distortions in regions where colloidal surfaces are orthogonal to  $\mathbf{n}_0$ , consistent with



**Fig. 5.2** A trefoil knot particle with tangential boundary conditions in an aligned liquid crystal. (a–c), Bright-field and polarizing optical micrographs taken without polarizers (a), between crossed polarizers whose directions are shown by white double arrows (b,c), and with an additional 530 nm retardation plate having its slow axis aligned as shown by the blue double arrow (c). Locations of boojums are marked by red arrows in (a,b). (d,e), 3PEF-PM slices obtained experimentally (d) and by numerical modelling (e). Each color within these superimposed images (green and red) represents the fluorescence signal from a single 3PEF-PM scan with imaging beam polarizations aligned along the color-coded directions shown by double arrows. (f), Computer-simulated  $\mathbf{n}(\mathbf{r})$  within the top-right part of the cross-section shown in (d,e). (g), 3D fluorescence pattern of the knotted particle and surrounding director distortions reconstructed from 3PEF-PM scans. The blue plane indicates the location of the single-slice images shown in (d,e). (h), 3D representation of  $\mathbf{n}(\mathbf{r})$  deviating away from  $\mathbf{n}_0$  due to the incorporated trefoil knot particle. Colors depict the azimuthal orientation of  $\mathbf{n}(\mathbf{r})$  when projected onto a plane orthogonal to  $\mathbf{n}_0$  and according to the scheme shown in the inset. The structure is visualized on a tube following the knotted particle's surface. Points where different colors meet are boojums. (i), 3D representation of computer-simulated  $\mathbf{n}(\mathbf{r})$  at the particle/liquid-crystal interface (black rods) and in the bulk (blue rods) induced by a trefoil knot particle. Green and magenta areas show regions of a reduced scalar order parameter of 0.42, corresponding to  $s = -1$  and  $s = 1$  2D defects at the liquid-crystal/particle interface, respectively. The knots in (g–i) are shown from different perspectives in order to depict different features of the ordering.

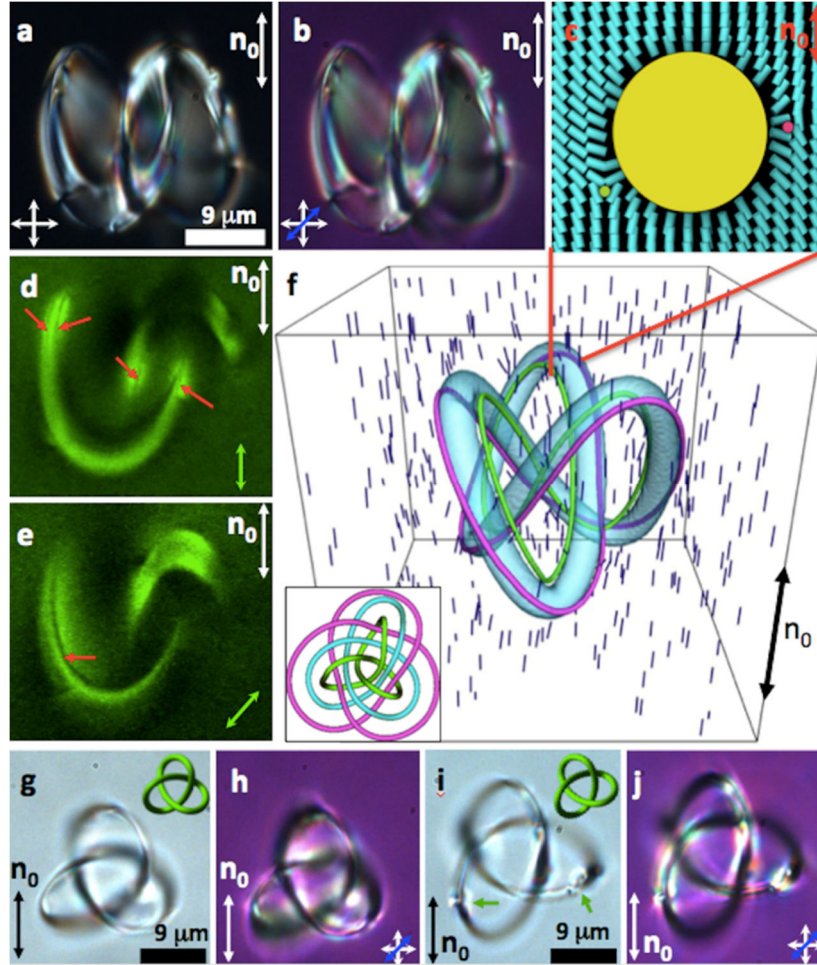
numerical modelling (Fig. 5.2g–i and Appendix Fig. C.4). Experimental 3PEF-PM textures in individual cross-sectional planes closely match their simulated counterparts, as shown for a sample region near boojums in Fig. 5.2d–g. To clearly identify positions of the surface defects, a

color-coded 3D representation of the azimuthal orientation of the director field around the particle is constructed, which reveals 12 boojums, forming nearby regions where the particle's surface is orthogonal to the far-field director (Fig. 5.2h). These boojums can be characterized by a winding number  $s$  of the 2D director field at the liquid-crystal/particle interface and also by the bulk topological charge  $m$  (refs 16, 23, 29). The winding number is an invariant commonly used to characterize 2D profiles of a field surrounding a defect—in our case, the field profile at the surface of the particle knot—and defines the number of times the director rotates by  $2\pi$  as one circumnavigates the defect core once. The nonpolar symmetry of the nematic director field allows integer numbers of  $\pi$  turns of the director around the defects, with positive and negative signs identifying defects with the director rotation being the same as or opposite to that of circumnavigation, respectively. The topological charge  $m$  is used to characterize point defects and loops of defect lines in three dimensions, and is a characteristic similar to  $s$  but describing the variation in the director-field profile around the defect objects in all three spatial dimensions. Its magnitude can be calculated using a simple integral of the director structure over an enclosing surface.[16, 23] By experimentally mapping and calculating the molecular orientational profile in the bulk and at surfaces around these defects, in agreement with topological theorems [4, 23], we find  $\sum_i s_i = \chi = 0$ , where  $i$  runs over all boojums and  $\chi = 0$  is the Euler characteristic of the knotted particle surface. Although this topological constraint could be satisfied in many different ways, the one observed experimentally corresponds to a local or global minimum of the total free energy. Both experiments and numerical modelling reveal that the stable field configuration around a trefoil particle knot with tangential boundary conditions contains 12 surface point defects: six  $s = 1$  boojums, which localize on the exterior tips of the knot, and their six  $s = -1$  counterparts, which reside on the diametrically opposite sides of the knotted tube (the



corresponding regions of the reduced scalar order parameter are depicted in Fig. 5.2i in magenta and green colors, respectively).

Trefoil particle knots with perpendicular surface boundary conditions align with a torus plane either orthogonal to  $\mathbf{n}_0$  in the ground state or at several metastable orientations, including those parallel to  $\mathbf{n}_0$  (Fig. 5.3 and Appendix Fig. C.5). These ground-state and metastable configurations, which correspond to global and local free-energy minima, respectively, can be accessed with the same particle by sequentially heating the sample with an objective-based temperature control system FCS-2 (from Biopetechs) to about 34 °C—which is right below the nematic–isotropic transition of the used liquid crystal—and then locally ‘melting’ the liquid crystal with a holographic optical-tweezers beam, followed by quenching it back to the nematic state. Optical micrographs of such a knotted particle are consistent with  $\mathbf{n}(\mathbf{r})$  near its surface being normal to it (Fig. 5.3). 3PEF-PM imaging with excitation light polarized perpendicular to  $\mathbf{n}_0$  yields a knotted tube of high intensity with an anisotropic cross-section (Appendix Fig. C.6). Individual depth-resolved 3PEF-PM ‘slices’ obtained for different polarizations show the presence of defect lines (marked by red arrows in Fig. 5.3d,e), which match our theoretical configuration with two singular  $s = -1/2$  defect lines following the knotted tube (Fig. 5.3c,f). These defect lines compensate for the director imposed by the particle’s surface, which resembles that of a knotted radial defect line with  $s = 1$ . Two linear defects tracing the knotted particle’s tube is also the basic feature of all metastable states, although they are often accompanied by their rewirings and linking to the knotted particle (Fig. 5.3g–j and Appendix Fig. C.5). This shows that knotted particles can generate defect loops in nematic fields by elastically distorting the liquid crystal in such a way that these loops are knotted too. For

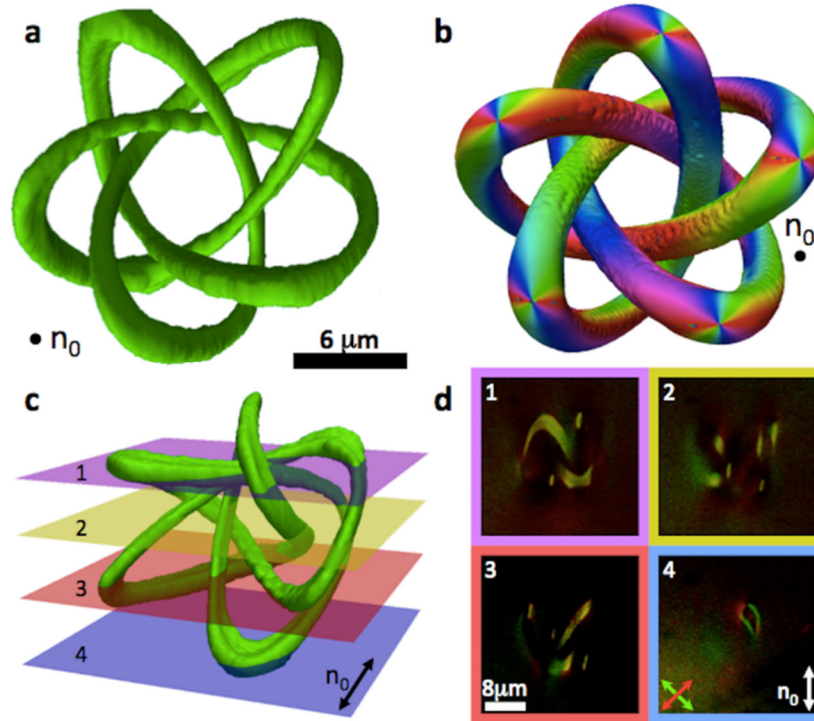


**Fig. 5.3** A colloidal trefoil knot with perpendicular surface boundary conditions. (a,b), Bright-field micrographs of a particle in an aligned nematic taken between crossed polarizers whose directions are indicated by the white arrows (a,b) and with a full-wave 530 nm retardation plate inserted with its slow axis at  $45^\circ$  (blue double arrow; b). (c), Computer-simulated  $\mathbf{n}(\mathbf{r})$  within a cross-section perpendicular to the knotted tube marked in (f). (d,e), 3PEF-PM images of  $\mathbf{n}(\mathbf{r})$  around the knotted particle shown in (a,b) and for excitation-light polarizations (green double arrows) at different orientations with respect to  $\mathbf{n}_0$ . Red arrows mark the defect lines. (f), Computer-simulated  $\mathbf{n}(\mathbf{r})$  around a trefoil knot with perpendicular boundary conditions and the torus plane orthogonal to  $\mathbf{n}_0$ . Green and magenta lines show regions with reduced scalar order parameter corresponding to the cores of the two knotted defect lines seen in the cross-sections (d,e). The inset shows a topological schematic of the mutual linking between the particle knot (blue) and defect knots (green and magenta). (g–j), Bright-field micrographs of colloidal knots aligned with the torus plane parallel to  $\mathbf{n}_0$ , and taken without polarizers (g,i) and between crossed polarizers with an inserted full-wave retardation plate (h,j). Green arrows in (i) indicate the locations of the rewirings of defect lines, similar to the ones visible in the model shown in Appendix Fig. C.5u,v.

the  $T(3,2)$  particle shown in Fig. 5.3, the two defect loops are both  $T(3,2)$  torus knots, mutually linked into a two-component link. This link of line defects is further linked with the particle knot (inset of Fig. 5.3f), effectively forming a three-component defect–particle link. In mathematics, linking of two closed curves in 3D space is commonly described by an integer called the ‘linking number’. Intuitively, this represents the number of times that each curve winds around the other, and it can be positive or negative, depending on the orientation of the two curves.[5] In a similar way, the observed linking of particles and defects can be characterized by two topological invariants: the linking number  $Ln$  of the particle with the induced defect loops in the nematic field, and the self-linking number  $Sl$  of the defect line, which labels how many times it turns around its tangent in the course of one loop.[29] The linking number of the particle knot with a chosen knotted defect loop  $Ln = 3$  emerges to be equivalent to the self-linking number  $Sl = 3$  of this loop,  $Ln = Sl$ , yielding a relation that connects the topology of the particle with that of the surrounding molecular field. This equivalence of two distinct topological invariants stems from the local compensation of the induced distortion—that is, the diametrically opposite elastic pinning of the two defect loops near the particle surface—and is valid for all studied particle knots with perpendicular boundary conditions, such as the  $T(5,2)$  and  $T(7,2)$  shown in Appendix Fig. C.7 (ref. 27), provided that the defects smoothly follow the particle’s knotted tube without irregular rewirings (Appendix Fig. C.8). Interestingly, the linking number of the knotted particle with the surrounding defect loops can be controllably changed, for example by reorienting the knotted particle into one of the metastable states (Appendix Fig. C.5). Another approach to characterize topological defect loops is by their topological charge[23, 29]: the homogeneous far-field director sets the net total topological charge of the particle and the defect loops equal to zero, and the trefoil knot particle has Euler characteristic  $\chi = 0$  (ref. 5), which also conditions the

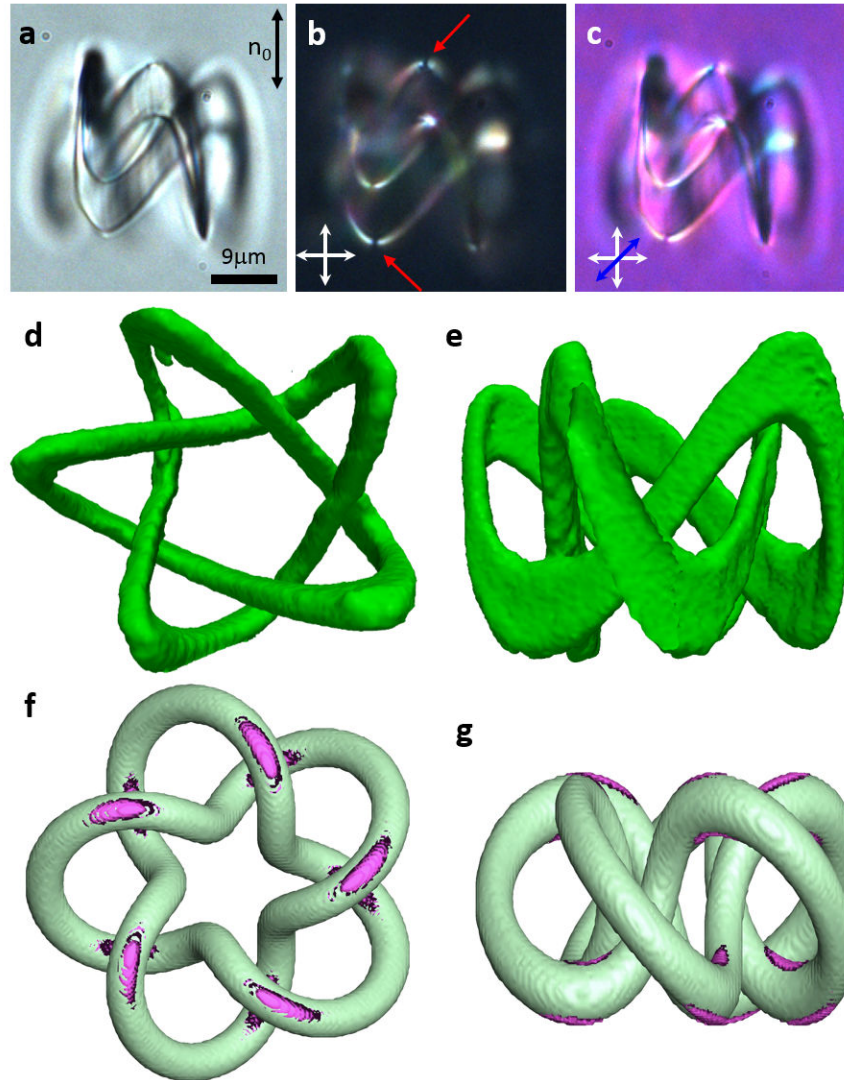
topological charge of the particle to be zero and puts the net topological charge of the two knotted defect loops equal to zero (under modulo 2; ref. 29). Indeed, these topological charges are also reproduced using a general formalism introduced in previous theoretical works.[29]

Our study can be extended to colloidal knots of higher complexity, such as the colloids in the form of  $T(5,3)$  torus knots ( $10_{124}$  in the Alexander–Briggs notation) with the crossing number  $c = 10$  that we show in Fig. 5.4 and Appendix Fig. C.9. These knotted particles with tangential anchoring induce boojums that obey the same topological constraint  $\sum_i s_i = 0$  as their trefoil counterparts, because  $\chi = 0$  for both, but the total number of boojums is now 20: 10 boojums with the winding number  $s = 1$  and 10 with  $s = -1$  defects in the 2D field at the liquid-crystal/particle interface. The  $T(5,2)$  torus knot particles also induce a total of 20 self-compensating boojums (Fig. 5.5). In general, the equilibrium  $\mathbf{n}(\mathbf{r})$ -structures induced by torus knots with tangential anchoring host  $|4p|$  self-compensating defects. This behavior for torus knots with  $p = 3, 5, 7$  and larger persists when the knotted tube’s diameter and overall particle dimensions are changed (Fig. 5.5 and Appendix Figs. C.10–C.12). However, in addition to the stable configurations, one also observes metastable states having different numbers and locations of boojums, yielding oblique orientations of the particle’s torus plane relative to  $\mathbf{n}_0$ , as we demonstrate using examples of several different knots shown in Appendix Figs. C.13 and C.14. Likewise, although the knotted particles with perpendicular boundary conditions and  $p = 3, 5, 7$  and higher are typically accompanied by two knotted defect lines with  $s = -1/2$ , by changing the diameter of the knotted tube relative to the overall particle size one can also achieve metastable configurations in which the two defects exhibit different rewirings (Appendix Fig. C.8). This demonstrates that the topological constraints allow for flexibility in terms of the precise ways of



**Fig. 5.4** A colloidal knot  $T(5,3)$  with tangential boundary conditions. (a), 3D reconstruction of 3PEF-PM intensity for the  $T(5,3)$  particle with director distortions around it. (b), 3D representation of  $\mathbf{n}(\mathbf{r})$  deviation from  $\mathbf{n}_0$  around the particle. Colors depict the azimuthal orientation of  $\mathbf{n}(\mathbf{r})$  projected onto a plane orthogonal to  $\mathbf{n}_0$  according to the scheme shown in the inset of Fig. 5.2h. The structure is visualized on a tube following the surface of the colloidal knot. The points where different colors meet are boojums. (c), A 3D perspective view of the  $T(5,3)$  particle shown in (a), with the four corresponding cross-sectional planes depicted in (d). (d), 3PEF-PM scans with superimposed green and red color-coded fluorescence images obtained for linear polarizations of excitation light along the double arrows of the same color marked in panel 4.

satisfying them. Therefore, by varying confinement, using liquid-crystal materials with different elastic constants, temperature quenching and the application of external fields, one can create an experimental arena for exploiting the means of control of this behavior. Finally, for all studied particles, field configurations and self-aligned colloidal orientation states, the chiral nature of knotted colloids causes mirror-symmetry breaking in the induced director field  $\mathbf{n}(\mathbf{r})$ , potentially allowing for the self-assembly of chiral colloidal superstructures in non-chiral nematic liquid crystals.



**Fig. 5.5** Torus knot  $T(5,2)$  particles with tangential boundary conditions. (a–c), Optical micrographs of the  $T(5,2)$  knotted particle obtained without polarizers (a), with crossed polarizers aligned as indicated by the white double arrows (b), and with crossed polarizers and an additional phase retardation plate (blue double arrow) aligned with its slow axis at  $45^\circ$  to crossed polarizers and  $\mathbf{n}_0$  (c). Locations of boojums visible within the optical micrographs are marked by red arrows in (b). (d,e), Two different perspective views of the reconstructed 3PEF-PM intensity pattern due to the  $T(5,2)$  colloidal knot particle and director distortions induced by the particle as viewed along the torus axis (d) and perpendicular to it (e). (f,g), Numerical model showing surface defects induced by a  $T(5,2)$  particle as viewed along the torus axis (f) and in a direction perpendicular to it (g). Green and magenta areas show regions of a reduced scalar order parameter of 0.42, corresponding to  $s = -1$  and  $s = 1$  defects in the 2D director field at the liquid-crystal/particle interface, respectively.

\*\*\*

Knots have been realized in the past either as material objects, such as knots of small molecules and polymer strands, or as knotted fields, whereas our nematic colloids can be a combination of both because the nematic field is guided by the particle knot. For perpendicular boundary conditions, the particle knot is even physically linked with the defect knots of the field, having particle-to-defect-loop linking number  $Ln = 3$ . Importantly, knotted particles energetically stabilize complex (knotted) nematic fields in time and space, allowing one to probe the details of their structure, which cannot be achieved in other knotted fields.[5] For example, as already envisaged by Kelvin, vortex lines in a fluid flow remain stable in time only if the fluid is ‘perfectly destitute of viscosity’[12]; in real fluids this always fails and knots decay in time.[7] In particle physics, glueballs are theoretically modelled as knotted flux tubes [30], but even the very experimental verification of glueball existence, not to mention probing their internal structure, is extremely difficult despite the advances in modern particle accelerators. Therefore, our colloidal knots offer the exciting opportunity of providing experimental insights into the physical realization of predictions from knot theory and its links to physical and material systems.

## **5.3 Methods**

### **5.3.1 Sample preparation**

Colloidal particles in the form of thin, rigid polymeric tubes shaped into knots of different chiralities (Fig. 5.1) were fabricated at rates of about 1,000 particles per hour using the automated set-up shown in Appendix Fig. C.1, as described in detail in the Appendix D.[26]

Each  $T(p,q)$  torus knot particle was obtained by looping  $p$  times a focused photopolymerizing laser beam through the hole of an imaginary torus, with  $q$  revolutions about the torus before joining the ends of the ensuing polymerized knotted tube. The tube diameter was tuned from 0.3 to 3  $\mu\text{m}$  and the overall size of particles was varied from 3 to 15  $\mu\text{m}$ . The particles were dispersed in either a single-compound nematic liquid crystal pentylcyanobiphenyl (5CB) or in a mixture ZLI-2806 (both from EM Chemicals). As-manufactured colloidal knots induced strong tangential surface boundary conditions, but some of them were chemically treated to induce perpendicular ones.[26] Colloidal dispersions were confined into 25–50  $\mu\text{m}$  cells made of parallel glass plates with inner surfaces treated to induce strong planar or perpendicular boundary conditions for  $\mathbf{n}(\mathbf{r})$ . Nematic fields around knotted particles were studied using the 3PEF-PM set-up shown in Appendix Fig. C.2 (refs 27, 28). 3PEF-PM images shown in Figs 5.2–5.5 depict fluorescence signals arising due to the nonlinear optical excitation of the dispersion. Unlike the (isotropic) IP-L polymer inside particles, nematic host 5CB (Appendix Fig. C.3a) exhibits a strong well-defined dependence of the fluorescence intensity on the orientation of the linear polarization of the probe beam. Close analysis of polarization-dependent 3PEF-PM image stacks composed of individual optical ‘slices’, such as the ones presented in Figs 5.2d, 5.3d,e and 5.4d, reveals that the induced  $\mathbf{n}(\mathbf{r})$  and defects depend on the boundary conditions and topology of the colloidal surfaces.

### 5.3.2 Numerical and topological modelling

The coupling between colloidal surfaces and  $\mathbf{n}(\mathbf{r})$  is also explored by a numerical approach based on Landau–de Gennes free-energy minimization. This approach phenomenologically combines



surface anchoring effects together with phase properties, nematic elasticity, variable degree of nematic order and its biaxiality into a free-energy functional based on the order parameter tensor  $Q_{ij}$  (refs 16, 22). Being particularly effective at micrometre scales and when modelling complex shapes, it allows for the theoretical characterization of  $\mathbf{n}(\mathbf{r})$  and defect-induced variations in nematic ordering that correspond to global or local minima of the free energy. Knotted particles are defined by an implicit declaration of knots and by assigning a fixed thickness to this definition. Minimization of the free energy is performed numerically for both tangential and perpendicular boundary conditions using an explicit finite-difference scheme on a cubic mesh.[27] This procedure yields spatial variations of the scalar order parameter and biaxiality in regions of defects and stable or metastable director fields  $\mathbf{n}(\mathbf{r})$ . They are subsequently used to computer-simulate 3PEF-PM textures with experimental imaging resolution [27, 28], allowing for a direct comparison of theory and experiments (Figs 5.2–5.5).

## 5.4 Conclusion

To conclude, we realized a colloidal system of particle knots coupled to nematic fields, providing insights into the interplay of their topologies. This interplay is controlled by varying surface boundary conditions and prompts the formation of topological defects, including boojums and knots of defect lines. The particles and field structures—for example, defect lines—can get mutually tangled, forming linked particle–field knots. Large quantities of colloidal knots can be obtained by combining two-photon photopolymerization with structured shaping of femtosecond laser light via spatial light modulators.[28] Therefore, our knotted colloids represent a vision towards the incomparable topological matter made of self-assembled knots envisaged by Kelvin.[12] As the types of particle-induced defect are governed by the topology of knotted

particles, these relations can be exploited to generate 3D patterns of vortices with varied symmetry and complexity, both at the surfaces of these particles and in the liquid-crystal bulk around them. On the one hand, these defects can mediate colloidal self-assembly by means of both anisotropic elastic forces [17-23] and entanglement.[29] On the other hand, particle-induced defects can mediate the generation of free-energy landscapes for nanoparticle entrapment [1], thus allowing one to controllably decorate the colloidal knots with metal and semiconductor nanoparticles, which may provide a means for achieving the hierarchical self-assembly of new topological composite materials. Therefore, by establishing general principles for the 3D control of defects, the demonstrated interplay of topologies of knotted colloidal surfaces and nematic fields provides a basis for highly unusual yet practically useful forms of self-assembly, potentially impinging on the design of mesoscale composite materials and applications, ranging from a new breed of information displays to metamaterials, nanophotonics and data storage.

## 5.5 References

1. B. Senyuk, *et al.*, *Nano Lett.* 2012, **12**, 955.
2. G. P. Alexander, B. G. Chen, E. A. Matsumoto, R. D. Kamien, *Rev. Mod. Phys.* 2012, **84**, 497.
3. U. Tkalec, M. Ravnik, S. Čopar, S. Žumer, I. Mušević, *Science* 2011, **333**, 62.
4. C. Livingston, *Knot Theory* The Mathematical Association of America, Indiana University-Bloomington, 1993.
5. L. H. Kauffman, *Knots and Physics 3rd edn*, World Scientific, 2000.
6. M. R. Dennis, R. P. King, B. Jack, K. O'Holleran, M. J. Padgett, *Nature Phys.* 2010, **6**, 118.
7. D. M. Kleckner, W. T. Irvine, *Nature Phys.* 2013, **9**, 253.
8. D. Yi-Shi, Z. Li, Z. Xin-Hui, *Commun. Theor. Phys.* 2007, **47**, 1129.
9. L. Faddeev, A. J. Niemi, *Nature* 1997, **387**, 58.
10. Y. Bouligand, B. Derrida, V. Poenaru, Y. Pomeau, G. Toulouse, *J. Physique* 1978, **39**, 863.
11. I. I. Smalyukh, Y. Lansac, N. Clark, R. Trivedi, *Nature Mater* 2010, **9**, 139.
12. W. Thomson, *Phil. Mag.* 1867, **34**, 15.
13. I. Chuang, R. Durrer, N. Turok, B. Yurke, *Science* 1991, **251**, 1336.
14. M. J. Bowick, L. Chandar, E. A. Schiff, A. M. Srivastava, *Science* 1994, **263**, 943.
15. A. M. Alsayed, M. F. Islam, J. Zhang, P. L. Collings, A. G. Yodh, *Science* 2005, **309**, 1207.
16. P. M. Chaikin, T. C. Lubensky, *Principles of Condensed Matter Physics*, Cambridge Univ. Press, 2000.
17. P. Poulin, S. Holger, T. C. Lubensky, D. A. Weitz, *Science* 1997, **275**, 1770.
18. D. R. Nelson, *Nano Lett.* 2002, **2**, 1125.
19. J. C. Loudet, P. Barois, P. Poulin, *Nature* 2000, **407**, 611.

20. A. Martinez, H. C. Mireles, I. I. Smalyukh, *Proc. Natl Acad. Sci. USA* 2011, **108**, 20891.
21. T. A. Wood, J. S. Lintuvuori, A. B. Schofield, D. Marenduzzo, W. C. K. Poon, *Science* 2011, **334**, 79.
22. M. Ravnik, S. Žumer, *Liq. Cryst.* 2009, **36**, 1201.
23. B. Senyuk, *et al.*, *Nature* 2013, **493**, 200.
24. Y. Wang, *et al.*, *Nature* 2012, **491**, 51.
25. M. C. Marchetti, *et al.*, *Rev. Mod. Phys.* 2013, **85**, 1143.
26. A. Martinez, T. Lee, T. Asavei, H. Rubinsztein-Dunlop, I. I. Smalyukh, *Soft Matter* 2012, **8**, 2432.
27. T. Lee, R. P. Trivedi, I. I. Smalyukh, *Opt. Lett.* 2010 **35**, 3447.
28. R. P. Trivedi, T. Lee, K. Bertness, I. I. Smalyukh, *Opt Express* 2010, **18**, 27658.
29. S. Čopar, S. Žumer, *Phys. Rev. Lett.* 2011, **106**, 177801.
30. R. V. Buniy, T. Kephart, *Int. J. Mod. Phys. A* 2005, **20**, 1252.

## Chapter 6

### Linked topological colloids in a nematic host

Adapted from: (2014). *Linked topological colloids in a nematic host*. Manuscript submitted for publication.

#### Chapter Overview

Geometric shape and topology of constituent particles can alter many colloidal properties such as Brownian motion, self-assembly, and phase behavior. So far, only single-component building blocks of colloids with connected surfaces have been studied, although topological colloids, with constituent particles shaped as freestanding knots and handlebodies of different genus, have been recently introduced. Here we develop a new type of topological colloids with constituent particles shaped as multi-component links. Using two-photon photopolymerization, we fabricate colloidal microparticle analogues of the classic examples of links studied in the field of topology, the Hopf and Solomon links, which we disperse in nematic fluids that possess orientational ordering of anisotropic rod-like molecules. The surfaces of these particles are treated to impose tangential or perpendicular surface boundary conditions for the alignment of liquid crystal molecules, so that they generate a host of topologically nontrivial field and defect structures in the dispersing nematic medium, resulting in an elastic coupling between the linked constituents.

The interplay between the topologies of linked discontinuous colloidal surfaces and the molecular alignment field of the nematic host reveals that linking of particle rings with perpendicular boundary conditions is commonly accompanied by linking of closed singular defect loops, laying the foundations for fabricating complex, composite materials with interlinking-based structural organization.

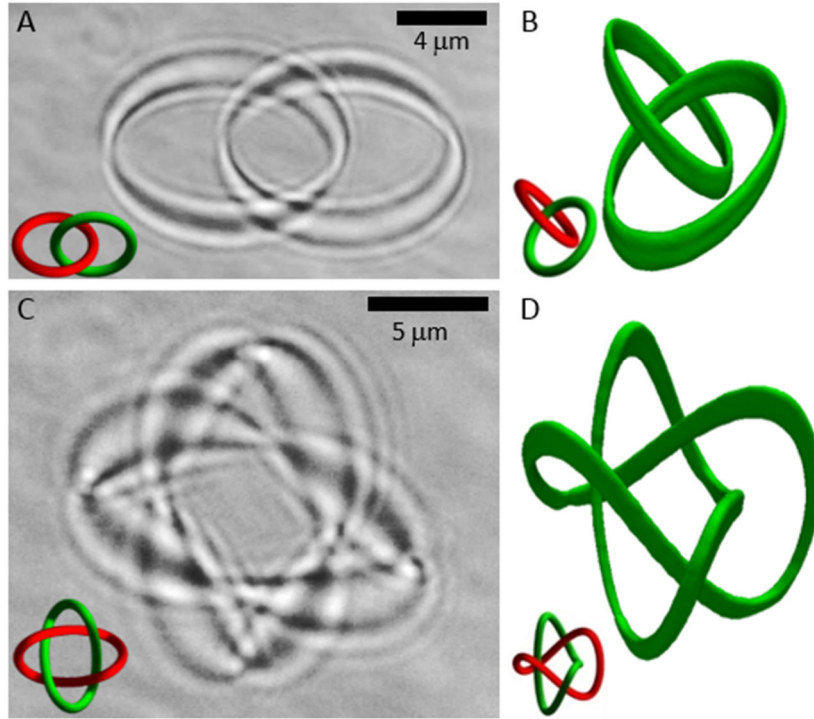
## 6.1 Introduction

Interlocking closed loops in physical field lines [1-3], small molecules [4], DNA and synthetic polymer chains [5], and various vortices [6-8] can lead to new physical behavior, biological functionality, and material properties that largely stem from the underlying topology [1]. For example, linking looped lines of liquid crystal (LC) molecular alignment field  $\mathbf{n}(\mathbf{r})$  [3], which describes spatial changes in local average orientations of constituent rod-like molecules [9], causes formation of topologically protected particle-like configurations that resemble the famous mathematical Hopf and Seifert fibrations [1, 3, 10, 11]. Similar field configurations with linked closed loops or linked torus knots of field lines are also predicted to exist in electromagnetic fields [2, 12, 13], in Bose-Einstein condensates [14, 15], and in magnetization of various ferromagnets [16-18], often defining novel types of physical behavior that arise from topological stabilization of such field configurations. However, the implications of topological linking on behavior of colloidal particles have not been considered so far, neither experimentally nor theoretically, although many types of complex-shaped colloidal particles have been recently fabricated [8, 19, 20].

In this work, we fabricate micrometer-sized colloidal particles with differently linked components shaped as closed solid polymer rings with disconnected surfaces that undergo Brownian motion both relative to each other and as a whole. When introduced into a nematic LC host [8, 19-23], these particles induce a large variety of field configurations, point defects and looped and linked vortex lines that entangle the linked components of the colloidal particles, resulting in elastic coupling between them. Using a combination of three-dimensional (3D) nonlinear optical imaging, videomicroscopy and non-contact laser manipulation [8, 24, 25], we characterize the interplay between topologies of colloidal surfaces,  $\mathbf{n}(\mathbf{r})$ -configurations, and defects, as well as probe the strength of elastic coupling between the colloidal particle's components. We supplement these experiments with a thorough theoretical analysis based on numerical minimization of the bulk Landau-de Gennes and surface free energies [26-29] that yields equilibrium configurations resembling (and topologically homeomorphic to) our experimental counterparts. Finally, we discuss the prospects for self-assembly-based fabrication of novel composites based on topological relations that we establish, as well as the potential for an experiment-driven, new fundamental exploration in the field of topology of links and knots, as well as their interaction with various nonpolar fields.

## 6.2 Results and Discussion

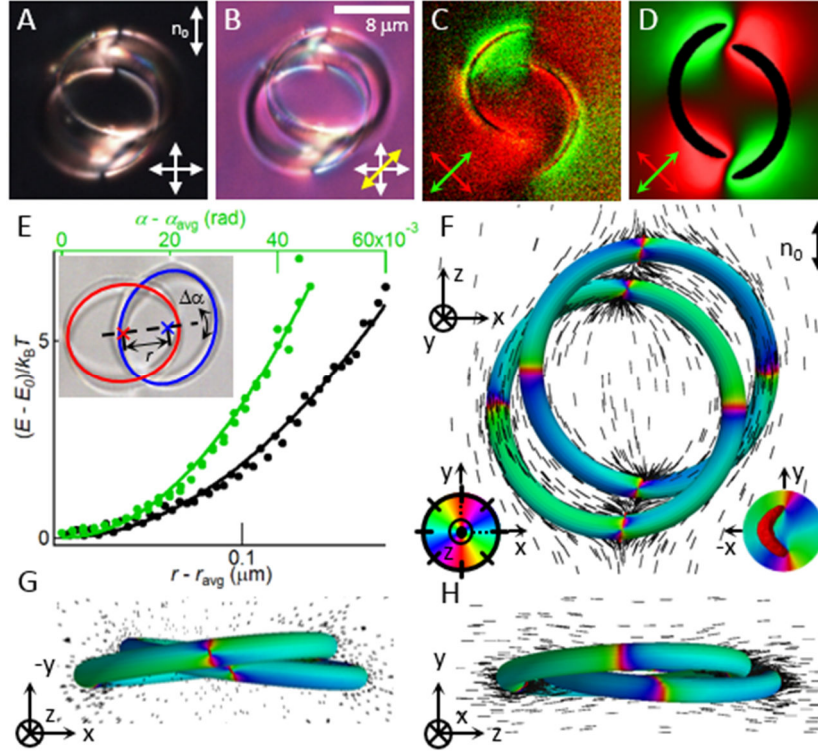
Using two-photon photopolymerization, we realize colloidal building blocks with topology of the classical Hopf link (Fig. 6.1A,B) consisting of two colloidal rings linked together once, the simplest two-component link [1]. They are characterized by a numerical invariant  $L_k = \pm 1$  dubbed “linking number” [1] representing the number of times that each closed colloidal loop winds around the other, with the sign dependent on the choice of orientations of the linked colloidal



**Fig. 6.1** Structure of photopolymerized colloidal links. (A) An optical brightfield micrograph of an as-fabricated Hopf-link particle attached to a glass substrate and (*inset*) the corresponding 3D model. (B) A 3D perspective view of the Hopf-link particle (corresponding to the model shown in the inset) obtained using 3PEF-PM imaging. (C) An optical brightfield micrograph of an as-fabricated Solomon-link particle attached to a glass substrate and (*inset*) the corresponding 3D model. (D) A 3D perspective view of the Solomon-link particle (corresponding to the model shown in the inset) obtained using 3PEF-PM imaging. The size of particles shown in (B,D) is the same as that of particles depicted in (A,C), respectively.

components [1]. In the colloidal Solomon's link of  $L_k = \pm 2$  (Fig. 6.2C,D), two closed, photopolymerized rings are doubly interlinked in an alternating manner, so that this colloidal building block exhibits four crossings of the two loops interweaving under and over each other [1]. 3D nonlinear optical imaging (Fig. 6.1B,D) reveals that the surfaces of the two linked components stay separated from each other, consistent with the topology of Hopf and Solomon links, respectively.

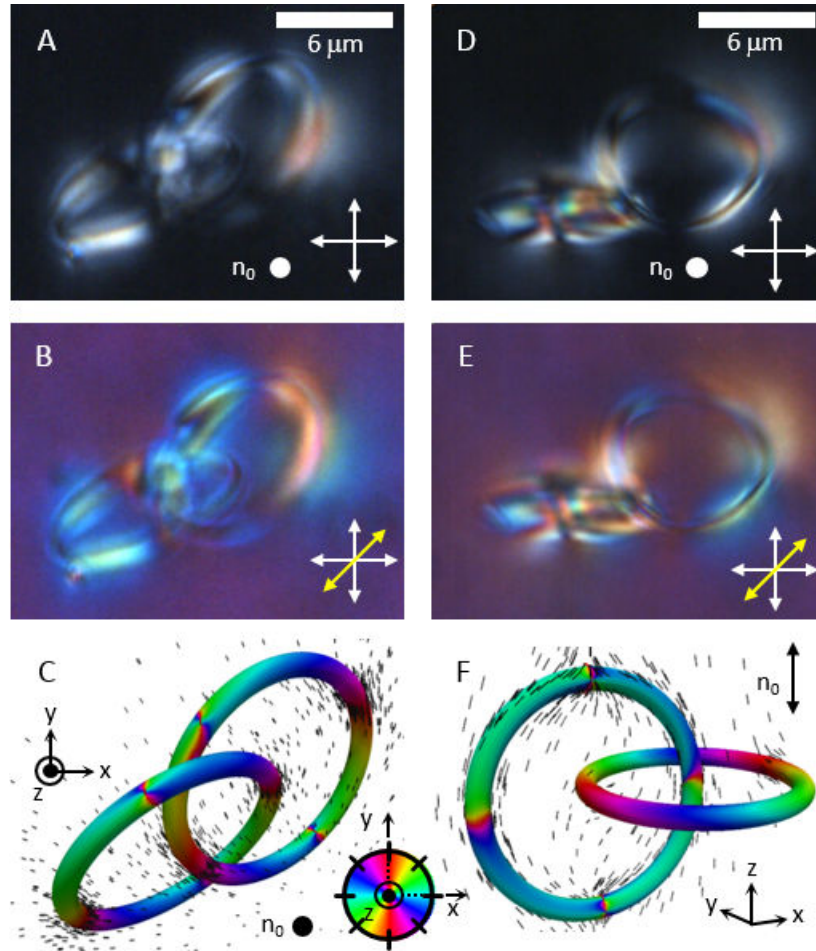




**Fig. 6.2** A Hopf-link colloidal particle with tangential anchoring in an aligned nematic LC. (A, B) Polarizing optical micrographs of a colloidal Hopf link in a nematic cell with the far-field director  $\mathbf{n}_0$  marked on the image as viewed between (A) crossed polarizers (white double arrows) and (B) between crossed polarizers and an additional 530nm full-wave plate (yellow double arrow) with a slow axis at  $45^\circ$  to them. (C) An in-plane cross-sectional composite 3PEF-PM image of a Hopf link and  $\mathbf{n}(\mathbf{r})$  around it obtained by superimposing two 3PEF-PM scans acquired using orthogonal, linear polarizations of excitation light along directions depicted by green and red double arrows; the fluorescence signals of the composite image corresponding to the two polarizations of excitation light are shown in green and red colors, respectively. (D) The corresponding theoretical 3PEF-PM cross-section based on the numerically calculated  $\mathbf{n}(\mathbf{r})$  shown in the panels (F-H); the green and red colors in the composite texture correspond to 3PEF-PM signals at polarizations of excitation light along the green and red double arrows marked on the image. (E) Elastic interaction energy versus deviation from the equilibrium center-to-center separation  $r-r_{\text{avg}}$  (black symbols and scale) and deviation from the equilibrium orientation  $\alpha-\alpha_{\text{avg}}$  (green symbols and scale). The inset defines the center-to-center distance and orientation, which were studied using optical videomicroscopy. (F-H) Three perspective views from mutually orthogonal directions of a numerically calculated  $\mathbf{n}(\mathbf{r})$  depicted using colors on the particle's surfaces and using rods in the LC bulk nearby. The colors on the particle surfaces show azimuthal orientations of  $\mathbf{n}(\mathbf{r})$  with respect to  $\mathbf{n}_0$  according to the color scheme shown in the bottom-left inset of F. The bottom-right inset shows details of the core structure of a boojum splitting into a semi-loop of a half-integer defect line with the handle-shaped region of reduced order parameter shown in red.

\*\*\*

When introduced into a nematic LC host (Fig. 6.2), as-fabricated linked particles define tangential boundary conditions for  $\mathbf{n}(\mathbf{r})$  at their surfaces. For Hopf-link colloids, while several stable and metastable  $\mathbf{n}(\mathbf{r})$ -configurations are found experimentally and theoretically (Figs. 6.2 and 6.3 and Appendix Fig. D.1), the most common one contains eight surface point defects dubbed “boojums”, four on each of the linked colloidal rings having their planes tilted away from the far-field director by 5-30°, depending on the particle (Fig. 6.2). Elastic distortions weakly couple the two linked components mechanically, defining the equilibrium center-to-center distance and locations at which the linked rings cross the planes of each other (inset of Fig. 6.2E), as well as the equilibrium angle  $\approx 20^\circ$  between the center-to-center separation vector and the far-field director  $\mathbf{n}_0$ . These elastic forces also stabilize the linked components against touching each other. Using videomicroscopy, we probe changes of the center-to-center distance and the angle that the separation vector makes with the far-field director,  $r-r_{\text{avg}}$  and  $\alpha-\alpha_{\text{avg}}$ , respectively, away from their equilibrium values  $r_{\text{avg}}$  and  $\alpha_{\text{avg}}$ , respectively, under the influence of thermal fluctuations (Fig. 6.2E). In both cases, the behavior is Hookean-like and can be characterized by spring constants  $k_r = 1.51 \text{ pN}/\mu\text{m}$  and  $k_\alpha = 24.45 \text{ pN } \mu\text{m}$ , respectively. Metastable colloidal and field configurations with different orientations of the rings and different numbers of boojums are also observed (Fig. 6.3 and Appendix Fig. D.1), including those with one boojum-free ring perpendicular to the far-field director but with usual four boojums on the other ring (Fig. 6.3F and Appendix Fig. D.1E). They also exhibit elastic coupling between the linked rings and with the orientation of the uniform far-field director through the minimization of elastic and surface anchoring free energies corresponding to the metastable states. Numerical modeling reveals that the boojums have split-core structure (Fig. 6.2F, lower-right inset) in the

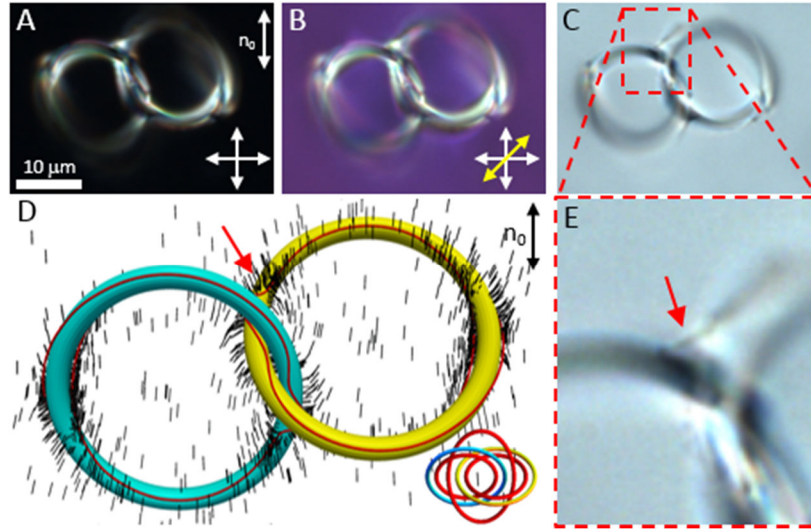


**Fig. 6.3** Metastable configurations of colloidal Hopf links with tangential surface anchoring in an aligned LC. (A,B,D,E) Polarizing optical micrographs of Hopf link particles in a homeotropic nematic cell viewed between (A,D) crossed polarizers marked by white double arrows and (B,E) between crossed polarizers and an additional inserted 530 nm full-wave plate with a slow axis at  $45^\circ$  to them (yellow double arrow). (C,F) The corresponding numerically calculated  $\mathbf{n}(\mathbf{r})$  depicted using colors on the particles' surfaces and using rods in the LC bulk nearby. The colors on the particles' surfaces show azimuthal orientations of  $\mathbf{n}(\mathbf{r})$  with respect to  $\mathbf{n}_0$  according to the color scheme shown in the inset. The theoretical configurations shown in (C,F) are similar to those depicted in panels (A,B) and (D, E), respectively; note that one of the rings in (F) contains no boojums.

form of semi-rings of half-integer defect lines, as previously seen for spherical and handlebody colloids with tangential anchoring [28, 29]. The boojums always appear in self-compensating

pairs of opposite winding numbers, which is consistent with the zero Euler characteristic of the individual rings of multi-component particles.

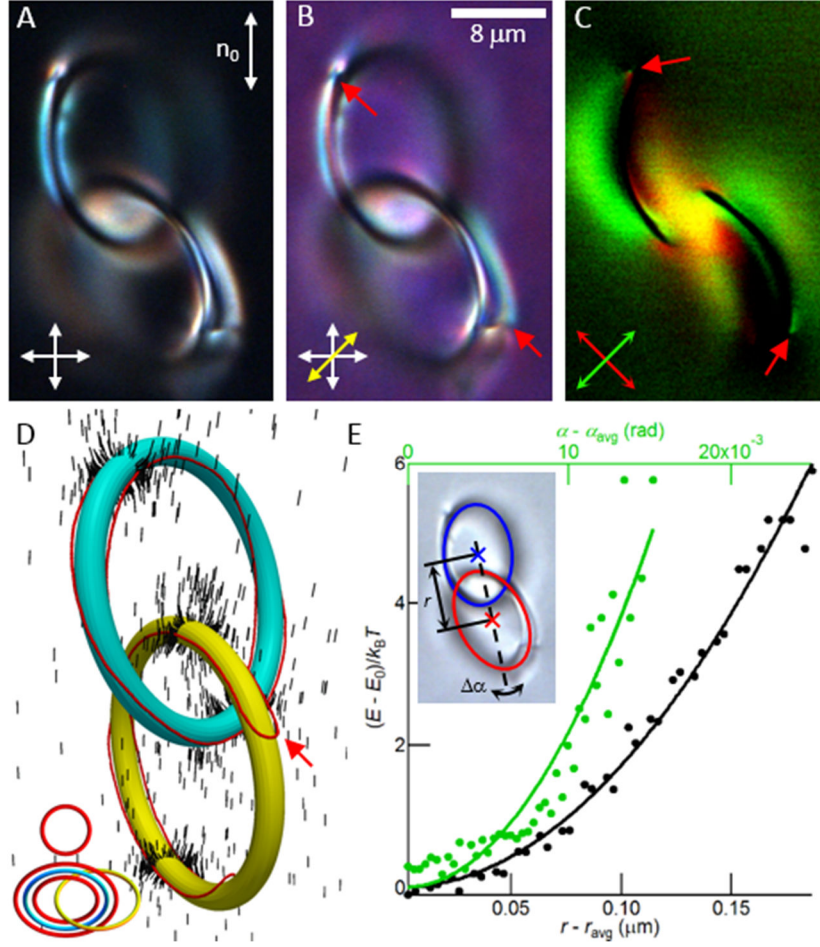
Even more exotic behavior of linked nematic colloids is observed when their surfaces are treated to impose homeotropic (perpendicular) surface boundary conditions for  $\mathbf{n}(\mathbf{r})$  (Figs. 4-6 and Appendix Fig. D.2). These particles tend to induce singular defect lines, which can be associated with individual colloidal components (Fig. 6.5) or jump from the proximity of one component to the other (Figs. 6.4, 6.6 and Appendix Fig. D.2). In addition to the purely elastic coupling of the linked components in the former case, the colloidal components in the latter ones become entangled by unknots of defect lines that act as elastic strings with elastic tension of the order of 50-70pN [22, 30]. The Hookean-like behavior describing angular and translational deviations of particle positions and the orientation of their center-to-center separation vector away from equilibrium are characterized by spring constants  $k_r = 1.4 \text{ pN}/\mu\text{m}$  and  $k_\alpha = 176.9 \text{ pN } \mu\text{m}$ , respectively. Interestingly, despite the constraints on the overall zero bulk hedgehog charges of defects imposed by topological theorems [19], the nonpolar nature of the director field, combined with the rich configuration space of the colloid itself, permits to accommodate topologically distinct configurations of closed defect loops, including the ones in which they are linked with none, one, or both colloidal ring components, or with other defect loops (Figs. 6.4 and 6.5 and Appendix Fig. D.2), or unlinked ones (Fig. 6.6). Importantly, the individual linked components of a colloidal entity move with respect to each other while having instantaneous field configurations governed by the elasticity of the surrounding nematic fluid. They are thus elastically locked to be at well-defined separations and orientations (Fig. 6.5E) corresponding to



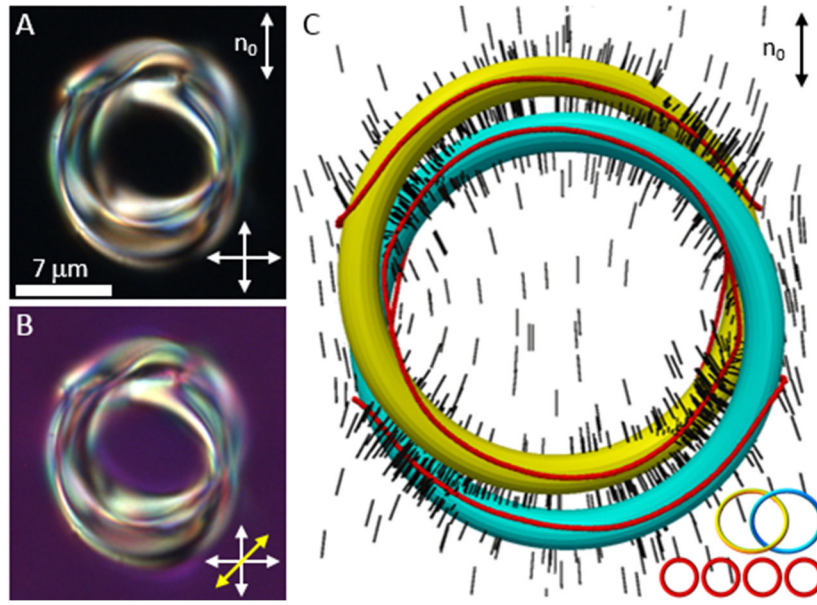
**Fig. 6.4** A colloidal Hopf link with perpendicular surface boundary conditions in an aligned nematic LC. (A, B) Optical micrographs of a Hopf-link particle in a nematic LC with the far-field director  $\mathbf{n}_0$  marked on the image viewed between (A) crossed polarizers (white double arrows), (B) between crossed polarizers and an additional inserted 530nm full-wave plate with a slow axis at  $45^\circ$  to them (yellow double arrow), and (C) without polarizers or wave plate. (D) A theoretical model of the studied colloidal Hopf link configuration revealing  $\mathbf{n}(\mathbf{r})$  (shown by rods) and defect lines (red closed loops). The inset shows a topological skeleton of linked colloidal and defect loops. (E) A zoom-in view of panel (C) focusing on the “jumping” disclination seen in both experiments and theoretical modeling, which we mark by red arrows in (D,E).

the local or global minima of the free energy associated with the metastable or equilibrium states, respectively.

As the particle’s linking number increases, so does the complexity of the observed field and defect configurations (Figs. 6.7, 6.8 and Appendix Figs. D.3 and D.4). The colloidal Solomon links with tangential boundary conditions tend to induce, on average, two times more boojums than their Hopf counterparts, with these surface point defects commonly seen at the regions of highest curvature at the tip points of the tubes forming the linked colloidal rings (Fig. 6.7). The large number of stable and metastable mutual positions and orientations of the linked components, as well as their orientation with respect to the far-field director  $\mathbf{n}_0$ , lead to a



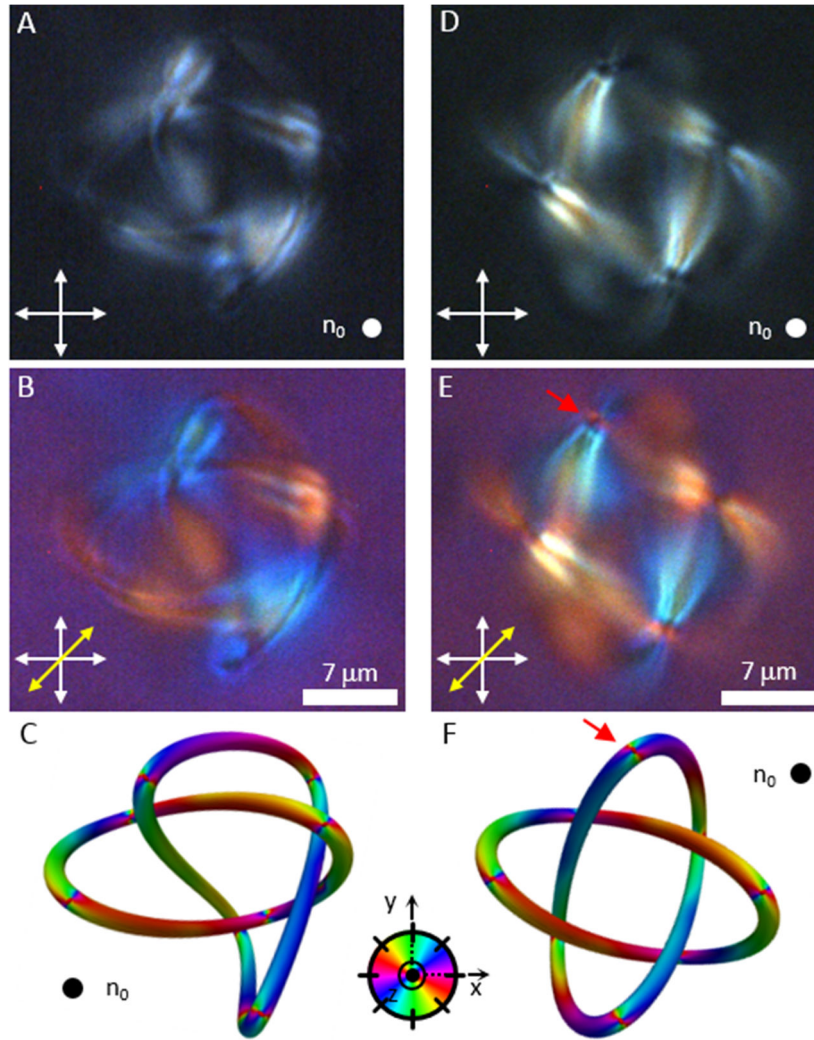
**Fig. 6.5** A metastable configuration of a colloidal Hopf link with perpendicular boundary conditions in a nematic cell. (A, B) Optical micrographs of a Hopf-link particle in a nematic LC with the far-field director  $\mathbf{n}_0$  marked on the image viewed between (A) crossed polarizers (white double arrows) and (B) between crossed polarizers and an additional inserted 530nm full-wave plate with a slow axis at  $45^\circ$  to them (yellow double arrow). (C) An in-plane cross-sectional composite 3PEF-PM image of a Hopf link and  $\mathbf{n}(\mathbf{r})$  around it obtained by superimposing two 3PEF-PM scans acquired using orthogonal, linear polarizations of excitation light along directions depicted by green and red double arrows; the fluorescence signals of the composite image corresponding to the two polarizations of excitation light are shown in green and red colors, respectively. (D) A 3D theoretical model of the colloidal Hopf link configuration revealing  $\mathbf{n}(\mathbf{r})$  (shown by rods) and defect lines (red closed loops). Characteristic locations of defect lines are marked by red arrows in (B-D). The inset shows a topological skeleton of linked colloidal and defect loops. (E) Elastic interaction energy versus deviation from the equilibrium center-to-center separation  $r - r_{\text{avg}}$  (black symbols and scale) and deviation from the equilibrium orientation  $\alpha - \alpha_{\text{avg}}$  (green symbols and scale). The inset defines the center-to-center distance and orientation, which were studied using optical videomicroscopy.



**Fig. 6.6** A compact metastable configuration of a colloidal Hopf link in a nematic LC. (A, B) Optical micrographs of a metastable-state Hopf-link particle in a nematic LC with the far-field director  $\mathbf{n}_0$  marked on the image as viewed between (A) crossed polarizers (white double arrows) and (B) between crossed polarizers and an additional inserted 530nm full-wave plate with a slow axis at  $45^\circ$  to them (yellow double arrow). (C) A 3D theoretical model of the studied colloidal Hopf link configuration revealing  $\mathbf{n}(\mathbf{r})$  (shown by rods) and defect lines (red closed loops).

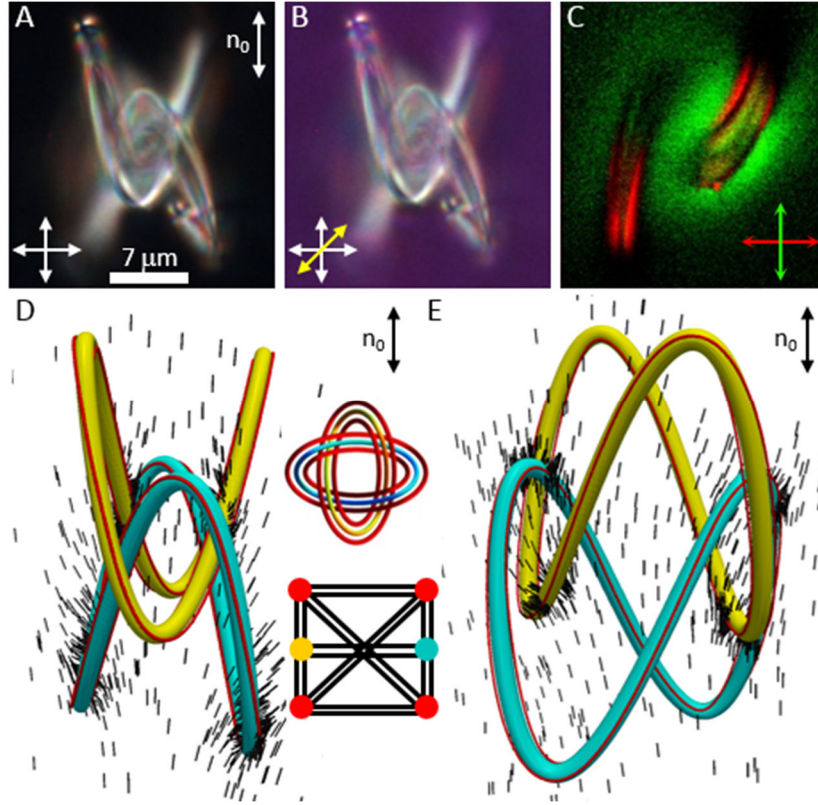
diversity of field configurations differing by the number of generated boojum-antiboojum pairs that are characterized by self-compensating, opposite winding numbers (Fig. 6.7C,F). The most frequently observed configuration due to a Solomon link with perpendicular surface boundary conditions involves pairs of individual looped defect lines following each of the linked components (Fig. 6.8D,E), being reminiscent of the types of defects induced by trefoil knots that we studied previously [8].

Numerical modeling based on the minimization of Landau-de Gennes bulk free energy of nematic LCs [26], supplemented by additional surface anchoring energy terms [9, 27-29], successfully reproduces the experimental topology of fields and defects resulting from the linked



**Fig. 6.7** Colloidal Solomon links with tangential surface boundary conditions in a nematic LC. (*A, B*) A Solomon link in a homeotropically aligned nematic cell as viewed between (*A*) crossed polarizers aligned along the white-arrows and (*B*) between crossed polarizers and an additional 530 nm full-wave plate with slow axis at  $45^\circ$  to them (yellow double arrow). (*C*) A numerically calculated model of  $\mathbf{n}(\mathbf{r})$  depicted using colors on the particle surfaces and using rods in the LC bulk nearby corresponding to the experimental images shown in (*A, B*). The colors on the particle surfaces show azimuthal orientations of  $\mathbf{n}(\mathbf{r})$  with respect to  $\mathbf{n}_0$  (normal to the page) according to the color scheme shown in the inset. (*D, E*) Another configuration for a tangentially anchored Solomon link in a homeotropic nematic cell viewed between (*D*) crossed polarizers without and (*E*) with an inserted additional full-wave plate. (*F*) A numerically calculated  $\mathbf{n}(\mathbf{r})$  depicted using colors on the particle surfaces and using rods in the LC bulk nearby corresponding to the experimental images shown in (*D, E*).














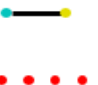







**Fig. 6.8** A Solomon-link particle with homeotropic surface boundary conditions in a nematic LC. (A, B) Optical micrographs of a Solomon-link particle in a nematic LC with the far-field director  $\mathbf{n}_0$  marked on the image as viewed between (A) crossed polarizers (white double arrows) and (B) between crossed polarizers and an additional inserted 530nm full-wave plate with a slow axis at  $45^\circ$  to them (yellow double arrow). (C) An in-plane cross-sectional composite 3PEF-PM image of a Solomon link and  $\mathbf{n}(\mathbf{r})$  around it obtained by superimposing two 3PEF-PM scans acquired using orthogonal, linear polarizations of excitation light along directions depicted by green and red double arrows; the fluorescence signals of the composite image corresponding to the two polarizations of excitation light are shown in green and red colors, respectively. (D, E) Two perspective views of a 3D theoretical model of the studied colloidal Solomon link configuration revealing  $\mathbf{n}(\mathbf{r})$  (shown by rods) and defect lines (red closed loops). In the insets of (D), the mutually linked, physical-particle unknots are shown as blue and yellow rings and filled circles, and the defect line loops are shown as red loops and filled circles, respectively; the double links are indicated by double black edges connecting the corresponding red-blue-yellow filled circles that represent colloidal or defect rings.

colloidal building blocks, although we also find some metastable structures that are not observed in experiments but only in theory (Appendix Figs. D.1, D.5-D.10) and vice versa (Appendix Figs. D.2-D.4). The agreement between the corresponding experimental and numerically

calculated structures is evident from a direct comparison of the experimental three-photon excitation fluorescence polarizing microscopy (3PEF-PM) textures, based on the minimum-energy ground-state  $\mathbf{n}(\mathbf{r})$ -configuration, with its theoretical counterpart (Fig. 6.2C,D). Essentially all field and defect configurations induced by linked colloids with tangential anchoring and of a given  $L_k$  are similar to each other and can be obtained through smooth deformation of the director fields and annihilation or generation of pairs of boojums with opposite winding numbers, as well as through rotating and translating the linked components with respect to each other. Since the studied colloids have linked colloidal components of Euler characteristic  $\chi=0$ , there is always an equal number of boojums with opposite winding numbers and with bulk hedgehog topological charges adding to zero. In contrast, the linked particles with perpendicular surface boundary conditions can induce topologically distinct configurations of defect lines at the same colloidal particle's linking number  $L_k$ . For example, in the case of Hopf link colloids we observe from two to four closed loops of half-integer defect lines, which can be linked with a single or both colloidal components or with each other. A summary of all observed topologically distinct defect configurations induced by Hopf-link colloids is presented in Table 6.1. The observed mixed, defect-colloidal, multi-component links typically cannot be morphed from one to another, unless crossing, splitting, or merging of different defect loops are allowed to occur. The associated energetic barriers thus stabilize the distinct topologies of the defect-colloidal multicomponent links which we can distinguish based on the total number of unknots in forms of colloidal rings or defect loops and the number of links between them visible from simplified topological skeletons and graph presentations of observed structures (Table 6.1 and inset of Fig. 6.8D). The states summarized in Table 6.1 that correspond to local and global minima of free energy do not exhaust all structural varieties of field configurations satisfying the constraint of

		Linking complexity			
Component number	4	 2	 7		
	5	 3	 3	 8	
	6	 1	 3	 8	 9
					
					
					
					

**Table 6.1 Topological skeletons and graph representations of inter-linked Hopf-link colloids and accompanying closed defect loops.** The mutually linked, physical-particle unknots are shown as blue and yellow rings and filled circles, and the defect line loops are shown as red loops and filled circles, respectively. The individual links are indicated by black edges connecting the corresponding red-blue-yellow filled circles that represent colloidal or defect rings; the overall number of links is indicated in-between the topological skeleton and graph representations of the structures reconstructed from theoretical and experimental data (Figs. 6.2-6.8 and Appendix Figs. D.1-D.10).

topological charge conservation, but it is interesting that a single Hopf link of colloidal rings can be accompanied by up to four defect loops with up to 9 links between them while in a long-term-stable metastable state, allowing for a detailed experimental exploration of the interplay between topologies of particles, field, and defects. The complexity increases further as one considers Solomon links or higher-order links of knotted loops of solid colloidal particles in LCs, and we

here restrict ourselves just to showing the simplest examples of the ground-state (Fig. 6.8) and metastable (Appendix Fig. D.4) structures.

Inseparability of the linked particle components considerably enriches their colloidal properties and physical behavior. Unlike in conventional colloids, many-body colloidal interactions can exist among the linked components belonging to the same composite particle, constrained by the physical linking, or to different multi-component particles. LC elasticity-mediated interactions between the linked rings of the same particle and the surrounding LC matrix are different from what one would expect for two unlinked rings with similar induced defects. For example, unlinking of the rings shown in Fig. 6.2, with four induced boojums per each ring, is expected to result in quadrupolar interactions and self-assembly similar to what we previously studied for platelets with holes [19, 20], very different from the equilibrium and metastable mutual arrangements of component rings of the linked pair (Figs. 6.2 and 6.3). Unlike the unlinked colloidal rings with perpendicular boundary conditions, which can exhibit both ring-like and point defects [19], their linked counterparts have not been observed to induce point singularities. Sharing or linking of defect loops induced by the linked rings provides an additional interaction mechanism due to the defect line tension (see, for example, Fig. 6.4), which is of the order of 50-70 pN for singular half-integer defect lines [22, 26, 30]. The colloidal configurations, like the one shown in Fig. 6.4, can have the colloidal component rings touching each other or not, depending on the competition of the defect line tension and repulsive elastic forces due to strong director distortions when two such rings approach each other. When the component rings touch, the colloid undergoes Brownian motion as an effective genus  $g=2$  handlebody, distinct from the surface topology of two separate rings. One can also expect that linking will alter interactions

between colloidal components when, for example, interactions originate from electrostatic or depletion forces, opening a new avenue for designing complex colloidal self-assembly architectures and functionality. On the other hand, our system with elastic closed loops of defect lines may provide an experimental platform for testing predictions of mathematical models for minimum ropelength of linked and knotted topological configurations [31], as well as a basis for expanding such theoretical calculations to the more complex cases of linked and knotted loops elastically repelling from each other, as in some of our experiments.

## **6.3 Materials and Methods**

### **6.3.1 Sample preparation**

We use LC cells constructed from two glass substrates, coated either with a thin film of rubbed polyimide (PI-2555, HD Microsystems) or a monolayer of DMOAP to induce tangential or perpendicular boundary conditions at the LC-substrate interface, respectively. We space the cell substrates with 25-30  $\mu\text{m}$  silica spheres mixed into a UV-curable glue (NOA-65, Norland Inc.), setting the cell gap thickness. Once cured, we seal two sides of the cell with epoxy and then fill it with LC containing a dispersion of linked colloidal particles via capillary action. For cells with rubbed polyimide-coated substrates, the LC flow during filling is chosen to be parallel to the rubbing direction. We used a single-compound nematic LC pentylcyanobiphenyl (5CB) and a mixture ZLI-2806 (both from EM Chemicals). After a cell is fully infiltrated with the LC, the two remaining cell edges are sealed with epoxy. Generally, we heat the LC to isotropic phase and then quench back to nematic phase to mitigate the flow-induced alignment effects. The nematic host exhibits strong well-defined dependence of 3PEF-PM fluorescence intensity on the orientation of linear polarization of the excitation beam relative to  $\mathbf{n}(\mathbf{r})$ . Polarization-dependent

3PEF-PM images reveal how  $\mathbf{n}(\mathbf{r})$  and induced defects depend on boundary conditions and topology of the colloidal building blocks.

### **6.3.2 Photopolymerization of colloidal particles and their dispersion in LCs**

The linked polymeric colloidal building blocks (Fig. 6.1) were fabricated using a two-photon photo-polymerization system shown in the Appendix Fig. D.11 [8, 34]. The two-photon photopolymerization setup was constructed around a home-built inverted microscope with a computer-guided nano-positioning stage (Physik Instrumente, model P-611.3SF, 0.2nm resolution). The laser beam from a femtosecond Ti:sapphire oscillator laser (from Coherent) at wavelength of 780 nm first passes through a half-wave plate and a Glan polarizer (used for beam power control) and then through two lenses forming a telescope designed to expand the beam from the initial diameter of 3 mm to about 5 mm to properly fill the back aperture of an objective lens. At the location between the two telescope lenses, where their foci meet, we place an aligned 100  $\mu\text{m}$  pinhole (Appendix Fig. D.11), which is used as a spatial filter to improve the beam quality. A computer-controlled fast shutter (Uniblitz, model LS3Z2, 200 Hz) is placed just after the pinhole and before the second lens. After the telescope, the beam is directed into the back aperture of the objective by mirrors, with the last dichroic mirror right before the objective reflecting light of wavelengths  $>750$  nm and transmitting visible light. This allows us to observe the polymerization process in real time using brightfield microscopy and a charge coupled device camera. The shutter and the nano-stage operate in concert with each other, as guided by our LabView-based software. The spatial translation of the nano-stage with a sample mounted on it is done in such a way that a focused femtosecond laser beam follows a trajectory prescribed by a set of parametric equations (Appendix D), yielding the photopolymerized particles of desired 3D

geometry and topology. The LabView-based software opens and closes the shutter at the beginning and in the end of each particle-defining 3D trajectory. The cross-sectional tube diameter of each closed polymeric ring in the multi-component colloidal link is tuned from 0.3 to 3  $\mu\text{m}$  and the overall size of particles is varied from 3 to 20  $\mu\text{m}$ . The average laser power utilized for polymerization of these particles ranged from 3 mW for small ones to 13 mW for the larger ones, as measured just before the objective. The colloidal links were photopolymerized within a specially constructed cell suspending a droplet of IP-L 780 photoresist (NanoScribe GmbH), which crosslinks (solidifies) when exposed to the high-intensity femtosecond laser light at 780 nm. This is done within glass cells consisting of a standard microscope slide and a 170  $\mu\text{m}$ -thick coverslip, spaced by 50  $\mu\text{m}$ -thick strips of Mylar films. As the beam focus is translated through the volume of the monomeric fluid droplet, we always begin the polymerization at the interface of substrate and monomeric fluid to effectively anchor the structure while it is being drawn. The fabricated arrays of particles are then detached from substrates by gentle sonication and dispersed into the LC. As-manufactured particles induced tangential surface boundary conditions for  $\mathbf{n}(\mathbf{r})$ , but some of them were additionally chemically treated for perpendicular ones [8].

## 6.4 Theoretical Modeling

Nematic configurations around colloids are obtained via numerical minimization of the phenomenological free energy functional

$$\begin{aligned}
 F = \int_V \left( aQ_{ij}^2 - bQ_{ij}Q_{jk}Q_{ki} + c(Q_{ij}^2)^2 + \frac{L_1}{2} \partial_k Q_{ij} \partial_k Q_{ij} + \frac{L_2}{2} \partial_j Q_{ij} \partial_k Q_{ik} \right) dV \\
 + W \int_{\partial V} f_s ds,
 \end{aligned}
 \tag{6.1}$$

$Q_{ij} = Q_{ji}, i, j = 1, \dots, 3$  and summation over repeated indexes is assumed. The volume integral in Eq. (6.1) is the standard Landau-de Gennes free energy functional, where  $a$  is a function of temperature  $T$ ;  $b, c$  are temperature independent material constants, and  $L_1, L_2$ , are phenomenological parameters related to the Frank-Oseen elastic constants. The second surface integral in Eq. (6.1) accounts for finite surface anchoring with the anchoring strength  $W$ . The explicit form of the surface free energy density  $f_s$  depends on the anchoring type, e. g. perpendicular or tangential. For the first case we use  $f_s^\perp = (Q_{ij} - Q_{ij}^s)^2$  with  $Q_{ij}^s = 3Q_b(\nu_i\nu_j - \delta_{ij}/3)/2$  being the surface-preferred order parameter;  $\boldsymbol{\nu}$  is the outward surface normal,  $\delta_{ij}$  is the Kronecker delta symbol, and  $Q_b$  is the bulk value of the scalar order parameter. The tangential (degenerate) anchoring is accounted for by  $f_s^\parallel = (\tilde{Q}_{ij} - \tilde{Q}_{ij}^\perp)^2 + (\tilde{Q}_{ij}^2 - \frac{3}{2}Q_b^2)^2$ , where  $\tilde{Q}_{ij} = Q_{ij} + \frac{Q_b}{2}\delta_{ij}$ , and  $\tilde{Q}_{ij}^\perp = (\delta_{ik} - \nu_i\nu_k)\tilde{Q}_{kl}(\delta_{lj} - \nu_l\nu_j)$  [26]. The free energy in Eq. (6.1) is numerically minimized by using adaptive finite elements methods [28]. The values of the model parameters and details on the numerical approach are provided in Appendix D.

## 6.5 Conclusion

To conclude, we have developed a new class of topological colloids with multiple linked components. We have demonstrated that, when dispersed in nematic host fluids, the linked colloidal building blocks induce field-defect configurations that can be topologically distinct from each other but always satisfy the topological constraints. Although we considered only tangential and perpendicular boundary conditions that are uniformly the same on all surfaces of the colloidal building blocks, this study can be extended to patched and optically controlled boundary conditions [32], potentially allowing for dynamic re-configurability. On the other



hand, in addition to linked genus-one rings, one can envision complex but interesting behavior of linked particles with larger genus and larger number of linked components. For example, defect lines emanating from surfaces of linked colloidal components with tangential boundary conditions and large genus could be connecting different components also by terminating on them, defining different-valence-like interactions [33] between the components of the colloidal building blocks. Linked multi-component particles, with the components made of the same or different materials, can be of practical interest when dispersed in both LC and isotropic fluid hosts as they are expected to substantially enrich colloidal self-assembly behavior and response to external stimuli.

## 6.6 References

1. L. H. Kauffman, *Knots and Physics* World Scientific Publishing, Singapore, 2000.
2. W. T. M. Irvine, D. Bouwmeester, *Nature Phys* 2008, **4**, 716.
3. I. I. Smalyukh, Y. Lansac, N. Clark, R. P. Trivedi, *Nature Mater* 2010, **9**, 139.
4. C. D. Pentecost, K. S. Chichak, A. J. Peters, G. W. V. Cave, S. J. Cantrill, J. F. Stoddart, *Angew Chem Int Ed* 2007, **46**, 218.
5. N. Hadjichristidis, A. Hirao, Y. Tezuka, E. Du Prez, Eds, *Complex Macromolecular Architectures*, Wiley, Singapore, 2011.
6. D. M. Kleckner, W. T. M. Irvine, *Nature Phys* 2013, **9**, 253.
7. U. Tkalec, M. Ravnik, S. Čopar, S. Žumer, I. Mušević, *Science* 2011, **333**, 62.
8. A. Martinez, M. Ravnik, B. Lucero, R. Visvanathan, S. Žumer, I. I. Smalyukh, *Nature Mater* 2014, **13**, 258.
9. P. M. Chaikin, T. C. Lubensky, *Principles of condensed matter physics*, Cambridge University Press, Cambridge, 1995.
10. H. Hopf, *Mathematische Annalen* 1931, **34**, 637.
11. J. H. C. Whitehead, *Proc Natl Acad Sci USA* 1947, **33**, 117.
12. A. F. Ronada, J. L. Trueba, *Nature* 1996, **383**, 32.
13. A. F. Ronada, J. L. Trueba, *Phys Lett A* 1995, **202**, 337.
14. Y. Kawaguchi, M. Nitta, M. Ueda, *Phys Rev Lett* 2008, **100**, 180403.
15. Y-K. Liu, C. Zhang, S-J. Yang, *Phys Lett A* 2013, **377**, 3300.
16. N. R. Cooper, *Phys Rev Lett* 1999, **82**, 1554.
17. P. Sutcliffe, *Phys Rev B* 2007, **76**, 184439.
18. A. B. Borisov, F. N. Rybakov, *JETP Letters* 2009, **90**, 544.

19. B. Senyuk, *et al.*, *Nature* 2013, **493**, 200.
20. C. P. Lapointe, T. G. Mason, I. I. Smalyukh, *Science* 2009, **326**, 1083.
21. P. Poulin, H. Stark, T. C. Lubensky, D. A. Weitz, *Science* 1997, **275**, 1770.
22. T. C. Lubensky, D. Pettey, N. Currier, H. Stark, *Phys Rev E Stat Nonlin Soft Matter Phys* 1998, **57**, 610.
23. G. P. Alexander, B. G. Chen, E. A. Matsumoto, R. D. Kamien, *Rev Mod Phys* 2012, **84**, 497.
24. R. P. Trivedi, D. Engström, I. I. Smalyukh, *J Opt* 2011, **13**, 044001.
25. R. P. Trivedi, T. Lee, K. Bertness, I. I. Smalyukh, *Opt Exp* 2010, **18**, 27658.
26. P. G. de Gennes, J. Prost, *The Physics of Liquid Crystals 2nd Ed.*, Clarendon, Oxford, 1993.
27. J. B. Fournier, P. Galatola, *Europhys Lett* 2005, **72**, 403.
28. M. Tasinkevych, N. M. Silvestre, M. M. Telo da Gama, *New J Phys* 2012, **14**, 073030.
29. Q. Liu, B. Senyuk, M. Tasinkevych, I. I. Smalyukh, *Proc Natl Acad Sci USA* 2013, **110**, 9231.
30. T. A. Wood, J. S. Lintuvuori, A. B. Schofield, D. Marenduzzo, W. C. K. Poon, *Science* 2011, **334**, 79.
31. J. Cantarella, R. B. Kusner, J. M. Sullivan, *Inventiones Mathematicae* 2002, **150**, 257.
32. A. Martinez, H. C. Mireles, I. I. Smalyukh, *Proc Natl Acad Sci USA* 2011, **108**, 20891.
33. D. R. Nelson, *Nano Lett* 2002, **2**, 1125.
34. A. Martinez, T. Lee, T. Asavei, H. Rubinsztein-Dunlop, I. I. Smalyukh, *Soft Matter* 2012, **8**, 2432.

## Chapter 7

# **Three-dimensional patterning of solid reduced graphene oxide microstructures through precise laser reduction of aqueous liquid crystalline dispersions of graphene oxide flakes**

Adapted from: (2014). *Three-dimensional patterning of solid reduced graphene oxide microstructures through precise laser reduction of aqueous liquid crystalline dispersions of graphene oxide flakes*. Manuscript submitted for publication.

### **Chapter Overview**

Graphene materials and structures have become an essential part of modern organic electronics and photovoltaics. However, despite many production methods, applications of graphene-based structures are hindered by high costs, lack of scalability and limitations in spatial patterning. Here we fabricate three-dimensional functional solid microstructures of reduced graphene oxide in an aqueous lyotropic nematic liquid crystal of graphene oxide flakes using a pulsed near-infrared laser. This reliable, scalable approach is mask-free, does not require special conditions

or chemical reduction agents, and can be implemented at ambient conditions starting from aqueous graphene oxide flakes. Orientationally ordered structure of liquid crystalline phases enable internal structures of complex three-dimensional reduced graphene oxide patterns with “frozen” orientational order of graphene oxide flakes, promoting their mechanical stability. The ensuing structures and particles are mechanically rigid, ranging from hundreds of nanometers to millimeters in size, as needed for many applications in electronics, photonics and display technology.

## **7.1 Introduction**

Owing to unusual physical properties[1, 2], graphene-based materials and devices are shaping the future of photonics, electronics, optoelectronics[3] and energy applications.[2, 5-8] For example, they promise to replace rare and brittle indium tin oxide transparent electrodes in the display industry.[1, 3] The most effective, low-cost and scalable approach to prepare graphene-based materials is the reduction of graphene oxide (GO)[9, 10], which can be produced in abundance. Graphene oxide can be reduced by multiple methods [5-26] including chemical reduction [10], photoreduction [6-8, 10-14], and even reduction mediated by biological microorganisms[15]. Most of these methods require specific precursors and conditions, which make them expensive and unsuitable for a large scale production. Multiple lithographic methods [5, 16] have been developed for post-production of reduced graphene oxide (rGO) and its micropatterning into useful structures and assemblies, but they are time and resource consuming and limited by advances in mask production. Recently, reduction of GO and micropatterning was achieved using laser irradiation.[6-8, 10-13, 17-23] However, its use so far has been limited to reduction and direct writing of patterns in dry two-dimensional (2D) solid films of GO.

\*\*\*

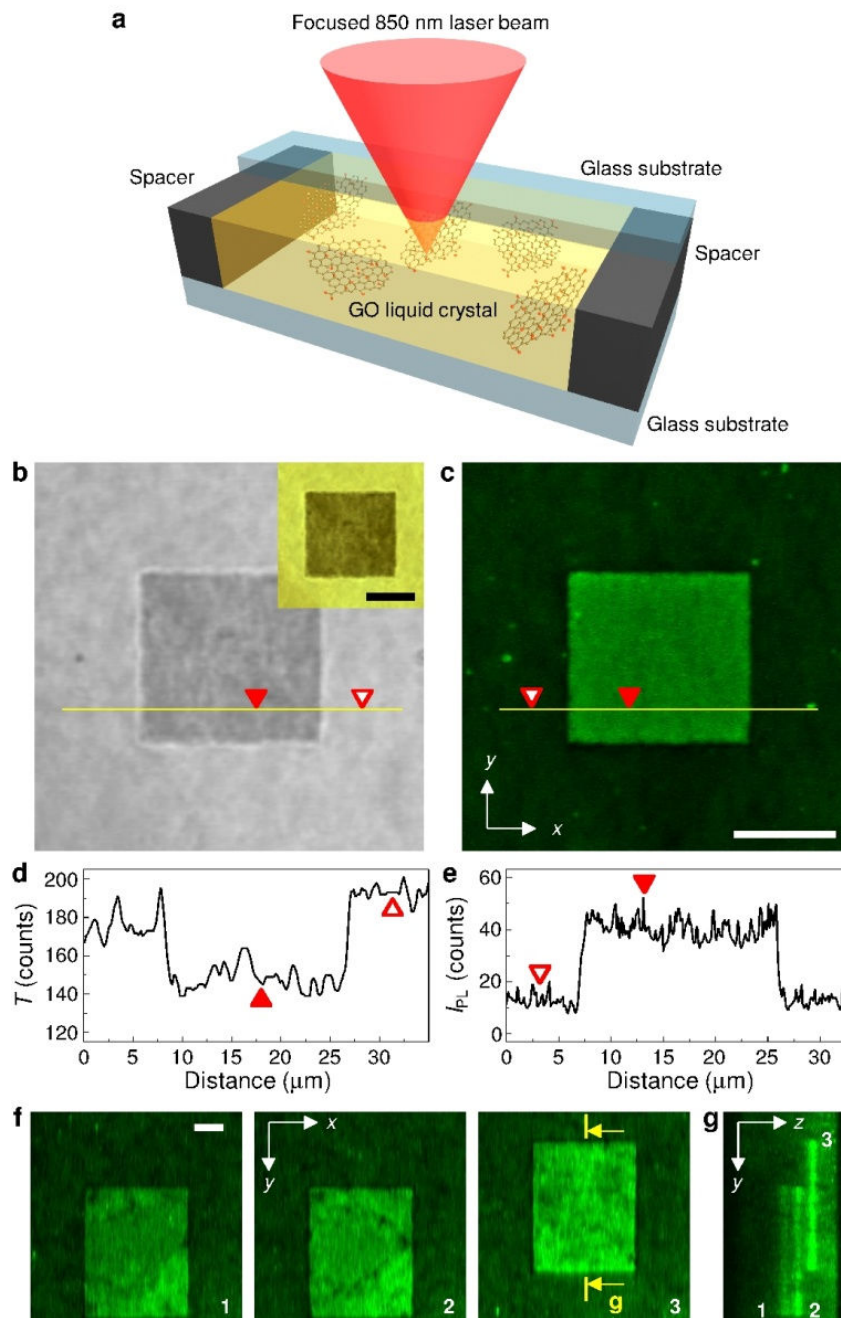
Here we produce fully three-dimensional (3D) functional solid microstructures of rGO in an aqueous nematic liquid crystal of two-dimensional GO flakes using a pulsed near-infrared laser scanning and characterize them using nonlinear optical microscopy. We show that photoluminescence of laser-reduced rGO is increased compared to pristine GO, which allows for using the same excitation beam for simultaneous reduction of GO into desired microstructures and their subsequent nonlinear photoluminescence imaging. Orientational order of liquid crystal (LC) phases promotes homogeneous internal structure of complex three-dimensional rGO patterns. Our approach is reliable and scalable, does not require special conditions or chemical reducing agents and can be used in ambient conditions in high concentration aqueous suspensions of GO flakes. Because laser reduction is an intrinsically depth-resolved nonlinear process, it can produce layered, sandwiched, as well as fully 3D microstructures, including nonplanar surfaces by programmable spatial steering of a tightly focused laser beam, without lithographic masks. Various 3D topologically nontrivial solid microstructures of rGO obtained with this approach can be used in electronic and optoelectronic devices and in basic research. Our findings also advance understanding of nonlinear photoluminescence from graphene-based materials.

## **7.2 Results and discussion**

Solid microstructures of rGO were produced in concentrated aqueous dispersions of pristine GO flakes [27, 28] (see Methods) sandwiched in between two clean untreated glass substrates (Fig. 7.1a). Graphene oxide flakes (Fig. 7.2a) are hundreds of nanometers wide graphene sheets with a basal plane and edges decorated by oxygen-containing groups including carboxyl, hydroxyl,

epoxides and others [10], which reduces interlayer forces between flakes and makes them strongly hydrophilic and stable in colloidal dispersions. They can be dispersed in deionized water to form different lyotropic discotic LC phases at higher concentrations.[28-31] We used aqueous GO flakes at 0.25-1 wt% to achieve a stable nematic LC phase (Fig. 7.1b,c). Flat GO flakes align edge-on at the interface with glass substrates[28, 30] and in the bulk orient along the LC director  $\mathbf{n}$ , which describes the average local orientation of normals to the disk-like flakes.[28] Nematic ordering of GO flakes is important because it yields homogeneous internal structure in produced rGO micropatterns (Figs. 7.1b,c, 7.4 and 7.5). Nematic samples of thickness within 10-30  $\mu\text{m}$  have a yellow brown color and are partially transparent to wavelengths ranging from about 400 nm too far into the near infrared region (bright areas in Fig. 7.1b and its inset), showing maximum absorbance at about 240 nm due to  $\pi$ - $\pi^*$  electron transitions of C-C bonds.[10, 28] Figure 7.1b shows a bright field microscopy texture of GO nematic when illuminated by a laser light at a wavelength 850 nm and the inset shows the same texture when observed under white light. Broad-band nonlinear photoluminescence [28] is detected from samples (Fig. 7.2g) under illumination by a femtosecond pulsed laser beam of low power (Methods section) at 850 nm allowing for nonlinear, intrinsically depth-resolved imaging of nematic textures [32] in GO LCs.[28] On the other hand, illumination of a GO nematic with a pulsed laser beam of high laser energy density, or fluence, results in a permanent physical change with properties drastically different from the pristine samples. We attribute this permanent change of illuminated area to a local reduction of GO flakes by a laser beam.[6-8, 10-13]

Figure 7.1b shows a bright field micrograph of a square area illuminated by a laser beam of high fluence,  $E \approx 60\text{-}70 \text{ mJ cm}^{-2}$ . Its appearance is dark (Fig. 7.1b) and its transmittance  $T$  is lower

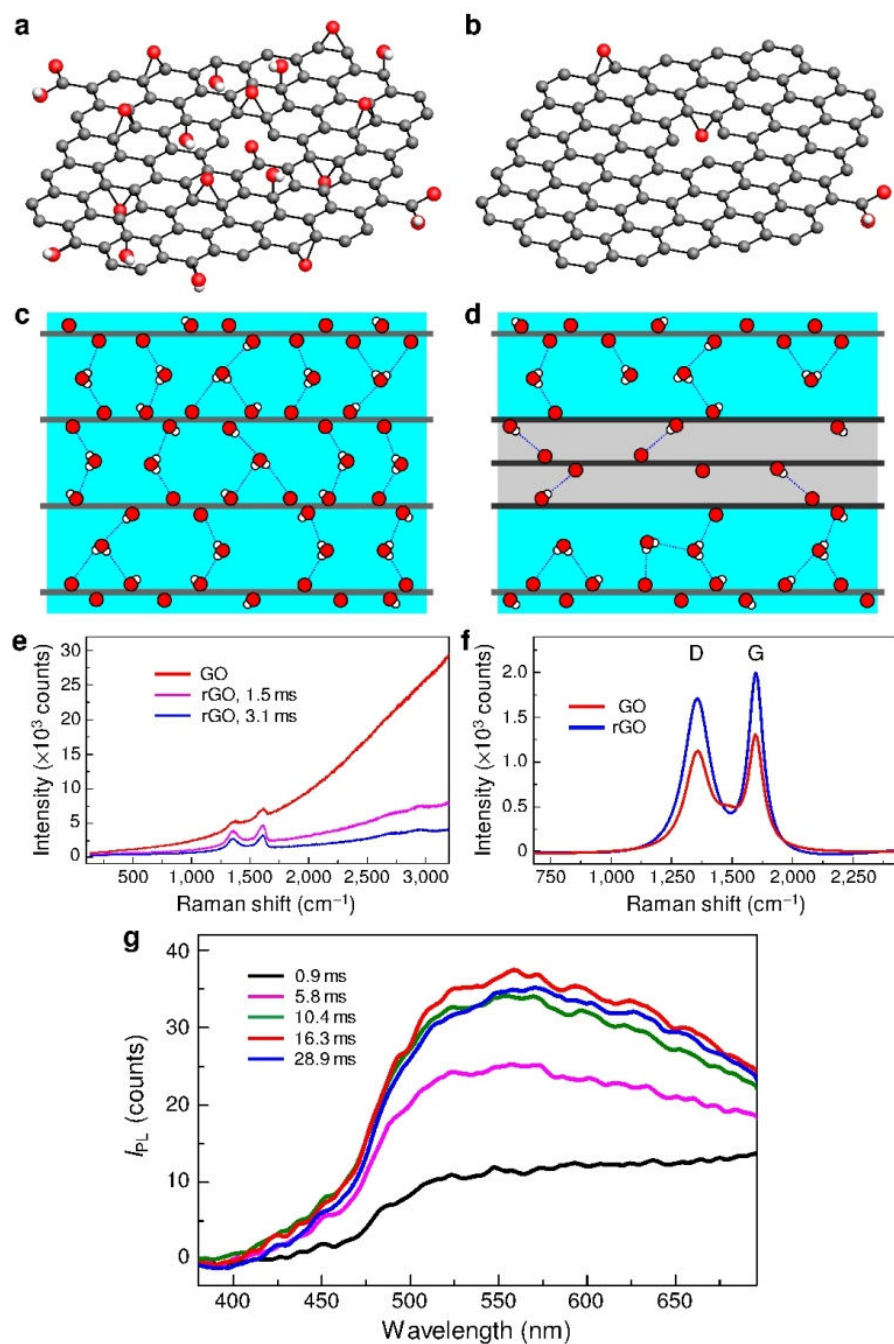


**Fig. 7.1** Laser-induced reduction of GO flakes in aqueous dispersion. (a) Schematic diagram of the experiment. (b) Transmission-mode optical micrograph of an rGO plane (darker square) in the aqueous dispersion of GO flakes obtained using 850 nm laser light; the inset shows the same sample area obtained using visible white light. (c) Photoluminescence texture of rGO plane (bright square) in the aqueous dispersion of GO flakes at excitation by 850 nm laser beam. (d,e) Transmission (d) and photoluminescence (e) along the yellow line respectively in (b) and (c). (e,f) In-plane  $x$ - $y$  (f) and cross-section  $z$ - $y$  (g) photoluminescent textures of three rGO planes produced in a thick ( $d \approx 33 \mu\text{m}$ ) sample of an aqueous dispersion of GO flakes. The scale bars are  $10 \mu\text{m}$ .



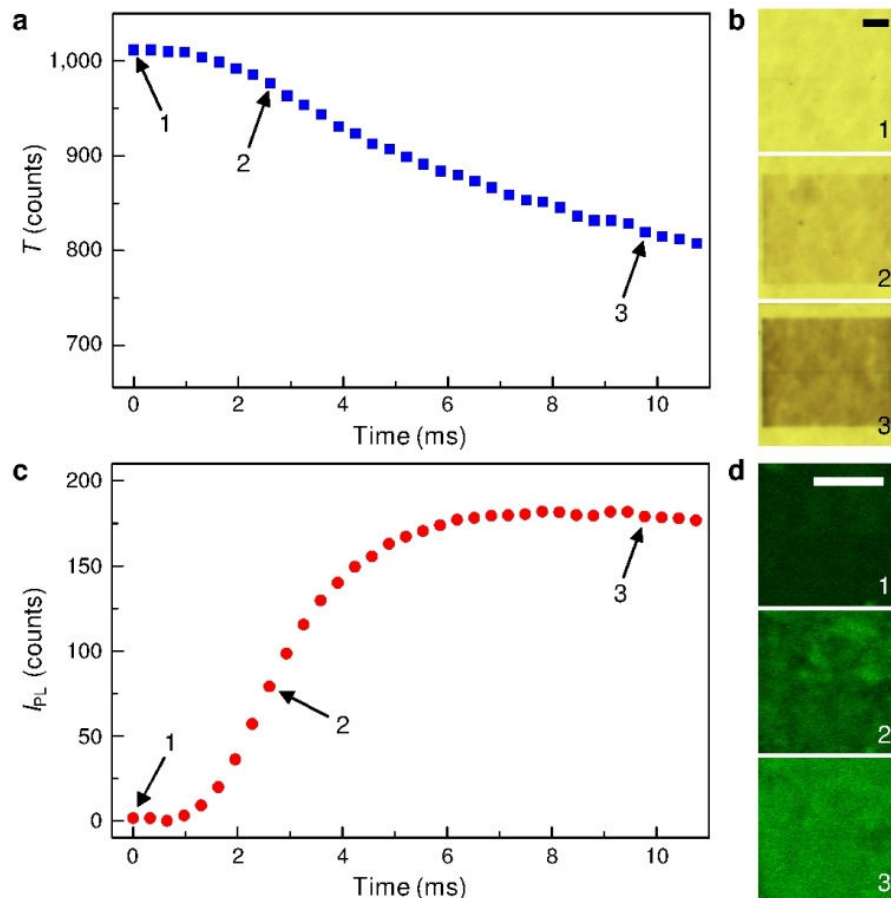
(Figs. 7.1d and 7.3a) than through the unaffected bright area. At the same time, the laser treated area produces significantly higher intensity of photoluminescence,  $I_{PL}$  (Figs. 7.1e, 7.2g and 7.3c), allowing for the simultaneous nonlinear photoluminescence imaging of a produced pattern (Fig. 7.1c). Due to the intrinsic depth-resolved nature of this nonlinear optical processes [33, 34], the laser reduction of aqueous GO is spatially localized in a small volume of about 300 nm in diameter defined by optical resolution.[32-34] This 3D localization allows for micropatterning of GO not only in the plane of the sample (Fig. 7.1b,c,f) but also across the sample thickness (Fig. 7.1g), which sets our approach apart from previous techniques [6-8, 10-13, 17-23] of photothermal or photo-induced reduction of GO and 2D micropatterning in thin dried films. Three planes of rGO of thickness determined by optical resolution were produced at different heights of a thick GO nematic dispersion sample (Fig. 7.1f) using a tightly focused laser beam. This is achieved without employing multi-layer lithography.[5] Programmable control of a scanning laser beam allows for precise reduction of GO and micropatterning not only in-plane at different heights (Fig. 7.1f,e) but also continuous reduction across a thick layer of a GO nematic.

To probe how a femtosecond pulsed laser beam at 850 nm modifies aqueous GO samples, we use UV-vis (Fig. 7.2g) and Raman (Fig. 7.2e,f) spectroscopy, as well as optical (Fig. 7.3a,b) and nonlinear photoluminescence (Fig. 7.3c,d) imaging. Raman spectra (Fig. 7.2e,f) collected from an untreated GO area and a reduced rGO region (Fig. 7.1) show pronounced peaks located at about  $1357\text{ cm}^{-1}$  and  $1598\text{ cm}^{-1}$  corresponding to a D band induced by structural disorder and G band associated with the vibration of  $sp^2$  bonded carbon atoms.[8, 10] The background fluorescence is significantly quenched in the rGO areas (Fig. 7.2e), depending on the duration of



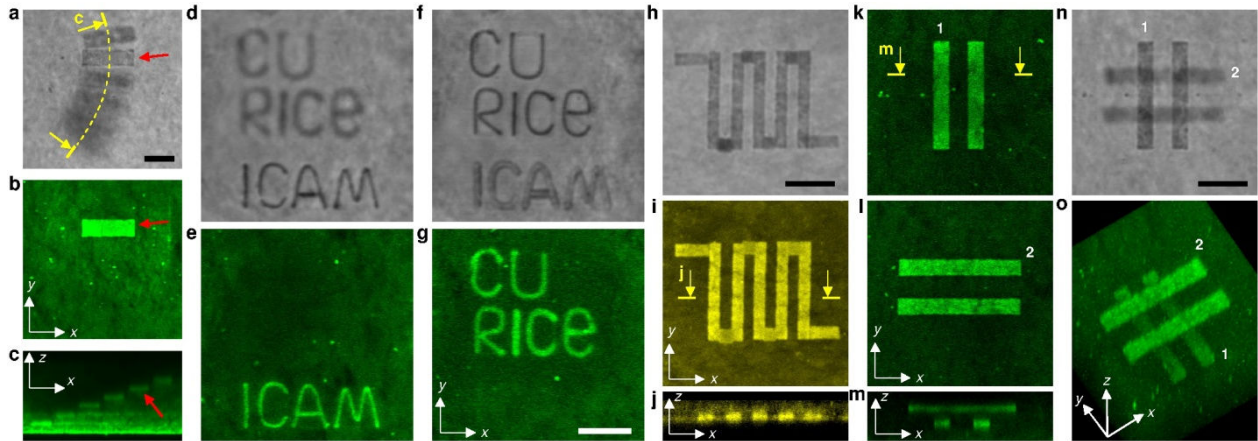
**Fig. 7.2** Reducing GO flakes in aqueous dispersion and their characterization. (a,b) Simplified structure of pristine (a) and reduced (b) GO flakes. Dark grey, red and white spheres depict carbon, oxygen and hydrogen atoms, respectively. (c,d) Schematic diagram of hydrophilic GO (c) and hydrophobic rGO (d) flakes (thick grey lines) in a water solution. (e) Raman spectra of GO and rGO flakes in a water solution taken using laser light at 514 nm. (f) Raman spectra of pristine and laser beam irradiated GO flakes near D and G peaks; laser fluence in (e, f) was  $E \approx 69 \text{ mJ cm}^{-2}$ . (g) Spectral dependence of photoluminescence intensity  $I_{PL}$  on dwell time at  $E \approx 61 \text{ mJ cm}^{-2}$ .

irradiation or dwell time at constant fluence. There is no significant shift of D and G peaks or change in a ratio between their intensities, but an absolute intensity of Raman signal is increased in the rGO regions (Fig. 7.2f). Compared to the GO areas, rGO regions show sharper D and G bands (Fig. 7.2f), which can be attributed to removal of oxygen-containing groups.[8, 10] Differences in properties between pristine and reduced GO are also detected by optical spectroscopy (Fig. 7.2g) and optical and nonlinear photoluminescence microscopy (Fig. 7.3). The absorbance of rGO areas increases in the visible range and the onset of the absorbance peak is red-shifted. The transmittance of rGO within the visible range is reduced by tens of a percent (Fig. 7.3a) as they change appearance from transparent light brown to opaque dark brown (Fig. 7.3b), controlled by the dwell time of the scanned beam. At the same time, the intensity of nonlinear photoluminescence from rGO areas increases (Figs. 7.2g and 7.3c,d), with its maximum being blue-shifted (Fig. 7.2g), depending on the dwell time. The increase of photoluminescence from reduced areas was also observed in dried films of giant [30] GO flakes; GO can be laser-reduced even within just a single giant GO flake. Interestingly, the transmittance,  $T$ , of rGO beyond a threshold irradiance continuously decreases almost linearly with irradiation time to a minimum (Fig. 7.3a,b), but the intensity of photoluminescence increases with irradiation time nonlinearly and reaches saturation after a rather short dwell time (Fig. 7.3c). This behavior of  $I_{PL}$  provides insights into the physical origins of photoluminescence from graphene-based materials [28, 35] and can be explained by quenching of the photoluminescence from GO flakes by oxygenous groups that are removed during reduction. Optical characterization reveals a qualitative picture of the reduction process and formation of solid structures of rGO flakes. Pristine GO flakes (Fig. 7.2a) in the lyotropic nematic are oriented, on average, in the same direction and kept apart by screened electrostatic repulsion,



**Fig. 7.3** Optical properties of rGO in aqueous dispersion. (a) Intensity of laser light at 850 nm transmitted through a thick ( $d \approx 27 \mu\text{m}$ ) sample versus dwell time. (b) Optical microscopy textures of sample areas irradiated for different times. Number of texture corresponds to a point in (b). (c) Photoluminescence intensity of rGO depending on dwell time with a laser beam of 850 nm. (d) Nonlinear microscopy in-plane textures of sample areas irradiated for different times. Number of texture corresponds to a point in (c). Laser fluence was  $E \approx 61 \text{ mJ cm}^{-2}$ . Scale bars are  $10 \mu\text{m}$ .

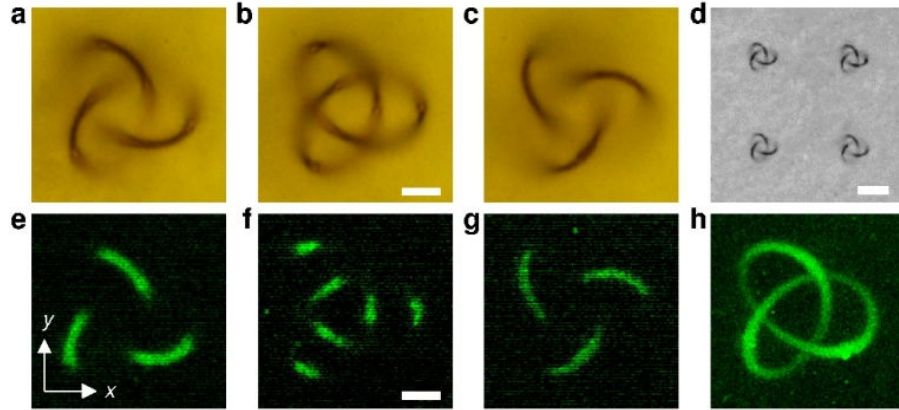
with the average spacing between these hydrophilic flakes determined by the volume fraction of GO in the suspension (Fig. 7.2c). Laser induced reduction largely removes oxygen-containing groups from the GO flakes (Fig. 7.2b) making them more hydrophobic and weakening the electrostatic repulsion (Fig. 7.2b). Consequently, hydrophobic rGO flakes collapse onto each other and form a solid continuous structure defined by the 3D illumination pattern (Fig. 7.2b). Such solid structures of rGO are rigid and preserve their shape even under the mechanical stress



**Fig. 7.4** Micropatterning of rGO structures in a bulk of a GO flakes aqueous dispersion. (a,b) Optical transmission (a) and nonlinear (b) microscopy in-plane textures of curved steps structure. (c) Nonlinear (b) microscopy cross-sectional texture of stairs-like structure acquired along a dashed yellow line in (a). Red arrows in (b,c) point to the same plane. (d-g) Optical transmission (d,f) and photoluminescence (e,g) micrographs of different parts of the text patterned at different depth. (h-j) Optical transmission (h) and photoluminescence (i,j) textures of a micropatterned resistor. (k-n) Photoluminescence (k-m) and optical transmission (n) micrographs of a micropattern mimicking a thin film capacitor or a field transistor. The same rGO buses in (k-n) are noted by numbers. (o) Three-dimensional perspective view of a structure in (k-n) reconstructed from photoluminescence data using Fluoview. Scale bars are 10  $\mu\text{m}$ .

induced, for example, by the flow of LC during shear of confining glass plates. Thus, this approach may allow for production of not only surface-attached micro- and nano-structures, but also complex-shaped colloids [33] made of ribbons of rGO that could be then redispersed into different fluid host media. Our findings indicate that, by leveraging the intrinsic ordering of GO flakes in a nematic phase, the shape anisotropy of ribbonlike cross-sections and the degree of reduction may potentially be controlled by varying the GO flakes concentration beyond the critical value of nematic formation.

Reduction of GO flakes in aqueous discotic nematic samples in a spatially confined nanosized spot allows for direct and precise micropatterning of various 3D solid structures of rGO (Figs. 7.4, 7.5) using computer-directed scanning of a laser beam. The degree of reduction can be



**Fig. 7.5** Topologically nontrivial rGO structures in a bulk of an aqueous GO flakes dispersion. (a-c) Optical bright field microscopy textures of an rGO trefoil knot focused on the bottom (a), middle (b) and top (c) of the knot. (d) Optical bright field microscopy texture of an array of rGO trefoil knots. (e-g) Nonlinear microscopy textures of an rGO trefoil knot scanned in the bottom (a), middle (b) and top (c) planes of the knot. (h) Three-dimensional perspective view of an rGO knot reconstructed from photoluminescence data using Fluoview. Reduction of the knot structure was done at  $E \approx 30 \text{ mJ cm}^{-2}$  and a laser beam scanning speed of  $37 \text{ } \mu\text{m s}^{-1}$ . Scale bar is  $20 \text{ } \mu\text{m}$  in (d) and  $5 \text{ } \mu\text{m}$  in other images.

controlled by changing the fluence and irradiation/dwell time (Fig. 7.3). Figure 7.4 shows different complex multi-level patterns of rGO in a bulk and at a surface of aqueous GO nematic imaged by optical and photoluminescence microscopy. Using transmission-mode bright field microscopy one can see all the elements of micropatterns at the same time, but blurred depending on a current focus (Figure 7.4a,d,f): an image is focused at a single level (Fig. 7.4a) of rGO “nanostairs” going from the top to the bottom substrate, or it is focused on the different parts of the text micropatterned on different levels in a GO nematic cell. At the same time, confocal photoluminescence microscopy allows the detection of the photoluminescence signal only from specific planes at different depths across the multi-level structures of rGO (see for example Fig. 7.4b,c,e,g), while other details outside of the laser scanned area are invisible (Fig. 7.4e,g). This property of selective reduction and photoluminescence detection can be used in high capacitance all carbon [6] information storage devices. Figure 7.4h-j shows an example structure that can be

used for a thin film two- or three-dimensional resistor. Intersecting multi-level or multi-layer structures (Fig. 7.4k-o), where insulating GO are sandwiched in between more conductive rGO, can be used in the electronics and optoelectronics applications for making thin film capacitors [7, 16, 18] or field transistors.[6] Importantly, our approach is suitable for direct mask-free production of not only in-plane or sandwiched structures and devices [6, 7, 15, 14, 22] but fully 3D interconnecting patterns, structures and nonplanar surfaces. To demonstrate this capability we produce an array of rGO trefoil knots (Fig. 7.5), which are topologically nontrivial 3D structures. Bright field optical (Fig. 7.5a-c) and photoluminescence (Fig. 7.5e-g) textures of the rGO trefoil knot are taken when focusing at the top, middle and bottom of the knot, respectively; a perspective view of the knot (Fig. 7.5h) was reconstructed from experimental 3D photoluminescence data. Because the internal orientation of rGO flakes matches that of the surrounding GO flakes, the fabricated knotted particles differ from the polymerized ones studied recently [33] in that they do not induce noticeable director distortions or topological defects (Fig. 7.5). This demonstrates that topological defects can be avoided when the director orientation on the surface of complex-shaped particles matches that of the surrounding LC, even when the colloidal inclusions exhibit nontrivial surface topology of torus knots.

## **7.3 Materials and Methods**

### **7.3.1 Sample preparation**

The improved, mostly single-layer GO flakes used in this work were synthesized by methods [27] modified for large-scale production and obtained as a dispersion in deionized water [28] at a concentration of  $2.5 \text{ g L}^{-1}$  (0.25 wt%). This dispersion was additionally tip-sonicated for 2 h at  $\sim 35 \text{ W}$  of ultrasonic power using a Branson 250 sonifier (VWR Scientific) operating at 20 kHz

and equipped with a microtip of diameter 4.8 mm, which allowed for achieving monodisperse flakes of smaller size.[28] A homogeneous nematic LC phase was obtained at higher concentrations of GO flakes in dispersions by controlled removal of excess water from dispersions subjected to centrifugation in a Sorvall Legend 14 centrifuge (Thermo Scientific) at 12 rpm for ~10-15 min. LC dispersions of GO were sandwiched between two glass substrates. Clean untreated glass substrates were used in samples for laser-induced reduction of GO flakes and optical and nonlinear microscopy observations. A gap between substrates was set using Mylar films (DuPont Teijin) of thickness 10-30  $\mu\text{m}$ . Dispersions of GO flakes were sonicated in a Cole-Parmer 8891 ultrasonic bath for ~5 min before assembling a cell. Evaporation of water during experiments was prevented by sealing samples with a UV curable glue (NOA 63, Norland Products, Inc.).

### **7.3.2 Laser-induced reduction, photoluminescence microscopy and optical characterization**

Nonlinear photoluminescence imaging of GO aqueous samples was performed at room temperature using a multimodal nonlinear optical microscopy setup [32] coupled to an inverted Olympus microscope IX-81. A tunable (680-1080 nm) Ti:sapphire oscillator (140 fs, 80 MHz, Chameleon Ultra II, Coherent) was used as an excitation source. The excitation beam was focused into the sample using Olympus high numerical aperture (NA) oil objective UPLSAPO 100 $\times$ /NA = 1.4. The spatial 3D position of the excitation beam in the volume of the sample was controlled with the galvanomirror scanning unit (Fluoview FV300, Olympus). An average laser power for photoluminescence imaging was < 1 mW in a sample to prevent the photo- and thermal damage. The excitation of GO flakes was performed at 850 nm, and the unpolarized photoluminescence light was detected in a range of 400-700 nm in a backward mode with a



photomultiplier tube H5784-20 (Hamamatsu). The polarization of excitation could be varied using a half-wave retardation plate mounted immediately before an objective. The same setup was used for a 3D reduction of aqueous GO flakes using a pulsed laser beam at 850 nm and laser fluence  $E > 100 \text{ mJ cm}^{-2}$ . The dwell time, or scanning speed, was also controlled by a scanning unit FV300. Olympus Fluoview software was used for data acquisition and image reconstruction, and ImageJ software was used for data processing and analysis. Polarizing microscopy observations of samples in visible light and measurement of photoluminescence spectra were performed using the same IX-81 equipped with crossed polarizers, CCD camera (Flea, PointGrey) and a spectrometer USB2000 (OceanOptics) mounted onto a microscope. Raman spectra were measured using Renishaw inVia Raman microscope with excitation at 514.5 nm and low power to reduce unwanted heating or optical effects induced by a laser.

## 7.4 Conclusion

In conclusion, we have demonstrated a selective reduction of GO flakes in the bulk of an aqueous GO flakes liquid crystal at ambient conditions using nonlinear excitation by a near-infrared femtosecond laser beam, which allows for mask-free micropatterning of 3D solid nonplanar structures and surfaces of reduced GO. Besides its simplicity, this reliable, scalable method does not require special conditions or chemical reduction agents, and can be implemented at ambient conditions just in aqueous suspensions of GO flakes. Advantages of micropatterning in a liquid crystal phase include producing patterns with more homogeneous internal structure and the potential to attain frozen orientational order of GO flakes orientation, which can also be modified before reduction by applying an electric field.[31] Our approach can be used for scalable production of graphene-based devices for photonics, electronics [20],

optoelectronics [12], information [22] and energy storage [7] applications. Furthermore, solid colloidal particles of rGO produced here can be used in other research areas like for example for probing the interplay of topologies of surfaces, molecular fields, and defects [33] in soft matter.

## 7.5 References

1. G. Eda, G. Fanchini, M. Chhowalla, *Nat. Nanotechnol.* 2008, **3**, 270.
2. F. Bonaccorso, Z. Sun, T. Hasan, A. C. Ferrari, *Nat. Photonics* 2010, **4**, 611.
3. S. Pang, Y. Hernandez, X. Feng, K. Müllen, *Adv. Mater.* 2011, **23**, 2779.
4. V. Yong, J. M Tour, *Small* 2009, **6**, 313.
5. F. Li, M. Xue, X. Ma, M. Zhang, T. Cao, *Anal. Chem.* 2011, **83**, 6426.
6. V. Strong, *et al.*, *ACS Nano* 2012, **6**, 1495.
7. R. Mukherjee, A. V. Thomas, A. Krishnamurthy, N. Koraktar, *ACS Nano* 2012, **6**, 7867.
8. H. Li, Ch. Bubeck, *Macromol. Res.* 2013, **21**, 290.
9. M. Segal, *Nat. Nanotechnol.* 2009, **4**, 612.
10. S. Pei, H-M. Cheng, *Carbon* 2012, **50**, 3210.
11. Y. Zhang, *et al.*, *Nano Today* 2010, **5**, 15.
12. C. Petridis, *et al.*, *Appl. Phys. Lett.* 2013, **102**, 093115.
13. L. Huang, *et al.*, *Carbon* 2011, **49**, 2431.
14. E. Orabona, *et al.*, *Opt. Lett.* 2014, **39**, 4263.
15. Y. Tanizawa, *et al.*, *J. Phys.: Conf. Ser.* 2012, **352**, 012011.
16. J.-Y. Hong, J. Jang, *J. Mater. Chem.* 2012, **22**, 8179.
17. D. A. Sokolov, K. R. Shepperd, T. M. Orlando, *J. Phys. Chem. Lett.* 2012, **1**, 2633.
18. W. Gao, *et al.*, *Nat. Nanotechnol.* 2011, **6**, 496.
19. H. F. Teoh, Y. Tao, E. S. Tok, G. W. Ho, C. H. Sow, *J. Appl. Phys.* 2012, **112**, 064309.
20. M. F. El-Kady, V. Strong, S. Dubin, R. B. Kaner, *Science* 2012, **335**, 1326.
21. R. Trusovas, *et al.*, *Carbon* 2013, **52**, 574.
22. X. Li, Q. Zhang, X. Chen, M. Gu, *Sci. Rep.* 2013, **3**, 2891.

23. V. Abdelsayed, *et al.*, *J. Phys. Chem. Lett.* 2010, **1**, 2804.
24. C. W. Chang, M. H. Hon, I. C. Leu, *J. Electrochem. Soc.* 2012, **159**, H605.
25. Q. Zhuo, *et al.*, *Carbon* 2013, **52**, 559.
26. R. Y. N. Gengler, *et al.*, *Nat. Commun.* 2013, **4**, 2560.
27. D. C. Marcano, *et al.*, *ACS Nano* 2010, **4**, 4806.
28. B. Senyuk, *et al.*, *ACS Nano* 2012, **6**, 8060.
29. J. E. Kim, *et al.*, *Angew. Chem., Int. Ed.* 2011, **50**, 3043.
30. B. Dan, *et al.*, *Soft Matter* 2011, **7**, 11154.
31. T.-Z. Shen, S.-H. Hong, J.-K. Song, *Nat. Mater.* 2014, **13**, 394.
32. T. Lee, A. Martinez, *et al.*, *Nat. Mater.* 2014, **13**, 258.
33. R. F. Gattass, E. Mazur, *Nat. Photonics* 2008, **2**, 219.
34. C. H. Lui, K. F. Mak, J. Shan, T. F. Heinz, *Phys. Rev. Lett.* 2010, **105**, 127404.

## **Chapter 8**

# **Light-driven dynamic Archimedes spirals and periodic oscillatory patterns of topological defects in anisotropic soft matter**

### **Chapter Overview**

Oscillatory and excitable systems commonly exhibit formation of dynamic non-equilibrium patterns. For example, rotating spiral patterns are observed in biological, chemical, and physical systems ranging from organization of slime mold cells to Belousov-Zhabotinsky reactions, and to crystal growth from nuclei with screw dislocations. Here we describe spontaneous formation of spiral waves and a large variety of other dynamic patterns in anisotropic soft matter driven by low-intensity light. The unstructured ambient or microscope light illumination of aligned, thin liquid crystal films in contact with a self-assembled azobenzene monolayer causes spontaneous formation, rich spatial organization, and dynamics of twisted domains and topological defects accompanied by the dynamic patterning of azobenzene group orientations within the monolayer. Linearly polarized incident light interacts with the twisted liquid crystalline domains, mimicking their dynamics and yielding patterns in polarization of transmitted light. This shows that the

delicate light-soft-matter interaction can yield complex self-patterning of both. We uncover underpinning physical mechanisms and discuss potential uses.

## 8.1 Introduction

Dynamics, pattern formation and other non-equilibrium processes in soft and biological matter attract a great deal of attention [1-7], especially when they are light-driven or field-controlled [8-13]. Beyond their fundamental importance in modeling similar processes in biology [1, 2], e.g. in testing Turing-type theories of morphogenesis, they potentially can be used in non-equilibrium self-organization of composite materials with a large structural diversity and dynamic control by weak external stimuli. For example, specially designed light-responsive active colloids form so-called “living crystals” [14] while biologically derived active nematic liquid crystals (LCs) exhibit constant generation and annihilation of topological defects [15, 16]. Examples of recently introduced light-driven non-equilibrium soft matter systems include arrays of Belousov-Zhabotinsky droplets and gels [7, 17]. In thermotropic LCs similar to the ones used in displays [18, 19], a large variety of dynamic patterns, including spiral waves, have been generated by rotating magnetic fields [8-13]. Interestingly, these patterns arise in the molecular alignment field, also called director field  $\mathbf{n}(\mathbf{r}, t)$  [18], which is tangent to the average direction of nanometer-sized elongated LC molecules that can exhibit patterns as a function of spatial coordinates and time. The characteristic length scales associated with the patterns can range from tens of micrometers to millimeters while characteristic timescales are larger than the typical millisecond LC realignment times [19]. In this work, we demonstrate that a rich variety of dynamic LC alignment patterns can also emerge when driven by low-intensity microscope or ambient light and when the thin quasi-two-dimensional LC film is in contact with light-

responsive azobenzene monolayer [20]. These patterns are explained by considering complex changes of the polarization state of initially linearly polarized light traversing through twisted, birefringent LC films of different thickness, combined with the surface anchoring-mediated [19, 21] coupling between this polarization and the easy axis orientation defined by the polarization-sensitive azobenzene monolayer [20]. The dynamic patterns within the LC's and azobenzene monolayer's orientational ordering are also mimicked by the similarly changing patterns of the polarization state of light after passing through the dynamically driven sample. The dynamic patterns of azobenzene molecular orientations within the monolayer significantly expands our abilities of controlling structural organization in such single-molecule-thick soft matter systems [22, 23]. Spiraling wave and other observed types of dynamics of topological defects and twisted solitons expand the defect control capabilities beyond their patterning into time-independent arrays [24] and elaborate three-dimensional spatial structures [25]. Our system may allow for light-driven rotation and assembly of anisotropic nematic LC colloids [26] and nanoinclusions [27].

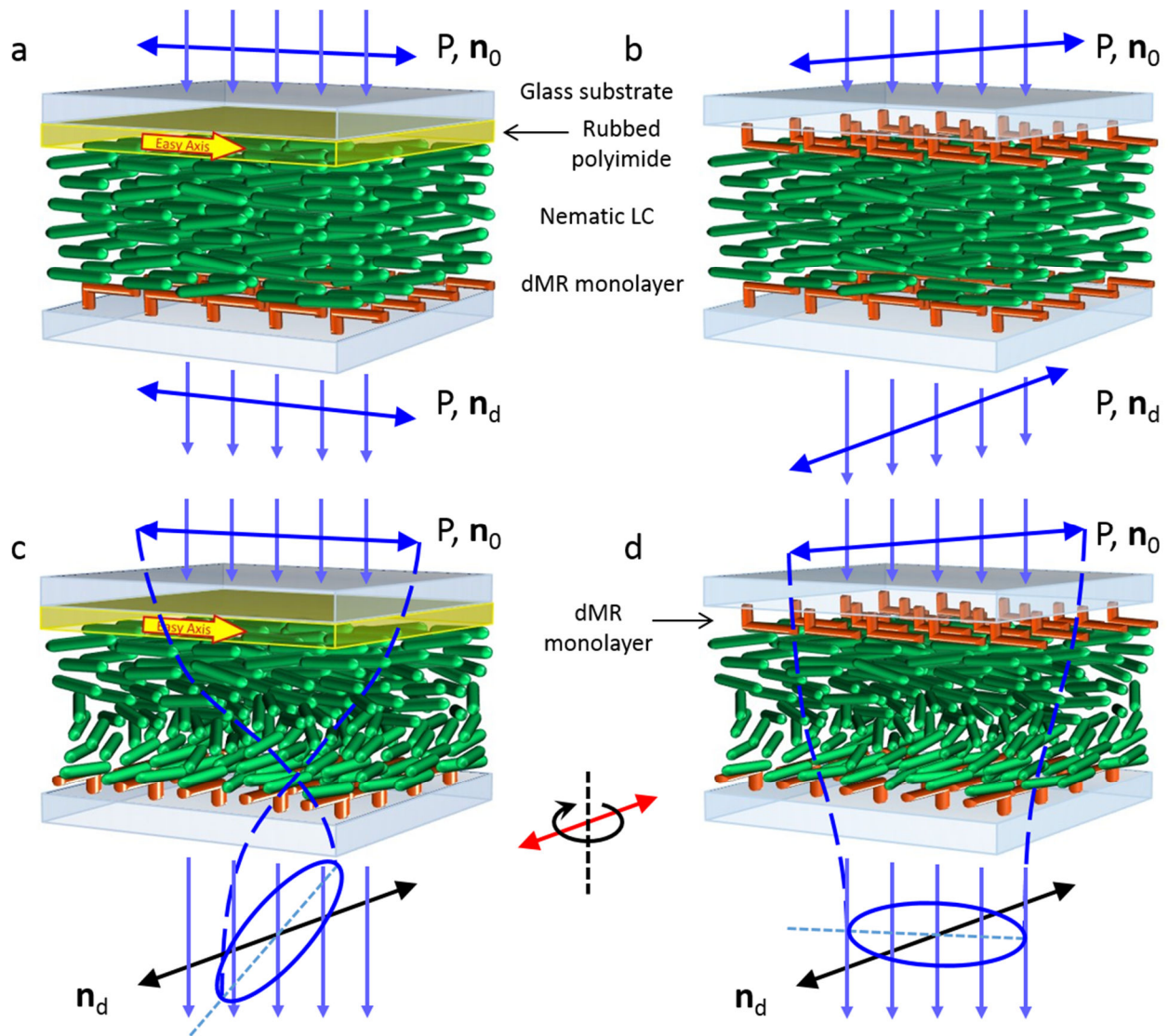
## **8.2 Experimental system, methods, and materials**

The LC cells studied here were constructed using both photo-responsive dMR coated substrates (prepared as described in sub-section 2.3.1 and in more detail in Appendix A.1) and ones coated with thin films of uniaxially rubbed polyimide (PI-2555), providing light-controlled and static planar boundary conditions at the LC-substrate interfaces, respectively. Nematic cells that exhibit these complex photo-driven dynamic and static patterns can be constructed using two photo-responsive substrates or just one. Cells with dual dMR plates can have any initial orientation with respect to the polarization of normally incident blue light without effect on the

patterns. However, cells containing one plate coated with rubbed polyimide introduce a complex dependence of the ensuing response with respect to this initial orientation. In some cases, the cells were spaced using 2-4  $\mu\text{m}$  glass spheres mixed into an acetone-diluted epoxy (we avoid using UV-curable glue due to the dMR sensitivity to UV light), while in others we used no spacers at all to achieve a submicron cell gap thickness. We then seal two opposite edges of the cell with more epoxy. If the cell contains a plate with polyimide, we generally seal the edges parallel to the rubbing direction. Once the epoxy has cured, we then fill the cell via capillary action with the thermotropic nematic 5CB. To mitigate the aligning effects of flow, we then heat the cell to the isotropic phase and then quench back to the nematic. The two remaining edges are then sealed as well.

For both driving patterns and imaging them, we used an Olympus BX51 upright polarizing optical microscope with a coupled Spot 14.2 Color Mosaic Camera (Diagnostic Instruments, Inc.). The polarized imaging light source itself is used to generate the dynamic and static patterns presented in this study. Cells with two dMR-coated substrates can be placed on the microscope's rotation stage with either substrate facing the imaging lamp (Fig. 8.1). The substrate through which the normally incident light passes first will be realigned to define an easy axis perpendicular to the polarization (in general, the major axis of the elliptical polarization state), while the far substrate interacts with the complex polarization field emerging after light is transmitted through the LC. Cells containing one substrate with polyimide (Fig. 8.1), however, are oriented so that the light passes through the static LC-polyimide interface first, before traversing the birefringent nematic medium and finally the photo-responsive dMR surface. To control the speed at which we drive the dynamic patterns, we tuned the intensity of white light





**Fig. 8.1** Pattern-forming photo-responsive LC cell construction. (a-d) Two LC cells constructed with (a, c) one substrate coated with a thin film of rubbed polyimide and another coated with a monolayer of the photo-responsive dMR or with (b, d) both substrates coated with dMR. The two cells are also shown in two states: (a,b) at the first moment of illumination with linearly polarized blue light and (c,d) in an evolved dynamic state sometime later when the second substrate is adaptively reorienting due to the photo-induced torque caused by polarized-light illumination. The polarization of the output light is, in general, elliptical and oriented with its long axis at some angle with respect to the director at the output plane,  $\mathbf{n}_d$ . In the “dynamic equilibrium”, the boundary condition  $\mathbf{n}_d$  for the director at the exit substrate is constantly adjusted to be orthogonal to the long axis of the polarization ellipse orientation of which is dependent on the twist of director throughout the cell while this, in turn, adjusts the amount of director twist and, subsequently, further alters the polarization state, thus providing the feedback mechanism needed for the pattern formation.

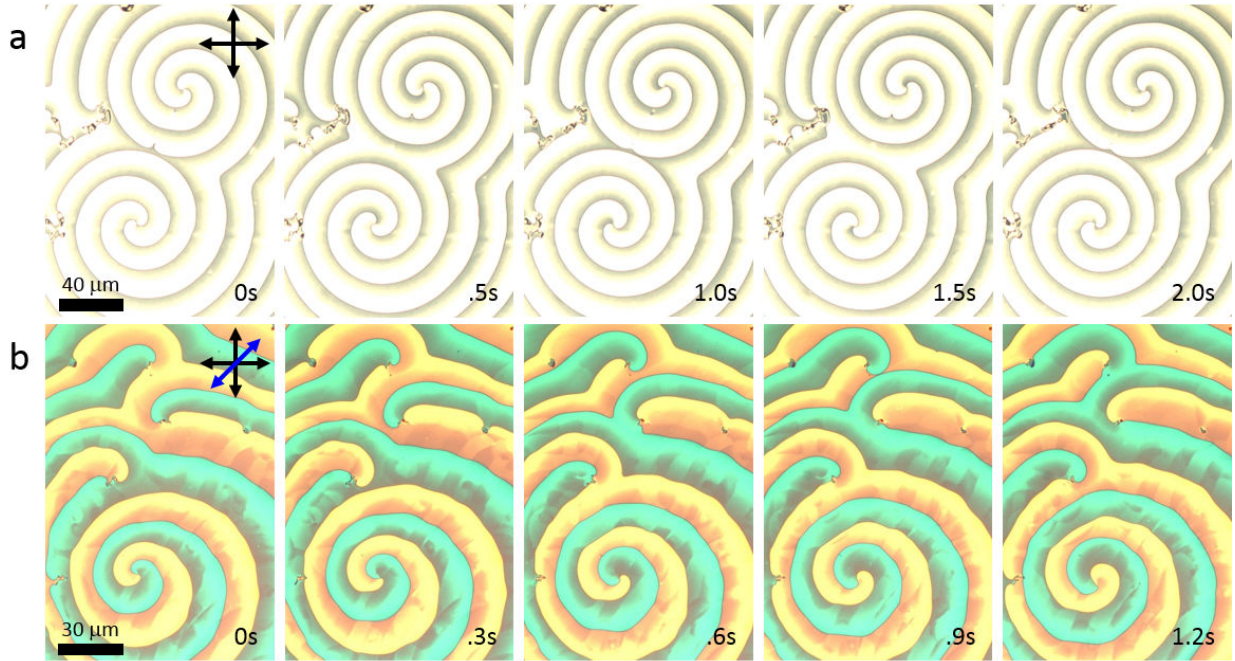
while also adjusting the camera's sensitivity to avoid dark or saturated images. Alternatively, we used broadband optical filters that block or transmit portions of the visible spectrum.

## 8.3 Results

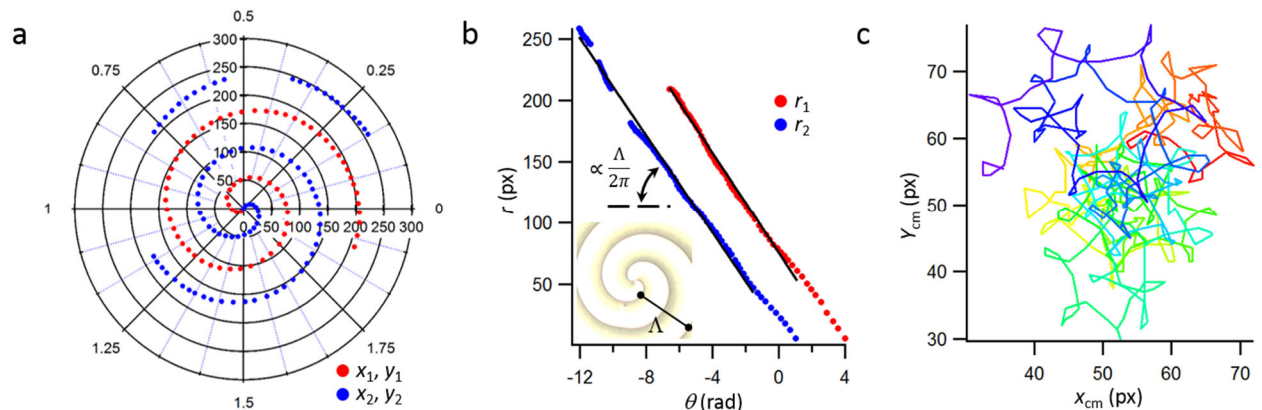
### 8.3.1 Experimental characterization of dynamic patterns

When relatively thin LC cells (of thickness in the range 0.7-1.2  $\mu\text{m}$ ) are illuminated by blue, ultraviolet or white light as depicted in Fig. 8.1, one observes rich dynamic behavior, with the most prominent dynamic pattern being that shown in Fig. 8.2. The pattern has a visual resemblance of that seen in Belousov-Zhabotinsky reactions and also in homeotropic nematic cells driven by rotating magnetic fields [1-13]. By tracking the inter-domain walls using ImageJ software, such as the ones presented in Fig. 8.2, we plot their coordinates at constant time (Fig. 8.3a,b). A close examination reveals that, apart from the regions in the very centers of these patterns, our experimental data, presented in terms of cylindrical coordinates  $r$  versus  $\theta$  for each of the two arms, fit to the geometry of an Archimedean spiral  $r = r_0 + \Lambda\theta/2\pi$  (Fig. 8.3b), where  $\Lambda$  is the distance between consecutive solitons for a given spiral arm, which we can call wavelength of the dynamic pattern. By tracking the pattern's tip point where the two arms of the spiral meet (Fig. 8.3c) based on videomicroscopy frames, we find that this point is meandering in the lateral plane of the cell, similar to that seen in the reaction diffusion oscillatory systems for geometrically similar Archimede's spiral patterns [5].

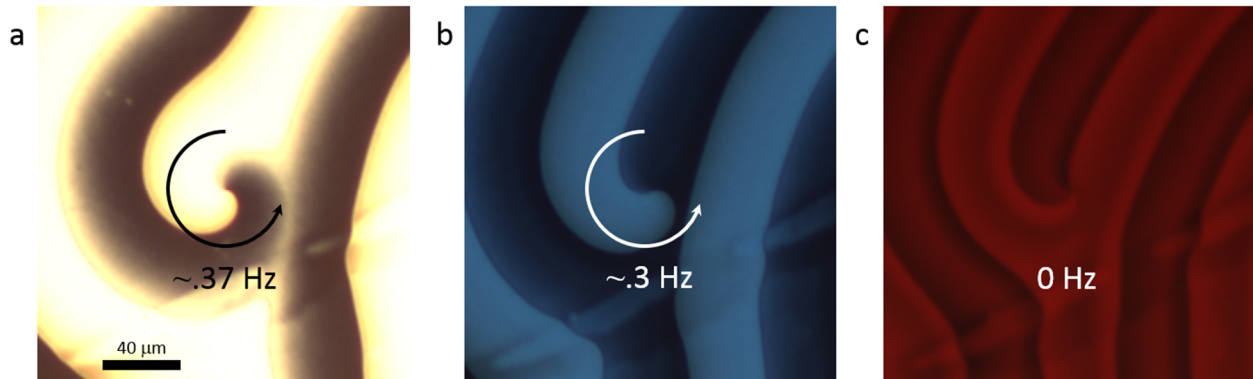
The observed dynamic behavior of the Archimede's spirals is highly dependent on the intensity and spectral composition of the illumination light (Fig. 8.4). For example, white-light



**Fig. 8.2** Dynamic spirals. (a, b) A series of videoframes, with elapsed time marked on them, for two spiral patterns shown between crossed polarizers and with (b) an additional half-wave plate inserted between the polarizers and having the slow axis oriented along the blue double arrow. The spiral arms in series (a) undergo  $2\pi$  rotation over about 2 seconds while the spiral arms in series (b) undergo  $\pi$  rotation over about 1.2 seconds.



**Fig. 8.3** Analysis of dynamic Archimedean spirals in optically driven nematic cells. (a) A polar plot of the spiraling domain coordinates in the  $r$ - $\theta$  cylindrical coordinate system, as measured experimentally for two spiral arms (red and blue filled circles). (b) Linear plots of  $r$  versus  $\theta$  for each arm fit to an Archimedean spiral geometric configuration defined as  $r = r_0 + \Lambda\theta/2\pi$ . The distance between consecutive solitons (wavelength) for a given spiral arm is defined as  $\Lambda$ , and is defined in the inset of (b). The two spiraling arms have wavelengths  $\Lambda_1 = 19.03 \mu\text{m}$  and  $\Lambda_2 = 18.5 \mu\text{m}$ . (c)  $x$ - $y$  coordinates of the center of mass tracked over time (color-coded) to illustrate that the center exhibits meandering behavior similar to that of Archimedes spirals in chemical reaction diffusion systems.



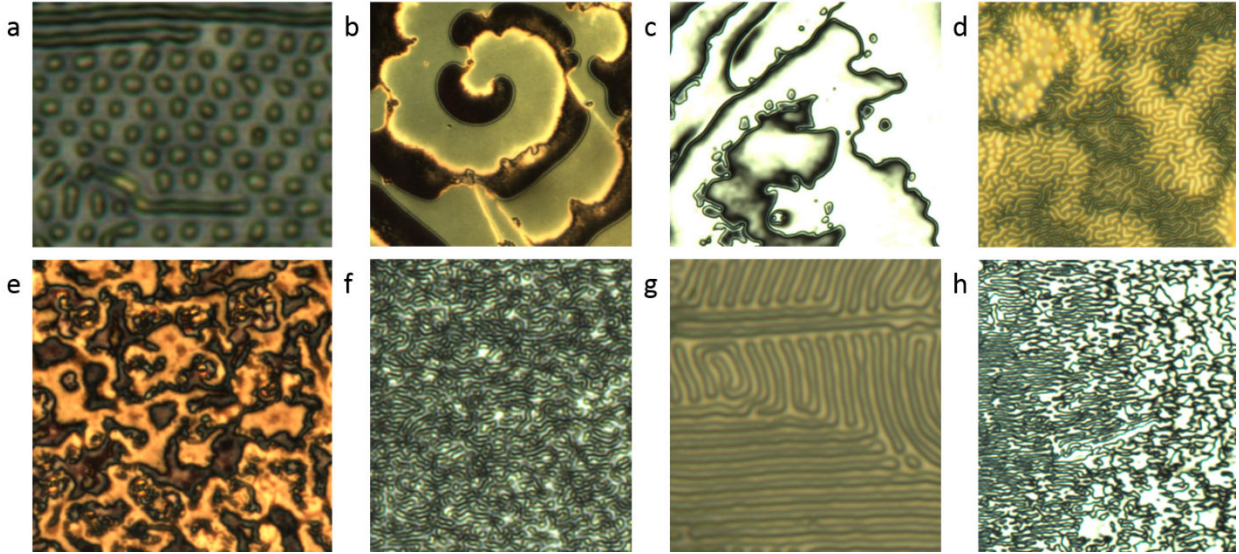
**Fig. 8.4** Color dependence of pattern dynamics. (a-c) Three frames of a single time series showing the dependence of defect dynamics on the color of illumination light. In panel (a), the pattern is driven by white light at a rate of  $\sim.37$  Hz. dMR being highly sensitive to blue light, the pattern is also effectively driven by blue light, as is seen in panel (b), although at a slightly lower rate ( $\sim.3$  Hz) due to decreased overall intensity. The optical micrograph in (c) shows that the interaction of the nematic cells with red light is negligible, so the pattern “freezes” under red illumination.

illumination in the polarizing microscope setting (Fig. 8.4a) yields a pattern rotation rate of  $\sim 0.37$  Hz. This rate drops only slightly down to  $\sim 0.3$  Hz as an absorptive color filter is inserted so that only blue light participates in the sample illumination (Fig. 8.4b). However, the pattern becomes static when the color filters are selected so that only red or longer-wavelength light participates in the sample illumination (Fig. 8.4c). This observation is rather natural as the self-assembled dMR monolayers are photosensitive only in the blue-ultraviolet parts of the optical spectrum. We also find that the cells with dMR-dMR alignment layers on both confining substrates and polyamide-dMR cells, with the photosensitive monolayer only on the exit plane of the cells while having the rubbed polyimide coatings on the entrance surface, both yield similar behavior, suggesting that the light-matter interaction within the LC and at the exit substrate is responsible for the feedback mechanism typically associated with such dynamic patterns [1-13].

As the cell thickness is varied, e.g. by means of producing wedge-shaped LC cells, the variety of observed patterns greatly increases (see Fig. 8.5 and the linked videos) and includes various periodic or quasi-periodic arrays of circular and linear stripe-like domains. Some of the patterns become static with time. For example, the stripe-like patterns shown in Fig. 8.5g has domains with static horizontally oriented stripes but dynamic vertically oriented stripes. In this particular case, the dynamic stripes are gradually replaced by horizontal ones and the entire pattern becomes static. However, this is not the case for all other types of patterns that we observed as they keep exhibiting different forms of dynamic behavior as long as the illumination light is on, or even in the ambient light.

### 8.3.2 Modeling of feedback mechanisms

To obtain insights into the underlying physics responsible for the observed dynamic patterns, as an example, we consider an initially planar LC cell with the dMR-LC interfaces at both confining substrates, as depicted in Fig. 8.1b. The direct coupling of the electric field of our illumination light and the LC director in the bulk of our cells can be neglected as the used intensities are much lower than what is needed for the optical Freedericksz transition [20, 24]. At the surfaces, however, the illumination light sets the polarization-sensitive boundary conditions with the director's easy axis orientations orthogonal to the linear polarization or to the long axis of the polarization ellipse. As the linearly polarized light illuminates the first dMR-LC interface at  $z = 0$ , it sets the easy axis orientation  $\mathbf{n}_0(x, y) = \mathbf{n}(x, y, z=0)$  to be orthogonal the initial linear polarization direction  $\mathbf{P}_0$ . However, it is important to note that, due to finite intensity-dependent surface anchoring,  $W_0(I)$ , the director can be forced to rotate away from this easy axis orientation. As this linearly polarized light traverses through the LC cell, its polarization is



**Fig. 8.5** Summary of dynamic and static patterns in addition to the propagating Archimedean spiral waves. (a-h) Eight examples of unique species of observed dynamic patterns, all driven with polarized white light.

altered by the birefringent LC medium. Generally, the outgoing light is elliptically polarized, with the azimuthal orientation,  $\psi$ , of the long axis of the polarization ellipse measured relative to the orientation of the director at the 2<sup>nd</sup> LC-dMR interface,  $\mathbf{n}_d(x,y) = \mathbf{n}(x,y,z=d)$ , and the ellipticity  $\varepsilon$  dependent on the LC film thickness as well as director twist across the cell. This causes a nontrivial interplay between the polarization of the outgoing light with the orientation of the long axis of the ellipse  $\mathbf{P}_a$  and  $\mathbf{n}_d(x, y)$ . Furthermore, dynamic changes of  $\mathbf{n}_d(x, y)$  in response to changes of the polarization state of outgoing light lead to changes of director structure across the cell thickness and thus further alter the polarization state itself, providing a feedback mechanism that is key to understanding the observed dynamic patterns. The total light's polarization-dependent surface anchoring (LPDSA) free energy at the two confining surfaces (Fig. 8.1b,d) can be written as

$$F_{LPDSA} = [W_0(I)/2] \int (\mathbf{P}_0 \cdot \mathbf{n}_0)^2 dS + [W_d(I, \varepsilon)/2] \int (\mathbf{P}_d \cdot \mathbf{n}_d)^2 dS \quad (8.1)$$

where  $W_0(I)$  and  $W_d(I, \varepsilon)$  are the light intensity and polarization dependent surface anchoring coefficients at the two confining surfaces and the positive sign in front of this term indicates that they are minimized when the easy axes  $\mathbf{n}_d$  and  $\mathbf{n}_0$  are orthogonal to the linear or elliptical polarization directions at these two planes,  $\mathbf{P}_d$  and  $\mathbf{P}_0$ , respectively (Fig. 8.1b,d). The LPDSA-driven director distortions are resisted by the bulk elastic free energy [18, 19]

$$F_{elastic} = \int \left\{ \begin{aligned} &\frac{K_{11}}{2} (\nabla \cdot \mathbf{n})^2 + \frac{K_{22}}{2} [\mathbf{n} \cdot (\nabla \times \mathbf{n}) + \frac{2\pi}{p}]^2 + \frac{K_{33}}{2} [\mathbf{n} \times (\nabla \times \mathbf{n})]^2 \\ &- K_{24} [\nabla \cdot [\mathbf{n}(\nabla \cdot \mathbf{n}) + \mathbf{n} \times (\nabla \times \mathbf{n})]] \end{aligned} \right\} dV, \quad (8.2)$$

where  $K_{11}$ ,  $K_{22}$ ,  $K_{33}$ , and  $K_{24}$  are Frank elastic constants for splay, twist, bend and saddle splay deformations, respectively. The competition of corresponding LPDSA and bulk elastic torques guides dynamics of the system that can be described by the dynamical equation for the LC director [18]:

$$\Gamma_v = \mathbf{n} \times \frac{\delta F}{\delta \mathbf{n}} \quad (8.3)$$

where  $\Gamma_v$  is the corresponding viscous torque and  $F = F_{elastic} + F_{LPDSA}$ . We assume that the backflow effects can be neglected and that the viscous torque is proportional to the angular velocity of the director about an axis perpendicular to itself [18, 19]:

$$\Gamma_v = -\gamma_1 \left( \mathbf{n} \times \frac{\partial \mathbf{n}}{\partial t} \right). \quad (8.4)$$

Due to the type of light-induced patterns, twist distortions are the most abundant, although other types of distortions are present in-between the domains of different direction and amount of twist. Within the uniformly twisted domains, the changes of polarization of light can be modeled

analytically using the Jones matrix approach [28], similar to that in twisted nematic displays. At sufficiently large intensities of illumination, one can assume that  $W_0(I)$  is large, which assures propagation of the ordinary mode of light within the LC, yielding an elliptically polarized outgoing light with the polarization state given by [28]:

$$\varepsilon = \tan\left(\frac{1}{2}\sin^{-1}\left[-\frac{\Omega\phi}{X^2}\sin^2 X\right]\right) \quad (8.5)$$

$$\tan 2\psi = \frac{2\phi X \tan X}{X^2 - (\phi^2 - \Omega^2/4)\tan^2 X} \quad (8.6)$$

where  $X = \sqrt{\phi^2 + \Omega^2/4}$ ,  $\Omega = 2\pi(n_e - n_o)d/\lambda$ ,  $\lambda$  is the central wavelength of the illumination light, the ellipticity  $\varepsilon$  is defined as the ratio of the minor and major axes of the ellipse, and  $\phi$  is the director twist angle across the cell of thickness  $d$ . The analysis of these equations reveals the rich behavior as a function of cell thickness, optical anisotropy of the LC, as well as the overall twist across the cell. This richness of altering the outgoing light's polarization state is responsible for the ensuing richness of feedback mechanisms and the large variety of observed dynamic patterns. A regime of particular interest is when the rotation of the long axis of ellipse upon exiting the cell is lagging the corresponding rotation of the LC director.

To obtain a rough qualitative description of the observed pattern dynamics, we (a) disregard the  $K_{24}$ -term of elastic free energy, (b) adopt the one elastic constant approximation with  $K=K_{11}=K_{22}=K_{33}$ , (c) assume that the surface anchoring at LC-dMR interface is infinitely strong so that the first term in Eq. (8.1) can be disregarded, as well as (d) introduce the characteristic director relaxation time of director rotation in response to the change of an easy axis orientation



at the  $z=d$  LC-dMR interface,  $\tau = 2\gamma_1 / W_d(I, \varepsilon)$ , and the surface anchoring extrapolation length,  $\xi = K / W_d(I, \varepsilon)$ . Although our system is much more complex as compared to the case of pattern formation in a magnetic field, we observe in the experiments that the frequency characteristic of the Archimedean spiral pattern is roughly constant in time (Fig. 8.2). The analysis of Eqs. (8.5, 8.6) reveals that the orientation of the director at the output plane of a relatively thin cell is lagging the director by an angle  $\alpha$ . In analogy with Ref. [8], we can then write a simplified torque balance equation in the form:

$$\xi^2 \nabla^2 \alpha - \tau \frac{\partial \alpha}{\partial t} + \omega \tau - \sin(2\alpha) = 0 \quad (8.7)$$

For the lateral dimensions much larger than  $\xi$  and  $d$ , which is the case in our experiments (Fig. 8.2), one can re-write Eq. (8.7) as an equation for a traveling wave  $\alpha = \alpha(r - v_w t)$ , where  $v_w$  is the wave velocity:

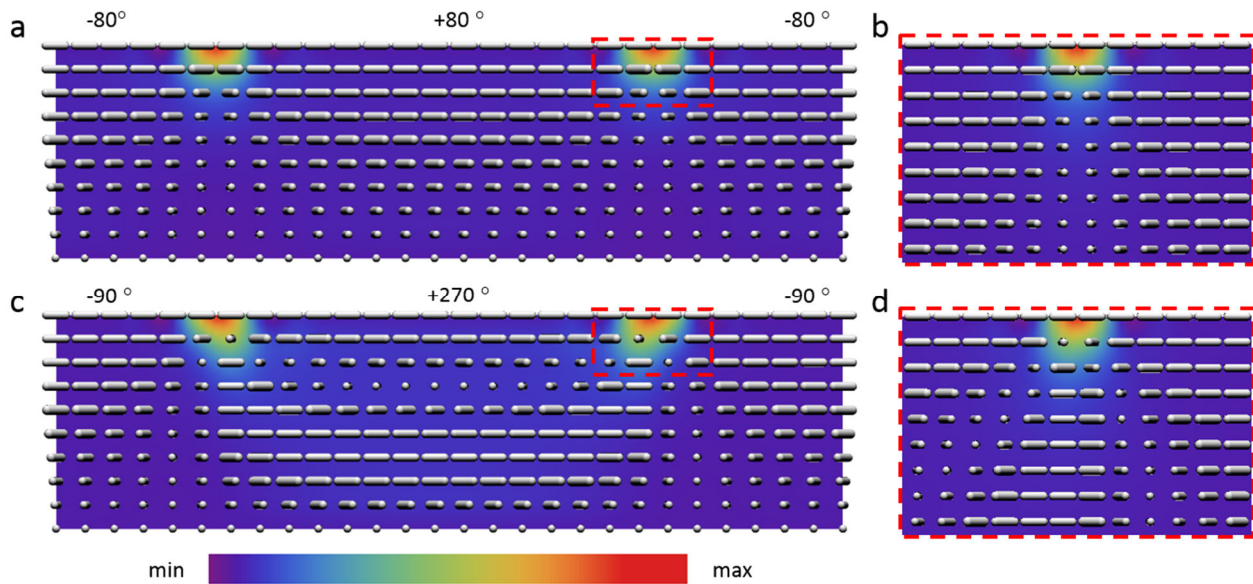
$$\xi^2 \frac{\partial^2 \alpha}{\partial r^2} + v_w \tau \frac{\partial \alpha}{\partial r} + \omega \tau - \sin(2\alpha) = 0 \quad (8.8)$$

Previous studies [8, 13, 30] showed that Eq. (8.8) contains stable propagating wave solutions that can describe Archimedes spiral dynamic patterns similar to the ones observed in our experiments (Figs. 8.2 and 8.3).

### 8.3.3 Wall structure in the pattern

The studied dynamic patterns contain domains with different directionality and different amounts of twist across the cell thickness. At the interface of the LC and light-controlled self-assembled monolayer, the director transitions between the different orientations in the neighboring domains

within a “wall” region of width which is expected to be comparable to the surface anchoring extrapolation length  $\xi = K / W_d(I, \varepsilon)$  [18]. The estimate of this width (Figs. 8.2 and 8.4) based on experimental images yields submicron or about one micron values, consistent with the ratio of an average elastic constant and azimuthal surface anchoring coefficient. To gain insights into the details of the inter-domain solitonic configurations, which are commonly referred to as Neel walls in analogy with magnetism [19], we have performed computer simulations of detailed director structures in the inter-domain regions. Since the domain width is 50-100 times larger than the cell thickness  $d$  and  $\xi$ , both  $\sim 1\mu\text{m}$  or smaller in the case of Archimedean spiral patterns, we focus on one inter-domain region between domains of different twist (Fig. 8.6) while neglecting its interaction with other domain walls. The field configurations are obtained by minimizing the elastic free energy using the so-called director relaxation method for set boundary conditions on confining substrates and far from the inter-domain region. The elastic free energy density plots, overlaid with the corresponding field configurations, reveal that the most energetically costly parts of the structure correspond to near-surface regions in-between the differently twisted domains (Fig. 8.6). Although the structure of the inter-domain walls is not necessarily close to that corresponding to the minimum elastic energy, as the structure of Archimedean spirals and other dynamic patterns never arrive to the equilibrium, these simulated field configurations provide insights into energetics involved in the pattern formation and also may well correspond to the static domain patterns such as the horizontal stripes shown in Fig. 8.5g.



**Fig. 8.6** Director structure of inter-domain regions. (a,b) Numerical modeling of field configurations and free energy density corresponding to the inter-domain regions with different direction of  $\pm 80^\circ$  twist, with (b) showing details of the structure within the region marked by a dashed rectangle in (a). (c,d) Numerical modeling of field configurations and free energy density corresponding to the inter-domain regions with different amount and direction of  $+270^\circ$  and  $-90^\circ$  twist, with (d) showing details of the structure within the region marked by a dashed rectangle in (a).

## 8.4 Discussion

Although pattern formation, including Archimedean-spiral-like patterns, due to laser beams in the experimental setting of LC Fabry-Perot interferometers is known [29], it commonly requires laser powers of the order of tens of milliwatts. A distinctive feature of our system is that even low-intensity ambient light can induce such pattern formation. Interestingly, in twisted nematic cells, the optical Fréedericksz threshold intensity for director realignment is typically orders of magnitude greater as compared to homeotropic LC cells, which is precisely due to the complex interplay between the polarization state of light propagating in the twisted birefringent LC, such as the linear polarization's Mauguin following of the director twist, and its coupling to the director field. However, in our surface-responsive system, this does not degrade the sensitivity

but rather provides a diverse set of feedback mechanisms responsible for the formation of a large variety of dynamic and static patterns.

The system can be maintained away from the equilibrium, resulting in the long-term dynamic patterns which only require low-intensity blue or ultraviolet light illumination to run for days and longer. This behavior is different from that of the chemical reaction diffusion systems, which slowly progress toward the thermodynamic equilibrium. Importantly, unlike the chemical systems exhibiting dynamic Archimedean spirals and other patterns, we can exquisitely control the speed of the propagating waves just by changing intensity of illumination light or by varying spectral composition of this light (e.g. using blue vs. ultraviolet, vs. red light). Despite the visual resemblance with the dynamic Archimedean spirals induced by the rotating magnetic field in Meyer's system, our patterns also show several key differences in their behavior: (1) the rates of counter-rotating spirals are the same in our patterns but different in Meyer's; (2) being induced in the bulk of homeotropic cells, Meyer's patterns exhibit dynamics of bulk while our solitons emerge at surfaces with dynamically controlled dMR layers; (3) In the very center of the spiral one expects having an umbilical defect in the Meyer's Archimedean spiral case, but we observe a boojum; (4) since the magnetic field in Meyer's Archimedes' breaks the counter clock wise vs. clock wise rotation symmetry, the stability and selected wavelengths of different dynamic Archimedean spirals in Meyer's case are not the same, unlike in our case, as light-induced patterns with different rotation directionality in our cells are kinetically and energetically indistinguishable; (5) our Archimedes spiral, unlike Meyer's, do not require dust particles or other inclusions to nucleate as imperfection in the spatial patterns of polarization state of the

illumination light can have the same effect, although physical imperfections can be responsible for this too.

## **8.5 Conclusion**

To conclude, we have developed a new light-driven dynamic pattern-forming soft matter system in which a strong nonlinear response due to an azobenzene-based alignment layer is combined with a feedback mechanism, through which the control of the polarization state by twisted birefringent LC structures, and vice versa, yields a large diversity of dynamic patterns, including propagating Archimedean spiral waves. Similar to the chaos theory, weak perturbations in the initial conditions of this system lead to dramatic changes in terms of the non-equilibrium dynamic behavior. Our light-driven pattern dynamics in LCs may provide an interesting model system of nonequilibrium biological phenomena, such as morphogenesis. Although our modeling qualitatively describes observations, more detailed mathematical models of these phenomena themselves will be of great theoretical interest and may provide insights into their analogies and differences with respect to Turing instability and other nonequilibrium theories. Finally, to the best of our knowledge, the described observations provide the only experimentally documented example where low-intensity-light-matter interaction can yield dynamic patterning in the matter itself and both in polarization and intensity of light interacting with it. From the practical applications viewpoint, our system may provide the means for generating dynamic patterns of time-varying polarization and dynamic optical vortices needed for singular optics uses.

## 8.6 References

1. J. Wesfreid, H. Brand, P. Monneville, G. Albinet N. Boccara, eds., *Propagation in Systems far from Equilibrium*, Springer, Berlin, 1988.
2. R.J. Field, M. Burger, eds., *Oscillations and Traveling Waves in Chemical Systems*, Wiley, New York, 1985.
3. F. X. Witkowski, L. J. Leon, P. A. Penkoske, W. R. Giles, M. L. Spano, W. L. Ditto, A. Winfree, *Nature* 1998, **392**, 78.
4. L. B. Smolka, B. Marts and A. L. Lin., *Phys. Rev. E* 2005, **72**, 056205.
5. J. Luengviriyaya, P. Porjai, M. Phantu, M. Sutthiopad, B. Tomapatanaget, S. C. Müller, C. Luengviriyaya, *Chem. Phys. Lett.* 2013, **588**, 267.
6. A.L. Belmonte, Q. Ouyang, J.-M. Flesselles, *Phys. II France* 1997, **7**, 1425.
7. N. Li, J. Delgado, H. O. Gonzalez-Ochoa, I. R. Epstein, S. Fraden, *Phys. Chem. Chem. Phys.* 2014, **16**, 10965.
8. K. B. Migler, R. B. Meyer, *Physica D* 1994, **71**, 412.
9. I. Janossy, K. Fodor-Csorba, A. Vajda, L. O. Palomares, *Appl. Phys. Lett.* 2011, **99**, 111103.
10. C. Zheng, R.B. Meyer, *Phys Rev E* 1997, **55**, 2882.
11. K. B. Migler, R. B. Meyer, *Phys. Rev. Lett.* 1991, **66**, 1485.
12. S. Nasuno, N. Yoshimo, S. Kai, *Phys. Rev. E* 1995, **51**, 1598.
13. T. Frisch, S. Rica, P. Couillet, J. M. Gilli, *Phys. Rev. Lett.* 1994, **72**, 1471.
14. J. Palacci, S. Sacanna, A. S. Steinberg, D. J. Pine, P. M. Chaikin, *Science* 2013, **339**, 936.
15. L. Giomi, M. J. Bowick, X. Ma, M. C. Marchetti, *Phys. Rev. Lett.* 2013, **110**, 228101.
16. T. Sanchez, D. T. N. Chen, S. J. DeCamp, M. Heymann, Z. Dogic, *Nature* 2012, **491**, 431.

17. Y. Zhang, N. Zhou, N. Li, M. Sun, D. Kim, S. Fraden, I. R. Epstein, B. Xu, *Chem. Soc.* 2014, **136**, 7341.
18. P. G. de Gennes, J. Prost. *The Physics of Liquid Crystals 2nd Ed*, Clarendon, Oxford, 1993.
19. P. M. Chaikin, T. C. Lubensky, *Principles of Condensed Matter Physics*, Cambridge Univ. Press, 2000.
20. A. Martinez, H. C. Mireles, I. I. Smalyukh, *Proc Natl Acad Sci USA* 2011, **108**, 20891.
21. I. I. Smalyukh, O. D. Lavrentovich, *Phys. Rev. Lett.* 2003, **90**, 085503.
22. N. Petit-Garrido, R. P. Trivedi, J. Ignés-Mullol, J. Claret, C. Lapointe, F. Sagués, I. I. Smalyukh, *Phys. Rev. Lett.* 2011, **107**, 177801.
23. N. Petit-Garrido, R. Trivedi, F. Sagués, J. Ignés-Mullol, I. I. Smalyukh, *Soft Matter* 2014, **10**, 8163.
24. P. J. Ackerman, Z. Qi, I. I. Smalyukh, *Phys. Rev. E* 2012, **86**, 021703.
25. A. Martinez, M. Ravnik, B. Lucero, R. Visvanathan, S. Žumer, I. I. Smalyukh, *Nature Materials* 2014, **13**, 258.
26. C. P. Lapointe, S. Hopkins, T. G. Mason, I. I. Smalyukh, *Phys. Rev. Lett.* 2010, **105**, 178301.
27. Q. Liu, Y. Yuan, I. I. Smalyukh, *Nano Lett.* **14**, 4071.
28. P. Yeh, C. Gu, *Optics of liquid crystal displays.*, Willey, New York, 1999.
29. P.-Y. Wang, W. Lu, D. Yu, R. G. Harrison, *Optics Comm.* 2001, **189**, 127.
30. M. Buttiker, R. Landauer, *Phys. Rev A* 1981, **23**, 1397.

## Chapter 9

### Conclusion

Throughout the thesis, my research demonstrated that the topology of soft condensed matter can be shaped by light, laying groundwork for experimental exploration of low-dimensional topology of fields and surfaces as well as for practical applications of topological relations in designing new forms of self-assembly. Among key outcomes of this work, we have demonstrated a unique approach for large-scale optical manipulation, both translational and rotational, of nano- and micro-sized objects that utilizes azobenzene-containing surface monolayers. We then showed that light can, not only allow for patterning of molecular orientation structures, but also induce rich and diverse topographical transformations of initially flat films composed of photoresponsive, azobenzene-functionalized liquid crystalline polymer networks, with the symmetry of the film's photoinduced response inherently coupled to the strength of the constituent defects within it. This demonstration of a ubiquitous approach to forming stimuli-responsive surface topographies based on topology of LC films may provide insight into self-assembly processes in nature and find practical uses in, for example, tactile displays. Extending this work, we demonstrated the feasibility of inducing monopole-like elastic distortions in NLCs by means of complex-shaped low-symmetry particles attached to the confining solid substrates of a liquid crystal cell and oriented differently from what would be their equilibrium orientation in the NLC bulk. Building on the advances in photopolymerization techniques, we realized a



colloidal system of particle-knots coupled to nematic fields, providing insights into the interplay of their topologies. This interplay was examined using knotted colloids of varying complexity and with varying surface boundary conditions which prompted the formation of point-like and knotted defect loops linked with the particles themselves. We have also developed a new class of topological colloids with multiple linked components demonstrating that, when dispersed in nematic host fluids, the linked colloidal building blocks induce field-defect configurations that can be topologically distinct from each other but always satisfy the topological constraints imposed by mathematical theorems. Realization of knotted configurations of reduced graphene oxide ribbons, realized through multi-photon-absorption-initiated processes in lyotropic LCs, demonstrates the capability of pre-engineered functionality in topologically complex structures and may lead to new methods of fabricating nanostructured colloids.

This work opens new avenues for exploiting soft matter topology in basic and applied science. Combining the two-photon photo-polymerization system with holographic shaping of femtosecond laser light via spatial light modulators, one can achieve large numbers complex colloids, paving a way towards an incomparable topological matter made of self-assembled knots and links, with the functionality potentially engineered through the uses of particles such as the ones based on reduced graphene oxide. Further, particle-induced defects can mediate the generation of free-energy landscapes for nanoparticle entrapment, which may provide a means for achieving the hierarchical self-assembly of new topological composite materials. Therefore, by establishing general principles for the 3D control of defects and fields, these unusual yet practically useful forms of self-assembly may find applications ranging from a new breed of information displays to metamaterials, nanophotonics and data storage.

## Bibliography

1. W. F. Brinkman, P. E. Cladis, *Physics Today*. 1982, **35**, 48.
2. M. Kleman, O. D. Lavrentovich, *Philosophical Magazine*. 2006, **86**, 4117.
3. G. S. Ranganath, *Current Science*. 1990, **59**, 1106.
4. T. W. Kibble, *J. Phys. A: Math. Gen.* 1976, **9**, 1387.
5. T. W. Kibble, *Phys. Rep.* 1980, **67**, 183.
6. W. H. Zurek, *Phys. Rep.* 1996, **276**, 177.
7. V. M. Pergamenschchik, V. A. Uzunova, *Condensed Matter Physics*. 2010, **13**, 33602-1.
8. I. Mušević, *Liquid Crystals*. 2014, **3**, 418.
9. Q. Liu, Y. Cui, D. Gardner, X. Li, S. He, I. I. Smalyukh, *Nano Letters*. 2010, **10**, 1347.
10. J. F. Joanny, *Science*. 1997, **275**, 1751.
11. C. P. Lapointe, *et al.*, *Science*. 2009, **326**, 1083.
12. C. D. Modes, M. Warner, *Phys. Rev. E*. 2011, **84**, 021711/1.
13. C. D. Modes, K. Bhattacharya, M. Warner, *Phys. Rev. E*. 2010, **81**, 060701.
14. C. D. Modes, M. Warner, C. Sanchez-Somolinos, L. T. de Haan, D. Broer, *Phys. Rev. E*. 2013, **86**, 060701/1.
15. C. D. Modes, M. Warner, *Europhys. Lett.* 2012, **97**, 36007/P1.
16. C. D. Modes, M. Warner, *Proc. SPIE*. 2012, **8279**, 82790Q/1.
17. A. Martinez, H. C. Mireles, I. I. Smalyukh, *Proc. Natl. Acad. Sci.* 2011, **108**, 20891.
18. M. E. McConney, A. Martinez, V. P. Tondiglia, K. M. Lee, D. Langley, I. I. Smalyukh, T. J. White, *Adv. Mater.* 2013, **25**, 5880.
19. A. Martinez, T. Lee, T. Asavei, H. Rubinsztein-Dunlop, I. I. Smalyukh, *Soft Matter* 2012, **8**, 2432.

20. A. Martinez, M. Ravnik, B. Lucero, R. Visvanathan, S. Žumer, I. I. Smalyukh, *Nat. Mater.* 2014, **13**, 258.
21. A. Martinez, L. Hermosillo, M. Tasinkevych, I. I. Smalyukh, (2014). *Linked topological colloids in a nematic host*. Manuscript submitted for publication.
22. B. Senyuk, N. Behabtu, A. Martinez, T. Lee, D. E. Tsentalovich, G. Ceriotti, J. M. Tour, M. Pasquali, I. I. Smalyukh, (2014). *Three-dimensional patterning of solid reduced graphene oxide microstructures through precise laser reduction of aqueous liquid crystalline dispersions of graphene oxide flakes*. Manuscript submitted for publication.
23. P. M. Chaikin, T. C. Lubensky, *Principles of Condensed Matter Physics*, Cambridge University Press, Cambridge, UK, 1995.
24. P. Poulin, S. Holger, T. C. Lubensky, D. A. Weitz, *Science* 1997, **275**, 1770.
25. I. Muševič, M. Skarabot, U. Tkalec, M. Ravnik, S. Žumer, *Science* 2006 **313**, 954.
26. I. I. Smalyukh, A. V. Kachynski, A. N. Kuzmin, P. N. Prasad, *Proc Natl Acad Sci USA* 2006, **103**, 18048.
27. T. C. Lubensky, D. Pettey, N. Currier, H. Stark, *Phys Rev E* 1998, **57**, 610.
28. L. Ramos, M. Zapotocky, T. C. Lubensky, D. A. Weitz, *Phys Rev E* 2002, **66**, 031711.
29. M. Ravnik, G. P. Alexander, J. M. Yeomans, S. Žumer, *Faraday Discuss* 2010, **144**, 159.
30. T. Yamamoto, H. Yokoyama, Y. Tabe, *Mol Cryst Liq Cryst* 2007, **478**, 967.
31. J. C. Loudet, P. Barois, P. Poulin, *Nature* 2000, **407**, 611.
32. M. Zapotocky, L. Ramos, P. Poulin, T. C. Lubensky, D. A. Weitz, *Science* 1999, **283**, 209.
33. O. P. Pishnyak, S. Tang, J. R. Kelly, S. V. Shiyankovskii, O. D. Lavrentovich, *Phys Rev Lett* 2007, **99**, 127802.
34. G. M. Koenig, I. H. Lin, N. L. Abbott, *Proc Natl Acad Sci USA* 2010, **107**, 3998.

35. V. M. Shalaev, *Nat Photonics* 2007, **1**, 41.
36. V. G. Veselago, *Sov Phys Uspekhi* 1968, **10**, 509.
37. J. B. Pendry, *Phys Rev Lett* 2000, **85**, 3966.
38. C. M. Soukoulis, S. Linden, M. Wegener, *Science* 2007, **315**, 47.
39. J. Valentine, *et al.*, *Nature* 2008, **455**, 376.
40. D. F. Gardner, J. S. Evans, I. I. Smalyukh, *Mol Cryst Liq Cryst* 2011, **545**, 1227.
41. A. Ashkin, J. M. Dziedzic, J. M. Bjorkholm, S. Chu, *Opt Lett* 1983, **11**, 288.
42. D. G. Grier, *Nature* 2003, **424**, 21.
43. P. Y. Chiou, A. T. Ohta, M. C. Wu, *Nature* 2005, **436**, 370.
44. R. Eelkema, *et al.*, *Nature* 2006, **440**, 163.
45. A. Jamshidi, *et al.*, *Nat Photonics* 2008, **2**, 85.
46. R. C. Hayward, D. A. Saville, I. A. Aksay, *Nature* 2000, **404**, 56.
47. Y. Iwashita, H. Tanaka, *Phys Rev Lett* 2003, **90**, 045501.
48. V. G. Shvedov, *et al.*, *Phys Rev Lett* 2010, **105**, 118103.
49. A. N. Grigorenko, N. W. Roberts, M. R. Dickinson, Y. Zhang, *Nat Photonics* 2008, **2**, 365.
50. R. P. Trivedi, D. Engström, I. I. Smalyukh, *J Opt* 2011, **13**, 044001.
51. M. Schadt, H. Seiberle, A. Schuster, *Nature* 1996, **381**, 212.
52. S. J. Woltman, D. G. Jay, G. P. Crawford, *Nat Mater* 2007, **6**, 929.
53. C. L. van Oosten, C. W. M. Baastiansen, D. J. Broer, *Nat Mater* 2009, **8**, 677.
54. K. Ichimura, *Chem Rev* 2000, **100**, 1847.
55. W. M. Gibbons, P. J. Shannon, S-T. Sun, B. J. Swetlin, *Nature* 1991, **351**, 49.
56. J. Niitsuma, M. Yoneya, H. Yokoyama, *Liq Cryst* 2010, **37**, 31.
57. P. G. de Gennes, J. Prost, *The Physics of Liquid Crystals*, Clarendon Press, 1995.

58. V. M. V. Pergamenschchik, V. A. Uzunova, *Phys Rev E* 2009, **79**, 021704.
59. C. Lapointe, et al., *Science* 2004, **303**, 652.
60. V. J. Anderson, H. N. Lekkerkerker, *Nature* 2002, **416**, 811.
61. I. I. Smalyukh, Y. Lansac, N. Clark, R. Trivedi, *Nat Mater* 2010, **9**, 139.
62. J. Leach, M. R. Dennis, J. Courtial, M. J. Padgett, *Nature* 2004, **432**, 165.
63. Y. Yi, M. J. Farrow, E. Korblova, D. M. Walba, T. E. Furtak, *Langmuir* 2009, **25**, 997.
64. S. Murata, H. Kurokawa, *IEEE Robot. Autom. Mag.* 2007, **14**, 71.
65. A. D. Rey, *Soft Matter* 2010, **6**, 3402.
66. Y. Bouligand, *C.R. Chim.* 2008, **11**, 281.
67. S. C. Cowin, *J. Non-Newton. Fluid* 2004, **119**, 155.
68. D. P. Knight, F. Vollrath, *Philos. T. R. Soc. B* 2002, **357**, 155.
69. M. E. McConney, T. J. White, V. P. apg, L. V. Natarajan, D.-k. Yang, T. J. Bunning, *Soft Matter* 2012, **8**, 318.
70. K. Urayama, Y. Okuno, T. Kawamura, S. Kohjiya, *Macromolecules* 2002, **35**, 4567.
71. K. D. Harris, R. Cuyper, P. Scheibe, C. L. van Oosten, C. W. M. Bastiaansen, J. Lub, D. J. Broer, *J. Mater. Chem.* 2005, **15**, 5043.
72. C. L. van Oosten, K. D. Harris, C. W. M. Bastiaansen, D. J. Broer, *Eur. Phys. J. E* 2007, **23**, 329.
73. Y. Yu, M. Nakano, T. Ikeda, *Nature* 2003, **425**, 145.
74. M. Yamada, M. Kondo, J.-i. Mamiya, Y. Yu, M. Kinoshita, C. J. Barrett, T. Ikeda, *Angew. Chem. Int. Edit.* 2008, **47**, 4986.
75. M. Yamada, M. Kondo, R. Miyasato, Y. Naka, J.-i. Mamiya, M. Kinoshita, A. Shishido, Y. Yu, C. J. Barrett, T. Ikeda, *J. Mater. Chem.* 2009, **19**, 60.

76. T. J. White, N. Tabiryan, V. P. Tondiglia, S. Serak, U. Hrozhyk, R. A. Vaia, T. J. Bunning, *Soft Matter* 2008, **4**, 1796.
77. T. J. White, S. V. Serak, N. V. Tabiryan, R. A. Vaia, T. J. Bunning, *J. Mater. Chem.* 2009, **19**, 1080.
78. S. Serak, N. Tabiryan, T. J. White, R. A. Vaia, T. J. Bunning, *Soft Matter* 2010, **6**, 779.
79. K. M. Lee, M. L. Smith, H. Koerner, N. Tabiryan, R. A. Vaia, T. J. Bunning, T. J. White, *Adv. Funct. Mater.* 2011, **15**, 2913.
80. K. M. Lee, H. Koerner, R. A. Vaia, T. J. Bunning, T. J. White, *Soft Matter* 2011, **7**, 4318.
81. K. M. Lee, T. J. Bunning, T. J. White, *Adv. Mater.* 2012, **24**, 2839.
82. T. J. White, *J. Polym. Sci. Polym. Phys.* 2012, **50**, 877.
83. K. M. Lee, H. Koerner, D. H. Wang, L.-S. Tan, T. J. White, R. A. Vaia, *Macromolecules* 2012, **45**, 7527.
84. Y. Sawa, F. Ye, K. Urayama, T. Takigawa, V. Gimenez-Pinto, R. L. B. Selinger, J. V. Selinger, *P. Natl. Acad. Sci. USA* 2011, **108**, 6364.
85. M. Kléman, *Rep. Prog. Phys.* 1989, **52**, 555.
86. N. D. Mermin, *Rev. Mod. Phys.* 1979, **51**, 591.
87. G. Toulouse, M. Kléman, *J. Phys. Lett.-Paris* 1976, **37**, 149.
88. M. Kléman, L. Michel, G. Toulouse, *J. Phys. Lett.-Paris* 1977, **38**, 195.
89. O. D. Lavrentovich, V. M. Pergamenschik, *Int. J. Mod. Phys. B* 1995, **09**, 2389.
90. F. C. Frank, *Discuss. Faraday Soc.* 1958, **25**, 19.
91. S. Nersisyan, N. Tabiryan, D. M. Steeves, B. R. Kimball, *Opt. Express* 2009, **17**, 11926.
92. L. T. de Haan, C. Sánchez-Somolinos, C. M. W. Bastiaansen, A. P. H. J. Schenning, D. J. Broer, *Angew. Chem., Int. Edit.* 2012, **51**, 12469.

93. S. Nersisyan, N. Tabiryan, D. M. Steeves, B. R. Kimball, *J. Appl. Phys.* 2010, **108**, 033101.
94. A. Y. G. Fuh, S.-W. Ko, S.-H. Huang, Y.-Y. Chen, T.-H. Lin, *Opt. Express* 2011, **19**, 2294.
95. K. M. Lee, N. V. Tabiryan, T. J. Bunning, T. J. White, *J. Mater. Chem.* 2012, **22**, 691.
96. P. Poulin, H. Stark, T. C. Lubensky and D. A. Weitz, *Science*, 1997, **275**, 1170.
97. U. Tkalec, M. Škarabot and I. Mušević, *Soft Matter*, 2008, **4**, 2402.
98. F. Brochard and P. G. de Gennes, *J. Phys. (Paris)*, 1970, **31**, 691.
99. B. I. Lev, S. B. Chernyshuk, P. M. Tomchuk and H. Yokoyama, *Phys. Rev. E: Stat., Nonlinear, Soft Matter Phys.*, 2002, **65**, 021709.
100. I. Dierking, G. Biddulph and K. Matthews, *Phys. Rev. E: Stat., Nonlinear, Soft Matter Phys.*, 2006, **73**, 011702.
101. V. M. Pergamenschchik and V. A. Uzunova, *Phys. Rev. E: Stat., Nonlinear, Soft Matter Phys.*, 2011, **83**, 021701.
102. M. Škarabot and I. Mušević, *Soft Matter*, 2010, **6**, 5476.
103. D. Engström, R. P. Trivedi, M. Persson, K. A. Bertness, M. Goksör and I. I. Smalyukh, *Soft Matter*, 2011, **7**, 6304.
104. J. S. Evans, C. Beier and I. I. Smalyukh, *J. Appl. Phys.*, 2011, **110**, 033535.
105. I. I. Smalyukh, J. Butler, J. D. Shrout, M. R. Parsek and G. C. L. Wong, *Phys. Rev. E: Stat., Nonlinear, Soft Matter Phys.*, 2008, **78**, 030701(R).
106. P. G. de Gennes, *Physics of Liquid Crystals*, Oxford University Press, London, 1st edn, 1974.
107. V. M. Pergamenschchik and V. A. Uzunova, *Phys. Rev. E: Stat., Nonlinear, Soft Matter Phys.*, 2007, **76**, 011707.

108. B. I. Lev and P. M. Tomchuk, *Phys. Rev. E: Stat. Phys., Plasmas, Fluids, Relat. Interdiscip. Top.*, 1999, **59**, 591.
109. J.-I. Fukuda, B. I. Lev and H. Yokoyama, *J. Phys.: Condens. Matter*, 2003, **15**, 3841.
110. J. B. Fournier, *Eur. J. Phys.*, 1993, **14**, 184.
111. K. Robbie, D. J. Broer and M. J. Brett, *Nature*, 1999, **399**, 764.
112. T. Lee, R. P. Trivedi and I. I. Smalyukh, *Opt. Lett.*, 2010, **35**, 3447.
113. R. P. Trivedi, T. Lee, K. A. Bertness and I. I. Smalyukh, *Opt. Express*, 2010, **18**, 27658.
114. H. Stark and D. Venzki, *Phys. Rev. E: Stat., Nonlinear, Soft Matter Phys.*, 2001, **64**, 031711.
115. I. Newton, *Philosophiæ Naturalis Principia Mathematica*, 1687.
116. J. Hermann, *Phoronomia, sive De viribus et motibus corpum solidorum et fluidorum libri duo*, 1716.
117. B. Senyuk, *et al.*, *Nano Lett.* 2012, **12**, 955.
118. G. P. Alexander, B. G. Chen, E. A. Matsumoto, R. D. Kamien, *Rev. Mod. Phys.* 2012, **84**, 497.
119. U. Tkalec, M. Ravnik, S. Čopar, S. Žumer, I. Muševič, *Science* 2011, **333**, 62.
120. C. Livingston, *Knot Theory*, The Mathematical Association of America, Indiana University-Bloomington, 1993.
121. L. H. Kauffman, *Knots and Physics 3rd edn*, World Scientific, 2000.
122. M. R. Dennis, R. P. King, B. Jack, K. O'Holleran, M. J. Padgett, *Nature Phys.* 2010, **6**, 118.
123. D. M. Kleckner, W. T. Irvine, *Nature Phys.* 2013, **9**, 253.
124. D. Yi-Shi, Z. Li, Z. Xin-Hui, *Commun. Theor. Phys.* 2007, **47**, 1129.



125. L. Faddeev, A. J. Niemi, *Nature* 1997, **387**, 58.
126. Y. Bouligand, B. Derrida, V. Poenaru, Y. Pomeau, G. Toulouse, *J. Physique* 1978, **39**, 863.
127. W. Thomson, *Phil. Mag.* 1867, **34**, 15.
128. I. Chuang, R. Durrer, N. Turok, B. Yurke, *Science* 1991, **251**, 1336.
129. M. J. Bowick, L. Chandar, E. A. Schiff, A. M. Srivastava, *Science* 1994, **263**, 943.
130. A. M. Alsayed, M. F. Islam, J. Zhang, P. L. Collings, A. G. Yodh, *Science* 2005, **309**, 1207.
131. D. R. Nelson, *Nano Lett.* 2002, **2**, 1125.
132. T. A. Wood, J. S. Lintuvuori, A. B. Schofield, D. Marenduzzo, W. C. K. Poon, *Science* 2011, **334**, 79.
133. M. Ravnik, S. Žumer, *Liq. Cryst.* 2009, **36**, 1201.
134. B. Senyuk, *et al.*, *Nature* 2013, **493**, 200.
135. Y. Wang, *et al.*, *Nature* 2012, **491**, 51.
136. M. C. Marchetti, *et al.*, *Rev. Mod. Phys.* 2013, **85**, 1143.
137. T. Lee, R. P. Trivedi, I. I. Smalyukh, *Opt. Lett.* 2010 **35**, 3447.
138. S. Čopar, S. Žumer, *Phys. Rev. Lett.* 2011, **106**, 177801.
139. R. V. Buniy, T. Kephart, *Int. J. Mod. Phys. A* 2005, **20**, 1252.
140. W. T. M. Irvine, D. Bouwmeester, *Nature Phys* 2008, **4**, 716.
141. C. D. Pentecost, K. S. Chichak, A. J. Peters, G. W. V. Cave, S. J. Cantrill, J. F. Stoddart, *Angew Chem Int Ed* 2007, **46**, 218.
142. N. Hadjichristidis, A. Hirao, Y. Tezuka, E. Du Prez, Eds, *Complex Macromolecular Architectures*, Wiley, Singapore, 2011.

143. D. M. Kleckner, W. T. M. Irvine, *Nature Phys* 2013, **9**, 253.
144. H. Hopf, *Mathematische Annalen* 1931, **34**, 637.
145. J. H. C. Whitehead, *Proc Natl Acad Sci USA* 1947, **33**, 117.
146. A. F. Ronada, J. L. Trueba, *Nature* 1996, **383**, 32.
147. A. F. Ronada, J. L. Trueba, *Phys Lett A* 1995, **202**, 337.
148. Y. Kawaguchi, M. Nitta, M. Ueda, *Phys Rev Lett* 2008, **100**, 180403.
149. Y-K. Liu, C. Zhang, S-J. Yang, *Phys Lett A* 2013, **377**, 3300.
150. N. R. Cooper, *Phys Rev Lett* 1999, **82**, 1554.
151. P. Sutcliffe, *Phys Rev B* 2007, **76**, 184439.
152. A. B. Borisov, F. N. Rybakov, *JETP Letters* 2009, **90**, 544.
153. J. B. Fournier, P. Galatola, *Europhys Lett* 2005, **72**, 403.
154. M. Tasinkevych, N. M. Silvestre, M. M. Telo da Gama, *New J Phys* 2012, **14**, 073030.
155. Q. Liu, B. Senyuk, M. Tasinkevych, I. I. Smalyukh, *Proc Natl Acad Sci USA* 2013, **110**, 9231.
156. J. Cantarella, R. B. Kusner, J. M. Sullivan, *Inventiones Mathematicae* 2002, **150**, 257.
157. G. Eda, G. Fanchini, M. Chhowalla, *Nat. Nanotechnol.* 2008, **3**, 270.
158. F. Bonaccorso, Z. Sun, T. Hasan, A. C. Ferrari, *Nat. Photonics* 2010, **4**, 611.
159. S. Pang, Y. Hernandez, X. Feng, K. Müllen, *Adv. Mater.* 2011, **23**, 2779.
160. V. Yong, J. M Tour, *Small* 2009, **6**, 313.
161. F. Li, M. Xue, X. Ma, M. Zhang, T. Cao, *Anal. Chem.* 2011, **83**, 6426.
162. V. Strong, *et al.*, *ACS Nano* 2012, **6**, 1495.
163. R. Mukherjee, A. V. Thomas, A. Krishnamurthy, N. Koraktar, *ACS Nano* 2012, **6**, 7867.
164. H. Li, Ch. Bubeck, *Macromol. Res.* 2013, **21**, 290.

165. M. Segal, *Nat. Nanotechnol.* 2009, **4**, 612.
166. S. Pei, H-M. Cheng, *Carbon* 2012, **50**, 3210.
167. Y. Zhang, *et al.*, *Nano Today* 2010, **5**, 15.
168. C. Petridis, *et al.*, *Appl. Phys. Lett.* 2013, **102**, 093115.
169. L. Huang, *et al.*, *Carbon* 2011, **49**, 2431.
170. E. Orabona, *et al.*, *Opt. Lett.* 2014, **39**, 4263.
171. Y. Tanizawa, *et al.*, *J. Phys.: Conf. Ser.* 2012, **352**, 012011.
172. J.-Y. Hong, J. Jang, *J. Mater. Chem.* 2012, **22**, 8179.
173. D. A. Sokolov, K. R. Shepperd, T. M. Orlando, *J. Phys. Chem. Lett.* 2012, **1**, 2633.
174. W. Gao, *et al.*, *Nat. Nanotechnol.* 2011, **6**, 496.
175. H. F. Teoh, Y. Tao, E. S. Tok, G. W. Ho, C. H. Sow, *J. Appl. Phys.* 2012, **112**, 064309.
176. M. F. El-Kady, V. Strong, S. Dubin, R. B. Kaner, *Science* 2012, **335**, 1326.
177. R. Trusovas, *et al.*, *Carbon* 2013, **52**, 574.
178. X. Li, Q. Zhang, X. Chen, M. Gu, *Sci. Rep.* 2013, **3**, 2891.
179. V. Abdelsayed, *et al.*, *J. Phys. Chem. Lett.* 2010, **1**, 2804.
180. C. W. Chang, M. H. Hon, I. C. Leu, *J. Electrochem. Soc.* 2012, **159**, H605.
181. Q. Zhuo, *et al.*, *Carbon* 2013, **52**, 559.
182. R. Y. N. Gengler, *et al.*, *Nat. Commun.* 2013, **4**, 2560.
183. D. C. Marcano, *et al.*, *ACS Nano* 2010, **4**, 4806.
184. B. Senyuk, *et al.*, *ACS Nano* 2012, **6**, 8060.
185. J. E. Kim, *et al.*, *Angew. Chem., Int. Ed.* 2011, **50**, 3043.
186. B. Dan, *et al.*, *Soft Matter* 2011, **7**, 11154.
187. T.-Z. Shen, S.-H. Hong, J.-K. Song, *Nat. Mater.* 2014, **13**, 394.

188. R. F. Gattass, E. Mazur, *Nat. Photonics* 2008, **2**, 219.
189. C. H. Lui, K. F. Mak, J. Shan, T. F. Heinz, *Phys. Rev. Lett.* 2010, **105**, 127404.
190. J. Wesfreid, H. Brand, P. Monneville, G. Albinet N. Boccara, eds., *Propagation in Systems far from Equilibrium*, Springer, Berlin, 1988.
191. R.J. Field, M. Burger, eds., *Oscillations and Traveling Waves in Chemical Systems*, Wiley, New York, 1985.
192. F. X. Witkowski, L. J. Leon, P. A. Penkoske, W. R. Giles, M. L. Spano, W. L. Ditto, A. Winfree, *Nature* 1998, **392**, 78.
193. L. B. Smolka, B. Marts and A. L. Lin., *Phys. Rev. E* 2005, **72**, 056205.
194. J. Luengviriyaya, P. Porjai, M. Phantu, M. Sutthiopad, B. Tomapatnanaget, S. C. Müller, C. Luengviriyaya, *Chem. Phys. Lett.* 2013, **588**, 267.
195. A.L. Belmonte, Q. Ouyang, J.-M. Flesselles, *Phys. II France* 1997, **7**, 1425.
196. N. Li, J. Delgado, H. O. Gonzalez-Ochoa, I. R. Epstein, S. Fraden, *Phys. Chem. Chem. Phys.* 2014, **16**, 10965.
197. K. B. Migler, R. B. Meyer, *Physica D* 1994, **71**, 412.
198. I. Janossy, K. Fodor-Csorba, A. Vajda, L. O. Palomares, *Appl. Phys. Lett.* 2011, **99**, 111103.
199. C. Zheng, R.B. Meyer, *Phys Rev E* 1997, **55**, 2882.
200. K. B. Migler, R. B. Meyer, *Phys. Rev. Lett.* 1991, **66**, 1485.
201. S. Nasuno, N. Yoshimo, S. Kai, *Phys. Rev. E* 1995, **51**, 1598.
202. T. Frisch, S. Rica, P. Couillet, J. M. Gilli, *Phys. Rev. Lett.* 1994, **72**, 1471.
203. J. Palacci, S. Sacanna, A. S. Steinberg, D. J. Pine, P. M. Chaikin, *Science* 2013, **339**, 936.

204. L. Giomi, M. J. Bowick, X. Ma, M. C. Marchetti, *Phys. Rev. Lett.* 2013, **110**, 228101.
205. T. Sanchez, D. T. N. Chen, S. J. DeCamp, M. Heymann, Z. Dogic, *Nature* 2012, **491**, 431.
206. Y. Zhang, N. Zhou, N. Li, M. Sun, D. Kim, S. Fraden, I. R. Epstein, B. Xu, *Chem. Soc.* 2014, **136**, 7341.
207. I. I. Smalyukh, O. D. Lavrentovich, *Phys. Rev. Lett.* 2003, **90**, 085503.
208. N. Petit-Garrido, R. P. Trivedi, J. Ignés-Mullol, J. Claret, C. Lapointe, F. Sagués, I. I. Smalyukh, *Phys. Rev. Lett.* 2011, **107**, 177801.
209. N. Petit-Garrido, R. Trivedi, F. Sagués, J. Ignés-Mullol, I. I. Smalyukh, *Soft Matter* 2014, **10**, 8163.
210. P. J. Ackerman, Z. Qi, I. I. Smalyukh, *Phys. Rev. E* 2012, **86**, 021703.
211. C. P. Lapointe, S. Hopkins, T. G. Mason, I. I. Smalyukh, *Phys. Rev. Lett.* 2010, **105**, 178301.
212. Q. Liu, Y. Yuan, I. I. Smalyukh, *Nano Lett.* **14**, 4071.
213. P. Yeh, C. Gu, *Optics of liquid crystal displays.*, Willey, New York, 1999.
214. P.-Y. Wang, W. Lu, D. Yu, R. G. Harrison, *Optics Comm.* 2001, **189**, 127.
215. M. Buttiker, R. Landauer, *Phys. Rev A* 1981, **23**, 1397.

# Appendix A

## Details of system and characterization of optoelastic manipulation

### A.1 Details of sample preparation

#### A.1.1 Preparation of dMR monolayers on glass substrates.

Thorough cleaning of glass plates is essential from the standpoint of obtaining uniform responsive dMR monolayers. For this, the glass plates are first cleaned by scrubbing the glass surface using a soft brush and detergent to wash away oils and remove large particles. The glass is then rinsed with deionized water and dried with compressed nitrogen gas. We then sonicate the substrate sequentially in acetone, isopropanol, and deionized water (five minutes each). We then dry the substrates again using compressed nitrogen gas. Plasma cleaning is then performed in a vacuum chamber with the plasma discharge at a pressure of  $\sim 1$  mTorr, voltage of 3 kV, and a 50 mA current. The glass substrates are exposed to the plasma for about 20 min, which allows for a complete removal of the residual organic surface contaminants. To obtain the photosensitive surface monolayer on the glass plates, we submerge them into a  $\sim 1$ wt.% solution of 2-(4-dimethylamino-phenylazo)-N-(3-triethoxysilane-propyl)-benzamide (dMR) [1] in toluene at elevated temperature of  $45^\circ\text{C}$  for 90 min to facilitate surface bonding of the dMR molecules (Fig. A.1). This is followed by a toluene rinse to wash away the excess dMR, blowing with dry

nitrogen, and curing at 115°C for 2 hours. These dMR-decorated glass substrates are then used for preparation of cells as described in the methods section of the main text.

### **A.1.2 Colloidal particles.**

The used melamine resin particles were obtained from Invitrogen in the form of an aqueous dispersion. Silver nanorods (nanowires) of 100 nm in diameter were obtained from Nanogap. Glass microrods of 3  $\mu\text{m}$  in diameter were obtained from Duke Scientific Corp. Silica microspheres were obtained in a powder form from Fluka. Gallium Nitride (GaN) nanorods were provided by Kris Bertness from NIST (Boulder) and were about 10  $\mu\text{m}$  in length and a hexagonal cross-section with  $\sim 150$  nm edge sides.[2,3] The GaN nanorods are first dispersed in isopropanol and then transferred into the LC by mixing and letting isopropanol evaporate by heating the mixture to about 60° C.[4]

## **A.2 Laser scanning system integrated with holographic optical tweezers**

For illumination by laser beam scanning, we use an Ar laser beam at 488 nm and scanned mirrors of the confocal imaging system FV-300 from Olympus integrated with holographic optical tweezers (HOT). This integrated setup is built around an inverted IX81 optical microscope from Olympus and is schematically shown in Appendix Fig. A.2. In the HOT part of the setup, the beam from an Ytterbium-doped fiber laser (1064 nm, IPG Photonics) is linearly polarized before it is expanded by a telescope [lenses  $L_1$  (100 mm) and  $L_2$  (250 mm)] to overfill the active area of the phase-only spatial light modulator (SLM, from Boulder Nonlinear Systems). A second telescope composed of lenses  $L_3$  (850 mm) and  $L_4$  (400 mm) reduces the size of the beam reflected off the SLM to slightly overfill the back aperture of the oil-immersion

microscope objective. The second telescope (in the so-called 4-f arrangement) also images the phase profile encoded by the SLM to the back focal plane of the microscope objective. The holograms displayed on the SLM create trap patterns in the focal plane of the microscope objective. A dichroic mirror (from Chroma) is used to reflect the trapping laser beam into the microscope objective. By displaying holograms on the SLM, the phase of the reflected light is controlled between 0 and  $2\pi$  on a pixel-by-pixel basis. The SLM has  $512 \times 512$  pixels, each of size  $15 \times 15 \mu\text{m}^2$ . New holograms can be generated on the SLM at a rate of 10-30 Hz. The positions of the traps are defined by the calculated holograms and controlled by the HOT software (Arryx, Inc.). Bright-field imaging with visible light is performed using a charge-coupled device (CCD) camera (Pointgrey, Flea 2, IEEE 1394b).

### **A.3 Free energy of director structures in cells with light-controlled boundary conditions**

The behavior of LC domains in response to the changes of surface boundary conditions as well as the manipulation of colloids dispersed in the nematic LC can be understood by considering the bulk elastic energy for the light-dictated surface boundary conditions controlled through the dMR surface monolayers. The Frank elastic energy of LCs can be expressed in terms of spatial gradients of the director field  $\mathbf{N}(\mathbf{r})$  as follows [5, 6]:

$$\int d^3\mathbf{r} \left[ \frac{K_{11}}{2} (\nabla \cdot \mathbf{N})^2 + \frac{K_{22}}{2} (\mathbf{N} \cdot (\nabla \times \mathbf{N}))^2 + \frac{K_{33}}{2} (\mathbf{N} \times (\nabla \times \mathbf{N}))^2 \right]$$

where  $K_{11}$ ,  $K_{22}$ , and  $K_{33}$  are three independent Frank elastic constants corresponding to “splay”, “twist”, and “bend” deformations, respectively, and the integration is carried out over the volume of the LC confined in the cell. Typically, the three elastic constants of thermotropic small



molecule nematic materials are of the same order of magnitude. Therefore, one often introduces the so-called one-elastic-constant approximation  $K = (K_{11} + K_{22} + K_{33})/3$ . For 5CB at room temperature  $K_{11} \approx 6.4$  pN,  $K_{22} \approx 3$  pN,  $K_{33} \approx 10$  pN and  $K \approx 6.5$  pN. We use analytical estimates of elastic energies involved in the optoelastic manipulation, as discussed in the main text, as well as numerical minimization of  $U_{el}$  (without the one-constant approximation) in order to obtain the static equilibrium and metastable director configurations in confined LC cells with light controlled boundary conditions (Fig. 2.5B and Fig. A.3H,I). This numerical minimization of  $U_{el}$  is implemented by use of Mathematica 8 software (obtained from Wolfram) with the assumption of infinitely strong surface anchoring boundary conditions.

#### **A.4 Effects of gravity**

In the LC cell with a uniform far-field director, elastic forces balance the gravitational force acting on a colloidal particle such as an elastic dipole formed by a sphere with vertical boundary conditions (Fig. 2.2F). These elastic forces repel the particle from the bounding plates with strong surface boundary conditions, so that the particle tends to localize in the LC cell midplane at vertical position  $z = h/2$  ( $h$  is the LC cell thickness), although gravity can displace it downward from this plane. This balance of forces can be expressed as  $F_g = F_0 - F_h$ , where  $F_g$  is the force due to gravity and  $F_0$  and  $F_h$  are the elastic forces originating due to the strong planar anchoring on the substrates at  $z = 0$  and  $z = h$ . In analogy with electrostatics, the interaction of elastic dipoles with bounding plates can be modelled using the method of images.[7, 8] By using a simple approximation of having two image elastic dipoles on the opposite sides of the confining

glass plates, the balance can be written explicitly in terms of the particle displacement from the cell midplane,  $\delta$ [7]:

$$\frac{4}{3}\pi R^3 \Delta\rho g = \frac{3}{2}\pi K C^2 \left(\frac{2R}{h-2\delta}\right)^4 - \frac{3}{2}\pi K C^2 \left(\frac{2R}{h+2\delta}\right)^4,$$

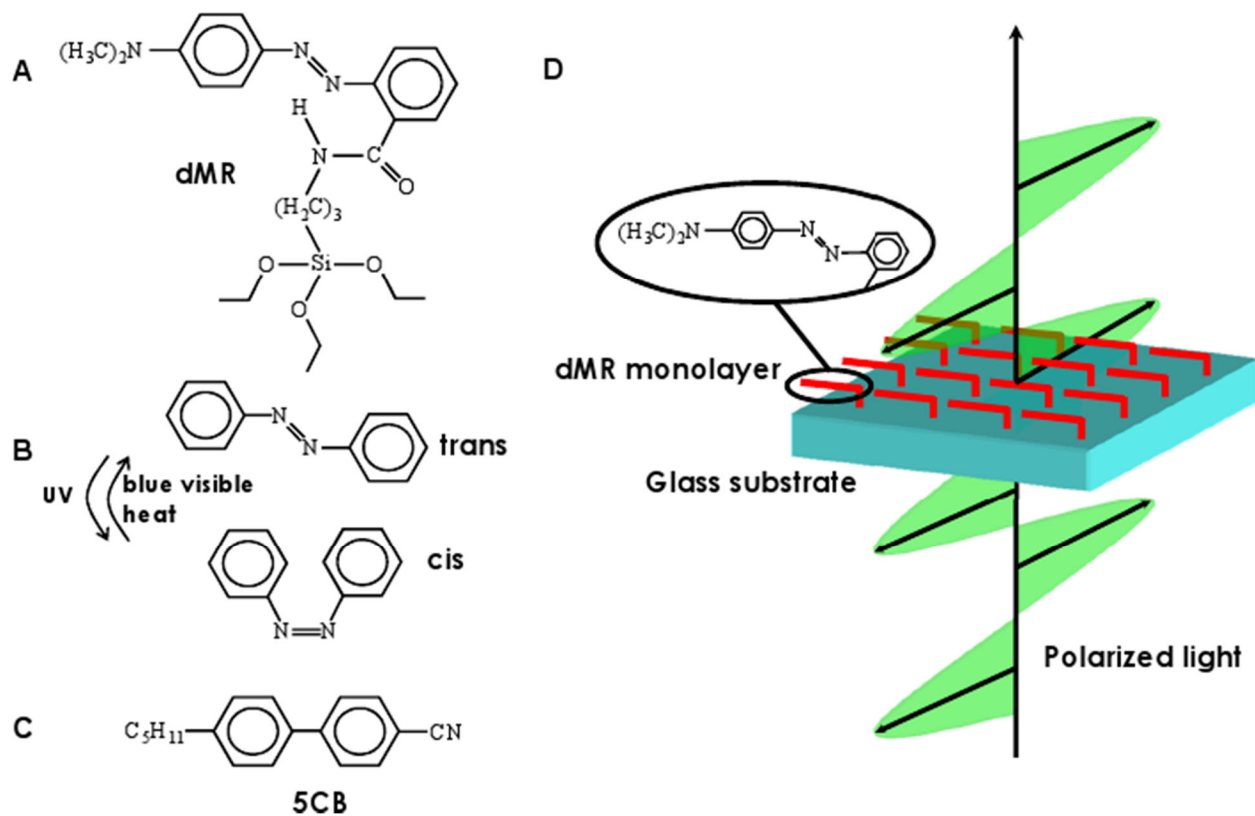
where  $C$  is a numerical factor,  $\Delta\rho$  is the difference between the densities of the particle and the host LC fluid, and  $R$  is the particle radius. Using this expression, we have plotted the relative displacement  $\delta/h$  as a function of  $\Delta\rho$  and  $R$  for three different cell thicknesses  $h$  (Fig. A.8). The results show that even particles having density much higher than that of typical LC materials, like those made of silver, can be localized very close to the cell midplane with  $\delta/h$  being close to 1%, provided that relatively thin LC cells of  $h \leq 5 \mu\text{m}$  are used (Fig. A.8). Clearly, the particles levitate in the LC bulk as gravity is balanced by the strong surface wall-dipole elastic repulsion. Interestingly, the vertical displacement due to gravity is more pronounced for smaller particles than for the ones of bigger size. This result is somewhat counter-intuitive and very different from the case of conventional optical trapping where gravitational forces preclude manipulation of bigger particles (tens of micrometers and larger). However, this finding can be explained by the fact that the elastic force scales with the particle size as  $R^4$  but the gravitational force scales as  $R^3$ , so that elastic forces dominate in the case of larger particles and localize them closer to the cell midplane. Therefore, unlike in the case of trapping by use of optical gradient forces, gravitational forces do not set the upper limit for the size of a particle that can be manipulated using the optoelastic approach. Importantly, although  $\delta/h$  can be substantial (especially in the thick cells), this relative displacement only somewhat modifies optoelastic manipulation. For example, in the case of a noticeable vertical displacement from the cell midplane, the colloidal structures in thick LC cells shown in Fig. 2.2A-E would be rotated by an angle different from

half the angle to which the easy axis at one of the confining glass plates is rotated. This, however, does not preclude or limit the optoelastic manipulation of particles in any way. Although the plots in the Appendix Fig. A.8 have been obtained for a range of particle sizes within (10-5000) nm, particles of small size  $R < 50\text{nm}$  (i.e., smaller than the surface anchoring extrapolation length) might not support the dipolar structure shown in Fig. 2.2F and a more rigorous analysis of the effects of gravitational forces on nanoparticles in LCs and how they can be balanced by wall-particle elastic forces would require a detailed knowledge of the director field around such colloids. Although the above analysis was focused on spherical particles with vertical surface anchoring and dipolar elastic distortions, can be extended to particles of other shapes and with different surface boundary conditions while yielding qualitatively similar conclusions.[8, 9]

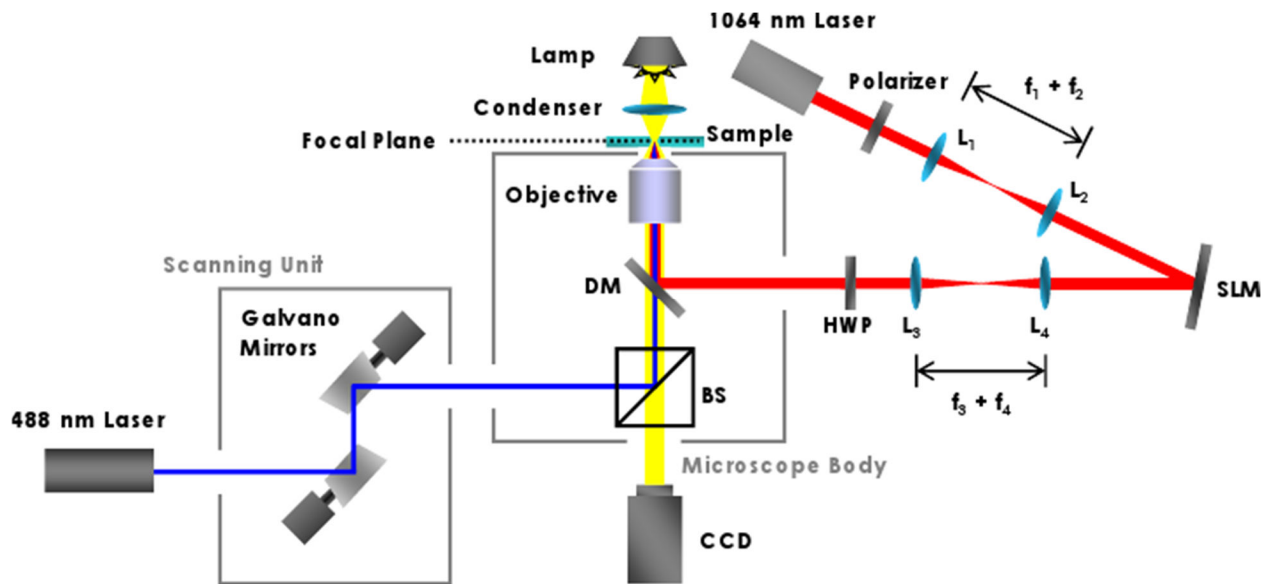
## **A.5 Force characterization**

Optoelastic forces are characterized using two complementary approaches. In the first approach, we utilize a holographic laser trapping system with calibrated force vs. power dependence (Appendix Figs. A2 and A7). For the laser manipulation, we use circularly polarized 1064 nm infrared beams to mitigate the effects of polarization dependence of optical gradient forces in LCs [10]. We control  $\mathbf{N}(\mathbf{r})$  by inducing various elastic distortions through the structured illumination of dMR (Fig. 2.1B-F) and then probe the landscape of ensuing optoelastic forces by slowly moving trapped particles by laser tweezers. From the balance of laser trapping forces and optically controlled elastic forces, we determine the latter.

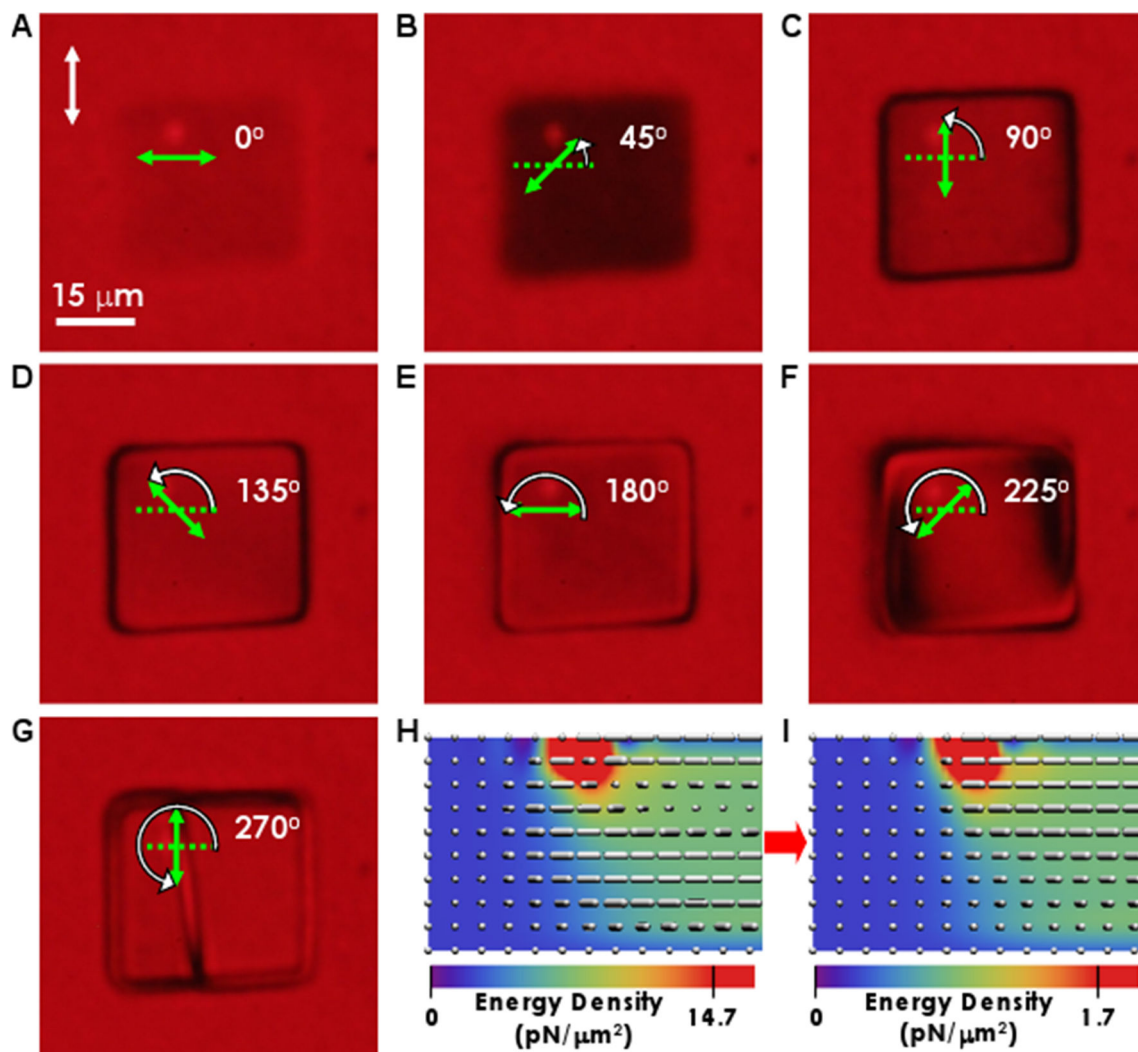
In the second approach, the optoelastic forces are characterized directly by use of their balance with viscous forces when video tracking particle motion due to elastic interactions. Starting from a uniformly aligned sample, we illuminate an area near a colloidal particle using the projection system and thus locally distort  $\mathbf{N}(\mathbf{r})$ . Depending on the symmetry of optically-induced distortions and those around the inclusion, the interaction between a particle and a barrier is either attractive, in which case the colloid moves towards the region with distorted  $\mathbf{N}(\mathbf{r})$  until it comes to rest within it (Fig. 2.5A), or repulsive - thus pushing the colloid away from the distortion until the elastic interactions become comparable to thermal fluctuations. We track the particle positions vs. time (inset of Fig. 2.5C) and determine their velocity  $v$ . We neglect the inertia effects (since particle motion is overdamped) and determine the optoelastic force from its balance with the Stokes' viscous drag force  $F_{oe} = 6\pi\eta_{eff}Rv$  (Fig. 2.5C), where  $\eta_{eff}$  is the effective viscosity coefficient for the particle with the surrounding "corona" of  $\mathbf{N}(\mathbf{r})$ -distortions.  $\eta_{eff}$  depends on the motion direction of the particle with respect to  $\mathbf{N}_0$  and on whether  $\mathbf{N}(\mathbf{r})$  is relatively uniform or has dipolar or quadrupolar structure. For example,  $\eta_{eff} = 86.4$  mPa·s for a particle with dipolar  $\mathbf{N}(\mathbf{r})$  in 5CB (Fig. 2.2F) when measured for the particle motion orthogonal to  $\mathbf{N}_0$ .<sup>[5]</sup> Typical dependencies of  $F_{oe}$  and trap stiffness on the amount of  $\mathbf{N}(\mathbf{r})$ -twist across the cell in the trap are shown in Fig. 2.5.



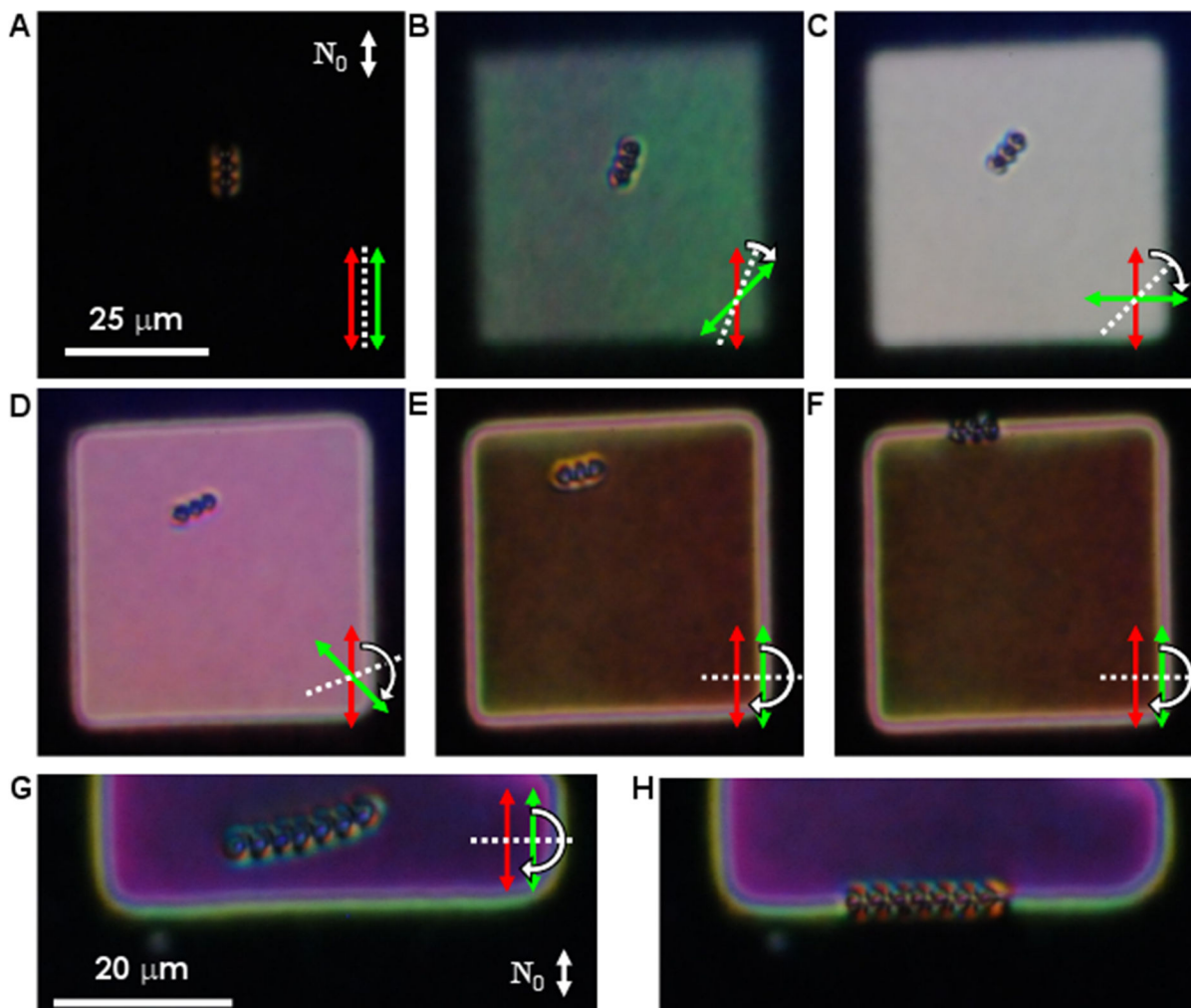
**Fig. A.1** Chemical structures of used molecules and schematics of optical control of the dMR surface monolayers. (A) Molecular structure of the dMR. (B) Azobenzene moiety of the dMR in the trans and cis states. (C) Molecular structure of pentylcyanobiphenyl (5CB). (D) A schematic depicting the photo-alignment of dMR molecules within a surface monolayer using polarized incident light.



**Fig. A.2** Schematic of the integrated laser-scanning illumination and holographic optical trapping system. Integrated setup of the conventional optical trapping and the laser-scanning illumination system is built around an inverted Olympus IX81 microscope. The laser trapping system utilizes a 1064 nm laser and a spatial light modulator (SLM). The laser scanning system is a part of the FV-300 Olympus Fluoview confocal scanning unit and controls the lateral patterns of scanned focused 488 nm Ar ion laser beam used for patterned structuring of  $\mathbf{N}(\mathbf{r})$  through the control of dMR monolayers.

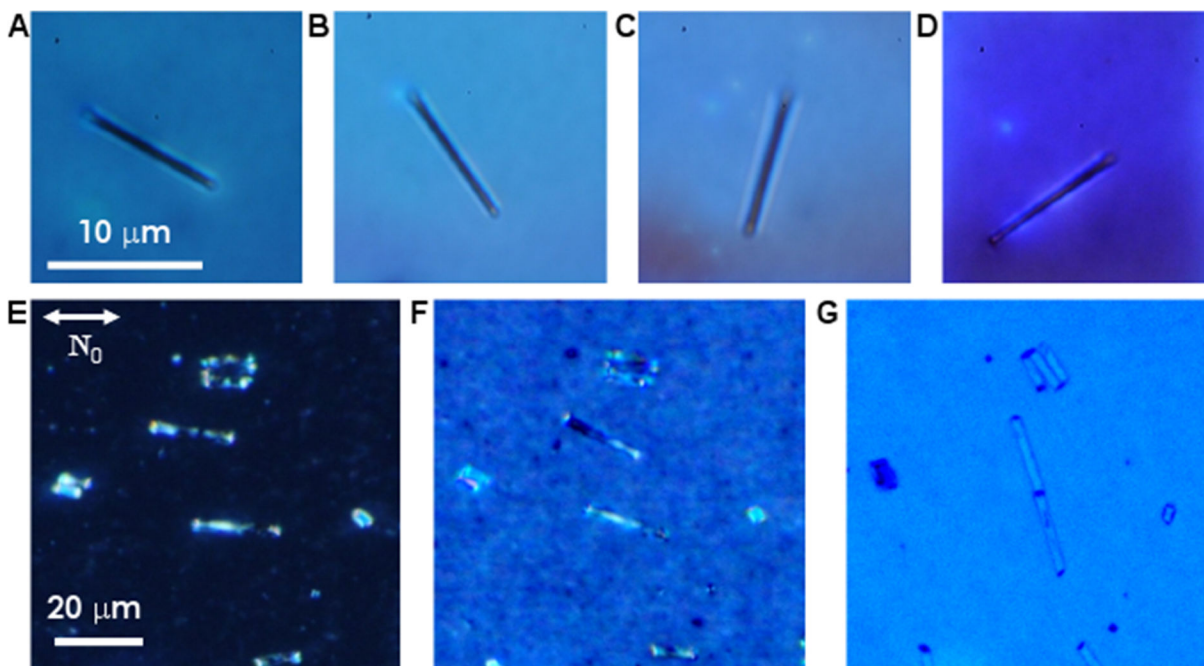


**Fig. A.3** Relaxation of elastic distortions in strongly twisted nematic domains. (A-G) A square region within a uniformly twisted sample is illuminated with blue light having linear polarization direction indicated by the green double arrows. Continuous rotation of the light polarization as marked on the images changes the amount of twist inside the illuminated square. As the bulk elastic energy increases with increasing the amount of twist, (G) a line defect within the LC domains propagates to minimize energy via transformation of the structure into the one with a less twisted state. (H,I) director structures (depicted by use of cylinders) and elastic energy densities (shown using the color scales) for (H) a domain with the light-induced  $3\pi/2$ -twist distortion and (I) a relaxed state with the  $\pi/2$ -twist obtained after propagation of the defect line that relieves some of the distortions by transforming it to the less twisted state. The polarizing microscopy images (A-G) have been obtained between uncrossed polarizers and using red probing light. The vertical cross-sections of the sample shown in (H,I) are obtained by numerical minimization of elastic free energy and correspond to the experimental image shown in (G) for cases before and after the defect line propagation.

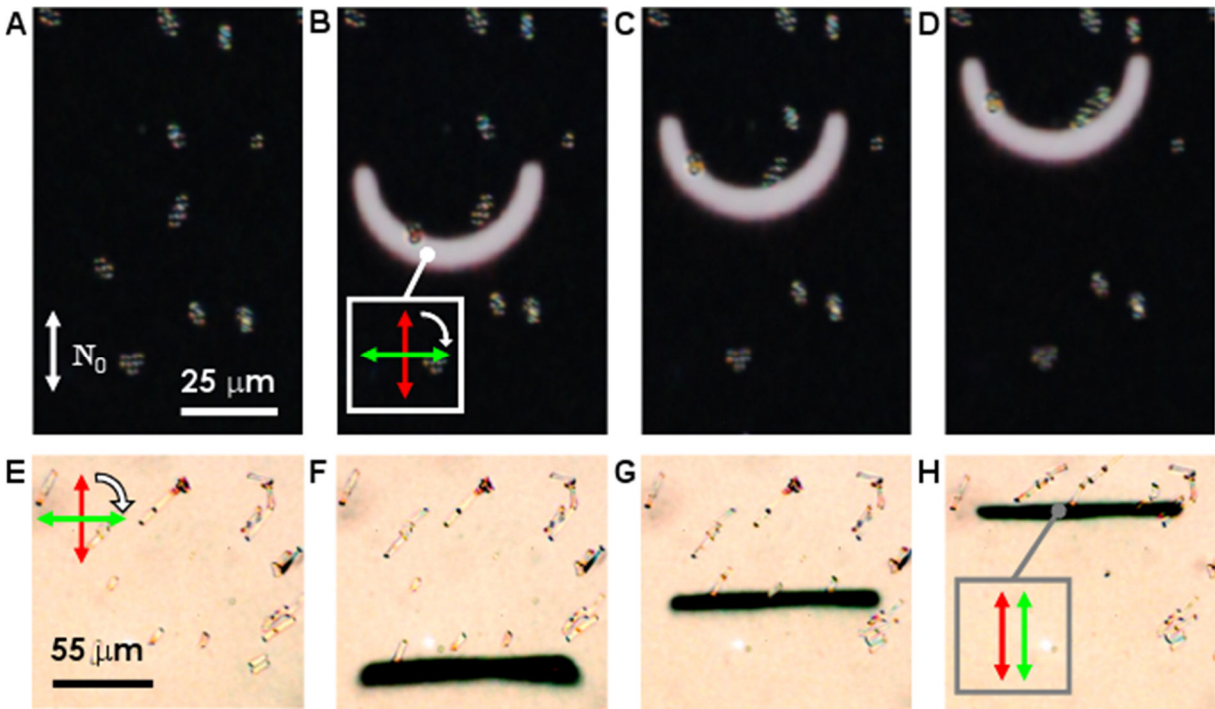


**Fig. A.4** Optoelastic control of colloidal self-assemblies. (A) A dipolar chain in a uniform sample oriented along  $\mathbf{N}_0$  (white double arrow). The red arrow represents the orientation of the trans-state azobenzene of dMR molecules and director at the bottom substrate within the square domain, while the green arrow represents their orientations at the top substrate. The director orientation in the central plane is shown by the white dotted line. (B-F) As the polarization of the projected illumination is rotated clockwise, the trans-state dMR molecules and  $\mathbf{N}$  at the top substrate follow but remain unchanged at the bottom surface. The orientation of  $\mathbf{N}$  and that of a colloidal chain in the middle plane is halfway between the bottom and top surfaces. Note that rotation of the chain in (B-F) is taking place simultaneously with its attraction to the boundary between twisted and untwisted domains, similar to that shown in Fig. 2.5A for an individual particle. (G,H) Images showing attraction of a long colloidal chain to the boundary between  $\pi$ -twisted and untwisted LC domains.

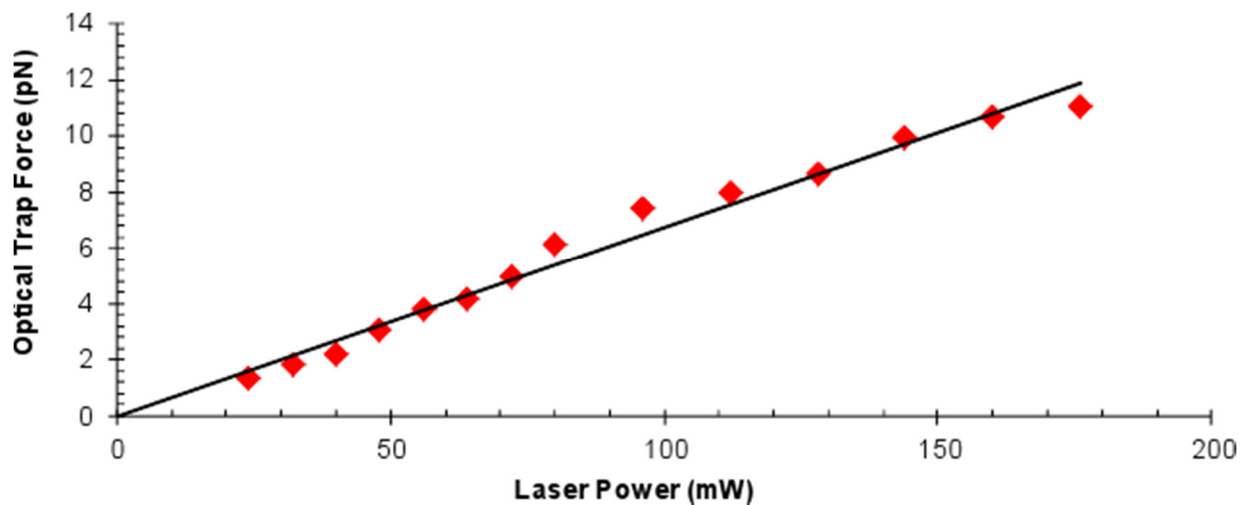




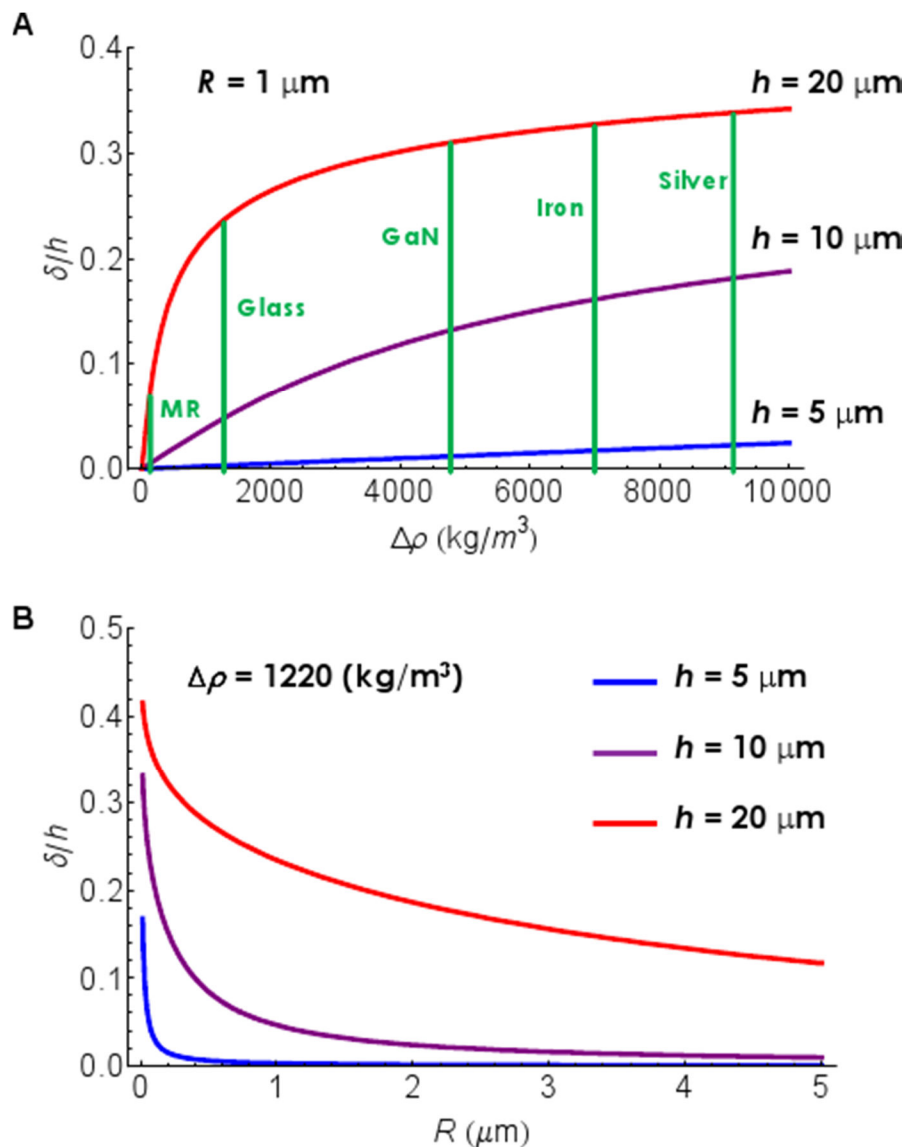
**Fig. A.5** Optoelastic rotation of rods of various material compositions. (A-D) Gallium nitride nanowire rotating with the local  $\mathbf{N}$  as polarization of the illumination light and azobenzene molecules within the surface monolayer are rotated. (E-G) Simultaneous rotation of glass rods using the laser scanning system. The used illumination source is an Ar ion laser (488 nm) from the laser scanning system shown in Fig. A.2.



**Fig. A.6** Translation of various colloids by use of optically controlled twisted and untwisted domains. (A) Melamine resin spheres (3  $\mu\text{m}$  in diameter) dispersed within the LC with a uniform alignment along  $N_0$ . (B-D) Translation of the spheres by use of a semi-circle pattern focused onto a dMR-decorated cell substrate. The polarization of the projected light is rotated to create a  $90^\circ$  twisted director structure within the semi-circle domain as depicted by the red and green arrows showing  $N$  at the bottom and top substrates, respectively. The semi-circle-shaped trap effectively collects and moves the particles as the projected pattern is translated laterally. (E) A dispersion of 3  $\mu\text{m}$  diameter glass rods in a cell with a  $90^\circ$ -twisted director. (F-H) Translation of an untwisted rectangular LC domain (obtained by adjusting the polarization of the corresponding projected illumination pattern) allows for an effective translation of the rods trapped at the domain interface.



**Fig. A.7** Calibrated trap escape force vs. laser power of a circularly-polarized 1064 nm laser beam used to probe optoelastic forces. The dependence is obtained for melamine resin spheres (3  $\mu\text{m}$  in diameter) dragged through the 5CB at increasingly higher velocities: as the particle barely escapes from the trap, the optical trap escape force is equal to the calculated Stokes drag force.



**Fig. A.8** Displacement of nanoparticles from the LC cell midplane due to gravity. (A) Relative displacement vs. mismatch of density of a colloidal particle and the LC host for different cell thicknesses  $h$ ; the vertical green lines mark the values of density mismatch  $\Delta\rho$  between density of different particle materials and that of 5CB. In the images in Fig. S8 “MR” stands for melamine resin and “GaN” stands for Gallium Nitride. (B) Relative displacement as a function of particle radius  $R$  for different  $h$  for the case of silica spheres in 5CB.

□

## A.6 References

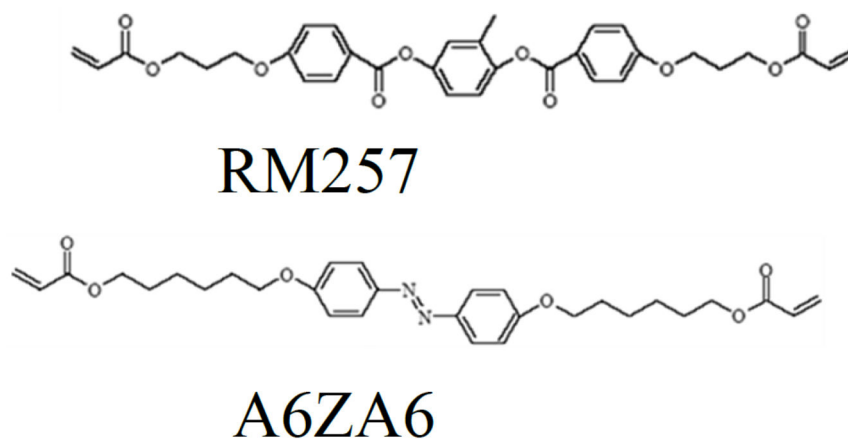
1. Y. Yi, M. J. Farrow, E. Korblova, D. M. Walba, T. E. Furtak, *Langmuir* 2009, **25**, 997.
2. K. A. Bertness, *et al.*, *J. Cryst. Growth* 2008, **310**, 3154.
3. J. B. Schlager, K. A. Bertness, P. T. Blanchard, L. H. Robins, A. Roshko, N. A. Sanford, *J. Appl. Phys.* 2008, **103**, 124309.
4. R. P. Trivedi, T. Lee, K. Bertness, I. I. Smalyukh, *Opt. Express* 2010, **18**, 27658.
5. H. Stark, D. Ventzki, *Phys Rev E* 2001, **64**, 031711.
6. P. G. de Gennes, J. Prost, *The Physics of Liquid Crystals*, Oxford University Press, New York, 1995.
7. O. P. Pishnyak, S. Tang, J. R. Kelly, S. V. Shiyankovskii, O. D. Lavrentovich, *Phys Rev Lett* 2007.
8. V. M. V. Pergamenschik, V. A. Uzunova, *Phys Rev E* 2009, **79**, 021704.
9. C. Lapointe, *et al.*, *Science* 2004, **303**, 652.
10. R. P. Trivedi, D. Engström, I. I. Smalyukh, *J Opt* 2011, **13**, 044001.

## Appendix B

### Materials, deformations and effects of boundary conditions on photoinduced topographies

#### B.1 Materials

As described in the experimental section, the mesogenic mixture that was photopolymerized with green light at elevated temperature consisted of RM257 (Merck), A6ZA6 azobenzene monomer (BEAM Co.), and green light photoinitiator Irgacure 784 (Ciba). The chemical structure of the monomers is presented below in Fig. B.1.



**Fig. B.1** Chemical structures of diacrylate monomers RM257 and A6ZA6.

## **B.2 Specific Description of Film Deformation**

The deformation of the  $+1/2$  defect can be described as a raised/depressed line (or a valley) that radiates from the center of the defect outward towards the edge of the film. The deformation of the  $+1$  defect can be described as a dimpled cone, very similar to the predicted deformation. The deviation from a perfect cone likely comes from the boundary conditions of this study, deviation from the zero-thickness assumption of the prediction, as well as the photochemical mechanism of the effect (nonuniform absorption through the film thickness). The  $+3/2$  defects autonomously deforms into a tear-shaped dimple morphology and a valley region, both radiating from opposite side of the center of the defect. The  $+2$  defect, with 2-fold symmetry, deforms into two tear shaped dimples radiating from opposite sides of the center of the defect. The photo-induced deformation of the  $+5/2$  defect can be described as 3 tear-shaped dimples radiating from the center. The self-molded shape of the  $-1/2$  defect can be described as three valleys radiating from the center at  $120^\circ$  offset with respect to each other. The photoinduced deformation of the  $-1$  defect is made up of four valleys pointing towards the center.

## **B.3 Boundary Conditions:**

Without properly mounting the samples, a range of resulting topographies were obtained. Upon initial exposure the sample would curl due to a bimorph-like deformation caused by the top surface deforming more than the bottom surface (because of intensity gradient across sample due to absorption). While it is possible to obtain relatively repeatable results by exposing both sides evenly, it still proved difficult. Fig. B.2 presents such a sample. All the samples presented in the paper, with the exception of the arrays were exposed by mounting the samples on an o-ring glued to a glass substrate. Water was deposited around the o-ring in order to wet the interface between

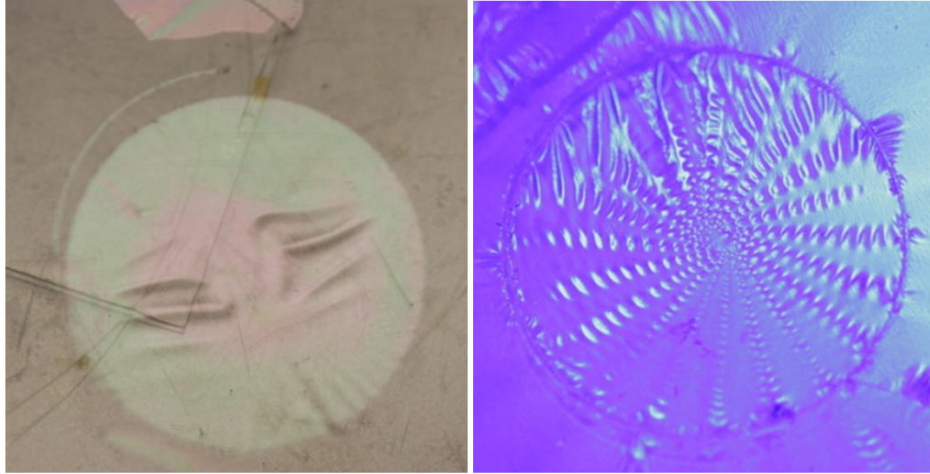
the o-ring and the sample. This allowed the sample films to slide with respect to the o-ring and also created a uniform tensile force around the sample from the capillary forces. The arrays were exposed in a method much like the sample presented in Fig. B.2. In Fig. 3.4 as well as Fig. 3.2, the samples are not perfectly flat.



**Fig. B.2** An example of a +2 defect with fractal-like topography with two generations of 2-fold dimples. Exposed with two sided illumination.

It is very important to notice that the sample in Fig. B.2 there are two sets of self-similar dimples. The inner set of dimples point towards the camera and the outer set of dimples point towards the velvet the sample is resting on. This fractal behavior was rarely seen in the plus defects, but was definitely still apparent numerous times. It is the opinion of the authors that that this self-similar behavior would be seen much more commonly if the samples were larger and/or had higher strains. Part of the reason why this was uncommon maybe due to the tensile strain presented by the boundary conditions of the wet o-ring.





**Fig. B.3** Films exposed on the surface of water (left is a +2 defect and right is a -9 defect)

Other controllable boundary conditions were also explored such as placing the sample on the surface of water, as presented in Fig. B.3. The image on the left is of a +2 defect and the image on the right is of a -9 defect (during exposure). Notice that in the image on the left the resulting two dimples are flattened, due to capillary forces, thus creating more of a buckled shape. On the right, the expected 20-fold geometry is present, but the shape of the deformations is very different than the minus defects presented in Fig. 3.3. Specifically, there are 20-regions of numerous equally spaced self-similar buckles that point nearly perpendicular to the defect center and are separated by 20 flat regions.

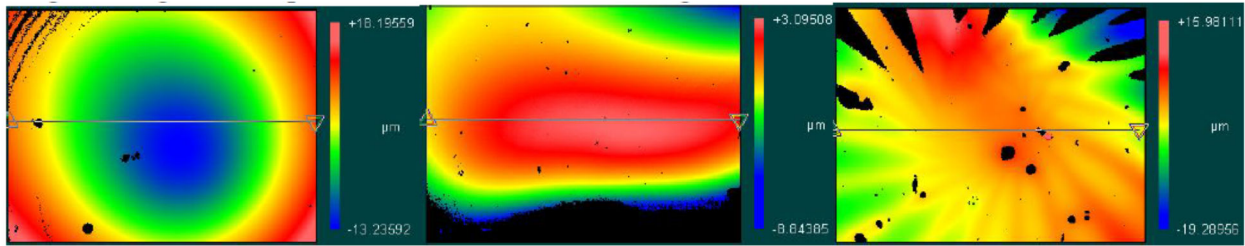


**Fig. B.4** The deformation of -1 defect flattened and pulled taut.

Another manner in producing very repeatable deformations was to prepare the samples by exposing them evenly while they sat on a flat surface (see text regarding Fig. B.1) and then to pull the sample taut by taping the edges to a flat substrate. This is essentially taking the deformed surface and presenting the non-developable geometry when the sample is flattened as best as possible. The -1 defect presented in Fig. B.3 has the expected 4-fold geometry but the shape somewhat different than presented in Fig. 3.2 of the text. The 4 valleys radiating from the center are present, but the self-similar struts are much more apparent in this sample than in the samples prepared with the o-ring substrates. It is not too surprising that this sample-mounting approach leads to similar deformations as the o-ring approach because they both apply tensile forces at the edge of the sample in the same direction.

## **B.4 Interferometry**

To inform the illustrations presented in Figs. 3.2, 3.3, and 3.4 we employed white light interferometry (Zygo). Raw data from these experiments presented in Fig. B.5 detail the height changes of a representative set of defect strengths.



**Fig. B.5** White light interferometry of defect deformations. The deformations resulted from: a) +1 defect, b) +1/2 defect and c) +10 defect.

The height scale is indicated to the right of the image based on color. The +1 and +1/2 images have lateral dimensions of 0.70 mm by 0.53 mm. The +10 height image has lateral dimensions of 2.83 by 2.12 mm. The +1 and +10 were centered near the defect center, whereas the +1/2 image is offset from the defect center to include the whole deformation in the image window. The black regions are where the interferometer dropped pixels because noise levels were too high. Lastly it should be stated that the +1/2 and +1 defect images were taken from samples that were incompletely deformed. The incompletely deformation of the films was intentional to allow for accurate examination of the topography with this instrumentation.

## Appendix C

### Materials, methods, design and modeling of knotted colloids

#### C.1 Fabrication of Knotted Colloids with Different Surface Boundary

##### Conditions

We fabricate colloidal knots within glass cells consisting of a standard microscope slide and a 170  $\mu\text{m}$ -thick coverslip, spaced by 50  $\mu\text{m}$ -thick strips of Mylar films. The cell is “sandwiching” a droplet of IP-L (780) photoresist (obtained from NanoScribe GmbH). An example of such a cell is shown mounted on the translation stage of the polymerization setup (Appendix Fig. C.1). The multiphoton polymerization setup consists of a tunable femto-second pulsed Titanium:Sapphire laser operating at wavelength of 780 nm, piezo-electric nano-positioning stage (Physik Instrumente, model P-611.3SF, 0.2 nm resolution), and a fast shutter (Uniblitz, model LS3Z2, 200 Hz). The pulsed laser beam is first passed through a half-wave plate (Appendix Fig. C.1) and subsequently through a Glan laser polarizer for polymerizing beam’s power control. The average laser power used ranged from 3mW for small knots to 13 mW for larger ones, as measured just before the objective (note that the power in the sample is further reduced by about a factor of two due to light absorption of the objective and confining glass plates in the near infrared part of spectrum). The beam passes through the shutter and is then directed to the back aperture of the objective using a dichroic mirror and focused within the bulk of the monomeric sample. An oil-immersion objective with 100x magnification and high numerical aperture of 1.4 (obtained from Olympus) is used for focusing. Due to the nonlinear

nature of the multiphoton-absorption-based photoinitiation process, polymerization occurs in the vicinity of the focused beam's focal point, with the sub-diffraction limited resolution dependent on the used laser power. A LabView-based homemade computer software controls both the shutter and nano-positioning stage in concert to polymerize arbitrary three-dimensional topological colloids. Shapes of knots are described by a set of parametric equations programmed in LabView (the same equations are used to define the particle in numerical modeling):

$$\left. \begin{aligned} \mathbf{r}_{T(3,2)} &= R(2.1(\cos \phi - 2.25 \cos 2\phi), 2.1(\sin \phi + 2.25 \sin 2\phi), 6 \sin 3\phi) \\ \mathbf{r}_{T(5,2)} &= R(2.3(\cos 3\phi - 3 \cos 2\phi), 2.3(\sin 3\phi + 3 \sin 2\phi), 9 \sin 5\phi) \\ \mathbf{r}_{T(5,3)} &= R(2.7(\cos 2\phi - 2.25 \cos 3\phi), 2.7(\sin 2\phi + 2.25 \sin 3\phi), 8 \sin 5\phi) \end{aligned} \right\} \quad (\text{C.1})$$

where  $R$  determines the physical size of the knot and  $\phi \in [0, 2\pi]$ . As the program executes, the nano-stage translates the cell and, effectively, the beam focus is steered along a 3D trajectory prescribed by these equations. In this way, arrays of surface-attached particles are created. Fig. 5.1 shows such particle knots imaged with brightfield optical microscopy and scanning electron microscopy (SEM). Once the particles have been “drawn”, the unpolymerized material is rinsed away with IPA solvent, leaving only arrays of polymer knots weakly attached to the glass surface (Fig. 5.1b). Once dry, the glass substrate is placed under a microscope and the particles are submerged within a droplet of a nematic LC ( $\sim 10 \mu\text{L}$ ). Using a syringe needle mounted on a fine, three-axis translation stage, the particles are detached from the surface by careful poking (usually done using a microscope equipped with a 10x objective lens). Once the entire array of particles is retrieved, so that these particles are suspended within the LC droplet, the ensuing nematic colloidal dispersion is pipetted into a vial and sonicated. In addition, we were also polymerizing similar particles in NOA-63 (obtained from Norland Inc.), IP-G (obtained from NanoScribe GmbH), and the ultraviolet sensitive photopolymer SU-8 commonly used in photolithography. In

the latter two cases, the particles could be photopolymerized in the bulk of the photopolymerization cell, so that no detachment from surfaces was needed. The use of solvents and their exchange then allow one to introduce these colloidal particles into LCs.

The polymerized IP-L photoresist induces strong tangentially degenerate anchoring at the interface between the polymer and thermotropic nematic fluids such as 5CB. Therefore, as-prepared knot-shaped particles impose tangential boundary conditions at their surfaces. To achieve homeotropic anchoring, we prepared mixtures containing 75-98wt.% IP-L photoresist and 2-25wt.% (~8wt.% for the particle presented in Appendix Fig. C.6c) Styrylethyltrimethoxysilane (Gelest, Inc.), whose chemical structure is shown in the Appendix Fig. C.3b. After rinsing the polymerized structures (attached to glass surface) as described above, they are submerged in a 0.5wt.% solution of N,N-Dimethyl-N-octadecyl-3-aminopropyltrimethoxysilyl chloride (DMOAP, chemical structure shown in the Appendix Fig. C.3c) in IPA for several minutes to allow bonding between the silane chemical moieties in DMOAP to those exposed on the surface of the polymerized mixture. They are then rinsed again with IPA before being detached from the surface for retrieval. Appendix Figure C.6c shows a trefoil knot colloidal particle treated in this way and then imaged with two-photon excitation fluorescence polarizing microscopy (2PEF-PM) when introduced into a nematic LC ZLI-2806 doped with 0.02 wt.% of dye BTBP (Appendix Fig. C.3d). Alternatively, instead of doping IP-L with styrylethyltrimethoxysilane, we also used plasma treatment (for about 5 min) of the photopolymerized colloids composed of IP-L without additives, followed by surface modification with DMOAP using a procedure similar to that described above. Particles prepared using the latter approach and dispersed in 5CB are shown in Fig. 5.3 and Appendix Fig. C.5.

## C.2 Integrated Optical Manipulation and Imaging Setup

Shown in Appendix Fig. C.2 is an integrated system for simultaneous optical manipulation and 3D imaging built around an inverted microscope IX 81 (Olympus). The holographic optical trapping (HOT) part of the setup is centered on a reflective, electrically addressed, phase-only spatial light modulator (SLM) obtained from Boulder Nonlinear Systems (XY series, P512-1064). The SLM has 512 x 512 pixels, each 15 x 15  $\mu\text{m}^2$  in size. The HOT setup employs an Ytterbium-doped fiber laser (YLR-10-1064, IPG Photonics) operating at 1064nm. The laser is linearly polarized with a Glan-laser polarizer and the polarization direction is adjusted with a half-wave retardation plate to optimize the phase modulation efficiency of the SLM. Before the beam is incident on the SLM, it is expanded to overfill the active area of the SLM using lenses L1 and L2 and then is resized using lenses L3 and L4 so as to overfill the back aperture of the objective. The SLM controls the phase of the beam on a pixel-by-pixel basis according to the computer-generated holographic patterns supplied at a refresh rate of 30 Hz for the entire pixel array. This spatially phase-modulated beam is imaged at the back aperture of the microscope objective, which recreates the 3D spatial trap pattern in the sample. A custom-designed dichroic mirror (obtained from Chroma Technology Corp.) reflects the trapping beam at 1064 nm while allowing visible light (used for imaging purposes) to transmit through it to the confocal microscopy scanning head and charge-coupled device (CCD) camera. In both two-photon excitation fluorescence polarizing microscopy (2PEF-PM) and three-photon excitation fluorescence polarizing microscopy (3PEF-PM), we have employed a tunable (680-1080 nm) Ti-Sapphire oscillator (Chameleon Ultra II, Coherent) emitting 140 fs pulses at the repetition rate of 80 MHz. In the 2PEF-PM experiments, we tune the wavelength to 980 nm for the two-photon

excitation of the dye BTBP. The three-photon excitation and 3PEF-PM imaging of 5CB-based samples is done without the use of dyes as 5CB molecules strongly fluoresce themselves as a result of the three-photon-absorption-based excitation at 870 nm.[1] The focus of the beam is steered laterally throughout the focal plane in the sample with galvano mirrors. The 2PEF-PM signal from the BTBP dye and 3PEF-PM signal from 5CB molecules is collected in epi-detection mode with a photomultiplier tube (H5784-20, Hamamatsu) and a series of interference filters. We use oil-immersion objectives with high numerical aperture (NA), 60x (NA=1.42) and 100x (NA=1.4), both purchased from Olympus. The same objectives are used for imaging as well as optical trapping. The integrated setup for holographic optical manipulation and 3D imaging is described in more details elsewhere.[1]

### **C.3 Sample Preparation**

LC cells are constructed with two glass substrates, each coated with a thin film of unidirectionally rubbed polyimide PI-2555 (from HD Microsystems) for planar alignment or treated with DMOAP for homeotropic (perpendicular) alignment of the LC director on their inner surfaces. The substrates are spaced and held together with UV-curable glue (NOA-65, from Norland Inc.) containing a dispersion of silica spheres to define the cell gap (e.g. particles of diameter 25  $\mu\text{m}$  allow us to define the cell gap in the range 25-26  $\mu\text{m}$ ). After curing, the cells are filled with the LC containing the dispersion of colloidal knots via capillary action and the cell edges are then sealed with epoxy. The LC cells are typically heated to isotropic-phase temperatures and then quickly quenched back into the nematic phase to help facilitate uniformity of the LC director throughout the cell while assuring that particles do not sediment to a substrate or aggregate due to the nematic-isotropic phase front propagation.



## C.4 Numerical Modeling of Nematic Colloidal Knots

Free-energy-minimization-based numerical modeling is used to explore the inter-related topologies of colloidal particle-knots and the knotted molecular orientational field. The modeling is based on the mean-field nematic order parameter tensor  $Q_{ij}$ , which characterizes the time (or equally ensemble) average of orientational degrees of freedom of nematic molecules, including the average orientation – the director  $\mathbf{n}$  – as the eigenvector of the largest eigenvalue. Using tensorial invariants of  $Q_{ij}$ , free energy is constructed, which is composed of contributions characterizing nematic elasticity, variable nematic degree of order, and surface anchoring of nematic molecules at the surfaces of the particle-knots. In the Landau-de Gennes form, the bulk elastic and order free energy reads:

$$F = \frac{1}{2}L \int_{LC} \left( \frac{\partial Q_{ij}}{\partial x_k} \right) \left( \frac{\partial Q_{ij}}{\partial x_k} \right) dV + \int_{LC} \left( \frac{1}{2}A Q_{ij} Q_{ji} + \frac{1}{3}B Q_{ij} Q_{jk} Q_{ki} + \frac{1}{4}C (Q_{ij} Q_{ji})^2 \right) dV \quad (\text{C.2})$$

where  $L$  is the single nematic elastic constant,  $A, B, C$  are nematic material parameters, and LC indicates integration over the whole volume of the liquid crystal. The single elastic constant approximation is used in calculations. This is appropriate as in typical nematic LC materials, like 5CB used in our experiments, the splay, bend and twist elastic constants have comparable values. The bulk free energy is combined with the surface anchoring free energy: (i) of Rapini-Papoular form for particle-knots with homeotropic anchoring or (ii) with Fournier-Galatola formulation for the planar degenerate anchoring.[2] Free energy is minimized using explicit Euler finite difference relaxation method on a cubic mesh,[2] within a homeotropic nematic cell. The top and

bottom substrates of the cell induce strong anchoring and fixed homogenous boundary conditions are assumed along lateral XY directions.

The numerical allocation of the knot-shaped particle within the cubic mesh is performed by scanning with a sphere (having diameter equal to the actual thickness  $D$  of the particle-knot) along the parametrically defined knotted line. The parameterizations for the T(3,2), T(5,2) and T(5,3) knots are described by Eq. (C.1) in section C.1 and are the same as what we used for “drawing” knotted particles in the two-photon photopolymerization experiments. Taking discrete scanning steps of length  $l/N$ , where  $l$  is the length of the knotted line and  $N$  is an integer, and making multiple full turns along the knotted line (typically 10-100 times) allow for a good allocation of the particle-knot designated as the volume covered by the spheres at least once within the scanning. Snapshot of the knot-particle allocation at the beginning of the scanning process is shown in the Appendix Fig. C.15. In addition, if the sphere is filled with radial hedgehog nematic director field at every time step, the surface points of the knot-particle get assigned locally homeotropic (perpendicular to the surface) boundary conditions for the director field as a result of the scanning process. The following parameters of a standard nematic liquid crystal and particles with strong surface anchoring (as in experiments) are used in calculations:  $L=40$  pN,  $A=-0.172$  MJ/m<sup>3</sup>,  $B=-2.12$  MJ/m<sup>3</sup>,  $C=1.73$  MJ/m<sup>3</sup>,  $W=10^{-3}$  J/m<sup>2</sup>, cell thickness of 3  $\mu\text{m}$ , and the ratio  $R/D=10/8$ . Running at the upper level of our computational resources, the presented simulations are performed at effectively equal conditions as in experiments but at smaller physical dimensions of the particle and the confining cell (particle size parameter  $R=0.1$   $\mu\text{m}$ ). However, when performing a direct one-to-one size comparison of the experiments and theory, the calculated director field can be scaled (in particular for knots with tangential anchoring) by

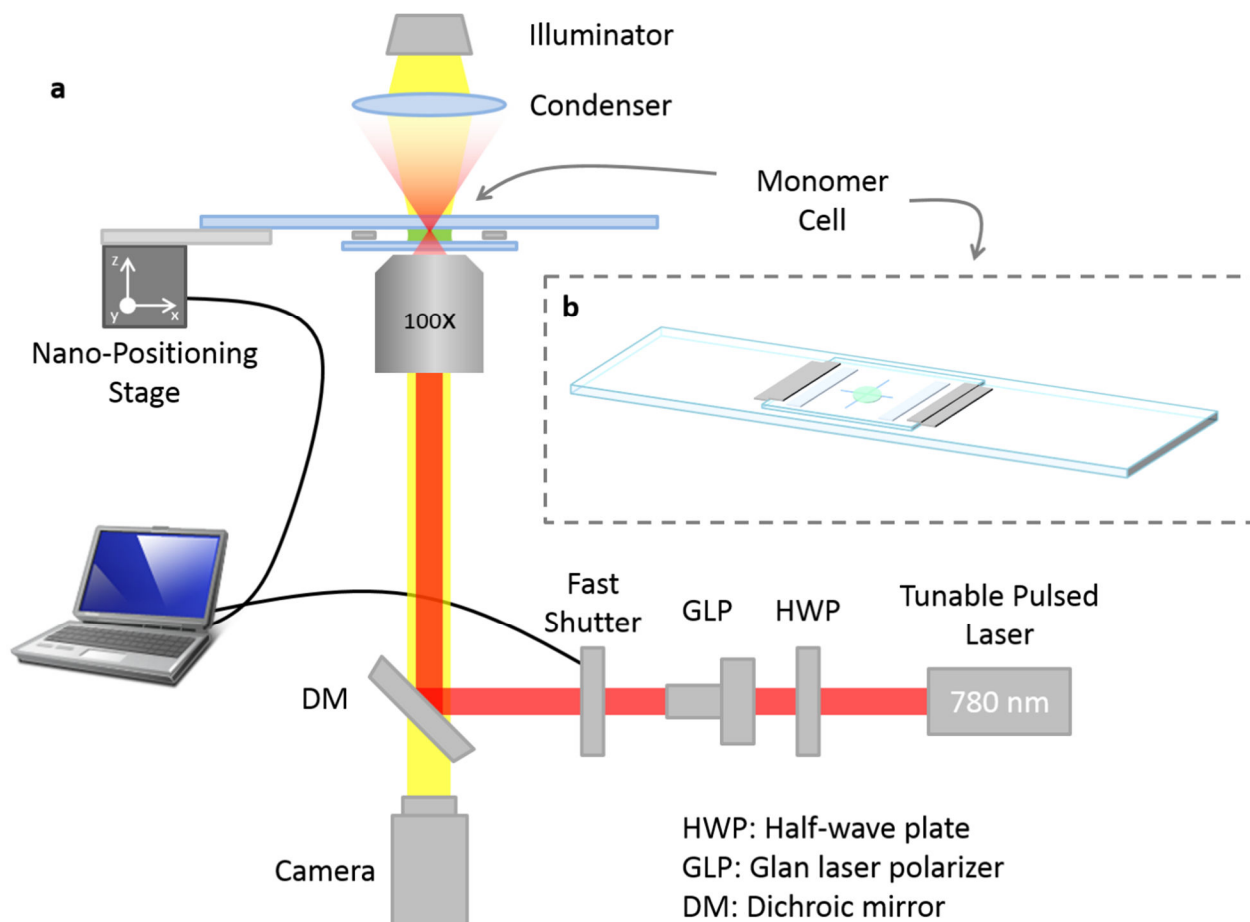
appropriately rescaling the physical dimensions of the simulation box as a whole and the anchoring strength on the particle walls. Effectively, such rescaling yields thinner defect lines (relative to the knotted tube of the particle) for the knotted colloids with homeotropic surface anchoring (Fig. 5.3), and more localized regions of reduced nematic degree of order around the boojums for the knotted particles with tangential anchoring conditions.

### C.5 Computer Simulations of 3PEF-PM Textures

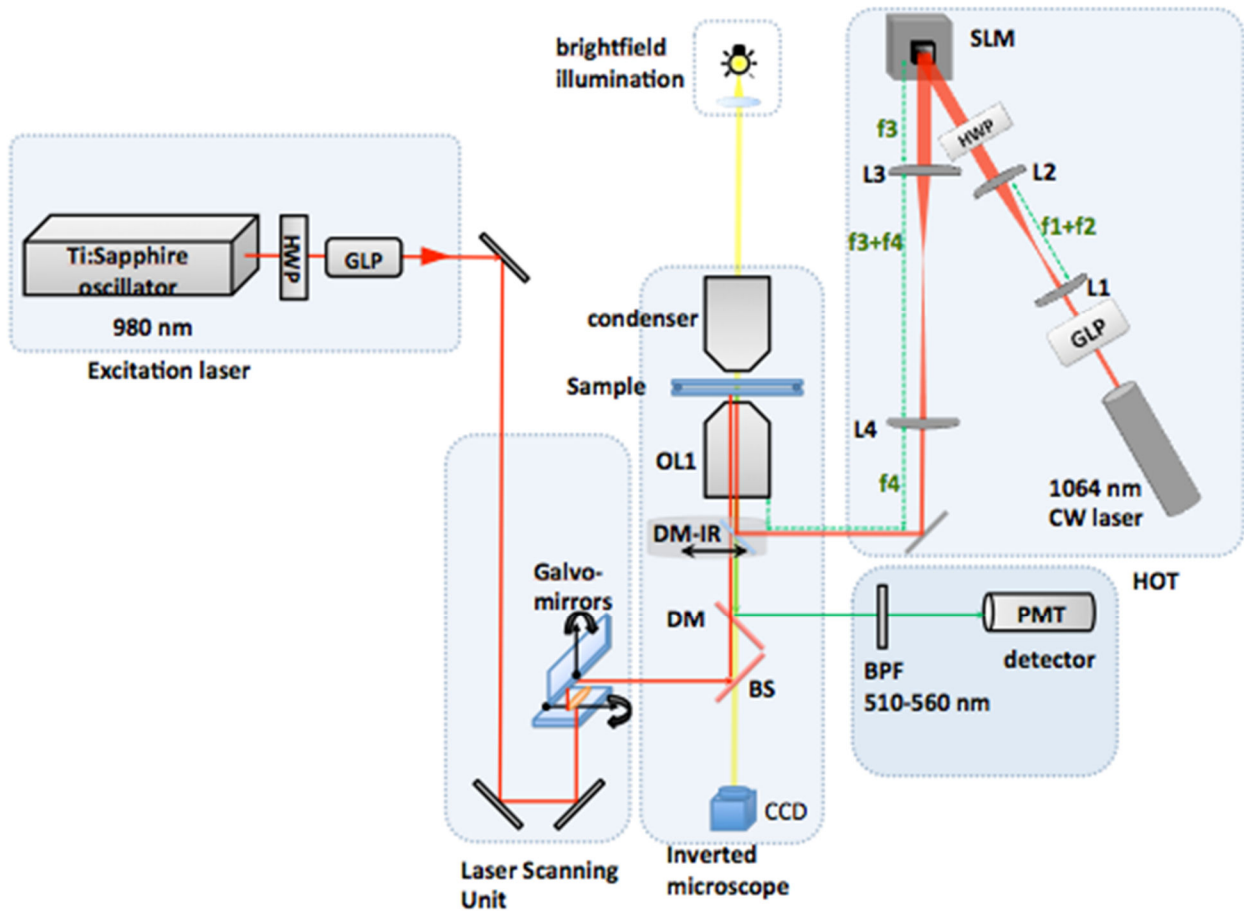
Since diameter of the tube forming knotted particles is comparable to the diffraction-limited resolution of optical imaging,[1] 3PEF-PM textures are determined not only by orientation of  $\mathbf{n}(\mathbf{r})$  relative to focal-plane polarization of excitation light, but also by finite optical resolution effects. For example, at the LC-polymer interface, where  $\mathbf{n}(\mathbf{r})$  is parallel to the particle surface, the polarization-dependent fluorescence intensity is changing gradually rather than discontinuously for polarizations of probing light both parallel and perpendicular to the interface (Fig. 5.2d). To directly compare the results of numerical modeling with experiments, we computer-simulate 3PEF-PM textures while accounting for the finite resolution effects, which result in “blurring” of textures over distances determined by lateral and axial resolution. We first calculate the theoretical 3PEF-PM texture that one could expect for resolution-unlimited imaging as  $I_{3PEF-PM}(x', y', z') \propto \cos^6 \theta(x', y', z')$ , where  $\theta$  is the angle between the probe light’s linear polarization and  $\mathbf{n}(\mathbf{r})$ . Intensity of each pixel of the 3PEF-PM image expected at finite resolution is then calculated by integrating this fluorescence intensity over a diffraction-limited volume:

$$I_{3PEF-PM}(x, y, z) \propto \iiint I_{3PEF-PM}(x', y', z') T(x - x', y - y', z - z') dx' dy' dz', \quad (\text{C.3})$$

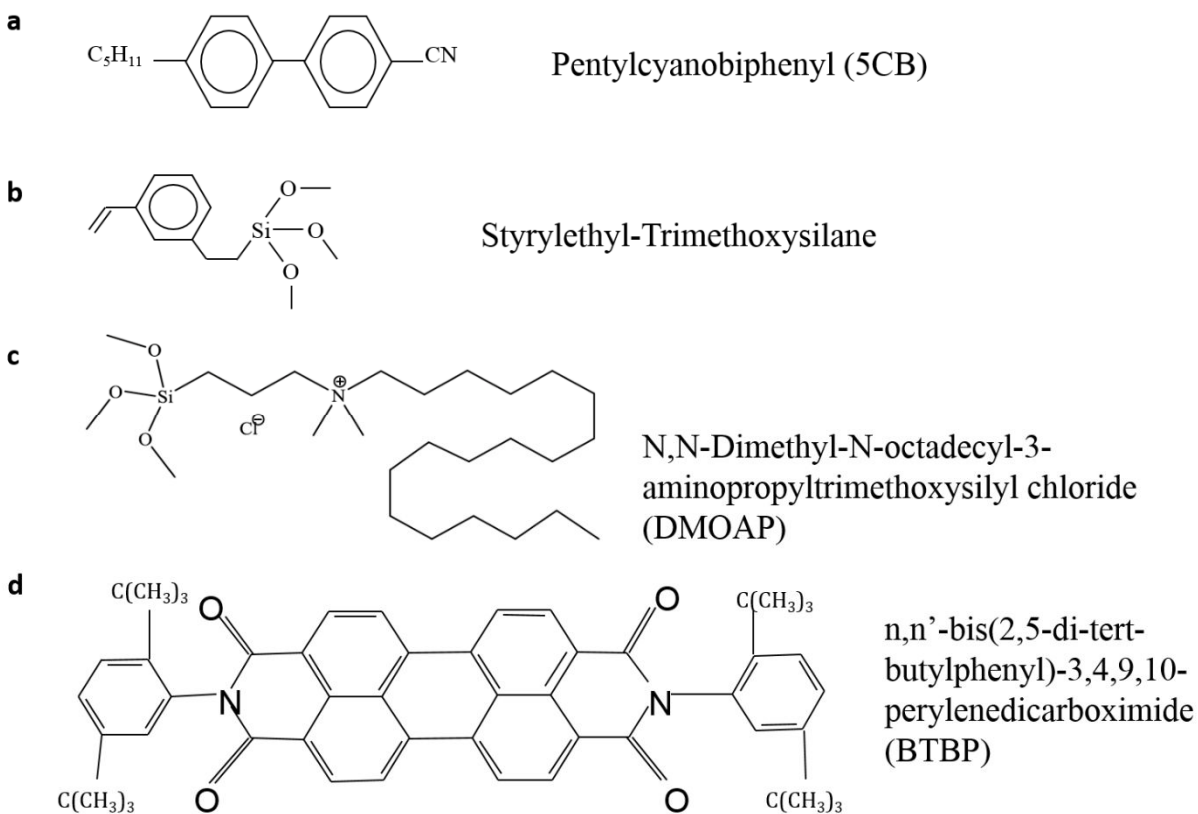
where  $T$  is the weight function assumed to be Gaussian of width corresponding to lateral resolution  $\Delta r$  in the plane perpendicular to the microscope's axis and  $\Delta z$  along it.[1] In addition to the finite resolution effects, we have used the extended Jones matrix method and experimental material and sample parameters (such as optical anisotropy and cell thickness) to account for the changes of polarization of the excitation light propagating through the LC during 3PEF-PM imaging. To do this, an LC sample was split into a set of thin slabs with known director orientation, which were based on numerical modeling and corresponding to the 3PEF-PM optical "slices". While traversing through the cell, light splits into ordinary and extraordinary waves that have electric fields perpendicular and parallel to the in-plane projection of  $\mathbf{n}(\mathbf{r})$ , respectively. These waves "see" ordinary refractive index and an effective extraordinary refractive index  $n_{ee}(\beta)$  dependent on the angle  $\beta$  between  $\mathbf{n}(\mathbf{r})$  and the light's propagation direction, respectively. The effect of each thin slab on the excitation light polarization is equivalent to that of a phase retardation plate with spatially varying optical axis in the lateral plane but constant orientation of the optical axis across its thickness and can be described by a coordinate-dependent Jones matrix. The net effect of the excitation light propagation through the LC is modeled by successive multiplication of the Jones matrices corresponding to a series of thin nematic slabs with coordinate-dependent phase retardation. With the finite resolution effects and LC-caused polarization changes accounted for, the computer-simulated and experimental 3PEF-PM textures show a good agreement (Fig. 5.2d,e).



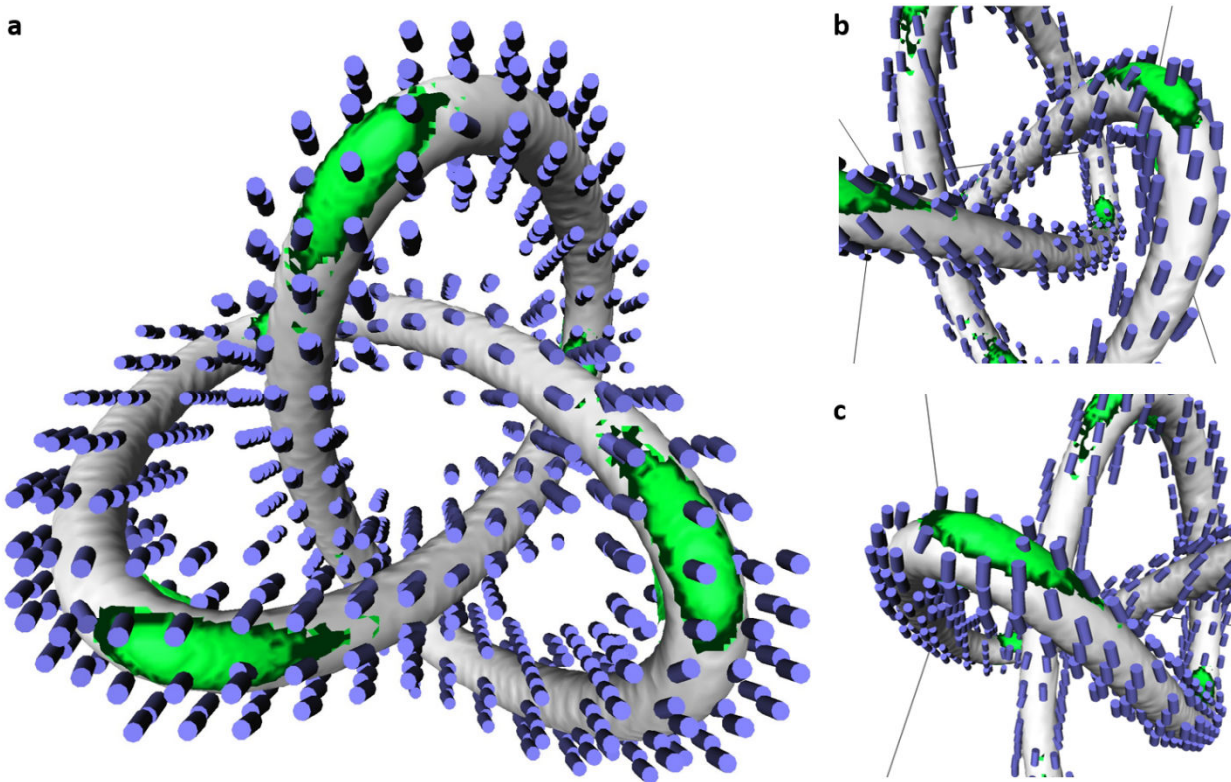
**Fig. C.1** Two-Photon Photopolymerization Setup. (a) A simplified schematic depicting key components of the two-photon photopolymerization system. A computer controls timing between the fast shutter and a nano-positioning stage in order to “draw” desired structures of polymerized solid particles. (b) A schematic view of the photopolymerization cell with monomer and photoinitiator in the form of a droplet sandwiched between a glass slide and a microscope coverslip of 170  $\mu\text{m}$  in thickness.



**Fig. C.2** A schematic of the integrated 3D HOT manipulation and imaging setup. HWP: half-wave retardation plate. GLP: Glan laser polarizer. DM: dichroic mirror. BPF: bandpass filter. OL: objective lens. SLM: spatial light modulator. L1-L4: plano-convex lenses.  $f_1$ - $f_4$ : focal length of the lenses. PMT: photomultiplier tube. BS: beam splitter.

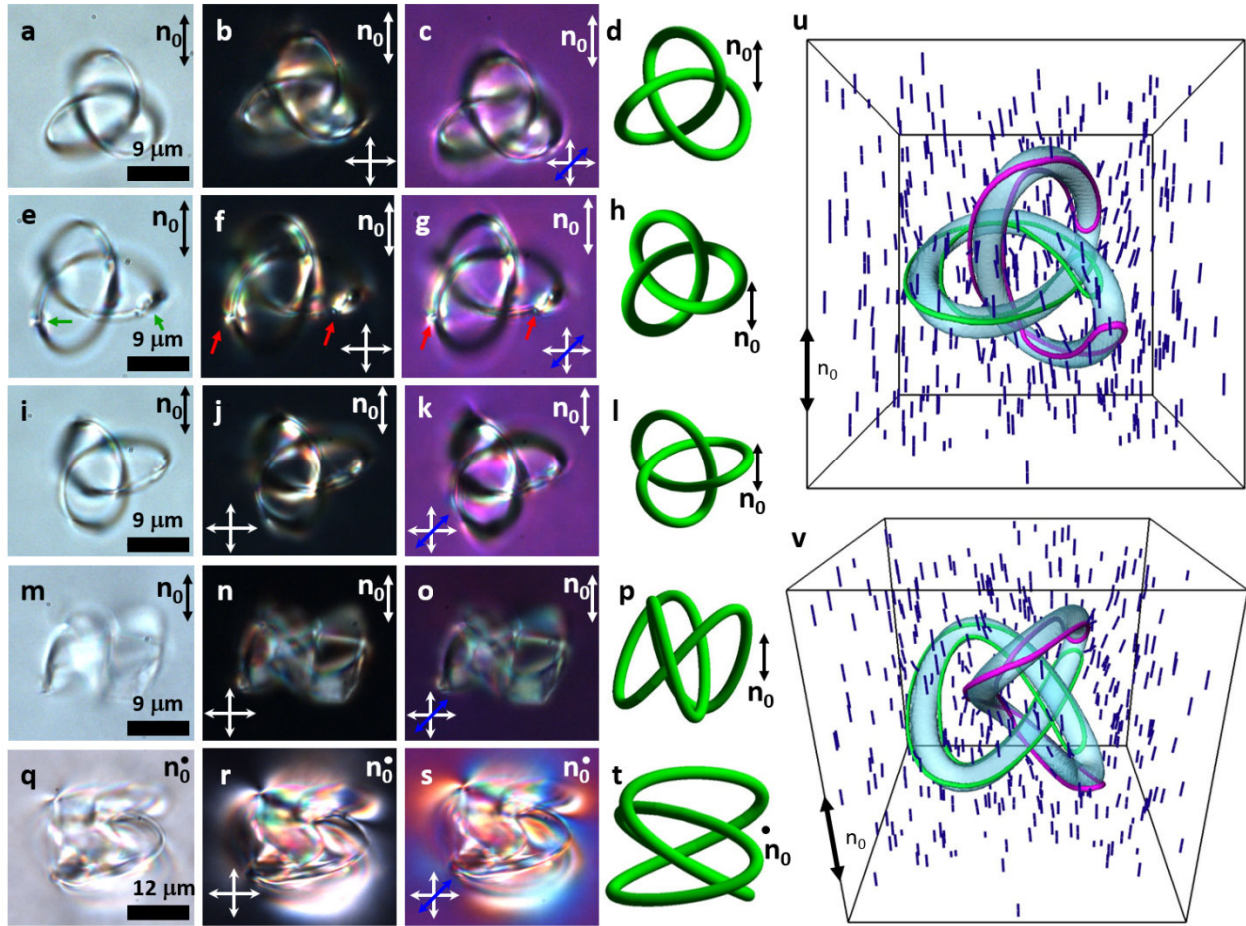


**Fig. C.3** Chemical structures of used materials. (a) Liquid Crystal molecule of 5CB. (b) Styrylethyl-Trimethoxysilane used to surface-functionalize the knotted particles with DMOAP. (c) Chemical structure of the DMOAP molecule. d, BTBP dye used for two-photon excitation fluorescence imaging of structures around colloids when dispersed in the ZLI-2806 nematic mixture.

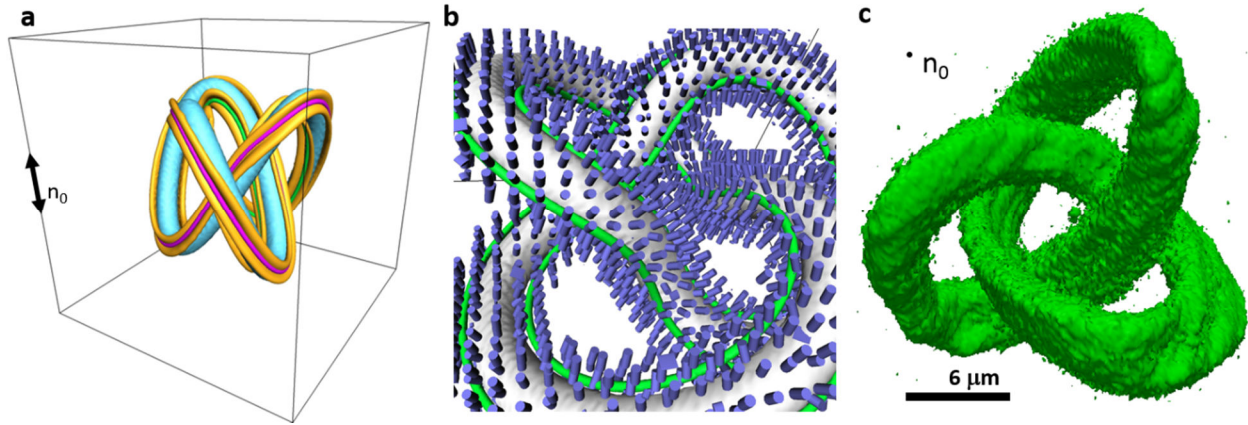


**Fig. C.4** Director distortions in the vicinity of the knotted particle with tangential surface anchoring conditions for the LC director. (a) A view along the axis of the torus knot parallel to the far-field director. (b, c) Zoomed-in perspective views of different regions around the boojum defects. The green patches depict regions of reduced scalar order parameter. Note that this figure shows a left-handed knot while Fig. 2 in the main text shows a right-handed one; the knotted tubes and the induced director fields corresponding to the knots of opposite chirality are mirror (non-superimposable) images of each other.

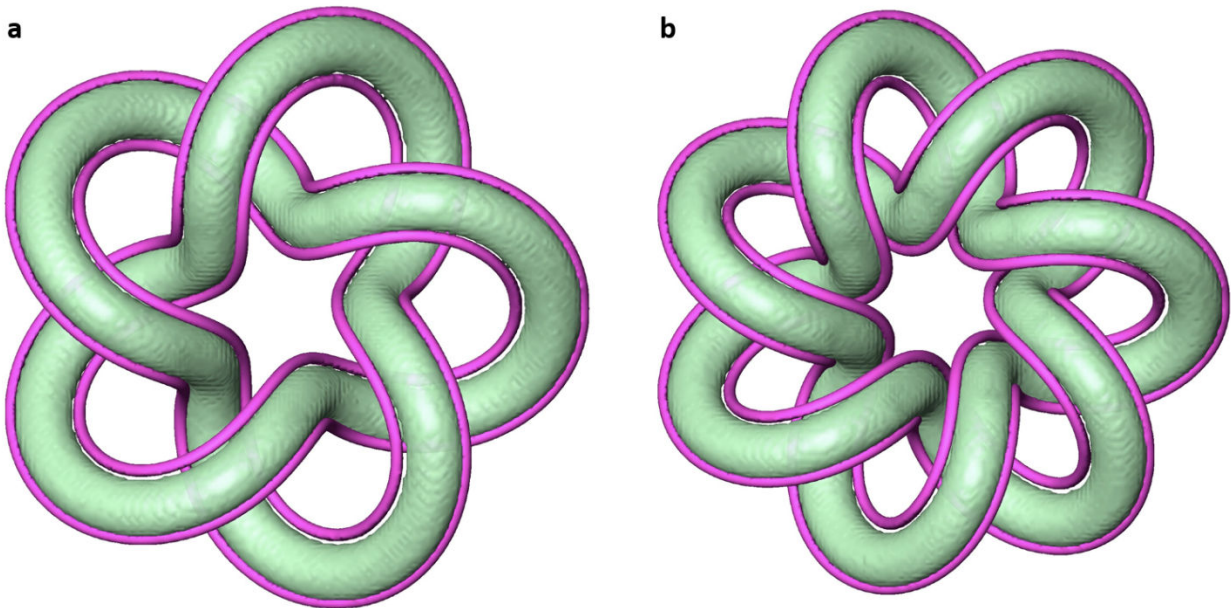




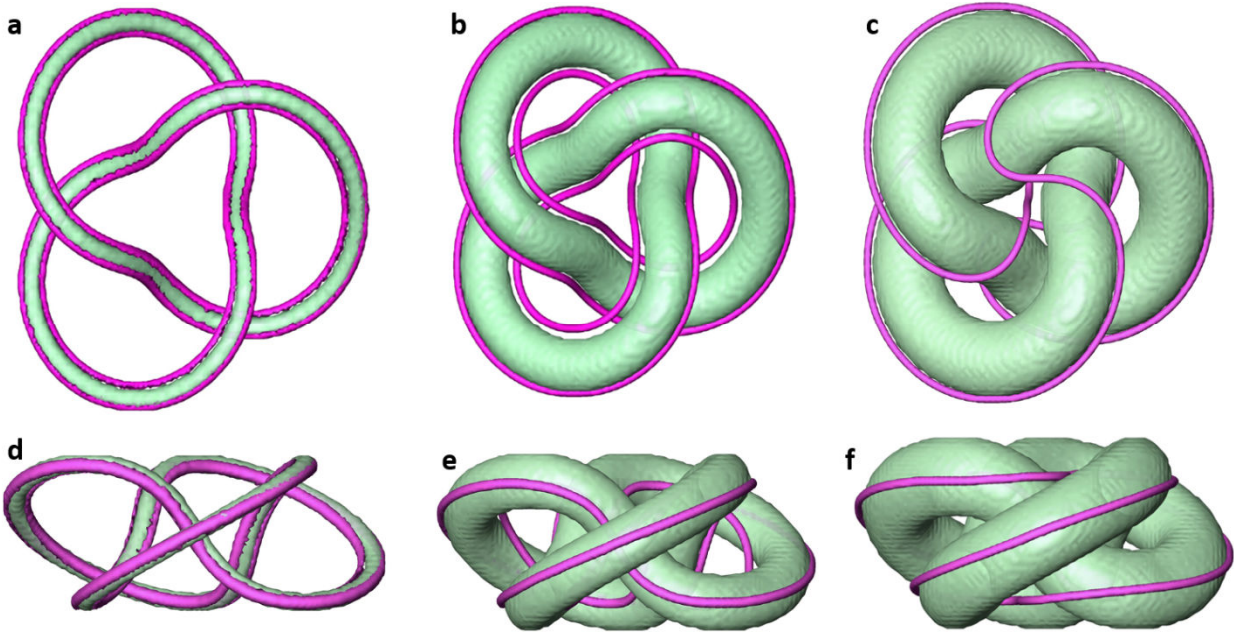
**Fig. C.5** Metastable states of knotted particles aligned at different orientations with respect to the far-field director. The images were obtained in (a-o) planar LC cells and (q-s) in a homeotropic LC cell. (a, e, i, m, q) brightfield transmission-mode images; (b, f, j, n, r) polarizing optical micrographs obtained between crossed polarizers marked on the images; (c, g, k, o, s) polarizing optical micrographs obtained between crossed polarizers and with an additional 530 nm phase retardation plates inserted with the slow axis as shown on the images by blue double arrows. The orientations of studied particles with respect to the far-field director are depicted using models of knots in (d, h, l, p, t). (u, v) Two different perspective views of one of the metastable numerically simulated director structures and defects induced by the colloidal particles shown as an example. The green and magenta lines in (u, v) show regions with reduced scalar order parameter corresponding to the cores of two half-integer disclinations that are tracing the knotted particle tube. The location of rewirings in (f, g) is marked by red arrows.



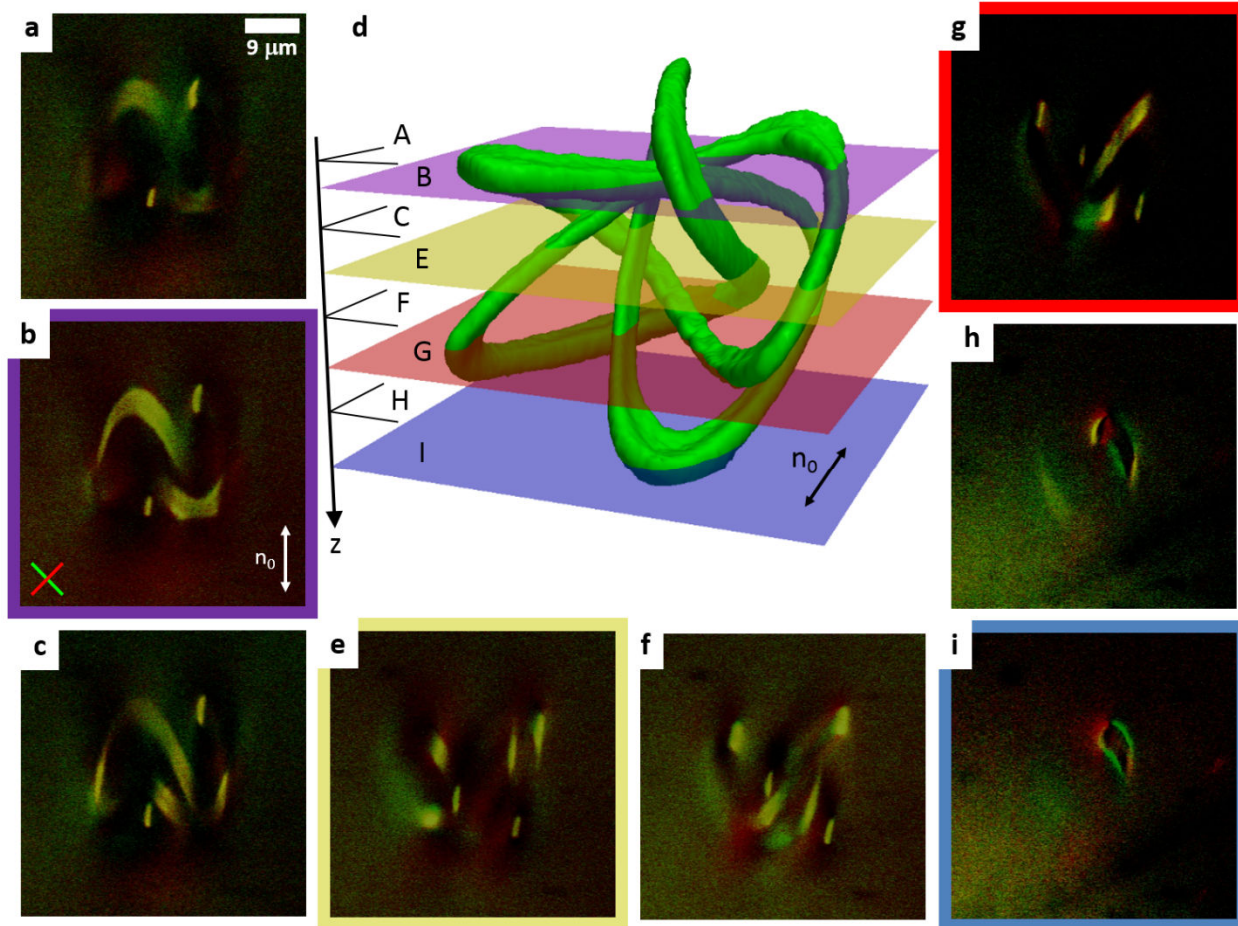
**Fig. C.6** Director structure induced by a T(3,2) trefoil knot with perpendicular anchoring in a stable orientational state. (a) Visualization of regions with the strongest elastic distortions induced by a trefoil knot colloidal particle depicted in orange color. The particle itself is shown in blue color and the disclination cores with reduced scalar order parameter are depicted using magenta and green colors. (b) Director distortions in the vicinity of a knotted particle with perpendicular surface anchoring conditions for the LC director; the disclination cores are shown as green lines of the reduced scalar order parameter. (c) 2PEF-PM image of a trefoil knot in a nematic LC oriented with the torus plane roughly perpendicular to  $\mathbf{n}_0$ .



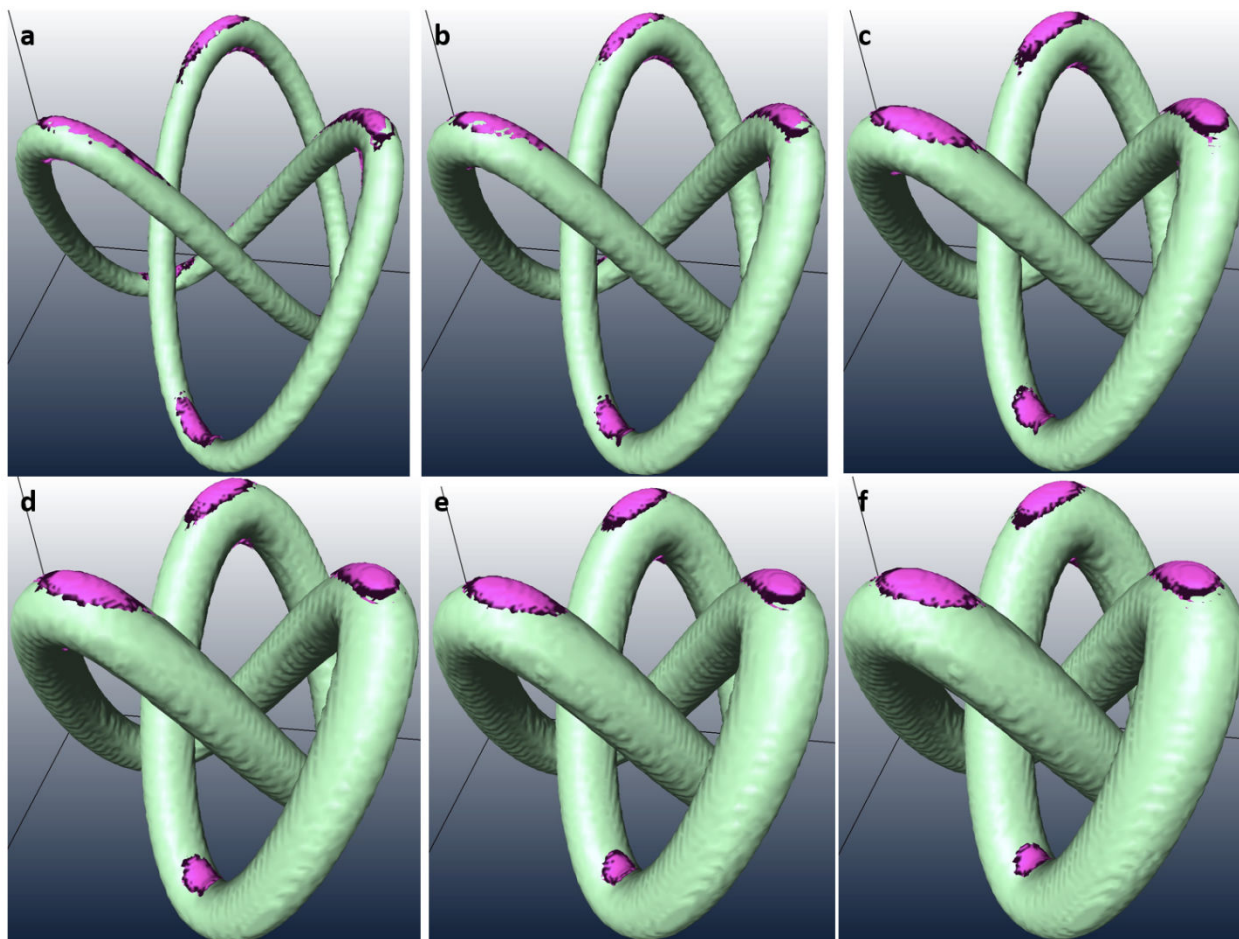
**Fig. C.7** Nematic colloidal (a) T(5,2) and (b) T(7,2) torus knots and the induced knotted pairs of  $s=-1/2$  defect lines in the otherwise smoothly varying director field. The disclination cores are shown via plotting the tube-like regions of reduced scalar order parameter (shown in magenta color). The torus planes of the colloidal knots are perpendicular to the far-field director.



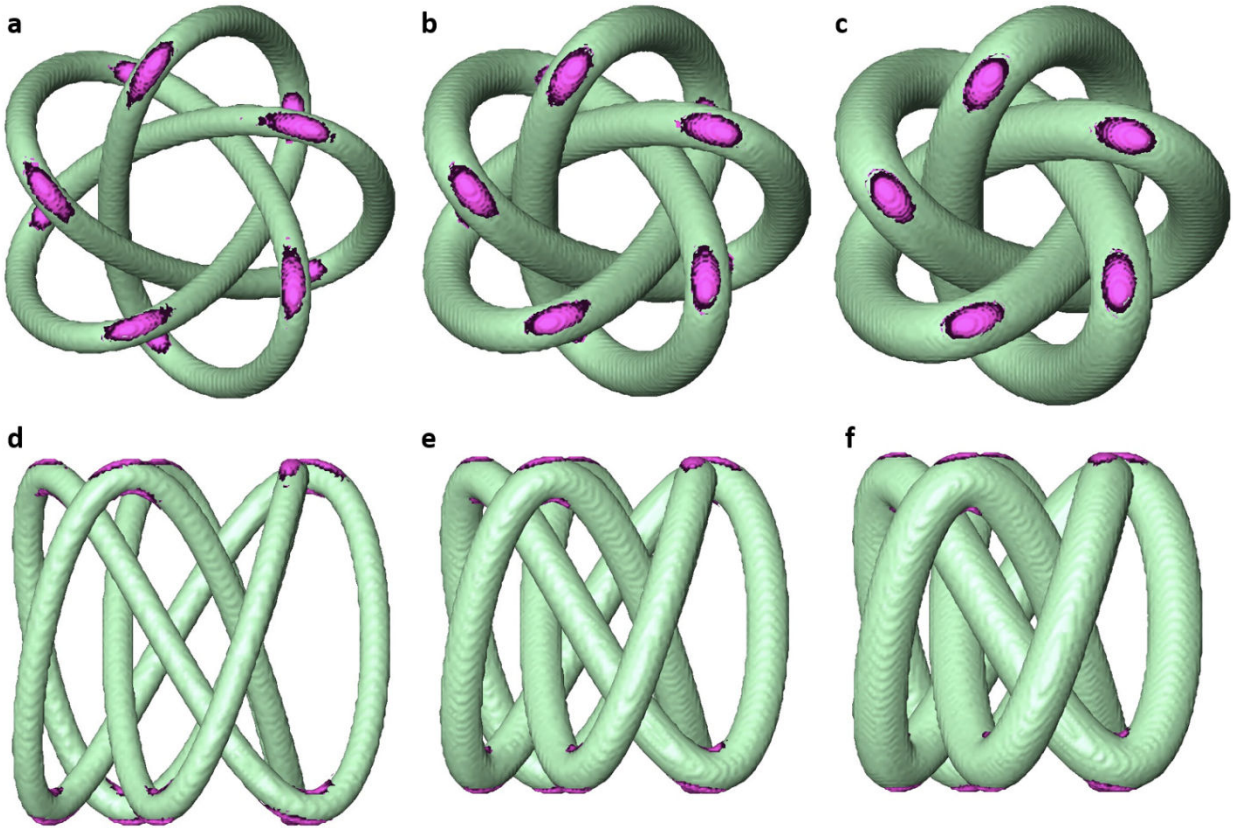
**Fig. C.8** Flattened T(3,2) knotted particles with perpendicular surface boundary conditions and different diameters of the knotted tube as viewed (a-c) along the axis of the torus knot and (d-f) in a direction perpendicular to it. The torus planes of the colloidal knots are perpendicular to the far-field director. The type and location of defects cores are depicted via showing regions with a reduced scalar order parameter (magenta color). The reduced-order regions of disclinations in otherwise continuously varying director field were obtained by minimizing the total free energy of the LC containing particles with knotted tubes of different diameter and imposing strong perpendicular surface anchoring boundary conditions.



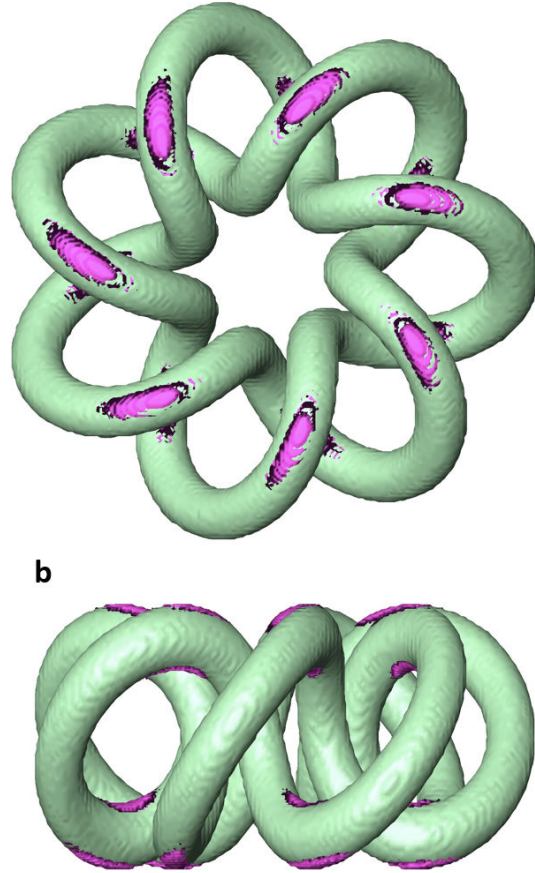
**Fig. C.9** Probing the director structure around a T(5,3) colloidal knot via 3PEF-PM slicing (a-c and e-i) of an aligned nematic LC sample with the particle. The locations of two-dimensional cross-sections of the particle and the induced director distortions are marked in the perspective view in (d) that was reconstructed from such optical slices. The knotted particle is aligned with its torus plane perpendicular to the far-field director.



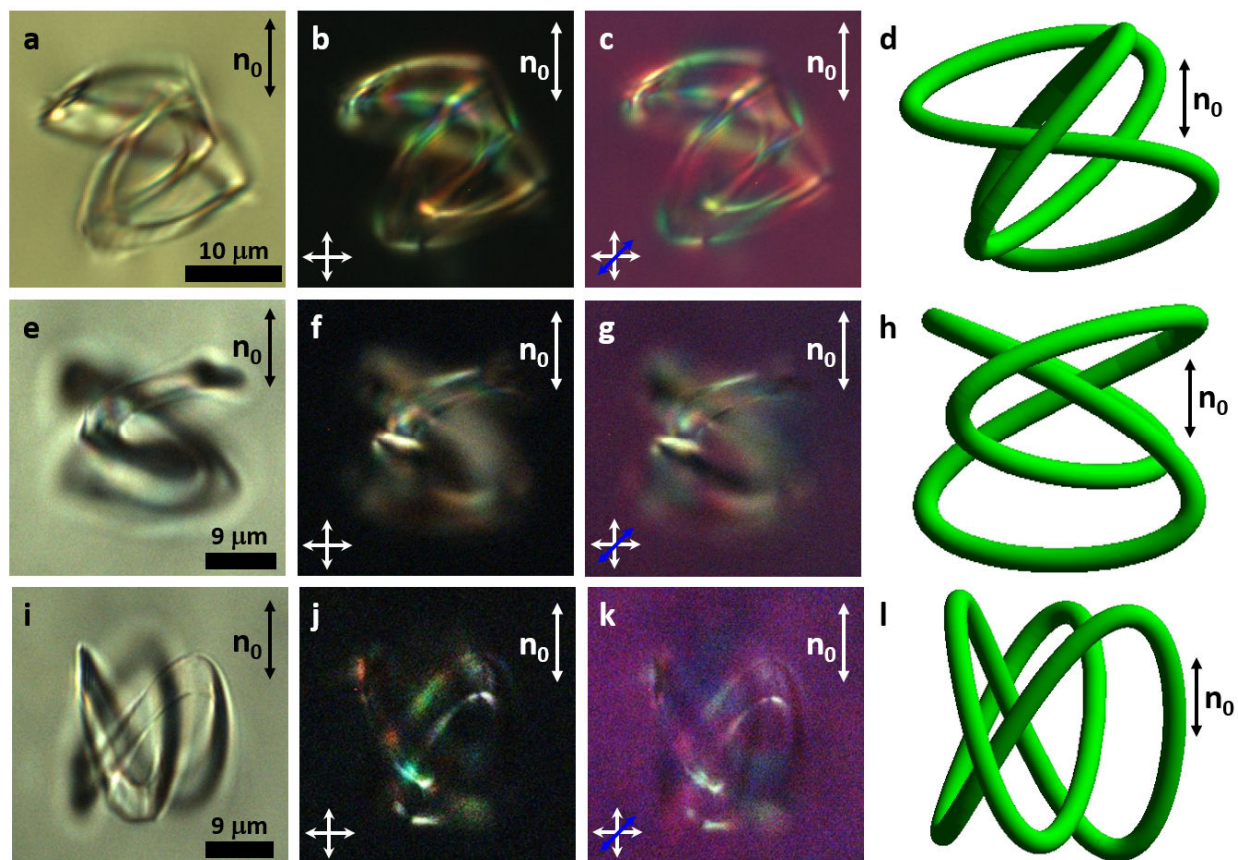
**Fig. C.10** Numerical study of boojum defects induced by a trefoil knot particles of different tube diameter. The torus planes of the colloidal knots are perpendicular to the far-field director. The results are presented by showing the regions with reduced scalar order parameter (depicted using magenta color) for trefoil knots of varying tube diameter. The reduced-order regions and the corresponding director field distortions were obtained by minimizing the total free energy of the LC with incorporated knotted particles in the form of solid tubes having tangential boundary conditions and different diameter.



**Fig. C.11** Numerical study of boojum defects induced by a  $T(5,3)$  particle knot. The defects are visualized via showing regions with reduced scalar order parameter (depicted using magenta color) for a  $T(5,3)$  colloidal knots of varying tube diameter. The reduced-order regions shown in (a-f) were obtained by minimizing the total free energy of the LC with knotted particles of different tube diameters. The torus planes of these colloidal knots are perpendicular to the far-field director.

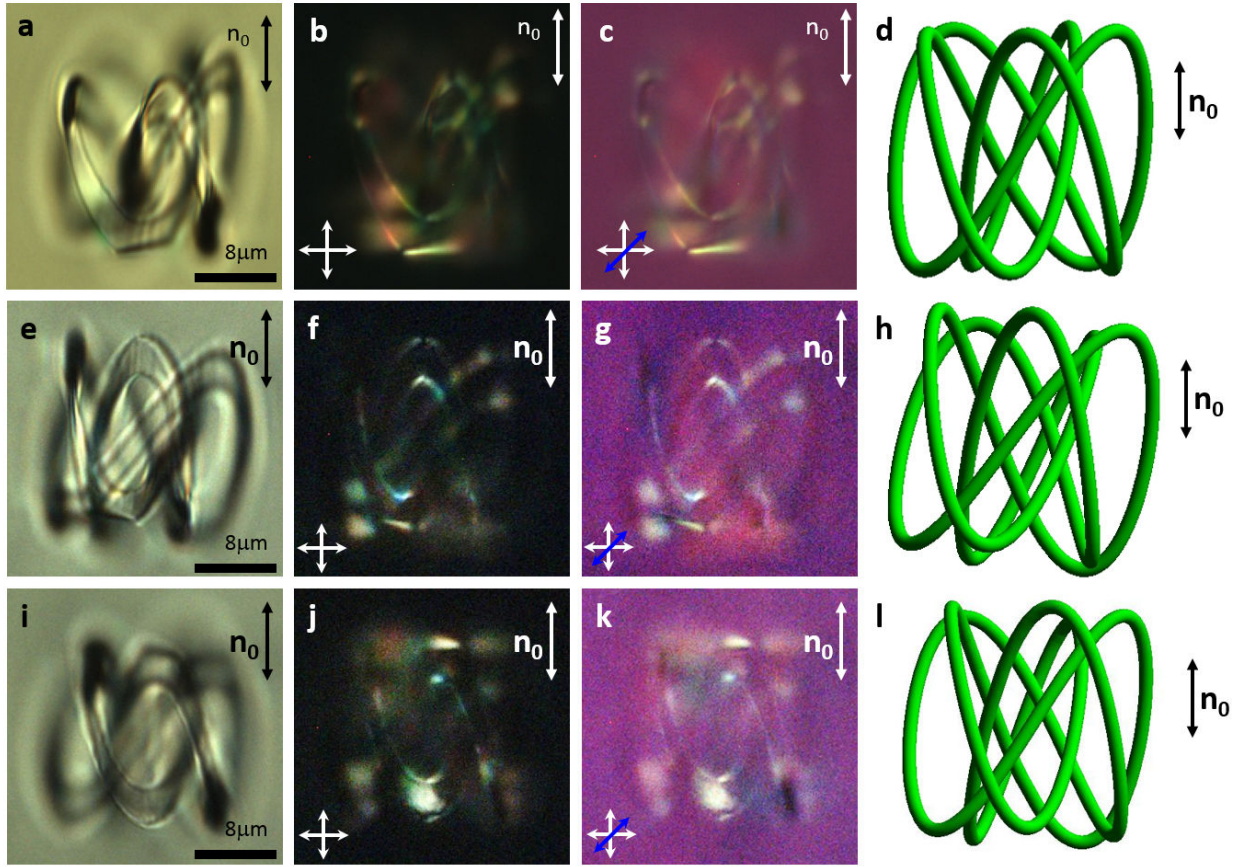


**Fig. C.12** Numerical study of boojums induced by a torus knot  $T(7,2)$  particle with tangential boundary conditions. (a, b) Perspective views of a numerical model showing boojums (seen as magenta regions of reduced scalar order parameter) induced by a  $T(7,2)$  particle, as viewed (a) along the torus axis and (b) perpendicular to it.

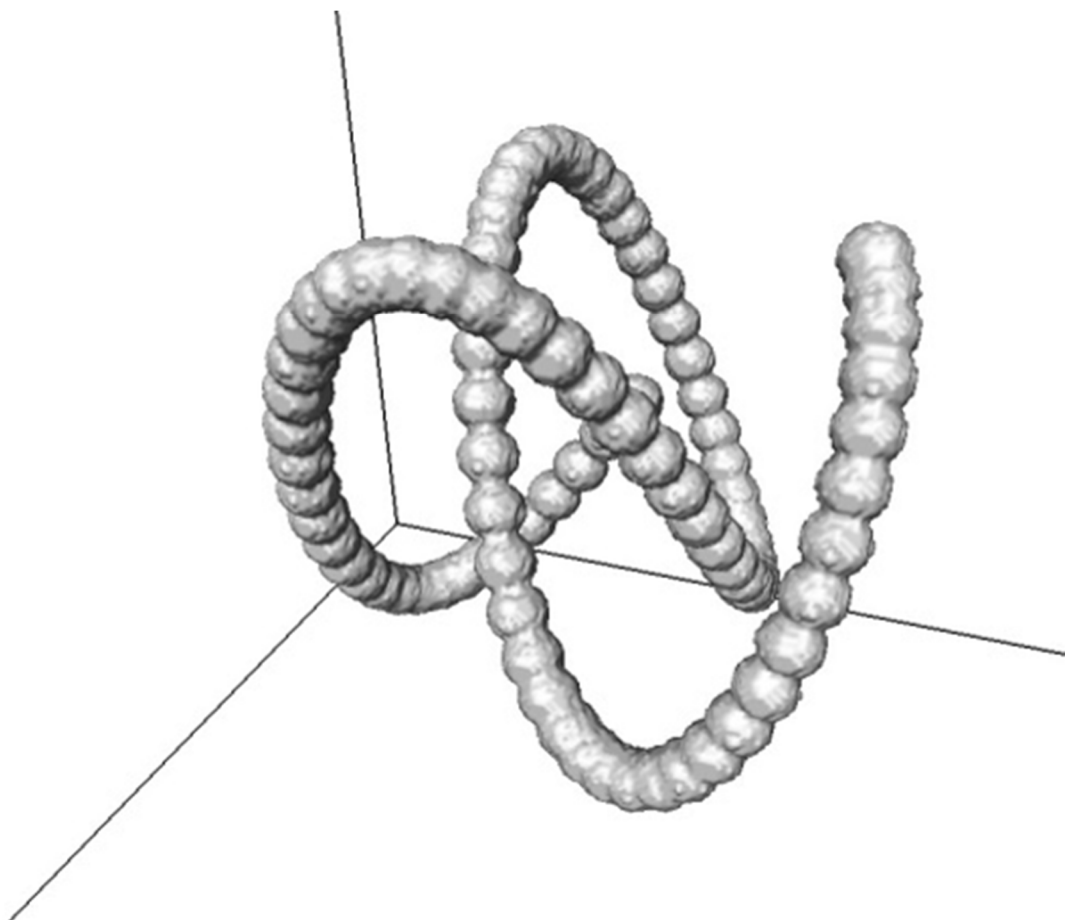


**Fig. C.13** Trefoil-knot  $T(3,2)$  colloidal particles at different angles between the torus axis and the far-field director. a-c, e-g, and i-k, Optical micrographs of metastable orientational states of trefoil knots with tangential surface boundary conditions in a 5CB nematic LC with the used polarizers and retardation plate labeled on the corresponding figure panels. These images were taken (a, e, i) without polarizers, (b, f, j) between crossed polarizers and (c, g, k) between crossed polarizers with a full-wave retardation plate inserted with slow axis at  $45^\circ$  to crossed polarizers (shown by blue double arrows). (d, h, l) The computer-generated 3D schematics depict metastable orientations of the studied topological colloids with respect to the far-field director.





**Fig. C.14** T(5,3)-knot colloidal particles at different angles between the torus axis and the far-field director. (a-c, e-g and i-k) Optical micrographs of metastable orientational states of T(5,3) knots with tangential surface anchoring in a nematic LC; the polarizers (white double arrows) and retardation plates (blue double arrows) used for imaging are labeled on the corresponding figure panels. These images were taken (a, e, i) without polarizers, (b, f, j) between crossed polarizers and (c, g, k) between crossed polarizers with a full-wave plate inserted with slow axis at  $45^\circ$  with respect to the crossed polarizers. (d, h, l) The computer-generated 3D schematics depict the metastable orientations of the studied colloids with respect to the far-field director.



**Fig. C.15** Knot-particle allocation by scanning a sphere of fixed radius along the knotted line. The snapshot shows allocation after 90 scanning steps (typically we use a total of 10000 for the knotted particle allocation).

## C.6 References

1. R. P. Trivedi, T. Lee, K. Bertness, I. I. Smalyukh, *Opt Exp* 2010, **18**, 27658.
2. M. Ravnik, S. Žumer, *Liq. Cryst.* 2009, **36**, 1201.

## Appendix D

### Description of shape and modeling for linked colloids

#### D.1 Geometric shapes of linked colloidal building blocs

To define colloidal links using two-photon photopolymerization, we used the following equations:

$$\begin{array}{llll} & x_1 = s \cos \theta & x_2 = s (\cos \theta + 1) & \\ \text{Hopf link} & y_1 = s \sin \theta \sin \phi & y_2 = s \sin \theta \sin \phi & 0 \leq \theta \leq 2\pi \\ & z_1 = s \sin \theta \cos \phi & z_2 = -s \sin \theta \cos \phi & \end{array}$$

$$\begin{array}{llll} & x_2 = 2s \cos \theta & x_1 = 2s \cos \theta & \\ \text{Solomon link} & y_2 = s \sin \theta & y_1 = s \sin \theta & 0 \leq \theta \leq 2\pi \\ & z_2 = 2s \sin 2\theta & z_1 = 2s \sin(-2\theta) & \end{array}$$

In these equations,  $s$  is a sizing factor and  $\phi$  defines the relative tilt ( $2\phi$ ) between the linked rings.

In our two-photon photo-polymerization experiments, we initially set  $\phi = \pi/4$  during the fabrication but this angle is free to change once the particles are detached from substrates and dispersed in the LC. The subscripts (1 and 2) in these equations refer to the individual rings within the link. Typically, we draw the particles, automatically and one by one, in small arrays ranging from four to sixteen. By manually printing multiple arrays, we can generally fabricate a couple hundred to about 1,000 links per hour.

From the theory standpoint, we exploit the Open Source *Gmsh* library [1] to triangulate the surfaces of the individual components of Hopf and Solomon link colloids. We set  $s = 1 \mu\text{m}$  and  $s = 0.75 \mu\text{m}$  for Hopf and Solomon link respectively. In both cases the components have a circular cross-section with the radius  $r = 0.1 \mu\text{m}$  for Hopf link and  $r = 0.05 \mu\text{m}$  for Solomon link.

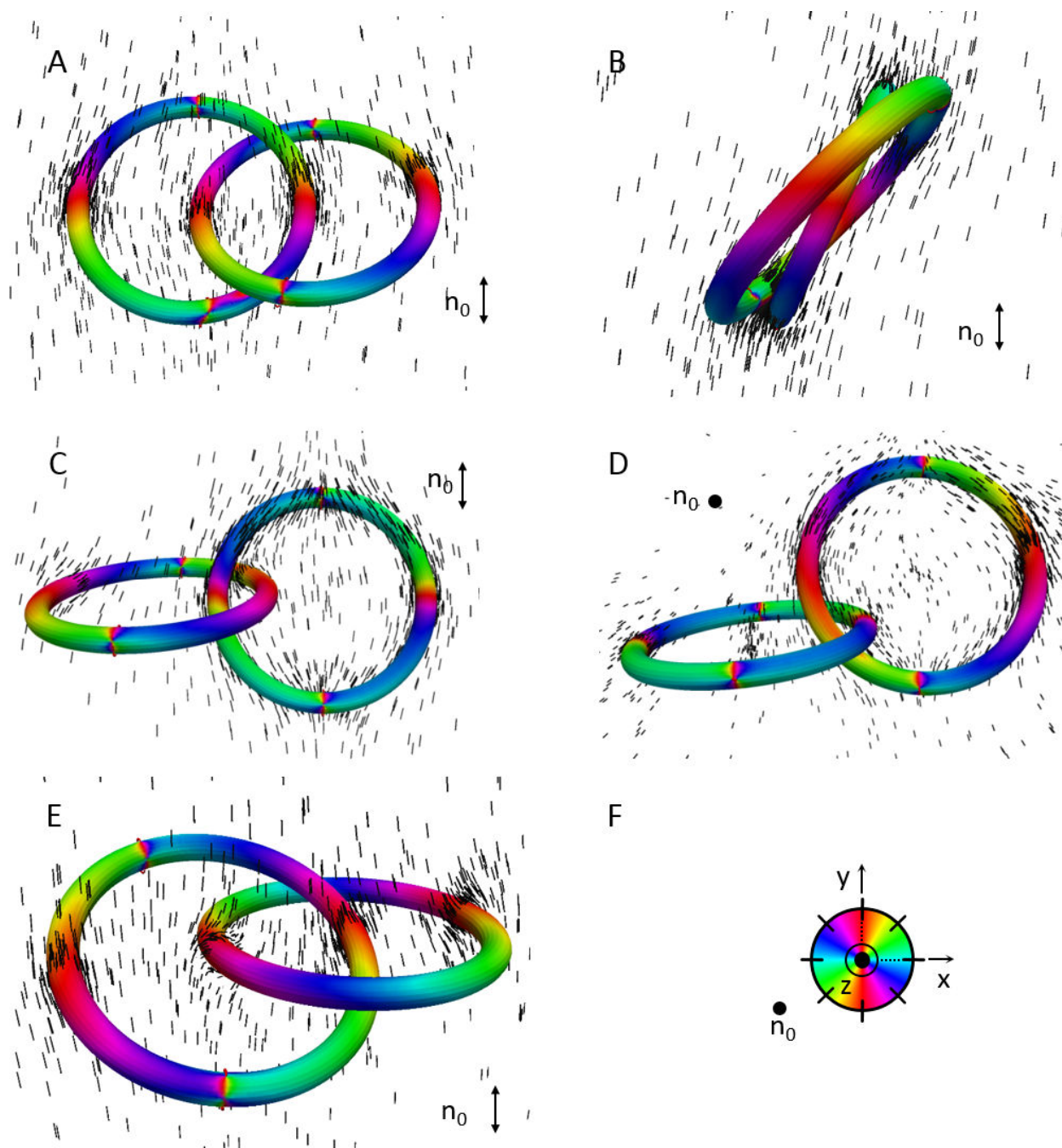
## D.2 Details of the numerical approach and specification of the model parameters

The volume discretization is performed with the *Quality Tetrahedral Mesh Generator* [2]. Linear triangular and tetrahedral elements are used and the integration over the elements is performed numerically by using fully symmetric Gaussian quadrature rules [3-5]. The discretized Landau-de Gennes functional is minimized with the help of *INRIA's MIQN3* optimization routine [6].

For spatially uniform uniaxial ansatz  $Q_{ij} = 3Q_b(n_i n_j - \delta_{ij}/3)/2$  the Landau-de Gennes free energy in Eq. (D.1) predicts the isotropic-nematic coexistence takes place at  $\tau \equiv 24ac/b^2 = 1$  and that the bulk nematic scalar order parameter

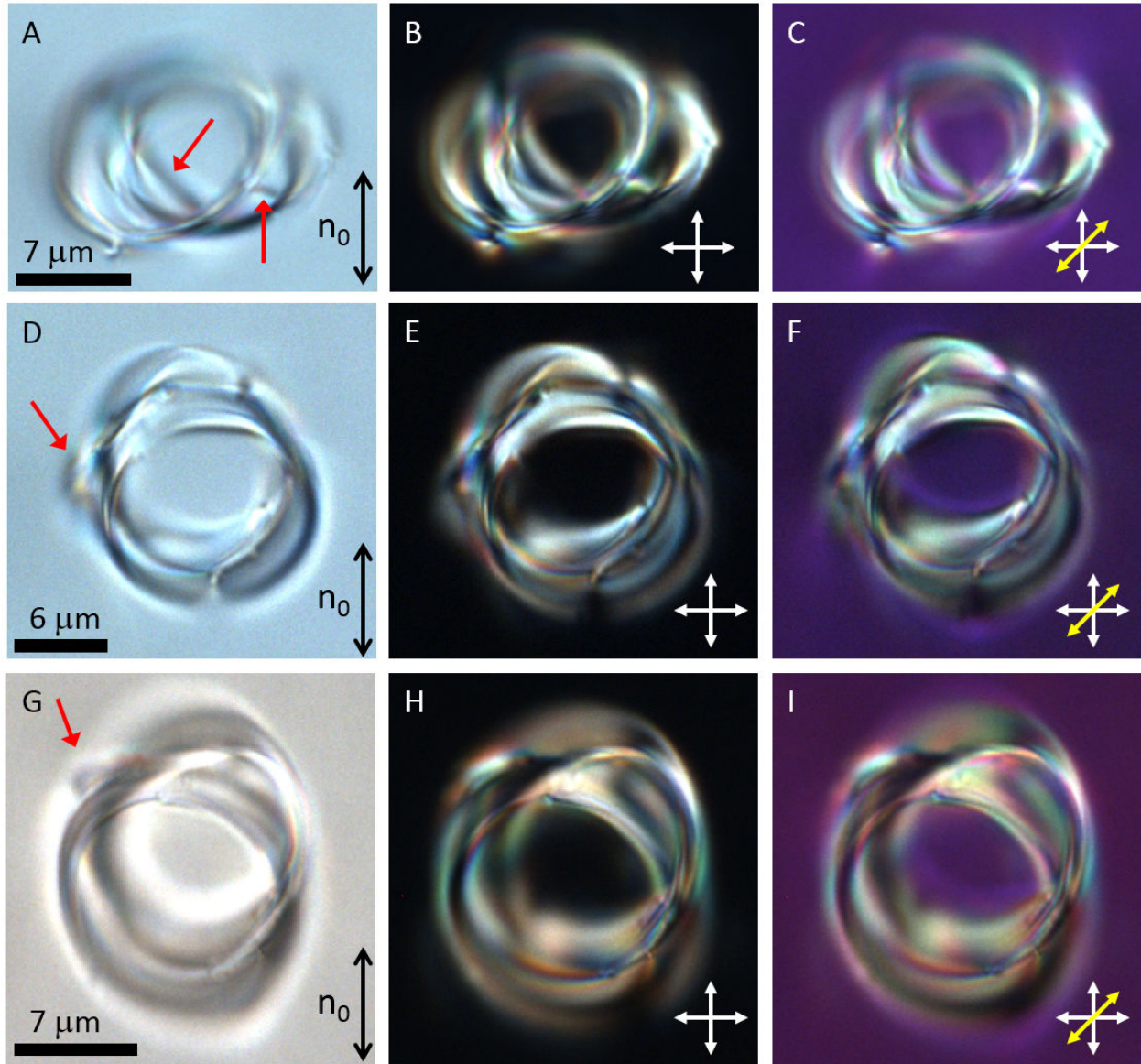
$$Q_b = \frac{b}{8c} \left( 1 + \sqrt{1 - \frac{8\tau}{9}} \right). \quad (\text{D.1})$$

We assume  $a(T) = a_0(T - T^*)$  and  $a_0$  is a phenomenological material dependent parameter,  $T^*$  is the supercoiling temperature of the isotropic phase. We use  $a_0 = 0.044 \times 10^6 \text{J/m}^3$ ,  $b = 0.816 \times 10^6 \text{J/m}^3$ ,  $c = 0.45 \times 10^6 \text{J/m}^3$ ,  $L_1 = 6 \times 10^{-12} \text{J/m}$ , and  $L_2 = 12 \times 10^{-12} \text{J/m}$ , (typical values for 5CB [7])  $T^* = 307 \text{ K}$ . The size of topological defect cores is of the order of the bulk correlation length  $\xi = 2(2c(3L_1 + 2L_2))^{1/2}/b \simeq 15 \text{nm}$  at the isotropic-nematic transition [8].

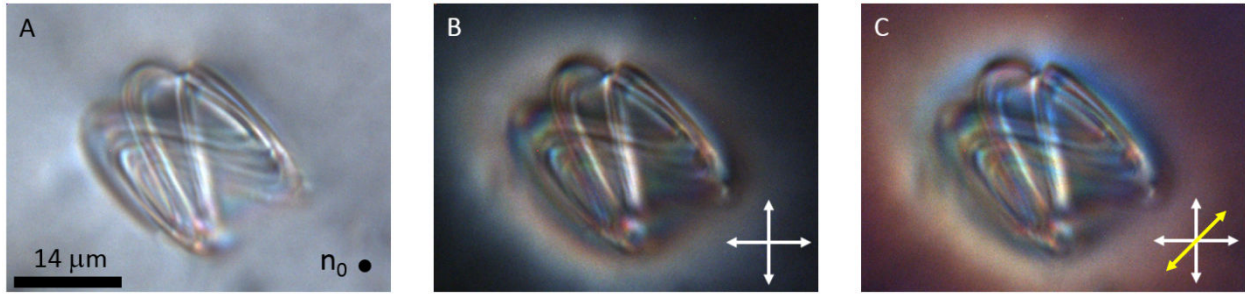


**Fig. D.1** Simulations of planar Hopf Links. (A,B) Two more perspective views of the Hopf link simulation corresponding to the configuration observed in Fig. 6.3A,B. (C,D) Two more perspective views of the Hopf link simulation corresponding to the configuration observed in Fig. 6.3D,E. (E) A simulation with parameters slightly deviated from the simulation shown in Fig. 6.3F. The vertically (parallel to the farfield) oriented ring was slightly rotated away from vertical, resulting in a configuration lacking boojums on the surface of the horizontally

(perpendicular to the farfield) oriented ring, which is observed in the case shown in Fig. 6.3D,E. (F) Legend mapping molecular orientation at the surfaces of the link to color.

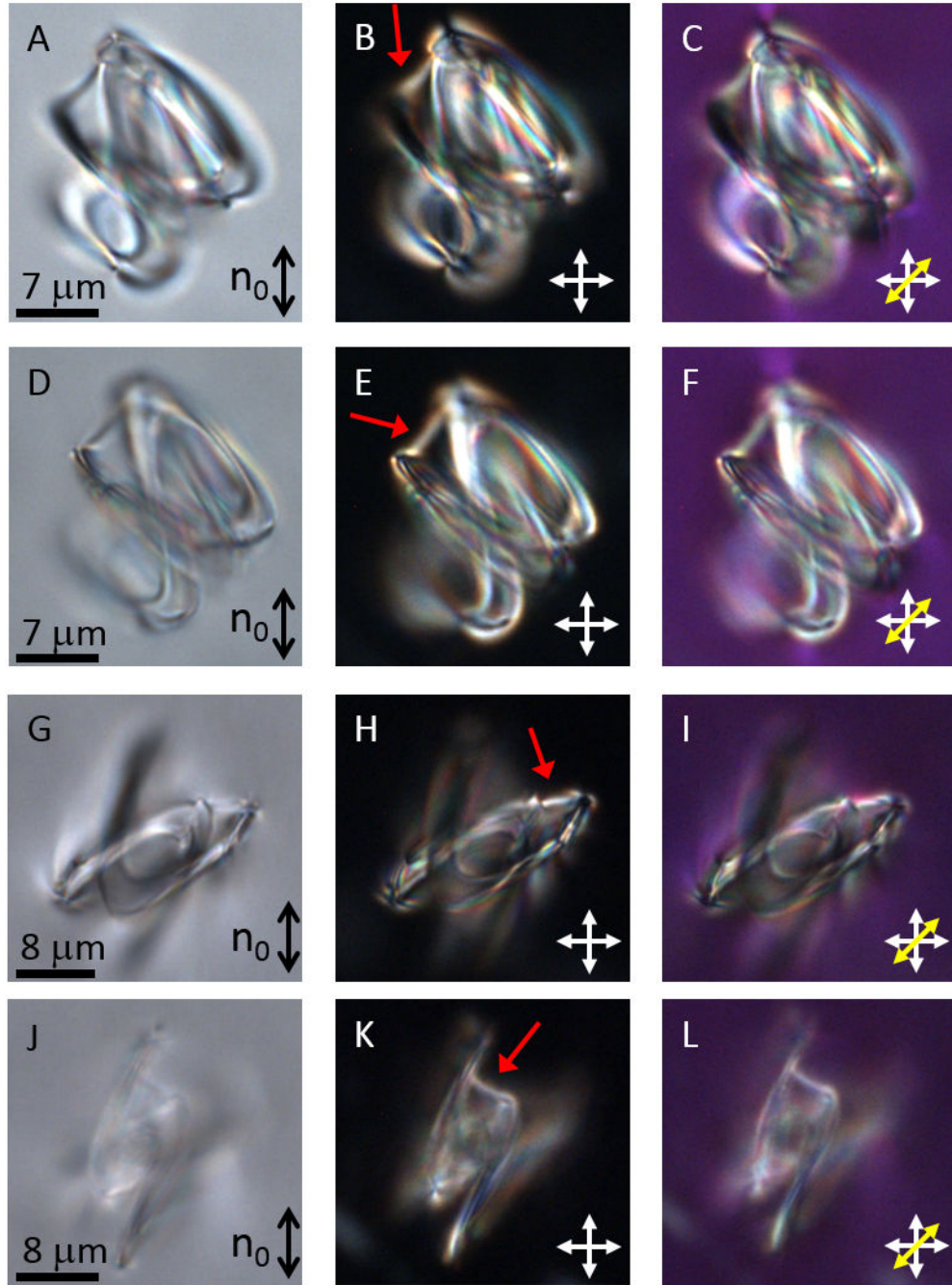


**Fig. D.2** Metastable states of compact homeotropic Hopf Links. (A-I) Hopf links with homeotropic boundary conditions in a vertically aligned nematic field. Panels A, D and G show three unpolarized brightfield images of links with similar configurations to that in Fig. 6.6. The same links are shown imaged between crossed polarizers in panels B, E, and H and between crossed polarizers with an inserted full waveplate (slow axis along the yellow double arrow) in panels C, F, and I. The red arrows point out interesting defect lines induced by the colloidal link.



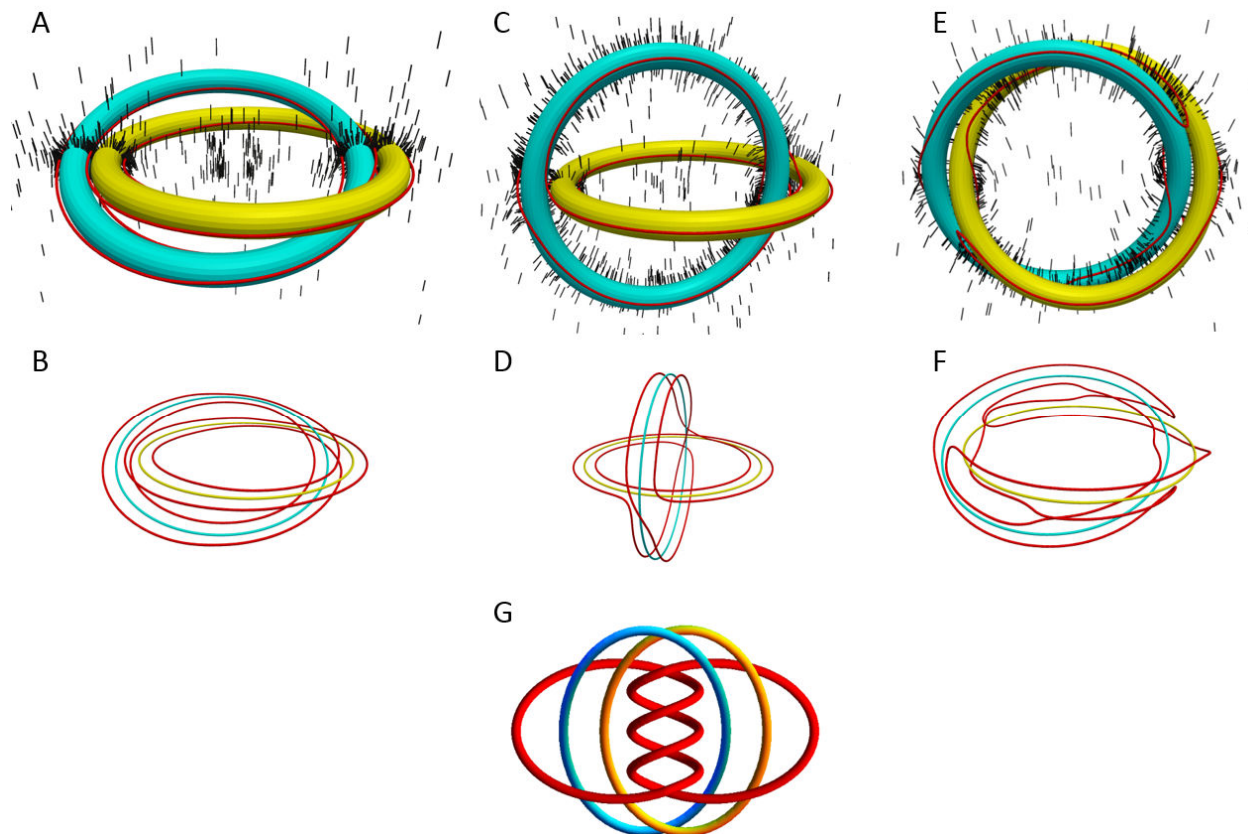
**Fig. D.3** Another metastable state of a planar Solomon Link. (A) Solomon link with planar boundary conditions in a homeotropically aligned nematic field. Panel A shows an unpolarized brightfield image of a link with a similar configuration to that in Fig. 6.7A,B. The same link is shown imaged between crossed polarizers in panel B and between crossed polarizers with an inserted full waveplate (slow axis along the yellow double arrow) in panel C.



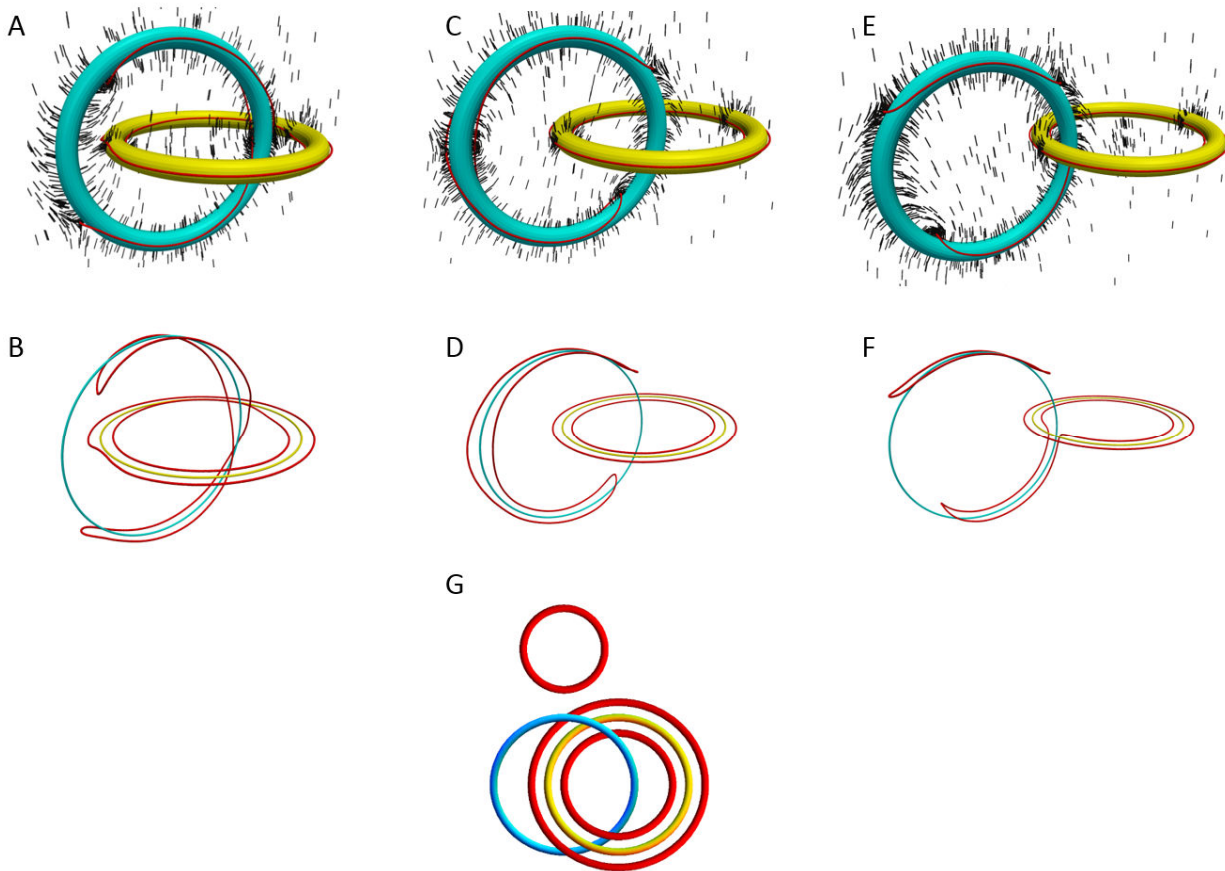


**Fig. D.4** Metastable states of homeotropic Solomon Links. (A-L) Solomon links with homeotropic boundary conditions in a vertically aligned nematic field. Panels A, D, G and J show four unpolarized brightfield images of links with similar configurations to that in Fig. 6.6. The same links are shown imaged between crossed polarizers in panels B, E, H and K and between crossed polarizers with an inserted full waveplate (slow axis along the yellow double arrow) in panels C, F, I and L. Panels (A-C) and (G-I) show the same links in panels (D-F) and (J-L),

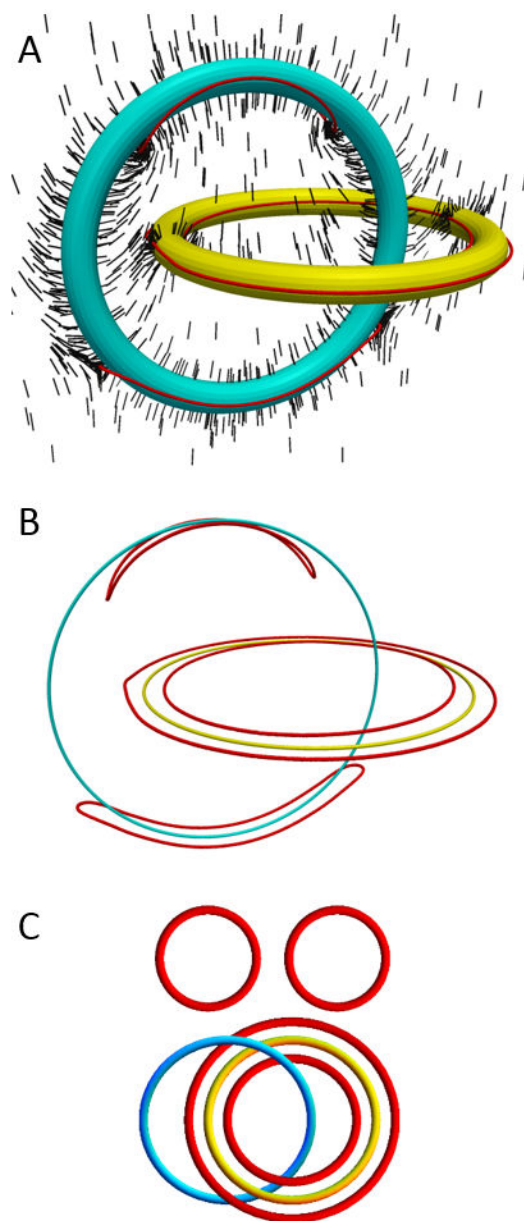
respectively, but focused at two different depths. The red arrows point out interesting defect lines induced by the colloidal link.



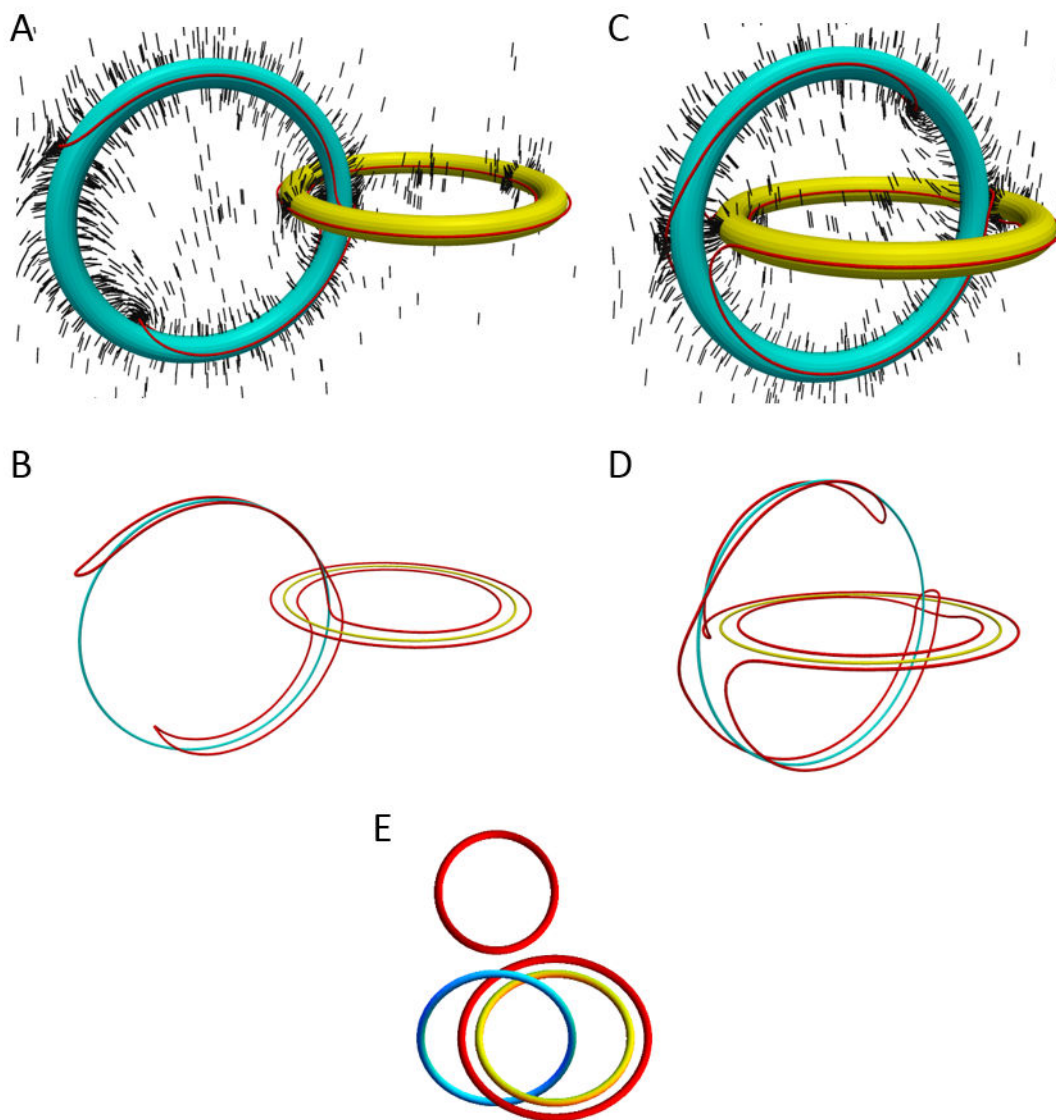
**Fig. D.5** Simplified topologies of various simulated configurations of homeotropic Hopf links. (*A, C, E*) 3D models of three distinct simulated Hopf links with homeotropic boundary conditions. The cyan and yellow rings represent physical colloidal particles dispersed in a nematic LC, the red lines show defect loops following the colloid-LC interface and black lines in a cross-sectional plane depict a slice of the surrounding molecular field orientations. (*B, D, F*) The same simulations shown in (*A, C, E*) with the cyan and yellow tubes reduced in thickness. (*G*) Simplified diagram revealing the common linked topology of all three configurations.



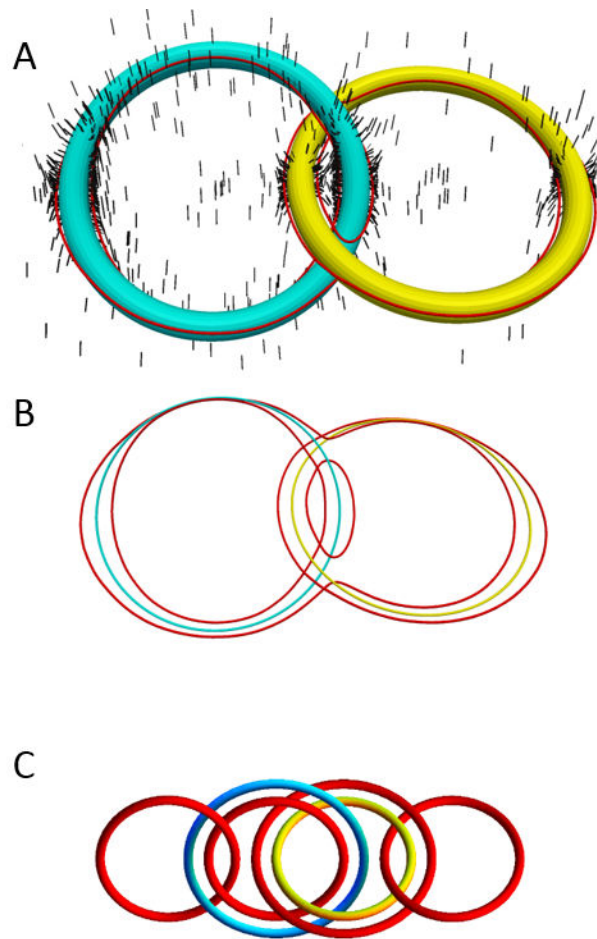
**Fig. D.6** Simplified topologies of various simulated configurations of homeotropic Hopf links. *(A, C, E)* 3D models of three distinct simulated Hopf links with homeotropic boundary conditions. The cyan and yellow rings represent physical colloidal particles dispersed in a nematic LC, the red lines show defect loops following the colloid-LC interface and black lines in a cross-sectional plane depict a slice of the surrounding molecular field orientations. *(B, D, F)* The same simulations shown in *(A, C, E)* with the cyan and yellow tubes reduced in thickness. *(G)* Simplified diagram revealing the common linked topology of all three configurations.



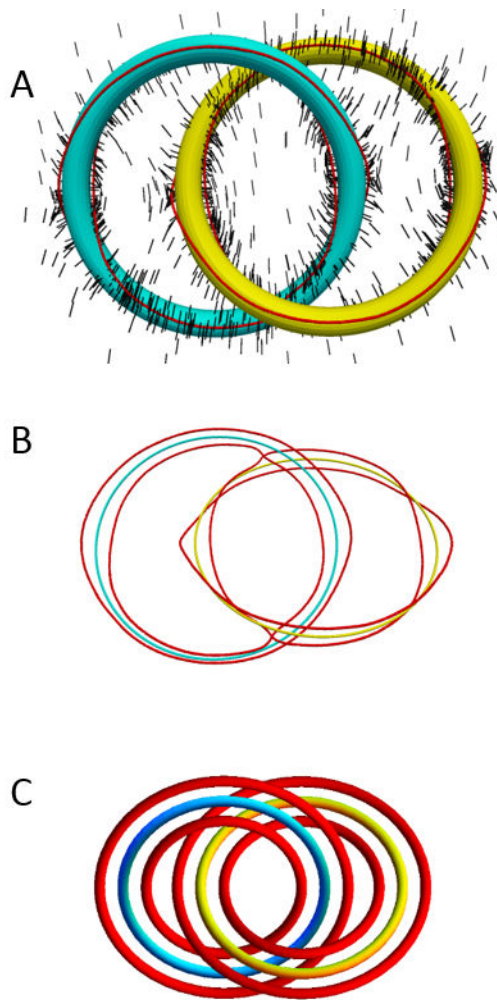
**Fig. D.7** Simplified topologies of a simulated configuration of a homeotropic Hopf link. (A) A 3D model of a simulated Hopf link with homeotropic boundary conditions. The cyan and yellow rings represent physical colloidal particles dispersed in a nematic LC, the red lines show defect loops following the colloid-LC interface and black lines in a cross-sectional plane depict a slice of the surrounding molecular field orientations. (B) The same simulations shown in (A) with the cyan and yellow tubes reduced in thickness. (C) Simplified diagram revealing the linked topology of this configuration.



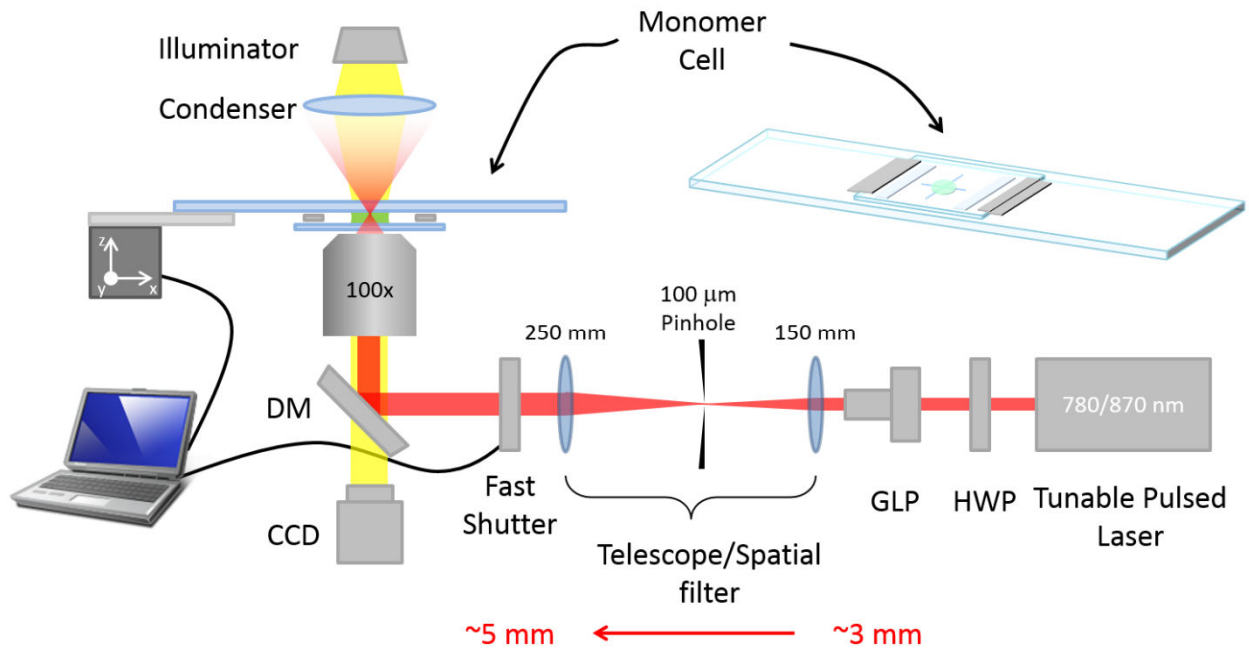
**Fig. D.8** Simplified topologies of two simulated configurations of homeotropic Hopf links. (*A*, *C*) 3D models of two distinct simulated Hopf links with homeotropic boundary conditions. The cyan and yellow rings represent physical colloidal particles dispersed in a nematic LC, the red lines show defect loops following the colloid-LC interface and black lines in a cross-sectional plane depict a slice of the surrounding molecular field orientations. (*B*, *D*) The same simulations shown in (*A*, *C*) with the cyan and yellow tubes reduced in thickness. (*E*) Simplified diagram revealing the common linked topology of both configurations.



**Fig. D.9** Simplified topologies of a simulated configuration of a homeotropic Hopf link. (A) A 3D model of a simulated Hopf link with homeotropic boundary conditions. The cyan and yellow rings represent physical colloidal particles dispersed in a nematic LC, the red lines show defect loops following the colloid-LC interface and black lines in a cross-sectional plane depict a slice of the surrounding molecular field orientations. (B) The same simulations shown in (A) with the cyan and yellow tubes reduced in thickness. (C) Simplified diagram revealing the linked topology of this configuration.



**Fig. D.10** Simplified topologies of a simulated configuration of a homeotropic Hopf link. (A) A 3D model of a simulated Hopf link with homeotropic boundary conditions. The cyan and yellow rings represent physical colloidal particles dispersed in a nematic LC, the red lines show defect loops following the colloid-LC interface and black lines in a cross-sectional plane depict a slice of the surrounding molecular field orientations. (B) The same simulations shown in (A) with the cyan and yellow tubes reduced in thickness. (C) Simplified diagram revealing the linked topology of this configuration.



**Fig. D.11** Schematic diagram showing the two-photon photo-polymerization system used for fabrication of complex-shaped microstructures with an added spatial filter for improved beam quality. A monomer-containing cell is mounted on a computer-controlled nano-positioning stage over the microscope objective (100x). A tunable pulsed laser beam passes through a half-wave plate (HWP), glan laser polarizer (GLP), and a spatial filter before being switched by a computer controlled shutter. A dichroic mirror (DM) reflects the beam into the back aperture of the objective. A charge-coupled device (CCD) camera captures light transmitted by the dichroic mirror and allows for real-time observation of the polymerization process.



### D.3 References

1. *Gmsh: a three-dimensional finite element mesh generator* (2014) available at <http://geuz.org/gmsh/>.
2. Si H (2011) Tetgen: A quality tetrahedral mesh generator and a 3D Delaunay triangulator. Available at <http://wias-berlin.de/software/tetgen/>.
3. Cools R (2003) An Encyclopaedia of Cubature Formulas. *J Complexity* 19:445 453. Available at <http://nines.cs.kuleuven.be/ecf/>.
4. P. Keast, *Mech Eng Comput Methods Appl Mech Eng* 1986, **55**, 339.
5. A. H. Stroud, *Approximate calculation of multiple integrals*, Prentice-Hall, Englewood Cliffs, N.J., 1971.
6. Gilbert JC, Lemaréchal C (1989) Some numerical experiments with variable storage quasi-Newton algorithms. *Math Program* 45:407 436. Available at <https://who.rocq.inria.fr/Jean-Charles.Gilbert/modulopt/optimization-routines/m1qn3/m1qn3.html>.
7. S. Kralj, S. Žumer, D. W. Allender, *Phys Rev A* 1991, **43**, 2943.
8. S. Chandrasekhar, *Liquid Crystals, 2nd ed.*, Cambridge University, 1992.